UNIVERSITÀ DEGLI STUDI DI PADOVA

Sede Amministrativa: Università degli Studi di Padova

Dipartimento di Ingegneria dell'Informazione

SCUOLA DI DOTTORATO DI RICERCA IN INGEGNERIA DELL'INFORMAZIONE
INDIRIZZO: SCIENZA E TECNOLOGIA DELL'INFORMAZIONE
CICLO XXIV

Advanced Control of Power Converters for Efficient Use of Distributed Energy Resources in Future Smart Microgrids

Direttore della Scuola: Ch.mo Prof. Matteo Bertocco
Coordinatore d'indirizzo: Ch.mo Prof. Andrea Neviani

Supervisore: Ch.mo Prof. Simone Buso
Correlatori: Ch.mo Prof. Paolo Tenti
Ch.mo Prof. Paolo Mattavelli

Dottorando: Alessandro Costabeber

Alla mia famiglia
e a tutte le persone
a cui voglio bene

I treni

I treni viagia par l'eternità.

No i riva mai a la stazion.

Se i ghe rivasse

se i se fermasse

partiria la stazion.

Ernesto Calzavara

"Ombre sui veri", 1990

Acknowledgments

I want first of all to manifest my gratitude to my supervisors Prof. Simone Buso, Prof. Paolo Mattavelli and Prof. Paolo Tenti for their support and encouragements during my Ph.D.. I owe them most of the successful results obtained in the past three years and my scientific and personal growth. My gratitude is also due to all the other people of the Power Electronics (PEL) research group in Padova, Prof. Giorgio Spiazzi, Dr. Luca Corradini, Dr. Marco Stellini and Mr. Renato Sartorello and of the Mechatronics laboratory in Vicenza, in particular to Prof. Mauro Zigliotto and Dr. Luca Peretti. All of them have been a valuable source of suggestions and stimulus for my research activity, and dear friends. With them I want to thank the people met during these years. Somebody only for a short time, somebody else for a longer period but all have been a fundamental human value added to the experience of my Ph.D.. Hoping to be able to remember everybody, but conscious of my unreliable memory, thanks to Matteo Carraro, Francesco Sichirollo, Elisabetta Tedeschi, Helmo Kelis Morales Peredes, Roberto Losco, Antonio Stocco, Nicolo Ronchi, Daniela Trombetti, Federica Grossi, Dario Silvello, Flavio Alessandro Serrão Goncalves and Koichi Sakata.

A special mention is for all the people I met in Nottingham during my research period there. Thanks to Prof. Mark Sumner and Prof. Pericle Zanchetta for their supervision, support and encouragement during my work. Thanks to all the other people of the PEMC group, Elisabetta Lavopa, Marco Degano, Liliana De Lillo, Lee Empiringham, Andrew Trentin, Alex Agbedahunsi, Tony Yu Duan, Chris Hill, Juako Norniella, Kwaku Amankwah, Puvan, Alan Watson, Edward Christopher, and all the technicians, in particular to Colin Blackburn and Matthew Cooper. Thanks also to the guys met during the intense and memorable football matches at the university sport centre. Thanks to all the other dear friends met in Nottingham, who gave me good times and memories, as well as a sofa when needed: Ismael Botti, Amelie Mazet, Thomas Dyjas (Bunbury St.), Luca Tarisciotti, Paolo Giangrande, Michael Galea, Ivan Capello, Antonella Capello, Pauline Melka, Claretta Onnis, Phil Street, Dan Dan Wang, Jamie Fraser, Eugenio Porcu, Valeria Sarritzu, Mario Genna, Mariann Okland (Station Rd.).

Padova, January 2012

Abstract

This work proposes a vision on the growing scenario of Smart Grids, where a pervasive introduction of distributed generators and innovative power management schemes forces a deep review of the power distribution network establishment. Despite a potentially general value of the proposed approach, the analysis is focused on low voltage microgrids as the most flexible and open architectures to demonstrate the feasibility of the network renewal. In recent years, distribution network has experienced a massive introduction of Distributed Generators (DGs). So far, this has been done based on a hierarchical government of the network, where utilities set regulations and keep control of the connections from the top of the structure. The final user has a passive role in the management, even participating to generation, owning a DG unit. This is basically due to historical reasons: the distribution architecture has been built starting from a centralized controller driven paradigm, and all the updates have been done in the same direction. This approach has been valid until the electrical generation was supplied by a limited number of large plants: huge amounts of power with all the related control challenges, but static generation infrastructure.

The upcoming scenario is instead a generation that is strongly decentralized toward distributed energy resources. At the same time, development of Information and Communication Technologies (ICT) is constantly rising. The combination of these two phenomena has the potential to change completely the power distribution system, both in the architecture and in the roles of players in the energy market.

From an architectural point of view, distributed generation units could become a combination of renewable sources such as solar, wind, small hydro turbines, fuel cells etc. and traditional sources like gas or diesel generators required for supply continuity of sensible loads. Coupled to the primary energy sources, Energy Storage (ES) can be used to introduce a degree of freedom in energy management: large storage units like batteries or flywheels can absorb the excess of generation, to provide energy during peak demand times, or perform more complex optimizations. Small energy sources, like super capacitors, can be used to improve power quality during transients such as voltage sags or frequency variation transients. These generation and storage units shall be equipped

with an intelligent digital controller able to measure all the required local variables and perform local control of power converters and also capable to communicate in a bidirectional way, for example via Power Line Communication, with other generators. The power topology of these conversion units can be generally represented as a first conversion stage, dependent on the kind of energy source, and a second stage that is a current controlled inverter. Such devices are named “Energy Gateways” (EG) and represent the basic elements of future Smart Grids in the vision presented in this work.

To limit the system complexity, a microgrid is considered: the microgrid is connected to the main low voltage distribution network and presents a number of distributed generators, all equipped with EG. In the proposed approach control of the micro grid is distributed, without centralized controllers: the microgrid internal behaviour can be optimized, as well as the microgrid behaviour seen by the main grid, based on EG to EG communication and control architecture. Considered the degrees of freedom of the resulting system, different optimizations could be performed.

In more details, the optimization considered in this work is the distribution loss minimization and it is obtained by properly controlling converters active and reactive power references in a distributed way. In particular, the normal overrating of power converters opens the possibility of injecting distributed reactive power, that can be locally delivered to the loads, reducing the absorption from the main grid and the consequent losses and voltage drops. Also the active power can be partially controlled, depending on the availability of energy storage or controllable generation units.

Different techniques have been proposed: stand-alone Energy Gateways with power references control based on local measurement only, without need for communication, or distributed solution where each EG communicates with the surrounding EGs, computes its optimum local power reference and leaves the control to another EG with a Token Ring logic: iterating the local optimization, the system converges to a global optimum of the loss. The optimization is a constrained optimization, depending on power availability, limited by converters power ratings and by distributed generators and storages, and the effects of these constraints are taken into account in the distributed optimization analysis. The analysis have been performed first analytically and then by simulation, developing a specific set of Matlab scripts that gives a flexible tool to define and test every microgrid and its generators and loads, over which the distributed control algorithms have been developed. Some of the major limits of these techniques have been addressed, among them the need for transmission of synchrophasor with tight real-time requirements. At the end, a sub-optimum controller is proposed, expecting to overcome the over mentioned limits that will be developed in the continuation of this research activity.

In parallel to this first topic, a second more specific problem has been investigated, representing another aspect of the Smart Grid paradigm. As part of a visiting period with the PEMC (Power Electronics Machines and Control) group at the University of Nottingham, the combination of a STATCOM with energy storage and an engine powered synchronous generator has been studied to smooth the frequency variations during sudden load changes. This represents one of the applications of limited energy storage with high dynamic capabilities, like supercapacitors and is of interest both as retrofit of existing synchronous generators, that could experience disconnection problems in a more dynamic environment represented by the Smart Grid, and as a way of ensuring power quality in a microgrid fed by a backup generator. The first application requires a radical increase in the power size of the system, while the second one is more centred on Smart microgrids: independently on the control approach, a microgrid has to be designed to support islanded operation, i.e. to be able to feed loads even when disconnected from the main power network, and one of the options for this backup supply of the microgrid is the use of synchronous generators as emergency voltage sources, typically with diesel engines as prime movers. This second scenario has been considered and studied and an innovative control technique has been proposed able to ride through step changes in the load demand without changes in the prime mover speed and therefore without large changes in the voltage frequency. This has been achieved through fast active power injection from the energy storage as soon as the load transient is detected. From a qualitative point of view, the new load power demand is supported by the storage until the synchronous generator prime mover overcomes the related transient. This technique has been investigated in simulation and validated in a 10kVA experimental setup, representing a simple isolated microgrid with a single generator and resistive loads, confirming the effectiveness of the proposal.

Abstract

Questo lavoro ha l'obiettivo di analizzare alcuni aspetti del nuovo scenario delle Smart Grid, dove la vasta introduzione di generazione distribuita e di tecniche innovative di gestione dell'energia sta forzando una profonda revisione dell'attuale rete di distribuzione. Nonostante i temi affrontati abbiano validità generale, l'analisi presentata si concentra sulle microreti in bassa tensione. Questo perché la bassa tensione, a maggior ragione se limitata a una specifica area identificata da una microrete, è l'architettura più flessibile ed aperta all'introduzione di soluzioni innovative. Recentemente, la rete di distribuzione ha visto l'introduzione di un gran numero di generatori distribuiti, introduzione finora basata su una rigida struttura gerarchica all'interno della rete, dove i gestori mantengono il completo controllo sull'installazione e sulla gestione degli impianti. Questo è legato soprattutto a ragioni storiche: la rete di distribuzione si basa su un paradigma di controllo centralizzato, dove i flussi di potenza sono unidirezionali. La generazione avviene in un numero limitato di centrali e la potenza viene distribuita ai carichi, in un'architettura rigida e totalmente controllata.

Lo scenario emergente delle Smart Grid propone invece una generazione fortemente decentralizzata, basata su un gran numero di sorgenti di energia distribuite, anche di potenza medio bassa. Allo stesso tempo, il settore dell'ICT (Information and Communication Technology) è in continua crescita. La combinazione di generazione distribuita e ICT ha la potenzialità di cambiare completamente il sistema di distribuzione dell'energia, sia da un punto di vista architetturale che del ruolo delle parti nel mercato dell'energia.

Da una prospettiva architetturale, la generazione distribuita potrebbe evolvere verso una soluzione ibrida tra sorgenti rinnovabili quali fotovoltaico, eolico, celle a combustibile ed idroelettrico e fonti tradizionali a combustione, quali turbine a gas e generatori diesel, queste ultime in grado di garantire continuità di alimentazione ai carichi più sensibili in qualsiasi condizione. Inoltre, un accumulo energetico (Energy Storage, ES) può essere usato per introdurre un grado di libertà aggiuntivo nella gestione dell'energia: batterie o flywheels possono assorbire la generazione in eccesso, per fornire energia durante i picchi di carico. Accumuli energetici di ridotta capacità,

quali i supercondensatori, possono invece aumentare la qualità della potenza fornita ai carichi, essendo in grado di rispondere velocemente a transitori della microrete, quali variazioni di frequenza e buchi di tensione. Queste unità di generazione ed accumulo devono essere interfacciate alla rete attraverso un convertitore di potenza, equipaggiato con un controllore digitale in grado di misurare e controllare variabili locali per il corretto funzionamento del convertitore stesso, ma anche in grado di comunicare in modo bidirezionale con altri controllori, ad esempio attraverso PLC (Power Line Communication). La struttura di conversione risultante è stata definita in questo lavoro "Energy Gateway", (EG), e rappresenta l'elemento portante delle future Smart microgrids nella visione proposta da questo lavoro.

Per limitare la complessità del sistema, l'analisi proposta è focalizzata sulle microreti: una microrete è connessa alla rete di distribuzione tradizionale a bassa tensione, e presenta al suo interno un certo numero di generatori distribuiti, tutti equipaggiati con EG. Nell'approccio proposto, il controllo della microrete è distribuito, senza la presenza di un controllore centrale che gestisce tutte le sorgenti di energia. Il comportamento interno della microrete può così essere gestito da interazioni tra le diverse sorgenti, allo scopo di mostrare al punto di connessione con la rete tradizionale un certo comportamento equivalente desiderato, oppure per ottimizzare il funzionamento della microrete secondo parametri prestabiliti.

Entrando nel dettaglio, l'ottimizzazione considerata in questo lavoro è la minimizzazione delle perdite di distribuzione all'interno della microrete, ed è ottenuta controllando opportunamente i riferimenti di potenza attiva e reattiva dei convertitori con un approccio distribuito. In particolare, il normale sovradimensionamento dei convertitori permette di iniettare nella microrete potenza reattiva distribuita, che viene fornita ai carichi localmente. In questo modo si riduce l'assorbimento dalla rete di distribuzione principale, così riducendo perdite e cadute di tensione. Anche l'iniezione di potenza attiva può essere parzialmente controllata, a seconda della disponibilità di energia accumulata negli EG o di sorgenti di energia totalmente controllabili (i.e. gas turbines, diesel generators, fuel cells).

Questo lavoro propone diverse soluzioni per minimizzare le perdite di distribuzione di una microrete: Energy Gateways con riferimenti di potenza controllati usando come informazioni solo variabili misurate localmente, senza nessuna comunicazione, oppure soluzioni distribuite dove gli Energy Gateways comunicano e ognuno di essi esegue una minimizzazione locale delle perdite, basandosi solo su informazioni ricevute dai generatori vicini. Iterando l'ottimizzazione locale, la microrete converge al minimo globale delle perdite di distribuzione. L'ottimizzazione è analizzata considerando i vincoli imposti dai limiti di dimensionamento dei convertitori degli Energy Gateways. L'analisi è stata sviluppata prima analiticamente e successivamente in simulazione, sviluppando un codice Matlab per definire la microrete e testare le diverse soluzioni di ottimizzazione distribuita.

In parallelo alla minimizzazione delle perdite è stato sviluppato anche un secondo argomento, che rappresenta un altro aspetto del paradigma delle Smart Grid. Durante il periodo all'estero speso presso il PEMC (Power Electronics Machines and Control) group all'università di Nottingham, è stata studiata la combinazione tra uno STATCOM con accumulo energetico e un generatore sincrono mosso da un motore diesel, allo scopo di minimizzare la variazione di frequenza del generatore, che si verifica durante variazioni a gradino del carico. L'applicazione è importante sia come adattamento di impianti di generazione esistenti, che potrebbero trovarsi in situazioni di criticità in una rete in cui si verificano frequenti variazioni di carico, e sia come tecnica con cui garantire stabilità in frequenza in una microrete alimentata da un singolo generatore diesel di backup in mancanza della rete principale. Questo secondo caso è stato investigato nel dettaglio, in quanto più orientato alle microreti: ogni microrete deve prevedere un backup energetico per garantire il funzionamento in isola, e il generatore diesel è una delle possibili soluzioni. In questo lavoro è stata proposta una tecnica di controllo innovativa, capace di superare transitori di carico con variazione trascurabile della frequenza generata. L'obiettivo è stato raggiunto grazie ad un'iniezione di potenza attiva attraverso lo STATCOM durante il transitorio di carico. Da un punto di vista qualitativo, lo STATCOM e il suo accumulo energetico sopperiscono al maggior o minor carico nell'intervallo di tempo necessario al motore diesel per aggiornare la sua potenza di uscita. La tecnica è stata prima testata in simulazione e successivamente validata su un prototipo sperimentale che ha ricreato una microrete elementare con generatore sincrono e STATCOM da 10kVA e carichi resistivi, confermando l'efficacia della soluzione proposta.

Contents

List of Figures

List of Tables

Chapter 1

Smart Grids: Introduction and State of the Art

1.1. Introduction

Smart Grids are one of the most recent and attractive research topics. New research opportunities and the challenge of contributing to what is expected to be a "revolution" of energy distribution and transmission are attracting interest in the global scientific community. In recent years, the expected diffusion of renewable energy sources has triggered the need for development of a smarter grid. A rapidly increasing number of distributed energy sources has completely changed the structure of power systems designed almost fifty or more years ago in a totally different energy paradigm. Indeed, the energy production is normally centralized in large power plants using synchronous generators and electric power delivered to the end user within a rigid top-down structure, whit unidirectional power flow and a fully centralized control by the utility companies, managing plants and market. Different factors are pushing the overturning of this structure toward a new energy organization, that in a qualitative discussion can be divided into technological and human factors. Technological factors include huge efforts in development and installation of renewable energy sources, from large plants such as wind farms to small domestic systems such as photovoltaic systems. Human factors are represented by an increased sensibility toward the need for preservation of the environment and a more efficient use of the available resources, also considering the limited availability of fossil fuels and its negative impact on the quality of life. Moreover, people are moving from the passive role of customers to the active role of energy producers if they invest in small renewable system or simply to the active role of "aware customers".

This is in few words the background where the idea of Smart Grid was born few years ago. Starting from the assumption that a direct and complete definition of Smart Grid is still far to come, and this is reasonable because at this stage everybody casts the term in his own experience and technical field, an intuitive and general introduction is given here. Another factor has to be taken into account, to set all the bases. In the past ten years, ICT (Information and Communication

Technology) had a development somehow comparable with renewable energy sources, but with a much larger market, thanks to mobile telephony and internet related application, and thus thanks to consumers market. The net result is the availability of a large number of protocols and technologies, and even more important the easy accessibility to these technologies, thanks to integration and low production costs. Translating in practical terms this means that any electronic apparatus could be easily equipped with one or more communication modules with minimum investments, thus permitting the addition of new functions and controls. Merging together all these concepts, a preliminary idea of Smart Grid can be given. Consider that all the distributed generators are interfaced with the grid through a power converter. The power converters technology is almost mature, improvements come from new devices and new materials able to offer higher integration and efficiency, and from control solutions, while topologies, at least in their basic structures, are consolidated. What is normally missing in power conversion systems is the capability of processing information interacting with the external world. Indeed, the usual scenario in distributed generation sees small power converters with only local knowledge of the grid, and no communication with the rest of the grid. Larger plants have usually remote control signals, with low bandwidth control signals. Transforming what is called a "grid connected converter" into a conversion and communication unit, a sort of "energy gateway" as it will be named in this work, adding communication and data processing capability is a first step toward a real Smart Grid. In fact, an Energy Gateway can interact with the centralized area supervision unit, communicating its state and responding to active and reactive power demand signals. This upgrade can completely change the power management, also maintaining the old control infrastructure, simply increasing the number of information and possible control actions. In addition, similarly to power conversion, also data measurement has become more accessible in terms of costs. Therefore another consistent problem can be solved in power systems: normally, the amount of known data, i.e. voltages, currents, powers, is limited, and a state estimation is necessary to know the conditions of the system and perform the consequent control actions. Increasing the knowledge on the system and possibly using faster communication links, the control performances can be improved at the same time improving the reliability.

The previous are very basic examples of how Smart Grid concepts can improve the energy delivery. In particular, the mentioned advantages are interesting for grid companies, that have now the opportunity of upgrading and better use the available infrastructures. Of course, when discussing about power transmission a radical change in system organization is not conceivable, for the critic importance of transmission links and the tight centralized control required for their safe and stable operation. Where the envisioned revolution of Smart Grid can actually take place showing its potential is the distribution side of power delivery. In particular, low voltage distribution system,

being the last ring of power delivery chain, can be the first part of the system where the energy paradigm can be turned upside down.

Indeed, a complete deregulation of the distribution could take place there. The meaning of "deregulation" is not intended in terms of absence of rules and standards. On the contrary, a clear and strict standardization is required to permit a change in the physical and economical control of the grid: from centralized control made by grid utility delivering a service to the final customer, to a fully decentralized approach where a number of independent agents, the "prosumers" (Producers and Consumers) generate, consume, store and manage energy in an open architecture and market, where utility companies are only one of the agents, for sure a fundamental one taking care of the infrastructure and providing a large amount of energy, but not the exclusive one deciding and imposing rules and market prices for the others. In such a vision, all the agents require cooperation with the others, but at the same time are independent in case of faults or other contingencies. For this reason the currently centralized control has to move toward a distributed control, thanks to the increased intelligence equipping distributed energy sources.

When using the word "distributed" at least three levels have to considered. "Distributed" is the control in the sense that energy gateways have to coordinate and cooperate for a common result, such as for example supply of loads in an islanded portion of the network, or optimization, based on a specific cost function, of part of the grid. An example is the loss minimization investigated in this work. "Distributed" is the energy, from a physical point of view: many different generators, of various sizes and different energy production profiles, with the desirable presence of Energy Storage to be able to implement energy management schemes and to create units able to operate independently on a possible failure of the main supply. "Distributed" is the market, because prices are no longer "unidirectional" but defined in an open market logic depending on what an agent, or a cluster of agents, is able to offer to the others in terms of required services. It is interesting to note how the expected revolutionary change has many aspects in common with the internet development and in general with the world of communication: in the past, few national companies where responsible for the infrastructures, the communication lines, and where managing all the communication market, mainly telephony, without any competition and providing limited services because of the limited available technology. Once technology has reached higher levels, and more importantly highly accessibility in terms of costs for investments and pay-back times, the market literally exploded, leading to the current situation, with a large number of operators and companies offering services in information technology, i.e. internet providers, data storage and security etc. Of course the dynamic of changes in ICT world is faster because only data are involved, while in the grid data and power have to be managed together, with the obvious caution that comes when discussing about power flows.

As any other new vision, also the Smart Grid vision, in this latter and more radical declination, has to be cast in a specific scenario. In this work, it is considered reasonable to start from the low voltage distribution side, identifying the portions of distribution network connected to MV/LV substations as “microgrids” where the diffusion of intelligence and the deregulation can reasonably take place. These microgrids have normally low power, between 100kVA and 1MVA, a single PCC (Point of Common Coupling) connection to the main utility through a MV/LV three phase transformer and a number of residential and industrial single phase and three phase loads and generators. It is intuitive to think that the microgrid can have a specific regulation that guarantees voltage and frequency stability and power quality taking advantage of its own the energy gateways. Within the microgrid, any kind of optimization oriented to performances improvement can be decided, coordinating the agents, their roles and their economical treatment. In this situation, the only relation with the main utility would be at the PCC, so that the microgrid becomes a single equivalent active load for the rest of the grid. At the PCC the energy exchange between microgrid and main grid is managed in a bidirectional way, possibly through a dedicated interface converter and controller. Once the microgrid needs active or reactive power that cannot be autonomously produced, the interface controller will absorb the required amount from the grid, dispatching it to the requiring units in the microgrid. Similarly, when the grid needs power, a request can be forwarded to the microgrid, and distributed generators able to satisfy the demand can respond and negotiate the costs. Adding an amount of energy storage in the microgrid, or backup generators, new opportunities arise for this power exchange with the grid, and the microgrid has the possibility of operating in islanding conditions in case of main grid faults, highly increasing the reliability of the loads supply. Of course, all the energy gateways in the microgrid have to cooperate to support the system. From the point of view of the main grid, this “equivalent load” like behaviour of the microgrid is a valuable simplification, because load scheduling and forecast, that currently is one of the statistical aspects of the power systems management, can become more deterministic, especially during the peak demand, making easier to control the required generation.

This first part of the introduction was intended to draw the vision of Smart Grid followed in this work. In the next, the analysis of the contributions on Smart Grids in scientific literature is reported. A preliminary remark is necessary to explain the adopted approach. As a general observation, being the interest on the topic rapidly rising, the production of scientific works is raising at least at the same speed. The result is an incredible amount of papers from a large number of different engineering areas: power electronics, communication, control, power systems among the others. As a consequence, this review of the state of the art has chosen a selection of these papers, trying to cover all the faces of the topic. Considering the whole complexity of the subject, the different works have been separately classified in six main affiliation areas, as follows:

1. Vision and Architecture
2. Control
3. Devices and technologies
4. Information and Communication Technology
5. Power Systems
6. Experiments and Simulations

The aim of this classification is simply the definition of an ordering criterion that enables a systematic approach to the topic review. The sections will be treated separately, but of course none of the papers appearing in each of the sections strictly belongs to a specific section only. Many times all the topics are included in a paper, and the choice of the section is made following a majority criterion. When a paper belongs to more than one section, it will be redundantly cited in different sections. In the analysis, the interdependencies of the sections will be highlighted as much as possible.

1.2. Vision and Architecture

As anticipated above, the meaning of "Smart Grid" and its possible practical implementation is something depending on specific technical backgrounds and expertises. From this consideration comes the idea of starting the analysis with the early works on Smart Grid, collecting all the opportunities and the challenges of the subject. Some of these works are general overview on the concept of Smart Grid. Among them, [1], [2], [3] offer a clear discussion of the subject as a whole, addressing the most important parts of the development. [1] in particular considers the development of a smarter grid as a fundamental step to exploit distributed generation, plug-in hybrid electric vehicles (PHEV) and energy storage (ES) that is becoming available also for small distributed generators. The first step is seen here as the need for a more advanced grid metering (AMI, Advanced Metering Infrastructures), able to make available a larger amount of data to the grid operators. This allows a more precise forecast of intermitting sources, such as wind and photovoltaic, thus permitting an optimization of the system. Load shaving and demand response with dynamic tariffs are considered among the possible evolutions. Emphasis is given on the impact that a smarter approach to the grid is having on both distribution and transmission sides, with the need for developments in both the sectors. In general, the approach presented here is in terms of upgrade of the existing established grid organization. A different perspective is given in [2] , where the strategic relevance of merging together Power Systems and Information and Communication Technology is considered a mandatory to optimize the use of energy and the related infrastructures.

Smart Grid is defined as a complement to the current infrastructures, better than a new architecture. Moreover, it identifies the distribution network as the weak part of the network, and therefore the first that should be updated to improve efficiency and reliability through distributed intelligence. Finally, the scenario adopted in this thesis is introduced, expecting the distribution side to become a set of microgrids, with loads, generators and energy storage managed by a distributed control and communication infrastructure. Each microgrid becomes an equivalent load or generator for the rest of the grid. In [3] a definition of Smart Grid is given based on the main functions that the new power infrastructure should be able to offer. Among them, the use of distributed intelligence has to facilitate faults diagnosis and restoration, network reconfiguration in case of lost generation units, reactive power control and demand response. Moreover, a larger standardization in distributed energy sources interconnection is expected. [4], [5] investigate similar topics but with more synthetic approach. [4] introduces the definition of "Energy Internet", followed by [6] to underline the parallel between the changes in the energy scenario due to the Smart grid and the development of internet, supported by ICT technologies. The paper highlights the differences between the internet of data and the internet of energy, stating that in data the information is generated and exchanged in a distributed way, while electricity is generate in a centralized way, data are stored in massive amount, while electricity is not and finally in data internet the provision of a service is more important than the quality of the service itself, while in electricity the quality is the first requirement. The first statement is questionable, because de diffusion of distributed energy sources is not take into account. Similarly, the second observation doesn't take into account the increasing availability of affordable energy storage solution, especially for small distributed plants. Similarly to [6], In the rest of the paper the internet like approach to the Smart Grid is intended more in terms of market and data exchange than in terms of a radical modification of the grid architecture. Indeed, the requirements for a Smart Grid are identified in smart metering, improved forecast capability and pricing models. On the contrary [5] gives the general vision of the US Department of Energy, highlighting the requirements of the Smart Grid and the instruments required to obtain the results. The Smart Grid has to be able to incorporate distributed generation and energy storage, to resist to malicious attacks and to be self-healing in case of faults, to guarantee power quality and efficient use of energy and infrastructures and finally to include the customers as active players in the energy market, thus enabling new markets and new forms of energy exchange. In the paper, the keys for these goals are: a distributed intelligence in a decentralization optic, the intense use of communication techniques and control solutions able to maintain the grid even without the need for a centralized supervisor, that can be present but leaving to local generators and power converters the decisions that can be made collecting local data. Finally, the need for standardization is reminded, to establish and consolidate the new technologies. Another general view is given in [7], focusing on critical aspects of Smart Grids and on the requirements to overcome these limits through information technology. The deep diffusion of renewable energy sources has the major drawback of the intermittent nature of

that sources. Wind and photovoltaic are strictly dependent on the climatic conditions, and a production forecast is intrinsically inaccurate. On the other hand a compensation comes from energy storage solutions, able to flatten both the demand and the generation profiles. As further support, the demand response is actuated through load control in case of overload, remotely disconnecting or reducing non-critical load to guarantee the system stability. Such a system requires an intelligent control that has to be distributed, to avoid massive exchanges of data. The distributed control has to take advantage of PMU (Phasor Measurement Units) and of data structures used in Internet technology, including cybersecurity. Finally, [8] proposes a centralized ASC (Adaptive Stochastic Control) able to simultaneously coordinate distributed generation and storage, utility operations and customer responses to stochastically varying system and market conditions. The goal is the optimization of an overall multivariable cost function, representing the best performances of the grid for a given set of side conditions, such as generation and storage availability, demand response availability etc.

This first group of papers offered a general overview on the Smart Grid vision, and it can be observed that even without a common frame on the specific implementation of the architecture, the main keywords are addressed, such as distributed generation, energy internet, energy storage, information and communication technology, security issues, microgrids, distributed control vs. centralized control. In the next, more detailed visions will be introduced, proposing the application of the Smart Grid paradigm to specific systems, such as power systems, low voltage distribution microgrids and DC microgrids. The first two are the dominant visions, assumed by the vast majority of the considered literature. Starting from the power systems, they are intended here mainly as the architectures used for power delivery such as centralized controllers, substations control, faults detections and ride through and protections. The terminal part of the system, the low voltage distribution level, can be excluded from this architecture, being the LV only an equivalent load for the transmission and MV distribution levels.

As already anticipated above, the vision of Smart Grid from the point of view of power systems is intended as an upgrade of the existing infrastructure, increasing the measurements, communication and control capabilities. This increases the reliability of grid state estimation and guarantees improvements in control and healing after faults, as well as fault prevention. A dedicated section will analyze the proposals in the details. As a first analysis it can be observed that a number of works [9, 10, 11, 12, 13] investigates the distributed reactive power support as a means of increasing the power system stability margins, obtaining voltage support or optimizing cost functions such as transmission loss. Another relevant topic is represented by the protections and fault detection: [14, 15, 16, 17] propose new techniques for smart fault detection, taking advantage of the increased available information from the grid, and new fault current limiters. New

opportunities to improve the power system state estimation are reported in [18], while the global advantages in power systems management and control using improved information and communication infrastructures are presented in [19, 20, 21, 22]. The fundamental topic of load forecast using prediction algorithms is introduced in [23]. It is worth to clarify that in all these approaches the Smart Grid is seen as an opportunity to improve the performances and the efficiency of an existing power and control infrastructure, thanks to the powerful ICT and measurement available instruments, adding new controls and measurements, but essentially maintaining the established power architecture and control system.

A completely different scenario arises analyzing the second of the identified main topics, the effects of a Smart Grid vision on low voltage distribution side. Apart from the national regulations that still oppose to any radical change in the system, the low voltage side has in the whole power grid the lowest inertia to structural changes, and therefore is the most attractive testbench for new architectural, i.e. distribution of generators and energy storage units, and control, i.e. distributed control, optimization, proposals. Moreover, at this stage of the research it can be observed that “low voltage” is always coupled with “microgrid”. This is somehow natural, because low voltage distribution is the most peripheral part of the power network. Once part of the low voltage distribution is clustered together, with its own distributed control, generation and energy storage it can be seen from the rest of the grid as an equivalent active load. This load is able to interact with the main grid, and therefore is as a subsystem, a sub-network similar to the different connected network composing the transmission system. Moreover, the microgrid can become an isolated system, self-feeding its own loads. This is fundamental to guarantee supply reliability in case of faults of the main grid, and also to relax the stability limits of the whole power network: in case of overload, the network operator could request a number of microgrids to disconnect from the network, or in case to support the power generation making available the storage resources. Also in this case the details of the papers will be analyzed in the specific section, being most of them related with inverters control. This kind of works represents the majority of the literature, with control solutions able to operate the microgrid either in grid connected operation or in islanded operation, guaranteeing a smooth transition and stability of the system. For a first overview, some examples among the others are [24, 25, 26, 27]. Some other works investigate the microgrids from a more general perspective. [28] in particular identifies the key features of a smart microgrid in the addition of a real-time monitoring system able to implement optimization algorithms that will add further functionality to the distribution management system. This can be done implementing an high speed distributed communication system. Within the possible optimizations the priority is given here to the distribution loss minimization. Similarly, [29] proposes an a vision of ICT architecture specifically designed for microgrids optimized for modelling, monitoring and control. The main features this system should provide are easy integration of distributed sources, reduced loss and increased

reliability. The control system has to be able to operate in islanded condition or in grid connected condition in the latter being able to offer services to the main grid, such as reactive support, demand response etc, exchanged over an open and flexible energy market. More specific investigations on smart microgrids are in [30] and [31], where the coordination of distributed energy storage is presented. [32] proposes the combination of distributed energy sources with a four legs inverter, able to compensate for the line voltage unbalance during grid connected operation. Finally, in [33] a framework is presented to optimize the microgrid behaviour using a multivariable function considering energy availability, storage, electricity price and demand.

So far, only the AC power networks have been associated to the Smart Grid. Actually, the development of HVDC (High Voltage DC) transmission links lead to an established technology in DC power systems. This development is reflected also in low voltage microgrids, that could efficiently operate in residential and commercial environments instead of the traditional AC. Further details on the advantages and limits of DC transmission and distribution can be found in literature, for instance [34, 35, 36]. When talking about Smart Grids, some authors are investigating the vision applied to DC microgrids. As a general comment, DC microgrids are new systems, and therefore are probably the best scenario where any innovation related with distributed control and ICT architectures can reasonably take place without the need for the modification of an existing system. In [37] a DC microgrid adaptive energy management is proposed, for data centres application. The system takes advantage of energy storage and DC sources to minimize the energy import from the AC network and to locally supply the loads. Shorter distance and reduced number of conversion stages guarantee loss reduction and therefore reduced cooling requirements, that in a data centre are one of most challenging issues, considering the usual power density of the installations. In a similar way, [38] proposes a DC microgrid for residential settlements, highlighting the simplified connection of renewable energy sources such as photovoltaic and the consequent simpler interface with energy storage units. [39] offers a deep comparative analysis of different DC microgrids architectures, focusing on the supply reliability. Different converters topology are also considered, from single input converters to multiple input converters. The effect of energy storage availability is also taken into account. To conclude this short review on DC microgrid in Smart Grid, [40] introduces the concept of residential DC nanogrid, as a further reduction in size of a microgrid, limited to the single building. The main drivers are again the increased efficiency achievable with DC distribution, directly interfacing renewables and energy storage with a lower number of conversion stages. Similarly, the loads supply is mainly DC, normally converted from the AC distribution. A single DC bus structure is envisioned here, with control guaranteed by DC voltage based droop control [41].

The other field where the Smart Grid vision can be applied is the in-home power management. A generic building can be considered as an AC nanogrid, similarly to the previously introduced DC nanogrid. In this case, a local power management and monitor can be implemented, using domotics and in-home power line communication do schedule the connections of heavy loads during the times where the electricity cost is lower. Of course the single building optimization has to be limited to energy savings, because the control of energy storage or renewable generators has to be demanded to a higher priority logic of cooperation within the microgrid where the home is located. Nevertheless, in-home management can become important for the grid and/or microgrid operators, because the load scheduling is an information that can be forwarded, to know in advance the needs for power, thus optimizing the generation, as proposed in[42].

Before passing to the other sections, a final comment has to be done on Smart Grid vision and architecture. At the current development stage, many of these visions are still stuck in the papers, without any application in the real world, apart from some valuable experiments that will be analyzed later on in this review. The main brake to the application is represented by two issues: the strict regulations when it comes to operate on the power grid, even if low voltage, and the absence of common view on the development steps. For sure, the second problem can be solved through standardization, defining control and communication protocols able to exploit the potential functionalities of the Smart Grid, as well as a standardization of the on board intelligence in power converters for distributed generation. Of course the standardization should be as opened as possible, to avoid the creation of further strict constraints, added to the already present regulations. Instead, the change of the regulations is a tough objective, because of the opposition from some utilities company, trying to avoid any modification to the current settings of the power network. A trade off can be found only with the efforts of normative committees, as well as with the contribution of IEEE. In this sense, [43] presents an overview on the vision of IEEE on Smart Grid standardization. In particular IEEE 1547 standard for distributed energy resources interconnection with the grid is assumed as background, highlighting the need for extensions to include data transmission, monitoring, control, metering and islanded operation, to give all the guidelines required for the Smart Grid implementation.

1.3.Control

The generality of the title given to this section is coherent with its content: consider that in a wide area such as Smart Grid, the world “control” assumes different meanings, from local control of power converters, to inter-converters control such as distributed optimization, to the global control and supervision when present. So far, Smart Grid has been introduced with two different declinations: from a power system point of view in terms of transmission and MV distribution improvement of existing infrastructures and from the low voltage distribution point of view as a

radical change of architecture and control principles, through the definition of smart microgrids interacting with the rest of the power network. The attention is here focused mainly on the latter case, where different control solutions can still be proposed, while in the first case the control solutions are well defined. A good definition and classification of microgrids control is given in [26], where a hierarchic approach is proposed. The first control level is represented by the power converters local control loops, current and voltage loops. The input of this level is represented by active and reactive power references, or voltage and current references, the output are the modulations for the power converters. The input to the first level comes from the so called "primary control" intended as any algorithm able to define the references for the local control. This can be a Voltage-Q Frequency-P droop controller in case of islanded operation or any other form of controller, for example defining the power references for each distributed energy source in the microgrid based on energy availability and prices. The upper level is the "secondary control", whose purpose is to monitor all the microgrid to ensure power quality and the respect of voltage and frequency levels, as well as to guarantee a seamless transition between grid connected and islanded operation or the ride through of any form of contingency due to local faults, overloads etc. The final level is the "tertiary control", in charge to manage the power exchange with the main grid, sending energy requests and replying to requests from the network, as well as contracting the bought and sold energy prices. This review is mainly focused on the primary control, in particular droop control for islanded operation and optimization techniques during grid connected operation. All the papers assume to have inverter interfaced energy sources in the microgrid. [44] proposes three main architectures resuming the possible behaviours of the distributed sources in a microgrid. During grid connected operation the inverters can perform as constant current or power source, receiving the references from the primary control. This mode is denoted as "grid supporting mode" , because the generators are either supplying their local load, thus lightening the total load seen by the main grid at the PCC, or responding to a power demand from the grid. In islanding mode, the inverters can either perform a droop control or a master unit can substitute the main grid as voltage source, while the other inverters maintain the power or current control. A different architecture is proposed in [45], where a back to back converter is connected between the microgrid and the main grid. The operation in islanding is similar to the previous case, while the advantage during the grid connected operation is the complete decoupling of the microgrid from the main grid voltage and frequency, increasing the reliability and the power quality in the microgrid, that become almost insensitive (within the limits of the back to back converter control) to disturbances from the grid. Another advantage is the easier resynchronization with the main grid during the islanding to grid connected transition. [46] presents a structure of a microgrid system through distributed power generators capable to operate in islanded, genset-connected, and grid-connected modes of operation, using a hybrid converters. The hybrid converter is a four-quadrant PWM bidirectional energy converter with integrated ac transfer switches and with the following modes of operation: Voltage-controlled source converter, Current-

controlled source converter, Active-rectifier mode with PFC. In islanded mode, the hybrid converter operates in voltage controlled source mode by controlling the ac voltage and frequency, with droop if multiple converters are feeding the microgrid. In grid connected operation, the converter is controlled as AC current source, or as active rectifier if an energy storage is connected and charged through the hybrid converter, absorbing energy from the grid. Experimental tests are carried out on a 6kVA converter. To complete this quick review on the possible operating modes of power converters in a microgrid, [32] proposes the addition of a series four legs inverters in each distributed generator output, to be able to compensate for unbalances in the PCC voltage. This proposal assume the voltage unbalance compensation to be done all the generators, another approach could consider the utilization of a single converter at the PCC, able to compensate for voltage unbalances from the PCC and showing to the PCC a microgrid corresponding to a balanced equivalent load, being usually the three phases of a microgrid connected to different loads. The rest of this section will present the different solutions proposed in literature for the primary control of a microgrid. The analysis has been divided in two main categories:

1. Droop methods in islanded operation

2. Microgrid optimizations in grid connected operation

Besides these main topics, some other side aspects such as demand response, security and pricing will be briefly introduced at the end. It has to be noted that the transition between grid connected operation and islanded operation is a fundamental component of microgrids control, and is often analyzed in the papers cited in the following paragraphs. Nevertheless, the analysis is here deliberately limited to the functional requirements of the transition, because a proper review would require a whole dedicated bibliographic analysis.

1.3.1. Droop methods

Droop methods are the most popular techniques for controlling a microgrid with inverter interfaced distributed energy sources when the microgrid is in standalone operation, i.e. in islanded operation. In normal grid connected operation, the PCC guarantees a voltage reference for the microgrid, as well as the power balance: if the internal generation is less than the load demand, the difference comes from the PCC, and similarly in case of excess of generation in the microgrid. The distributed generators can therefore be controlled as current or power sources. When in islanding, the control is switched to voltage mode, to substitute the absence of the grid reference. When operating in parallel a number of generators, the traditional control solution comes from power systems made of synchronous generators operating in parallel: when the connection cables between the paralleled generators are mainly inductive, active and reactive power flows, P and Q, can be controlled independently controlling the voltage and the frequency respectively. A review of the

technique is reported in Appendix A. Therefore, defining for each voltage source a P-f (active power-frequency) and a Q-V (reactive power-voltage) characteristics, the system converges in steady state to constant frequency for all the generators and corresponding active power shared as a function of the converter power rating (the sharing is guaranteed by a proper choice of the droop characteristics). Similarly, the voltages assumes the values required to guarantee reactive power sharing (the steady state voltages are different due to the voltage drops along the lines). The attractive feature of the technique, that has been the key for its success in the past, is that the operation of the paralleled units, also over a large area, is guaranteed without any communication link: the information is inherently exchanged through voltage and frequency states of the network. For these reasons the same technique is applied also within a microgrid where inverter based distributed generators substitute synchronous machines. A first important classifications has to be done between the works using the traditional droop method and the works adapting the method to the nature of a distribution cable, that can no longer be considered inductive but with both inductive and resistive component, and that in some cases becomes mainly resistive.

The first case happens when the paralleled generators are spatially close in the microgrid, for example when the parallel operation is not due to a large number of distributed generators but to the need for an equivalent generator equal to the sum of a number of modules. In that case the effect of the cable is negligible, and the power exchanges depend only on the filter inductance of each inverter module. In this scenario, [47] presents a stability analysis of the inverter based microgrid, showing first, with a small signal analysis, that the eigenvalues of the system are dominated by the P-f Q-V droop control. Normally, the stability of these systems is approached based on the entire microgrid state space model. This work presents a simplified approach to the stability analysis, based on a reduced-order mathematical model of the microgrid, where the droop laws acting on each inverter are examined separately and the inverters are transformed into equivalent networks. Stability conditions for inverter based microgrids are the main topic of the works adopting the traditional droop technique. Similar analysis but with different approaches in microgrid modeling can be found in [48] and [49]. A different perspective is offered by [50]: instead applying the tradition droop to the inverter based microgrid and consider the analysis of stability for the resulting system (different from the original one for power systems because the model of the power generators is different), the inverter behavior is changed to be as close as possible to a synchronous generator. Also the inertia of the synchronous machine is emulated using energy storage (substituting the kinetic energy of spinning mass). In [51], an important modification is made to the traditional droop method. The work starts from the observation that in a synchronous generators droop controlled system, the controlled variable is the frequency only because an integral relation exists in a synchronous machine with speed governor between speed (frequency) and angle. That is obviously due to the spinning nature of the generator. Actually, the active power flow between two

sources directly depends on the voltages phase difference. Therefore there are no reasons for using the frequency in the droop control of inverter based microgrids, but a direct phase droop can be used. The additional requirement compared to the traditional methods is the measurement of the frequency at the PCC of each inverter. The advantage of this solution is the possibility of achieving faster dynamics of the droop during transients, while keeping the steady state nominal frequency. In the same work, also a reactive power droop scheme is proposed that overcomes the usual dependence of the reactive power sharing on the line impedances. Finally, a small signals stability analysis is performed. References [52] and [53] present the CERTS (Consortium for Electric Reliability Technology Solutions) project, in the US, where an inverter based microgrid able to operate autonomously with traditional droop control has been experimentally implemented in a small scale (two sources with maximum power 15kW) setup.

If the impedances between the distributed voltage sources have a consistent resistive component, the P-f and Q-V droop is no longer valid, for the simple reason that it can no longer be stated that active power only depends on frequency and reactive power on voltage difference. The complete analysis of how the equations of active and reactive power transferred between two voltage sources change as a function of the line impedance is presented in [25]. Moreover, the work proposes two solutions to cope with this situation. The first is a linear transformation applied to active and reactive powers so that the new variables (no longer definable as “active power” and “reactive power”) are decoupled as in the inductive case. The transformation matrix depends of course on the ratio between resistive and inductive components of the line impedance, that has to be known. The extreme case of the transformation is with resistive cable, where the role of active and reactive power is exchanged, and thus the droop is P-V and Q-f. The second approach, less sensitive to the parameters, is the implementation of a virtual output impedance in the inverter voltage control loop: Simply, the current voltage reference is the nominal voltage minus a term depending on the output current. If this term is inductive, the small signal model corresponds to an increased output inductance without the need for larger and bulky output filter. Moreover, the proposed approach is similar to [51], being the droop control operated on phase difference instead of frequency difference. Also [54] considers the case of angle droop with resistive cables, modifying the droop function based on local power measurements. A complete small signals stability analysis is given for the proposed method. Despite the existence of other solutions, the most common technique is the virtual impedance, with slight modifications in different works. [55] uses the virtual inductor technique, adding a modification to improve the reactive power sharing, compensating the effect of the voltage drops on the output impedances, that normally cause a mismatch in power sharing. [56] extends and completes the virtual frequency and voltage frame power control scheme proposing a virtual frame operation range control strategy, to define the conditions that guarantee the respect of the voltage and frequency nominal tolerances. Assuming the output filter of the inverters to be

dominant with respect to line impedances, [57] focuses on the behavior of the P-f Q-V droop control during the transitions from grid connected to islanded operation and vice versa. [58] applies the virtual impedance droop in microgrid equipped with several line-interactive uninterruptible power supply (UPS) systems connected in parallel, focusing on the global control both in islanded and in grid connected operation. The control strategy depends on the condition of the grid connection switch: power sources behave as current sources in grid connected operation, automatically becoming voltage sources in islanded operation. In the latter case, the droop control is activated. A small signals analysis is presented to guarantee the stability of the control system, both in grid connected operation, focusing on the stability of local controllers, and in islanded operation, focusing on the droop stability. Experimental results are provided on a 12kVA microgrid fed by two 6kVA UPS systems, testing the effectiveness of the controllers especially in case of load transients and load harmonics. Remaining on the islanding transition, [27] proposes an architectural approach for the islanded operation: a converter is placed in the point of coupling with the main grid. When the grid is disconnected, the voltage is supported by the dedicated converter, and the grid can operate in islanding, either maintaining the current control of the other energy sources, or with droop control. The role of the interface converter is to detect the loss of the main grid and to manage the reconnection, guarantee a synchronized grid connection transients. Experimental results are provided for a scaled 2.2kVA prototype. Further discussions on droop control in islanded operation using virtual impedance can be found in [59, 60, 26, 61]. A valuable improvement of microgrid behavior in case of unbalanced loads is given in [62]. During the islanded operation, the droop is the conventional P-f Q-V for the positive sequence currents and voltages, i.e. positive sequence powers, while the droop is a Q^{-}-G for the negative sequence reactive power, due to the negative sequence of line voltages and negative sequence of load currents. During grid connected operation, the first two droops are disabled, while the Q^{-}-G droop shares among the distributed compensators the negative sequence reactive power due to the positive sequence of line voltage (now imposed by the grid) and the negative sequence of the load currents. G is the conductance controlled by the droop, defining the negative sequence of the inverter current reference based on the negative sequence of the voltages. The result is that not only the balanced powers but also the unbalanced powers are shared among the distributed generators in the microgrid.

As an alternative to droop solutions based on the traditional approach, [63] proposes the adoption of a dedicated communication link between the inverters, that will be preferably located in relatively close proximity. A central controller, common for all the inverters, controls the voltage reference and the power sharing. All the inverters behave like current sources, whose reference is sent by the central voltage controller depending on the voltage regulation needs. The single reference sent to each generator to form the overall current required by the voltage loop is decided depending on the power rating of each inverter. Moreover, the voltage control is frequency-partitioned: the central

controller only guarantees the voltage fundamental, that is slow and therefore it is possible to send the current references to the inverters. Locally, in each of the inverters, a high-frequency voltage control is implemented, that sets to zero the voltage harmonics, and that is ineffective in modifying the low frequency component of the current references.

Finally, a different droop approach is proposed that overcomes the traditional emulation of synchronous generators droop control. In particular, [24] bases the control of islanded microgrids on the consideration that most of the distributed generators are connected to the micro grid via a power-electronic inverter with dc link. New control methods for these inverters can be developed in to exploit the generation units in case of islanded operation. In literature, most control strategies for isolated microgrids relies on the conventional transmission grid droop control or depend on a communication infrastructure. In this paper, an innovative control strategy is proposed for low voltage microgrids. Starting from the hypothesis that a microgrid has resistive cables, the power transfer is mainly a function of voltage amplitudes. Therefore, power is balanced using a control strategy that modifies the set value of the microgrid voltage V_g at the inverter ac side as a function of the dc-link voltage. In addition, when a dc-link voltage threshold is surpassed, this control is combined with a P_{dc}/V_g droop, that changes the DC power reference to maintain the overall power balance. Good power sharing, transient behaviour and stability with no communication infrastructure is achieved. Similar results are reported in [64].

1.3.2. Microgrid optimization

Whit this second main category, an opposite scenario is considered, with the microgrid in grid connected operation. In this case, the microgrid voltage is imposed by the PCC, and all the distributed energy sources can behave as constant current or constant power sources, driven by an arbitrary controller, that could be centralized or distributed. Of course the currents demanded to the distributed generators will be constrained by the converters power ratings and by the capability of the PCC of absorbing power from the microgrid or injecting power in the microgrid. In the power references definition, there are two basic levels of action: the first is related with active power generation, that can be optimized in terms of energy prices, required power for the load in the microgrid and power demands coming from the PCC. Some energy sources, such as microturbines or diesel gensets are fully controllable, and therefore their output power is a degree of freedom for optimization algorithms. Renewable energy sources such as photovoltaic and wind have an intermittent nature, and a degree of controllability is achievable only if an energy storage is added. In general, neglecting the costs, the active power could be controlled for example in order to have optimum power flows in the microgrid, minimizing the loss. The other possible optimization is related with reactive power. All the converters interfacing the distributed generators with the grid have reactive power injection capability, that could be used to optimally supply the loads. In this

sense, [9] proposes a decentralized nonlinear auto-adaptive controller to reduce the losses in a portion of the medium voltage distribution grid by optimally injecting the reactive power. In the considered scenario, the reactive power is supplied by the inverters interfacing photovoltaic units. The proposed controller is decentralized, based on an artificial dynamic system, designed following Lyapunov theory to ensure stability. The approach is based on the classic architecture of a power system: an acquisition system collects measurements from the network, that are sent via telemetry to a central controller, solving the power flow equations and finally computing the optimal reactive power references for the grid connected generators with reactive power injection capability. The designed optimization is dynamic, and thus the reactive current references are continuously updated on-line. The stability design required for this dynamic optimization is based on Lyapunov theory. Experimental validation is provided, showing the effectiveness of the method in reducing distribution loss minimizing reactive power flows. Similarly, [65] proposes a solution to the reactive power dispatch that minimizes the loss applying a new particle swarm optimization approach based on multiagent systems (MAPSO). To obtain optimal solution quickly, each agent cooperates and communicates with its neighbours, in a fully distributed technique. Simulation results are provided based on the IEEE 30-bus power system and experimental tests have been done on a 118-bus real power system, showing the effectiveness of the technique in reducing distribution loss. An observation after these two works is that the attention in providing optimum reactive power dispatch has been so far mainly concentrated on the medium voltage side of distribution system, instead of on low voltage microgrids. [66] observes the problem of optimum reactive power flow from the transmission side of the power system: the power converters of distributed energy sources in the distribution side can inject an amount of reactive power requested by the transmission system. In this case, the objective function is no longer the loss but the voltage: reactive power is required to support the voltage in case of critical conditions. Also in this case a corresponding function to be minimized has been derived from the traditional power flow equations. In this case the problem is solved in a centralized fashion, knowing the network and remotely sending the optimum reactive power references to the distributed generators. Instead, [12] analyzes the provision of reactive power support from an economical perspective, assuming a deregulated energy market. The problem is approached first from the generators point of view defining how a network operator should remunerate the reactive power. The natural criterion is a remuneration increased as the reactive power generation modifies the scheduled active power plan. Then, the perspective is moved to the network operator, identifying the bid techniques adopted by the system operator to identify the best reactive power provision. The choice is made based on the demanded price and on the location where the available generators are installed, being inconvenient to have large reactive power flows that would increase the system loss. Further discussion on reactive power flow optimization for voltage support or loss minimization, based on the traditional power flow approach for power systems, can be found in [13]. [28] presents an infrastructure for distribution power systems that will

allow continuous and accurate monitoring and control to ensure protection against downed conductors, load levelization, loss minimization and enhanced reliability. The proposed infrastructure is a combination of software and hardware tools. The proposed system depends on a distributed high-speed communication system. The proposed control is centralized, even if a partial state estimation is performed locally, to reduce the data flow to the central system.

In general the optimization can be related with an arbitrary multivariable cost function that has to be minimized or maximized. An example is presented in [67], where the goal is to minimize the fuel consumption in a gas-turbines powered microgrid. Another example is in [68], where a microgrid is controlled by a central unit, defining the power references for the distributed generators in order to minimize a generically defined cost function. Similarly, in [69] a distributed control solution is proposed for microgrids in order to maximize the total economic benefit using an auction algorithm for the solution of the symmetric assignment problem. The approach is defined as distributed, but actually a central controller manages the microgrid, coordinating the distributed units, that take locally only a limited set of decisions, mainly related with the management of local loads and generators in order to respond to demands coming from the central controller.

Before passing to the next area of Devices and Technologies, some other works are included in this Control section. Their classification is out of the categories of droop control and grid optimization, and therefore they are presented here at the end of the section. In particular, demand response, security of islanded operation and pricing issues will be analyzed.

1.3.3. Other control aspects

Demand response is the mechanism by means of which the grid operator and the loads interact, so that the load is no longer a purely statistical information based on the previous history, but becomes a partially controllable variable. [70] proposes a technique to adapt the demanded power of a consumer based on the electricity prices information, coming from the grid operator. At the same time, the consumer sends to the grid operator the expected schedule for a given prediction horizon, and the maximum and minimum required powers. In this way, the consumers and the operator can cooperate, the first to minimize the costs, the second to optimize the generation. [71] proposes a fully distributed approach to optimize demand response, minimizing the total energy cost for the users in the microgrid using game theory. In this way, the loads interact with the grid operator as a large aggregated load, instead of having single interactions. [33] models a microgrid, powered with photovoltaic sources and batteries based energy storage, as a multi-agent system with consumers and generators and no explicit communication or coordination among the units. The approach takes into account the generation and storage availability, as well as the energy price in defining if the generated power has to be locally consumed, or stored, or sold to the grid operator. Finally, a

comprehensive review on the architectural requirements and data exchange for the exploitation of demand response capabilities is presented in [72].

Demand response is normally intended in terms of loads. The same approach is of course applicable also to generation, reversing the roles: the microgrid could become a generator for the main grid, responding to a power request that the grid operator could require to fulfill power demands in other parts of the network. In this perspective, [73] proposes to use part of the generation and storage available in low voltage microgrids as a power reserve for the upper level of MV distribution and HV transmission.

To conclude, [74] and [75] focuses respectively on the feasibility of intentional islanded operation of microgrids, and on security issues during islanded operation. The latter in particular investigates a crucial problem during islanded operation: the islanded microgrid requires sufficient energy reverses to feed all the loads. If a possible intentional islanding is scheduled and usually its duration is defined in a proportional way to the stored energy (in batteries or fuel), different is the case of an unexpected islanding, due to a fault in the main grid. An artificial neural network is proposed and implemented in the microgrid central controller: the neural network gathers information from the microgrid and identifies possible security problems related with unsatisfied load vs. generation power balance that could arise during islanded operation. [76] analyzes the islanded operation of a synchronous generators fed microgrid.

1.4. Devices and technologies

The implementation of the Smart Grid is made possible by enabling technologies able to fully exploit the energy sources and their management techniques. As already said in the previous discussion, power conversion topologies can be considered a mature technology, and therefore only few representative examples will be cited here. Of course this doesn't mean that no research efforts and relevant innovations can be found in literature, but the details of topological aspects of converters are left to a degree of analysis higher than this general review on Smart Grids, that aims firstly at clarifying some basic aspects of the approach to the new topic. Similarly, the different possible distributed energy sources could be included, but also for them a dedicated review would be necessary: especially wind and photovoltaic are widely treated in literature and are considered as known background in this review. Also information and communication technology belongs to the general "Devices and technology" category, but will be discussed in the dedicated section. Concluding this preface, the main objective of this section will be the analysis of energy storage solution and its application within the Smart Grid. Moreover, some other contributions regarding power conversion structures and grid monitoring devices will be included.

Starting from the energy storage, two levels of analysis are reported here. The first is the investigation on the possible storage technologies, the second is integration and management of energy storage within the Smart Grid. A good review of the principal energy storage solutions can be found in [77, 31, 78, 24] and is summarized in the following paragraphs. The first classification of energy storage is there made dividing large (and therefore centralized) energy storage technologies and small (and therefore distributed) energy storage technologies. The centralized reserves use the off-peak power generation to store the excess energy, that becomes available during load demand peaks. Pumped hydro reserves are the most common large energy storage solutions worldwide. They consist on a large mass of water, pumped at a sufficient altitude: neglecting the pumping loss, the electrical energy is converted in gravitational potential energy, and stored. The storage is therefore a mechanical storage. The reverse transformation is made through hydro turbines, with a total efficiency of the process (electricity-storage-electricity) around 70%. These plants are rated for a power between 200MW up to 1GW, and their total capacity is around 100GW. The cited publications don't specify the correspondent amount of storage energy, but is reasonable to assume it to be in the order of 10^6 GWh. The other solution for large storage is compressed air (CAES, Compressed Air Energy Storage). The energy is stored in form of kinetic energy of a compressed gas, i.e. proportional to the pressure multiplied by the occupied volume, compressing the air in artificial or natural caverns. The conversion back to electricity is made driving with the compressed air the compressor of a gas turbine, thus increasing the generated power and the efficiency of the cycle. The first commercial CAES plant was a 290 MW unit built in Huhndorf, Germany, in 1978 and the second commercial site was a 110MWunit in McIntosh, AL, in 1991. The third technique for large energy storage is represented by large batteries or fuel cells, that will be analyzed later. Of course, these large plants are interesting for the Smart Grid if seen from the centralized generation and transmission side. From a distribution side point of view, both in MV distribution and in low voltage microgrids, where a number of small generators up to 100kW are installed, the opportunities given by a distributed storage technology are far more interesting. Therefore, the attention will be later focused only on those storage systems.

Smaller size energy storage includes batteries, supercapacitors, flywheels and superconducting coils. It is worth to observe that the power size and the energy capacity of a generic storage could theoretically become arbitrary small or large: costs and efficiency of the process are the drivers for the definition of the optimal trade off, together with the response speed. Also within the category of small storage a distinction has to be made both in terms of size and behaviour of the storage. First of all, large difference exists between supercapacitors and the others, being batteries, flywheels and superconducting coils able to reach powers in the orders of tens of MW, hundreds of kW and hundreds of MW respectively. Of course batteries are scalable to very low powers, and similarly flywheels are available for few kW power sizes, while superconducting coils have costs that don't

justify a small size plant. Moreover, in Smart distribution grids small storage can be intended as CES, Community Energy Storage, when a group of customers, for example a residential area, decide to aggregate and build a storage in the order of their total power requirement, typically few tens of kW, and with storage capacity dependent on the affordable investment. Typically a worst case scenario of islanded operation should be considered, sizing the plant to feed all the loads for a specified time interval, usually few hours. The other option is a dedicated storage for a single, industrial or residential user: the size will be smaller, as well as the energy capacity. In terms of response speed, in small energy storages the distinction between "power" energy storage and "energy " energy storage becomes important: a "power" energy storage guarantees fast delivery of the stored energy, and therefore fast response to high instantaneous power variations, but usually has limited available energy. Typical examples are supercapacitors and superconducting coils, with the difference that the latter guarantees also high energy capability, and therefore could be classified in both the categories. On the contrary, "energy" energy storage has higher energy but slower response time, and therefore follows power peak variations with a slower dynamic. Of course this distinction between "energy" and "power" has no absolute value, being always related to the considered scenario.

Going into the details, a number of battery technologies exist, that can be adapted both for large scale and for small scale energy storage. For large scale storage, lead-acid has been used first, but other battery technologies like Sodium Sulphur (NaS) and Lithium ion are being installed. For small scale storage the market is more flexible, and the number of possible options is higher as it will be shown in the next paragraphs. Supercapacitors are electrochemical capacitors storing energy in the two series capacitors of the electric double layer (EDL), formed between each of the electrodes and the electrolyte ions. The resulting energy densities are low, in the order of tens of Wh per Kg. Superconducting Magnetic Energy Storage (SMES) is an emerging technology where energy is stored in the magnetic field created by the flow of direct current in a coil of cryogenically cooled, superconducting material. Flywheel systems store energy through the kinetic energy of a high speed (>20000 RPM) rotating mass. The latter two technologies are suitable for industrial applications, requiring higher powers and energy densities. The safety issues and installation costs, exclude the use of these sources for residential energy storage in microgrids.

Therefore, focusing on Smart microgrids, the most attractive solutions are batteries and supercapacitors. The lead-acid battery is the oldest and most mature among the battery technologies. Improvements in battery technology over the last 20 years have been mostly driven by the need for batteries in consumer electronics and UPS equipments. Among the alternatives to lead acid batteries, the sodium sulphur (NaS) battery is a high-temperature battery system that consists of a molten sulphur positive electrode and a molten sodium negative electrode separated by a solid beta alumina

ceramic electrolyte. These batteries are recently available in commercial modular units, with the main advantage of a larger number of charge-discharge cycles compared to lead acid. Nowadays, the battery technology with the larger base of applications is the lithium-ion battery. This technology can be applied in a wide variety of shapes and sizes, allowing the battery to efficiently fill the available space in any portable device. Nevertheless, not only portable devices are targeted by lithium batteries: the light weight and the energy density, made recently possible to use this technology also in backup power, such as UPS. The main limit is related with the higher cost, due to the scarcity of lithium reserves. Beyond these technologies, other batteries exists based on diverse electrochemical combinations such as lithium titanate, nickel cadmium etc., but with limited commercial availability for microgrid applications.

Before moving toward the advantages deriving from the utilization of distributed energy storage in microgrids, it is important to remind fuel cells as an alternative to batteries, a clean way to transform the hydrogen chemical power into electricity. On the other hand, fuel cells are better included in the possible distributed energy sources, being in this case the energy stored in the fuel, exactly like diesel or gas for gensets and gas turbines, and therefore the conversion process is unidirectional, losing the advantages of bidirectional energy exchanges (of course excluding for practical reason the extraction of hydrogen from the water generated by the fuel cell).

The main improvements derived from distributed energy storage in a microgrid (valid for the whole grid as well) are: local grid voltage support through injection of active or reactive power (depending on the nature of the line cables), as well as frequency support injecting active power in case of synchronous generators fed microgrids; load levelling and peak shaving, thus flattening the load demand of the microgrid and consequently simplifying the control of the upper levels of the power network; increased reliability due to the opportunity of ride through line faults guaranteeing the continuity of loads supply; new economical schemes arising with the possibility of managing the degree of freedom of the storage in the energy exchanges between the microgrid and the main grid. [79] proposes a storage control in order to smooth the effects of pulsed loads on electric ships microgrid: the main philosophy is that an energy storage element is coupled with the load and properly sized. When the load has to be connected, the storage is charged in advance following a charging profile that minimizes the impact on the power system and then the storage energy is used to fed the load without perturbing the rest of the system. A perspective on the reliability improvements achievable with energy storage is presented in [7]. Distributed energy storage is believed to be a benefit for the main grid operator through load levelling, reducing the risks of supply disruptions. [30] proposes a microgrid structure with energy storage at the PCC, and a centralized controller. The focus is on islanded operation, where a two layers control scheme is proposed: a fast voltage and frequency control is operated by the energy storage, able to inject or

absorb active or reactive power with large bandwidth as soon as a variation due to a transient event is experienced. With slower dynamic, the rest of the generators in the microgrid are operated in parallel with centralized controller ensuring steady state voltage and frequency regulation with zero power drown from the energy storage. An alternative and commonly accepted vision on distributed energy storage is presented in [80], where the electric vehicles, when not in use, can be used as normal batteries and interfaced with the grid not only for the charge but also to provide services such as active power support. The work assumes the presence of an aggregator, as an intermediate level between the grid operator and the vehicles, in charge of the economical optimization of the system. On the same topic of electric vehicles, [81] analyzes the opportunity in terms of feasibility, due to the consistent initial investment for the system, that could be paid back thanks to the developing market of services offered to the grid. It is also highlighted how the presence of a large number of electric vehicles could be an advantage for the distributed energy storage, but could also become a threat for the grid in case of massive numbers of cars charged at the same time. For these reasons, a connection standard and management has to be developed. [82] and [83] propose a combined energy storage system (CESS), based on different battery technologies, supercapacitors and a flywheel. The systems has the goal of taking advantage from the different behaviours of different technologies to optimize both the external behaviour of the system in terms of response to power demands from the grid and the total lifetime and costs. The energy storages are controlled by a single controller, optimizing the system based on the requirements from the grid, on the information from the different characteristics and from statistical data. [84] offers the vision of the already mentioned CERTS project on microgrids: the energy storage is seen as a means of guaranteeing the same dynamic performances for different kind of energy sources connected in the microgrid. Adding a storage to each of them, and properly controlling the system, the external behaviour seen by the rest of the microgrid is independent on the nature of the source: photovoltaic, wind, gas and diesel engine can be considered dynamically equivalent, i.e. respond with the same dynamic to active and reactive power reference changes. This strongly simplify the design of the droop control of the microgrid in islanded operation, while guaranteeing a plug and play feature of each new generator inserted in the microgrid. [85] presents a solution to power fluctuation in wind energy sources, adding an energy storage able to flatten the net power profile of the system, better matching the load demand and fully exploiting the available wind energy. A final observation about energy storage can be found in [38]. In particular, the utilization of photovoltaic sources combined with energy storage is proposed for DC microgrids. In fact, it has to be noted that most of the energy storage solutions are DC, and therefore find their natural application in DC grids, with minimum conversion stage and increased efficiency. Of course many other references can be found in literature on the topic of energy storage and its conversion stages and control. Before passing to other devices, the last paper included in this section is [86]. Even if out of the proper energy storage management, it is important to mention that distributed sources based on fuel (gas turbines, diesel motors, fuel cells) can be successfully coupled

with renewable energy sources, such as wind or photovoltaic, to compensate the power fluctuation of these sources. Of course, being the generator unidirectional it can only compensate for undergeneration, while an excess of generation cannot be handled. The work proposes also a detailed model of the diesel engine, to properly design the control system. Finally, on a similar topic, [87] proposes a review on gas micro turbines modeling for smart microgrids.

The last part of this section will shortly introduce some innovative concepts in power conversion structures, from a system perspective rather than analyzing the details. In particular, [88] presents a power flow control technique based on a predictive current control technique for the UNIFLEX-PM, a back-to-back multilevel power conversion structure providing a flexible electronic interface to control the power flows between low voltage loads and distributed generators, energy storage and the MV distribution network in a fully bidirectional way. The converter could be defined as a "node" converter, managing the power fluxes converging at the node. Experimental results are provided on a 300kVA experimental prototype. From a microgrid perspective, it could be successfully used as interface with the PCC. Also [46] proposes a converter architecture for Smart microgrids with distributed power generators capable to operate in islanded, genset-connected, and grid-connected modes of operation, using a hybrid converter. The hybrid converter is a four-quadrant PWM bidirectional energy converter with integrated ac transfer switches and with the following modes of operation: Voltage-controlled source converter, Current-controlled source converter, Active-rectifier mode with PFC. In islanded mode, the hybrid converter operates in voltage controlled source mode by controlling the ac voltage and frequency, with droop if multiple converters are feeding the microgrid. In grid connected operation, the converter is controlled as AC current source, or as active rectifier if an energy storage is connected and charged through the hybrid converter, absorbing energy from the grid. Experimental tests are provided on a 6kVA converter.

Before passing to the next section, the final paragraph of this section introduces other devices, different from power conversion stages and energy storage, developed for the Smart Grid. Among them, [14] analyzes the problem of the increased fault currents caused by distributed energy sources, and proposes a fault current controller (FCC) named "smart FCC". The device is a superconducting coil with a freewheeling diode, four thyristors, and a control unit. Smart FCC can not only limit but if necessary also control the current in case of fault. The advantage is that the device can adapt to dynamic changes in the grid topology and number of generating units, while the previous current limiters where designed for a specific condition. Of course the application of FCC is intended for the MV distribution side, rather than for the low voltage. Instead, [22] presents a review on the power electronics interfaces required for PLC (Power Line Communication), fault detection and grid monitoring and remote control.

1.5. Information and communication technology

In all the discussion so far presented, one of the building blocks of the Smart Grid is represented by Information and Communication Technology. Even if the category should include also the control solutions, in this review the attention is focused on communication and data measurement. Therefore, ICT is seen from the perspective of a basic part, a background, over which the implementation of controllers (distributed or centralized) is possible. In this section, five main topics will be reviewed in ICT: the Architecture, investigating the proposals in literature for the organization of the ICT infrastructure in the Smart Grid; Power Line Communication; Wireless communication; Data Measurement; Data Security.

1.5.1. ICT architecture

With the world "architecture" it is intended to analyze the proposals in terms of overall information system in a Smart Grid. Therefore, the works cited in this subsection will be naturally general, without specific details on the implementation but more oriented to the requirements of the system in the different proposed visions. As in the first section, different visions are superposed, from a high power systems architectures to systems for low voltage distribution microgrids. In this context, [89] presents a comparison between communication infrastructures needed for centralized and distributed measurement and control. In particular, the attention is concentrated on the comparison of latency times and reliability. It has to be observed that here the definition of "distributed" control doesn't mean that the grid agents cooperate for the grid control but that a number of control centres are placed in limited areas and communicate with the wide area controller. Therefore the vision is more suitable for Smart Grid infrastructures for transmission or MV distribution systems. [90] offers a more general perspective on the communication architecture. The system requirements are identified in: High reliability and availability; High coverage and distances; Large number of communication nodes; Appropriate communication delay and system responsiveness; Communication security ; Ease of deployment and maintenance. The solution to satisfy all these requirements is a two layers architecture: the higher level is represented by servers in an IP based environment, forming a sort of wide area network: this part of the system is dedicated to billing, metering and additional services market. This layer communicates with the lower level through access points (APs). The lower level includes meters, switches, protections and control equipment. The envisioned communication protocol is TCP/IP like, and the communication techniques can be wired, optical fibres, wireless or PLC based. [91] starts from the consideration that the Smart Grid will generate a massive amount of data, in fact it is reasonable to assume that a PMU, Phasor Measurement Unit, will generate a measurement for approximately each line cycle. Therefore, even if a centralized control is kept in the grid, the data cannot be all communicated to the central controller, but a decentralized data infrastructure is required, and the central controller

will communicate only with the aggregated data centres. Of course a priority logic has to be defined for sensitive data, i.e. power control references, together with security with respect to malicious attacks and failure ride-through capability. [92] analyzes from a general perspective the opportunities of Smart Grid for large power systems: the presence of a complex information and communication architecture is seen as the key for improving control, state estimation and reliability. Also in [93] the Smart Grid is seen as a simple upgrade of the current infrastructure. In particular, the AMR (Automatic Meters Reading) technology can incorporate a number of additional functions such as load monitoring and control. Finally, in [29] a communication system is proposed for MV and LV distribution, based on a web-services framework. An observation that follows from these references is that the ICT architecture for the Smart Grid is still far from a final definition and standardization. Especially in the low voltage side, few proposals have been made, being the attention more focused on the upgrading of the traditional grid communication system.

1.5.2. Power Line Communication

When looking for a communication technique able to satisfy the control requirements and data flows within the specific scenario of low voltage microgrids, PLC seems the most attractive solution, especially for the limited infrastructural costs related with the use of power cables as communication channel. Of course PLC can be used also in transmission and MV distribution, as already done at low bandwidth in remote meters reading. [94] offers an exhaustive review of PLC technologies for Smart Grid. Starting from the observation that an established standard is still not available, different solutions are presented highlighting advantages and weaknesses. In recent years, industrial interest has grown around the “high data rate” NB-PLC (Narrow Band) based on multicarrier schemes and operating in the band between 3–500 kHz. NB-PLC is only one of the technologies, that can be grouped in three main classes: Ultra Narrow Band (UNB) PLC, operating at very low data rate (100 bps) in the 0.3–3 kHz band; Narrowband (NB) PLC operating in the 3–500 kHz band, including the European CENELEC bands (3–148.5 kHz), the US FCC band (10–490 kHz), the Japanese ARIB band (10–450 kHz), and the Chinese band (3–500 kHz); Broadband (BB) PLC operating in the 1.8–250 MHz band with bit rate from several megabits per second to several hundred megabits per second. Examples of the latter technology are devices conforming to the TIA-1113 (HomePlug 1.0), IEEE 1901, ITU-T G.hn (G.9960/G.9961) recommendations. It has to be observed that a higher data rate corresponds to higher attenuation and therefore lower distance covered without regeneration. The work also defines the possible use of PLC in Smart Grid, in particular:

- PLC for High Voltage Networks: technologies operating over AC and DC HV lines up to 1100 kV in the 40–500 kHz band with data rates of hundreds of kpbs

- PLC for Medium Voltage Networks: substations at the MV level are usually not equipped with communication systems. Nevertheless fault detection and remote monitoring are becoming a priority in the new operating condition of the grid imposed by the largely distributed generation.

- PLC for Low Voltage Networks: at the state of art, most of the PLC applications on the LV side are in the area of AMR (Automatic Meters Reading), vehicle-to-grid communications and home energy management.

It is reasonable to assume that the standardization will move toward high data rate solutions, considering the large amount of data expected in the Smart Grid. To conclude, channel modelling is one of the critical aspects, considering that the communications system design must be matched to the specific channel. Deterministic or statistical models are used to identify the channel. A channel modelling is proposed in [95], while [96] investigates the model and the effect of noise generated by power devices on PLC performances. Finally, a noise reduction scheme is proposed. Similarly, [97] develops a simulation program to model the channel and the noise interference on PLC.

1.5.3. Wireless communication

In recent years, wireless networks have been widely used for distributed sensors systems, and the acquired knowhow can be extended to Smart Grids. Diverse works propose wireless solutions as an alternative to PLC in power systems. [98] proposes IEEE 802.15.4 compliant wireless nodes for non critical grid monitoring and equipment fault diagnosis. [99] investigates the specific scenario of machine-to-machine communication within the same HAN (Home Area Network). Different wireless standards have been compared: IEEE 802.15.3a-UWB, for high data rate requirements, IEEE 802.11-WiFi for large areas, IEEE 802.15.1-Bluetooth for data and audio transmission over short distances and IEEE 802.15.4-ZigBee. Among them, ZigBee is considered the best candidate for HAN wireless communication, due to the low power consumption. Also [100] identifies ZigBee as the best alternative to PLC for in home communication oriented to an efficient power management of the appliances. Extending the area of interest to low voltage microgrids, [28] proposes a bidirectional wireless communication link between the distributed energy sources and a central controller, to monitor and optimize the system. Remaining in the microgrid domain, [101] expands the hybrid tree routing of IEEE 802.11 family standards to guarantee a last mile communication robust to link failures. One of the critical aspects of wireless networks is the need for clock synchronization, to guarantee the coherence of data and commands exchanged among the sensors. In Smart Grid this is fundamental for the transmission of voltage and current phasors. [102] presents a comprehensive review of clock synchronization methods. On the same topic, [103] proposes a simple but effective distributed synchronization technique.

1.5.4. Measurements

One of the key technologies for Smart Grid development is the possibility of measuring and transmitting voltage and current phasors on a synchronized frame, thanks to PMU, Phasor Measurement Units. This is fundamental to improve the old power system infrastructure, where only powers and rms voltages were transmitted and supports the new visions on smart microgrids, making available all the information required for a tight control and optimization. [104] proposes an introduction to Phasor Measurement techniques. In most of the commercial PMUs the used data window is one period of the fundamental frequency of the input voltage or current. The phasorial representation is derived from data samples applying the discrete Fourier transform (DFT). The resulting measurement is named Synchrophasor, to underline that the phasor has been estimated at known instant of time. Synchronization is achieved using a sampling clock phase-locked to the one-pulse-per-second signal provided by a GPS receiver. It has to be noted that the output of a PMU is typically the positive sequence of voltages and currents. In some cases, the PMUs are also able to provide phasors for individual phase voltages and currents. Synchrophasors are used in [20] for relays control and islanding detection.

1.5.5. Data security

Compared to any other communication and data system, Smart Grid has a vital dependence on data security. Any malicious attack to control signals could have catastrophic impact on the network. Of course this is in contrast with the deregulated approach that the Smart Grid paradigm is proposing, at least in LV distribution. [105] proposes a layered definition of cyber security in Smart Grids, defining three categories of signals, based on indications from the Swedish National Grid operator: real-time operational communication requirements, administrative operational communication requirements, administrative communication requirements. The first category includes system control and teleprotection systems, with maximum latency time of 20ms, and the operator voice, still considered a fundamental signal in case of emergency actions, and has to provide maximum security level. The other two low-priority communications includes power sharing signals and other non time critical commands and information, with more relaxed security requirements. In a similar manner, [106] starts from aircrafts experience, where security is the most critical issue, proposing three levels of subsystem impact, corresponding to three different security requirements, classified as follows. Level A (or High): failure of these systems are likely to cause failure across a large number of vital nodes for the power system over a large area; Level B (or Medium): failure of these systems causes loss of power to a large number of nodes but in a smaller geographic area; 3) Level C (or Low): failure of these systems may cause local failure. [107] emphasizes the need for improved cryptography: currently smart meters uses an X.509 certificate for identification and cryptographic-session establishment. Cryptographic solutions in this context

should include a key management algorithm to periodically update keys, thus keeping the highest security level. Finally, in the scenario of possible cyber attacks to data in the power network, [108] analyzes the impact of malicious data injection in measurements used by the central controller to estimate the system state and proposes a strategic placement of fully secure measurement devices to minimize the attack impact.

1.6. Power Systems

The aim of this section is to collect a number of contributions in literature regarding the application of Smart Grid vision to the traditional power systems, i.e. the portion of power network that is expected to be only updated by the introduction of intelligence, while keeping the established organization and control. Doing so, a better picture of the trends in the sector can be given, also understanding the possible development. Starting from the general visions, [19] and [11] address the transmission side of power network. The fist contribution confirms how the Smart Grid is seen in the specific sector as a means of improving reliability of power delivery, through the increased measurements, control and communication, that are the main limits of the current infrastructure. Moreover, the concept of Smart Substation is introduced, defined as the use of intelligent systems to increase the automation of the substations, i.e. again measurements and communication with the central controller, together with faults diagnosis and control and management of possible distributed generators connect at lower level. The second contribution proposes an optimal partitioning of the power network in case of faults that could lead to cascading events and power disruptions. The technique reconfigures the power network in a number of islands, each of them with minimum active and reactive power imbalance between loads and generators. Instead, [109] moves toward the distribution system, observing that traditional distribution is radial, but when load density is high, and high reliability is required, the use of networking is possible also in distribution systems. Moreover, a vision on distributes sources, communication and control is proposed.

Another challenging topic in power networks at the higher level (transmission and MV distribution) is the impact of reactive power. On the mainly inductive line impedances, the flows of reactive power are a means of controlling the line voltages. On the other hand these reactive flows should be minimized, to reduce the loss. In [10, 110, 12, 13] different solution are proposed for the reactive power flow, also from a market oriented perspective. Effects on voltage regulation made by LTC (Load Tap Changers) transformers is investigated in [111], addressing the effects of distributed reactive power injection.

In general, Smart Grid is driving a change in all the traditional features of a power network: state estimation [18], load forecast [23], power flows calculation [112, 13, 113] can be enhanced by the widespread use of PMUs and communication infrastructures and protocols, thus increasing the

information received by the grid operator, with a consequent increased control capability. Particular attention is dedicated in literature to the fault detection and fault current limitation problems. In particular, [16, 17, 21] investigate the improvements in fault detection strategies. [114] focuses on faults management in low voltage distribution, emphasizing the requirements for a communication and control architecture that guarantees fast fault clearing, to have minimum impact on the users. [115, 14, 15] propose current limiting devices, that basically are controllable impedances connected in series with the power line. When the current increases for a fault in the case of [14] and [15], or for incorrect power sharing in [115], the impedance is increased to limit the current and to restore the sharing respectively.

1.7.Experiments and simulations

The last section of this review is dedicated to the most relevant experimental setups and simulation tools developed for the Smart Grid. A general observation is that most of the works in literature on Smart Grid propose architectural vision, control solutions and converters, but few of them are supported by consistent experimental results. When dealing with microgrids control, the proposed experimental setups are typically of small power size (tens of kW) and low complexity. Here, some examples of the largest projects and experiments on Smart Grid are reported. Of course this is done knowing that the scenario is continuously evolving and any list of experiments will become obsolete soon. First, [116] presents a complete overview of the projects on Smart Grid running in the United States. Among them, [52] presents the CERTS (Consortium for Electric Reliability Technology Solutions) three phase microgrid experiment. The sources operate in parallel to the grid or in island, providing uninterruptible power-supply services. The system can disconnect from the utility during faults or voltage collapses, and can also intentionally disconnect when the quality of power from the grid falls below certain standards. CERTS microgrid concepts are demonstrated in a full-scale test bed built in Columbus, OH, and operated by American Electric Power. Four distributed loads can be controlled to absorb an active power between 0 and 90kW and a reactive power between 0 and 45kVA, fed by three gas gensets rated to cover the whole load demand during islanded operation. Moving toward Europe, [117] presents the FENIX project. The projects introduces the concept of “VPP - Virtual Power Plant” aggregating small distributed energy sources and behaving like a real power plant with scheduled output, ramp rates, voltage regulation capability and reserves. These VPPs are inserted into the current power system at transmission or distribution level and operate like any other power plant. Architecture and control requirements are presented for the implementation of the system. [118] introduces the ADDRESS project under FP7, the prosecution of FENIX project. The goal is the development of a scalable and open communication architecture to make it possible to deal in real time with large numbers of consumers and support the active demand. The project is expected to provide the architecture in an experimental setup, together with a technical guide on telecommunication for Smart Grids. The

Smart Grid concepts finds application also in rural areas, where a proper power system doesn't exist, and a possible solution for energy supply is the creation of autonomous microgrid, managing diverse energy sources and storage: this is the case of [119], presenting the specifications and development of a standalone microgrid wind and photovoltaic sources, together with diesel backup and batteries, installed in Lençóis's Island, Cururupu, MA, in the north of Brazil. The microgrid is rated for the low power of 10kW, but is expected to grow in the next years.

To conclude, two works are cited regarding simulation tools for Smart Grid: [113] presents the GridLAB-D, an open source power system modelling and simulation environment developed by the United States Department of Energy specifically for the integration of detailed power systems and end-use models, including the low voltage distribution side. [120] proposes a hardware in-the-loop simulation (HILS) system as an alternative approach to develop and test control algorithms and microgrids. The hardware-in-the-loop simulation (HILS) is a used to develop and test complex, real-time embedded systems and includes the electrical emulation of sensors and actuators. In this way the reliability and the performances of the real control system can be implemented and tested using a simulated plant instead of the real network. HILS represents therefore an intermediate development step between pure simulation and direct tests in a real experimental setup.

PART I

Distribution Loss Minimization in Smart Microgrids

Chapter 2

Theoretical minimum distribution loss

2.1. Introduction

The aim of this section is to give a theoretical base to loss minimization algorithms that will be introduced in chapter 3. Before proposing the distributed generators control techniques, it is worth to introduce the ideal optimization, to define an instrument able to derive the minimum loss condition for a given microgrid, to be used as benchmark to check the effectiveness of the proposed loss minimization methods. The analysis is based on a number of assumptions, required to reduce the complexity of the system, being thus able to obtain an analytically, even if simplified, derivation of distribution loss. The introduced approximations will be used also in the prosecution of the analysis.

2.2. Assumptions

The minimum loss condition is hereafter derived assuming a microgrid with the following characteristics:

- Low voltage distribution, with radial distribution feeders. This is the normal topology for LV distribution systems. The resulting network graph is a tree. The derivation could be extended also to mashed networks, more common in MV distribution or in transmission.

- The microgrid nodes are either loads (passive nodes) or distributed generators (active nodes). Both are modelled as AC current sources, named i_a and i_p respectively. The current is considered absorbed both for loads and generators. An origin of the tree exists and is named “node 0”, corresponding to the connection of the microgrid to the rest of the distribution network. This operation mode of a microgrid is normally referred as “grid-connected”. The branch currents, i.e. the currents flowing from a node N to a node M through the distribution line, are oriented from the node closer to node 0 to the node farer to node 0. As consequence, the network graph will is oriented. Node zero guarantees the power balance between load and generation and it can be represented by the equation:

$$i_0 = -\sum_{n=1}^{N} i_n \tag{2.1}$$

Where N is the total number of active and passive nodes, excluding node 0 and i_n is the current absorbed (based on the over mentioned convention) by each node and i_0 the current absorbed by node 0.

- All the voltages and currents in the microgrid are sinusoidal in steady state, and thus the behaviour of the network can be studied using phasors. This means that all the transients related to power converters and loads control loops are here neglected.

- The microgrid is single phase. All the derivation are thus valid also for three phase balanced systems, while the case of unbalances is not treated here.

Fig. 2.1 resumes these features:

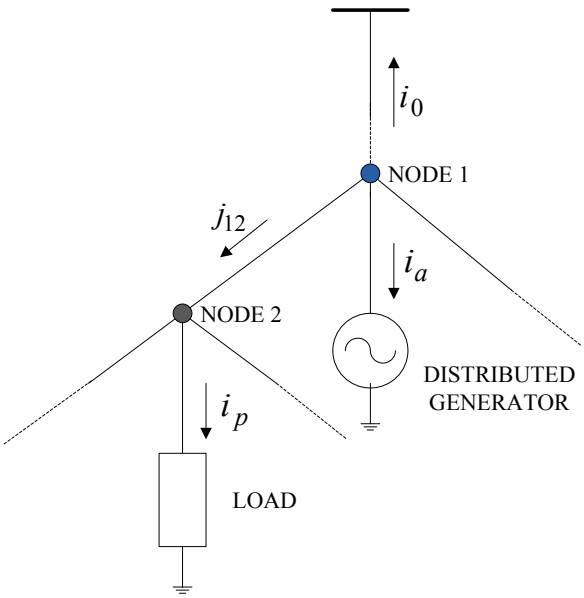

Fig. 2.1 Microgrid section with currents definition and direction

2.3.Distribution Loss in radial microgrids

Naming $\underline{A}$ the incidence matrix, $\underline{A} \in R^{LxN}$ where N is the total number of nodes (active and passive, including the empty nodes but excluding node 0) and L is the number of branches. Assuming a tree topology, N=L and the incidence matrix results squared and invertible. It is worth to recall the definition of incidence matrix for the currents, coherent with the defined directions of node currents, where in the row numbers are the branch labels, and in the columns the node labels:

$$\underline{A}(b,n)=\begin{cases}-1 & \text{if branch b exits node n}\\ +1 & \text{if branch b enters node n}\\ 0 & \text{otherwise}\end{cases} \tag{2.2}$$

If the convention were with injected node currents, the signs in (2.2) would have been opposite. Defining $\underline{\dot{J}}$ the column vector containing the phasors of the branch currents, with the same orientation of the correspondent branch, and $\underline{\dot{I}}$ the column vector of node absorbed currents, applying Kirchhoff's currents law (KCL) results:

$$\underline{\dot{I}}=\underline{A}^T\underline{\dot{J}} \quad \Leftrightarrow \quad \underline{\dot{J}}=\left(\underline{A}^T\right)^{-1}\underline{\dot{I}}=\left(\underline{A}^{-1}\right)^T\underline{\dot{I}} \tag{2.3}$$

Moreover, changing the direction of node 0 current from absorbed to injected, equation (2.1) can be rewritten as:

$$\dot{I}_o=\underline{1}^T\underline{I} \tag{2.4}$$

Where $\underline{1}^T$ is a row vector containing N=L ones. The final goal of this derivation is to express the distribution loss as a function of the node currents, instead of the branch currents, that are the direct cause of the loss over the series resistive component of line impedance, as reported in the next equation:

$$P_d=\underline{\dot{J}}^T\underline{R}\underline{\dot{J}}^* \tag{2.5}$$

Where * is the complex conjugate, and $\underline{R}$ the diagonal matrix containing in element (i,i) the resistive component of the i-th distribution branch impedance. From (2.5), distribution loss can now be rewritten as a function of the node currents:

$$P_d=\underline{\dot{J}}^T\underline{R}\underline{\dot{J}}^*=\underline{\dot{I}}^T\underline{A}^{-1}\underline{R}\left(\underline{A}^{-1}\right)^T\underline{\dot{I}}^*=\underline{\dot{I}}^T\underline{B}\,\underline{\dot{I}}^* \tag{2.6}$$

Naming $\underline{B}=\underline{A}^{-1}\underline{R}\left(\underline{A}^{-1}\right)^T\in R^{NxN}$. The matrix $\underline{B}$ is symmetrical, in fact:

$$\underline{B}^T=\left(\underline{A}^{-1}\underline{R}\left(\underline{A}^{-1}\right)^T\right)^T=\left(\left(\underline{A}^{-1}\right)^T\right)^T\underline{R}^T\left(\underline{A}^{-1}\right)^T=\underline{A}^{-1}\underline{R}\left(\underline{A}^{-1}\right)^T=\underline{B} \tag{2.7}$$

The demonstration is omitted, but the matrix $\underline{B}$ could be directly derived from branch resistances. The generic element in position (m,n) of matrix $\underline{B}$ is the resistance of the common part

of the paths connecting node m and node n with node 0. The elements in the diagonal (n,n) correspond to the resistance of the path connecting node n and node 0.

Assume now a microgrid with no distributed generators, so that all the nodes are passive loads, absorbing a currents vector $\underline{\dot{I}} = \underline{\dot{I}}_L$ with a certain $\left|\underline{\dot{I}}_L\right|$ and $-\frac{\pi}{2} < \angle \underline{\dot{I}}_L < \frac{\pi}{2}$, modelled as AC current sources. All the loads are fed by node 0, corresponding to the PCC (Point of Common Coupling) with the higher hierarchic level of the distribution system, i.e. the MV to LV substation. In these conditions, distribution loss will be maximum, corresponding to:

$$P_{dMAX} = \underline{\dot{I}}_L^T \underline{B}\, \underline{\dot{I}}_L^* \tag{2.8}$$

Starting from this worst case scenario, a number Na of generators are inserted in the microgrid, either in empty nodes or in loaded nodes. The generators are equipped with current controlled inverters. Naming $\underline{\dot{I}}_{Ga}$ the vector of the currents injected by the inverters, taken with the generators sign convention, the vector of the total absorbed currents at the N_a active nodes will become:

$$\underline{\dot{I}}_a = -\underline{\dot{I}}_{Ga} + \underline{\dot{I}}_{La} \tag{2.9}$$

Vector $\underline{\dot{I}}_a$ is a column vector of N_a elements. Fig. 2.2 reports the adopted signs convention for the generic active node:

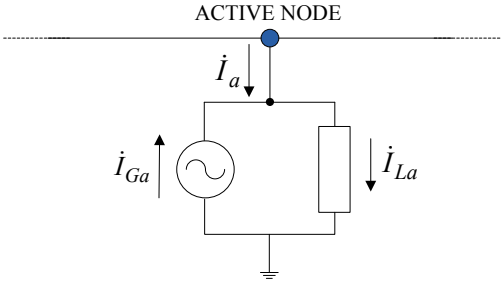

Fig. 2.2 Active node currents definition

The remaining N_p=N-N_a nodes are purely passive nodes, absorbing the currents vector $\underline{\dot{I}}_p$, equal to:

$$\underline{\dot{I}}_p = \underline{\dot{I}}_{Lp} \tag{2.10}$$

Again, $\underline{\dot{I}}_p$ is an N_p elements column vector. Both the active currents $\underline{\dot{I}}_a$ and the passive currents $\underline{\dot{I}}_p$ can be expressed as a function of the global currents vector $\underline{\dot{I}}$ as:

$$\begin{aligned} \underline{\dot{I}}_a &= \underline{K}_a \underline{\dot{I}} \\ \underline{\dot{I}}_p &= \underline{K}_p \underline{\dot{I}} \end{aligned} \tag{2.11}$$

$\underline{K}_a$ is an N_axN matrix, with all zero elements in each row, apart from the element corresponding to an active node, one for each row, that is equal to 1. The same holds for $\underline{K}_p$, that is an N_pxN matrix, with all zeroes in the rows apart from the element corresponding to a passive node. K matrices maintain the information related with the position of active and passive nodes in the microgrid even when the global node currents vector $\underline{\dot{I}}$ is split in the active and passive components. Moreover ,K matrices have the property:

$$\underline{K}_a \underline{K}_a{}^T = I \tag{2.12}$$

Where I is the N_axN_a identity matrix. Similarly, the reverse product $\underline{K}_a{}^T \underline{K}_a$ is an NxN matrix, with diagonal elements (n,n) corresponding to $n \in N_a$ equal to 1, and zeroes elsewhere. From these consideration follows that equations (2.11) can be combined into:

$$\underline{\dot{I}} = \underline{K}_a{}^T \underline{\dot{I}}_a + \underline{K}_p{}^T \underline{\dot{I}}_p \tag{2.13}$$

Based on these definitions, the distribution loss (2.6) can now be rewritten as:

$$\begin{aligned} P_d &= \begin{bmatrix} \underline{\dot{I}}_a^T & \underline{\dot{I}}_p^T \end{bmatrix} \begin{bmatrix} \underline{B}_{a,a} & \underline{B}_{a,p} \\ \underline{B}_{p,a} & \underline{B}_{p,p} \end{bmatrix} \begin{bmatrix} \underline{\dot{I}}_a^* \\ \underline{\dot{I}}_p^* \end{bmatrix} \\ P_d &= \underline{\dot{I}}_a^T \underline{B}_{a,a} \underline{\dot{I}}_a^* + \underline{\dot{I}}_a^T \underline{B}_{a,p} \underline{\dot{I}}_p^* + \underline{\dot{I}}_p^T \underline{B}_{p,a} \underline{\dot{I}}_a^* + \underline{\dot{I}}_p^T \underline{B}_{p,p} \underline{\dot{I}}_p^* \end{aligned} \tag{2.14}$$

Where (2.13) has been substituted in (2.6) . In particular results:

$$\begin{aligned} \underline{B}_{a,a} &= \underline{K}_a \underline{B} \underline{K}_a^T, \quad \underline{B}_{a,p} = \underline{K}_a \underline{B} \underline{K}_p^T \\ \underline{B}_{p,a} &= \underline{K}_p \underline{B} \underline{K}_a^T, \quad \underline{B}_{p,p} = \underline{K}_p \underline{B} \underline{K}_p^T \end{aligned} \tag{2.15}$$

As demonstrated in (2.7), $\underline{B}$ is symmetric, and thus $\underline{B}_{a,p} = \underline{B}_{p,a}{}^T$. In fact:

$$\left(\underline{B}_{p,a}\right)^T = \left(\underline{K}_p \underline{B} \underline{K}_a^T\right)^T = \left(\underline{K}_a^T\right)^T \underline{B}^T \left(\underline{K}_p\right)^T = \underline{K}_a \underline{B} \underline{K}_p{}^T = \underline{B}_{a,p} \tag{2.16}$$

Considering the second term of the second equation in (2.14), and using (2.16), it is easy to show that:

$$\dot{\underline{I}}_a^T \underline{B}_{a,p} \dot{\underline{I}}_p^* = \left(\left(\dot{\underline{I}}_p^T \underline{B}_{p,a} \dot{\underline{I}}_a^* \right)^T \right)^* \tag{2.17}$$

And thus, the final expression of distribution loss results:

$$P_d = \dot{\underline{I}}_a^T \underline{B}_{a,a} \dot{\underline{I}}_a^* + 2\Re\left(\dot{\underline{I}}_a^T \underline{B}_{a,p} \dot{\underline{I}}_p^* \right) + \dot{\underline{I}}_p^T \underline{B}_{p,p} \dot{\underline{I}}_p^* \tag{2.18}$$

Finally, it is verified that equation (2.18) is a scalar number. The first and the last terms are real from the definition of matrix $\underline{B}_{p,p}$ and currents vector $\dot{\underline{I}}_p$, while the central term is the real part of a complex number.

Applying the definitions of the matrices describing the microgrid and the applied active and passive currents vectors, and calculating (2.18), the system loss is analytically derived.

2.3.1. Ideal loss minimization

The first interesting result of the analysis is the possibility of calculating the set of active currents $\dot{\underline{I}}_a$ minimizing distribution loss in a microgrid for a given topology, defined by matrix $\underline{B}$, and a given set of passive nodes with passive currents $\dot{\underline{I}}_p$. The loads components of currents $\dot{\underline{I}}_a$ are neglected, the analysis will return the full currents required in the active nodes, from where the references for the distributed generators are calculated using (2.9). This optimization is referred as ideal because no constrains are given for the maximum values of the generated currents $\dot{\underline{I}}_{Ga}$ and for the total current i_0 injected by node 0. This is of course an unrealistic scenario, being all the generators rated for a maximum complex power S and being node 0 current potentially limited by substation requirements coming from the distribution network supervising system. The case of unconstrained optimization represents the best possible condition. The minimum loss condition is calculated setting to zero the Jacobian matrix of the loss function, that is the gradient of the scalar field P_d:

$$\frac{\partial P_d}{\partial \dot{\underline{I}}_a} = 0 \;\Rightarrow\; \begin{cases} \dfrac{\partial P_d}{\partial \underline{x}} = 0 \;\Rightarrow\; 2\underline{B}_{a,a}\underline{x} + 2\,\underline{B}_{a,p}\underline{a} = 0 \\ \dfrac{\partial P_d}{\partial \underline{y}} = 0 \;\Rightarrow\; 2\underline{B}_{a,a}\underline{y} + 2\,\underline{B}_{a,p}\underline{b} = 0 \end{cases} \Rightarrow\; \underline{B}_{a,a}\underbrace{\left(\underline{x} + j\,\underline{y}\right)}_{\dot{I}_a} + \underline{B}_{a,p}\underbrace{\left(\underline{a} + j\,\underline{b}\right)}_{\dot{I}_p} = 0 \tag{2.19}$$

Where $\dot{\underline{I}}_a = \underline{x} + j\,\underline{y}$ and $\dot{\underline{I}}_p = \underline{a} + j\,\underline{b}$.

The resulting active currents are:

$$\underline{\dot{I}}_{a,opt}^{grid} = -\underline{B}_{a,a}^{-1}\,\underline{B}_{a,p}\,\underline{\dot{I}}_{p} \tag{2.20}$$

And recalling equation (2.9), the optimum currents injected by the distributed generators result:

$$\underline{\dot{I}}_{Ga,opt}^{grid} = \underline{B}_{a,a}^{-1}\,\underline{B}_{a,p}\,\underline{\dot{I}}_{p} + \underline{\dot{I}}_{La} \tag{2.21}$$

Before introducing the constrained optimization, a simple example is given to summarize the ideal optimum currents derivation. Consider the small microgrid in Fig. 2.3 : the microgrid has four nodes, with two active and two passive nodes. The passive nodes and the load part of active nodes are represented as impedances, even if in the analysis are treated as current generators. The PCC voltage, corresponding to node 0 voltage, is not indicated: the approximation of assuming current generators both for loads and generators makes the loss minimization independent on the specific voltage level. $\dot{Z}_i$ are the branch impedances. The orientation of the branches is indicated with an arrow in the branch, instead of indicating the branch current. The values of $\dot{Z}_i$, together with the load currents $\dot{I}_{Li}$, are reported in Table 2.1 . The generators currents $\dot{I}_{Gi}$ will be derived later. Being this an example that shows the optimization procedure, the values of currents and impedances are arbitrarily chosen.

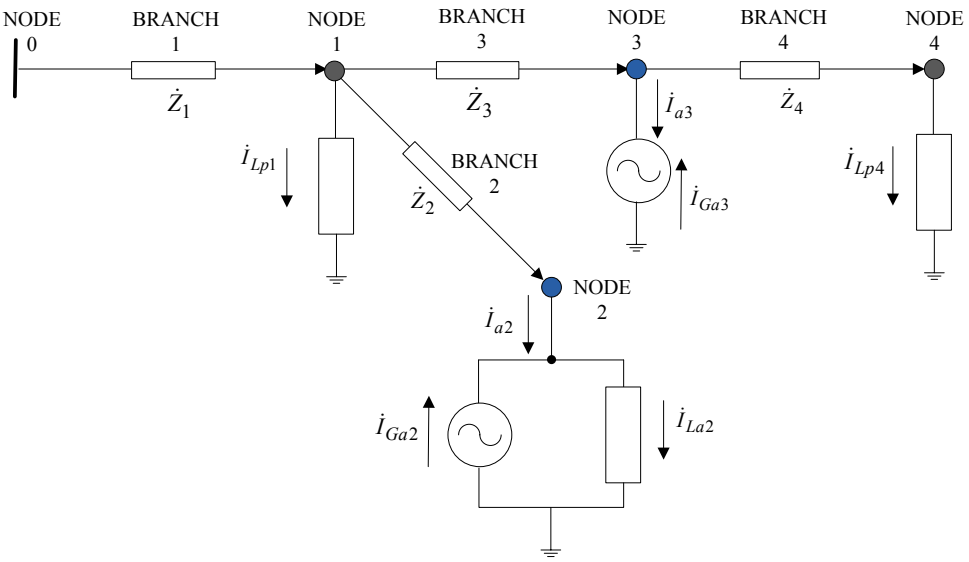

Fig. 2.3 Example of microgrid

Branch impedances	
Z_1	1+j1 Ω
Z_2	2+j2 Ω
Z_3	3+j3 Ω
Z_4	4+j4 Ω
Load currents	
I_{Lp1}	5+j5 A
I_{La2}	10+j10 A
I_{Lp4}	15+j15 A

Table 2.1 Impedances and currents for the microgrid in Fig. 2.3

For the proposed microgrid, the incidence matrix $\underline{A}$ is:

$$\underline{A} = \begin{bmatrix} 1 & 0 & 0 & 0 \\ -1 & 1 & 0 & 0 \\ -1 & 0 & 1 & 0 \\ 0 & 0 & -1 & 1 \end{bmatrix} \tag{2.22}$$

The matrix $\underline{R}$ of the branches resistances is:

$$\underline{R} = \begin{bmatrix} 1 & 0 & 0 & 0 \\ 0 & 2 & 0 & 0 \\ 0 & 0 & 3 & 0 \\ 0 & 0 & 0 & 4 \end{bmatrix} \Omega \tag{2.23}$$

And thus the matrix $\underline{B} = \underline{A}^{-1}\underline{R}\left(\underline{A}^{-1}\right)^T \in R^{NxN}$ results:

$$\underline{B} = \begin{bmatrix} 1 & 1 & 1 & 1 \\ 1 & 3 & 1 & 1 \\ 1 & 1 & 4 & 4 \\ 1 & 1 & 4 & 8 \end{bmatrix} \tag{2.24}$$

It is worth to recall that the generic element (n,m) with n≠m in matrix $\underline{B}$ is the resistance of the common part of the paths connecting node n and node m with node 0, while the element (n,n) is the resistance of the path connecting node n and node 0, as it can be easily checked in Fig. 2.3 . Moreover, $\underline{B}$ is symmetric as expected. With the generators switched off, all the nodes are passive, and the loss results:

$$P_{dMAX} = \underline{I}_L^T \underline{B}\, \underline{I}_L^* = \begin{bmatrix} 5+j5 & 10+j10 & 0 & 15+j15 \end{bmatrix} \begin{bmatrix} 1 & 1 & 1 & 1 \\ 1 & 3 & 1 & 1 \\ 1 & 1 & 4 & 4 \\ 1 & 1 & 4 & 8 \end{bmatrix} \begin{bmatrix} 5-j5 \\ 10-j10 \\ 0 \\ 15-j15 \end{bmatrix} = 5350\text{W} \tag{2.25}$$

Now the optimum currents for the generators are derived. First of all, the matrices $\underline{K}_a$ and $\underline{K}_p$ are:

$$\underline{K}_a = \begin{bmatrix} 0 & 1 & 0 & 0 \\ 0 & 0 & 1 & 0 \end{bmatrix} \qquad \underline{K}_p = \begin{bmatrix} 1 & 0 & 0 & 0 \\ 0 & 0 & 0 & 1 \end{bmatrix} \tag{2.26}$$

From which the sub-matrices $\underline{B}_{aa}$, $\underline{B}_{pp}$, $\underline{B}_{ap}$ are:

$$\begin{aligned} \underline{B}_{a,a} &= \begin{bmatrix} 3 & 1 \\ 1 & 4 \end{bmatrix}, \quad \underline{B}_{a,p} = \begin{bmatrix} 1 & 1 \\ 1 & 4 \end{bmatrix} \\ \underline{B}_{p,a} &= \begin{bmatrix} 1 & 1 \\ 1 & 4 \end{bmatrix}, \quad \underline{B}_{p,p} = \begin{bmatrix} 1 & 1 \\ 1 & 8 \end{bmatrix} \end{aligned} \tag{2.27}$$

The optimum generators currents are finally calculated:

$$\begin{aligned} &\dot{\underline{I}}_{Ga,opt}^{grid} = \underline{B}_{a,a}^{-1}\,\underline{B}_{a,p}\,\dot{\underline{I}}_p + \dot{\underline{I}}_{La} = \begin{bmatrix} 3 & 1 \\ 1 & 4 \end{bmatrix}^{-1} \begin{bmatrix} 1 & 1 \\ 1 & 4 \end{bmatrix} \begin{bmatrix} 5+j5 \\ 15+j15 \end{bmatrix} + \begin{bmatrix} 10+j10 \\ 0 \end{bmatrix} = \begin{bmatrix} 11.3636+j11.3626 \\ 15.9091+j15.9091 \end{bmatrix} \Rightarrow \\ &\begin{cases} \dot{I}_{Ga2,opt} = 11.3636 + j11.3626 \\ \dot{I}_{Ga3,opt} = 15.9091 + j15.9091 \end{cases} \end{aligned} \tag{2.28}$$

Corresponding to the optimum distribution loss:

$$\begin{aligned} &\begin{cases} \dot{I}_a = \begin{bmatrix} \dot{I}_{La2} - \dot{I}_{Ga2} \\ -\dot{I}_{Ga3} \end{bmatrix} = \begin{bmatrix} -1.3636 - j1.3626 \\ -15.9091 - j15.9091 \end{bmatrix} \\ \dot{I}_p = \begin{bmatrix} \dot{I}_{Lp1} \\ \dot{I}_{Lp4} \end{bmatrix} = \begin{bmatrix} 5+j5 \\ 15+j15 \end{bmatrix} \end{cases} \\ &P_{dMIN} = \dot{\underline{I}}_a^T\,\underline{B}_{a,a}\,\dot{\underline{I}}_a^* + 2\Re\left(\dot{\underline{I}}_a^T\,\underline{B}_{a,p}\,\dot{\underline{I}}_p^*\right) + \dot{\underline{I}}_p^T\,\underline{B}_{p,p}\,\dot{\underline{I}}_p^* = 1827.3\text{W} \end{aligned} \tag{2.29}$$

It is also significant to compare the current $\dot{I}_0$ absorbed at the PCC before and after the optimization:

$$\begin{cases} \dot{\underline{I}}_{prev} = \begin{bmatrix} 5+j5 \\ 10+j10 \\ 0 \\ 15+j15 \end{bmatrix} \Rightarrow \dot{I}_{0\,prev} = \sum_{n=1}^{4} \dot{\underline{I}}_{prev}(n) = 30 + j30A \\ \dot{\underline{I}}_{post} = \begin{bmatrix} 5+j5 \\ -1.3636 - j1.3636 \\ -15.9091 - j15.9091 \\ 15+j15 \end{bmatrix} \Rightarrow \dot{I}_{0\,post} = \sum_{n=1}^{4} \dot{\underline{I}}_{post}(n) = 2.7273 + j2.7273 \end{cases} \tag{2.30}$$

The current drawn from the PCC is reduced, because the loads are locally fed by distributed generators.

2.3.2. Loss minimization with PCC constraints

In this paragraph and in the next ones, constraints on the PCC current $\dot{I}_0$ and on distributed generators current capabilities will be introduced. In this paragraph, the constraint on PCC current is investigated. Without loss of generality in the approach, a specific case is considered where the microgrid is in islanded operation, thus absorbing zero current from the main grid. In other words, the microgrid generation units feed all the loads in the microgrid. This scenario could be caused by economical reasons: the microgrid maintains the connection with the main grid, but stops absorbing power when the price of electricity becomes higher, using storage capacity within the microgrid that had been charged during lower price windows. The other scenario is a typical islanding where the main grid is disconnected after a fault. In this case the PCC has to be substituted with another voltage source, to sustain the microgrid without the need for droop controls of generators. On the other hand, if microgrid distributed generation can self feed the loads, this voltage source can be small sized, with minimum investments in the microgrid. The loss minimization has thus to be rewritten adding the constraint:

$$-\sum_{n=1}^{Na} \dot{i}_{an} = \sum_{n=1}^{Np} \dot{i}_{pn} \tag{2.31}$$

Or in other words:

$$\dot{I}_0 = \underline{1}^T \underline{\dot{I}}_p + \underline{1}^T \underline{\dot{I}}_a = 0 \tag{2.32}$$

Remembering that P_d is a function of the active currents $\underline{\dot{I}}_a$, while the passive currents $\underline{\dot{I}}_b$ are known, the resulting constrained optimization problem is represents the typical case where the method of Lagrange Multipliers can be successfully applied, defining the Lagrangian function:

$$L(\underline{\dot{I}}_a, \lambda) = P_d(\underline{\dot{I}}_a) - \lambda \dot{I}_0 \tag{2.33}$$

The loss minimization in the set of $\underline{\dot{I}}_a$ satisfying the constraint (2.32) can be find setting to zero the gradient of (2.33), that is equivalent to a system where the first equation equalizes the gradient of the loss function P_d and the gradient of the constraint function multiplied by a scalar λ (assuming a single constraint as in this application), and the second equation is the constraint itself:

$$\begin{cases} \dfrac{\partial P_d}{\partial \underline{\dot{I}}_a} - \lambda \dfrac{\partial \dot{I}_0}{\partial \underline{\dot{I}}_a} = 0 \\ \dot{I}_0 = 0 \end{cases} \Rightarrow \begin{cases} 2\,\underline{B}_{a,a}\,\underline{\dot{I}}_a + 2\,\underline{B}_{a,p}\,\underline{\dot{I}}_p - \lambda \underline{1} = 0 \\ \underline{\dot{I}}_a^T \underline{1} = -\underline{\dot{I}}_p^T \underline{1} \end{cases} \tag{2.34}$$

Without loss of generality, $\lambda = 2\lambda'$ and the first equation can be multiplied by $\underline{B}_{aa}^{-1}$. Thus, the system can be rewritten as:

$$\begin{cases} \underline{\dot{I}}_a + \underline{B}_{a,a}^{-1}\,\underline{B}_{a,p}\,\underline{\dot{I}}_p - \underline{B}_{a,a}^{-1}\lambda' \underline{1} = 0 \\ \underline{\dot{I}}_a^T \underline{1} = -\underline{\dot{I}}_p^T \underline{1} \end{cases} \tag{2.35}$$

Being the sum of all the column vectors in the first equation of the system equal to zero, also the sum of all the elements is equal to zero:

$$\underline{1}^T \underline{\dot{I}}_a + \underline{1}^T \underline{B}_{a,a}^{-1}\,\underline{B}_{a,p}\,\underline{\dot{I}}_p - \underline{1}^T \underline{B}_{a,a}^{-1}\lambda' \underline{1} = 0 \tag{2.36}$$

From where λ' can be derived, recalling (2.32) and (2.21):

$$\lambda' = \frac{\underline{1}^T \underline{\dot{I}}_a + \underline{1}^T \underline{B}_{a,a}^{-1}\,\underline{B}_{a,p}\,\underline{\dot{I}}_p}{\underline{1}^T \underline{B}_{a,a}^{-1}\,\underline{1}} = \frac{-\underline{1}^T \underline{\dot{I}}_p + \underline{1}^T \underline{B}_{a,a}^{-1}\,\underline{B}_{a,p}\,\underline{\dot{I}}_p}{\underline{1}^T \underline{B}_{a,a}^{-1}\,\underline{1}} = \frac{-\underline{1}^T \underline{\dot{I}}_p - \underline{1}^T \underline{\dot{I}}_{a,opt}^{grid}}{\underline{1}^T \underline{B}_{a,a}^{-1}\,\underline{1}} = \frac{-\dot{I}_{0,opt}^{grid}}{\underline{1}^T \underline{B}_{a,a}^{-1}\,\underline{1}} \tag{2.37}$$

Where $\underline{\dot{I}}_{a,opt}^{grid}$ and $\dot{I}_{0,opt}^{grid}$ are the optimum active currents and the optimum PCC current in the unconstrained (grid connected) case. Finally, the optimum currents in the islanded condition are obtained substituting (2.37) in the first of (2.35):

$$\underline{\dot{I}}_{a,opt}^{isle} = -\underline{B}_{a,a}^{-1}\,\underline{B}_{a,p}\,\underline{\dot{I}}_p + \lambda' \underline{B}_{a,a}^{-1}\,\underline{1} = \underline{\dot{I}}_{a,opt}^{grid} - \dot{I}_{0,opt}^{grid} \frac{\underline{B}_{a,a}^{-1}\,\underline{1}}{\underline{1}^T \underline{B}_{a,a}^{-1}\,\underline{1}} \tag{2.38}$$

Recalling the example of Fig. 2.3 , the constrained optimization results:

$$\frac{\underline{B}_{a,a}^{-1}\,\underline{1}}{\underline{1}^T \underline{B}_{a,a}^{-1}\,\underline{1}} = \begin{bmatrix} 0.6 \\ 0.4 \end{bmatrix} \Rightarrow \underline{\dot{I}}_{a,opt}^{isle} = \begin{bmatrix} -1.3636 - j1.3636 \\ -15.9091 - j15.9091 \end{bmatrix} - \begin{bmatrix} 0.6 \\ 0.4 \end{bmatrix} (2.7273 + j2.7273) = \begin{bmatrix} -3 - j3 \\ -17 - j17 \end{bmatrix}$$

And the corresponding distribution loss:

$$P_{dMIN}^{\ isle} = \left(\underline{\dot{I}}_{a,opt}^{isle} \right)^T \underline{B}_{a,a} \left(\underline{\dot{I}}_{a,opt}^{isle} \right)^* + 2\Re \left(\left(\underline{\dot{I}}_{a,opt}^{isle} \right)^T \underline{B}_{a,p}\,\underline{\dot{I}}_p^* \right) + \underline{\dot{I}}_p^T \underline{B}_{p,p}\,\underline{\dot{I}}_p^* = 1860W \tag{2.39}$$

It can be observed that the introduction of constraints causes the increase of the minimum loss. In this particular case, while the unconstrained loss minimization reduces the loss from 5350W to 1827.3W activating the generators, for a total reduction of 65.84%, the islanded operation has an optimum that is the 65.23% of the original loss. Another important consequence of this analysis is that it provides the optimal currents (power) allocation during the islanded operation, that guarantees minimum distribution loss and thus extends the duration of the energy storage and the microgrid autonomy.

2.3.3. Power converters saturations

The second considered constraint for the loss minimization is the saturation of power converters interfacing the distributed generation with the microgrid. Each generator has in fact a maximum current dependent on its power rating. Assuming constant voltage in the microgrid, the power rating is equivalent to a current rating. The result in terms of distribution loss minimization is that not all the space of generator currents I_{Gan} is available for the minimization problem. In other words, the unconstrained minimization problem could lead to a solution requiring from the generators a set of currents that can't be generated. The set of inequalities are thus expressed in terms of maximum modules of generated currents:

$$\left|\underline{\dot{I}}\right|_{Ga}^{2} \leq \underline{I}_{GaMAX}{}^{2} \tag{2.40}$$

$\underline{I}_{GaMAX}$ is a vector of scalar numbers, defining the limits of the modules. The constraint can be rewritten as:

$$\left|\underline{\dot{I}}\right|_{Ga}^{2} - \underline{I}_{GaMAX}{}^{2} \leq 0 \tag{2.41}$$

In a practical microgrid, the resulting inequality constraints are more complex: normally, not only the total current rating constraint has to be satisfied, but it is necessary to take into account that only the injection of reactive power can be used for optimization purposes, while the generation of active power is constrained by the nature of the distributed energy source (wind, photovoltaic) or by economical reasons (fuel availability, energy storage management etc.). Depending on the actual active power generation, the maximum reactive power constraint changes. On the other hand, the optimum condition when injecting a purely active or reactive current (that can be approximated as pure active and reactive power as it will be shown in the distributed loss minimization chapter), follows from (2.19) simply considering only one of the two derivatives, i.e. only with respect to the real or only with respect to the imaginary part of active nodes currents $\underline{\dot{I}}_a$.

The minimization problem with inequality constraints can be rewritten as a minimization problem with equality constraints, based on the KKT (Karus, Kuhn e Tucker) conditions, by adding an auxiliary column vector $\underline{\vartheta}$. In the distribution loss function the conditions hold, being the minimization problem a convex optimization. The new constraint is:

$$\left|\underline{\dot{I}}\right|_{Ga}^2 - \underline{I}_{GaMAX}{}^2 \le 0 \Rightarrow \left|\underline{\dot{I}}\right|_{Ga}^2 - \underline{I}_{GaMAX}{}^2 + \underline{\vartheta}^2 = 0 \tag{2.42}$$

The new minimization problem can now be solved with the method of Lagrange multipliers, adding the diagonal matrix of the auxiliary positive variables $\underline{\lambda} \ge 0$. The resulting Lagrangian function is:

$$L(\underline{\dot{I}}_{Ga}, \underline{\lambda}, \underline{\vartheta}) = P_d(\underline{\dot{I}}_{Ga}) + \left(\underline{\dot{I}}_{Ga}{}^T \underline{\lambda} \underline{\dot{I}}_{Ga}{}^*\right) + \underline{1}^T \underline{\lambda}\left(-\underline{I}_{GaMAX}{}^2 + \underline{\vartheta}^2\right) \tag{2.43}$$

A minimum of the constrained loss function corresponds to the following conditions:

$$\begin{cases} \dfrac{\partial L}{\partial \underline{\dot{I}}_{Ga}} = 0 \Rightarrow \dfrac{\partial P_d}{\partial \underline{\dot{I}}_{Ga}} - \dfrac{\partial\left(\underline{\dot{I}}_{Ga}{}^T \underline{\lambda} \underline{\dot{I}}_{Ga}{}^*\right)}{\partial \underline{\dot{I}}_{Ga}} = 0 \\ \dfrac{\partial L}{\partial \underline{\lambda}} = 0 \Rightarrow + \dfrac{\partial\left(\underline{\dot{I}}_{Ga}{}^T \underline{\lambda} \underline{\dot{I}}_{Ga}{}^*\right)}{\partial \underline{\lambda}} - \underline{I}_{GaMAX}{}^2 + \underline{\vartheta}^2 = 0 \\ \dfrac{\partial L}{\partial \underline{\vartheta}} = 0 \Rightarrow 2\underline{\lambda}\underline{\vartheta} = 0 \end{cases} \tag{2.44}$$

Consider now, for simplicity, the case with $\underline{\dot{I}}_a = -\underline{\dot{I}}_{Ga}$, meaning that no loads are connected in the active nodes.

$$\begin{cases} \dfrac{\partial L}{\partial \underline{\dot{I}}_{Ga}} = 0 \Rightarrow -2\underline{B}_{a,a}\underline{\dot{I}}_{Ga} + 2\,\underline{B}_{a,p}\underline{\dot{I}}_p - 2\underline{\lambda}\underline{\dot{I}}_{Ga} = \left(-\underline{B}_{a,a} - \underline{\lambda}\right)\underline{\dot{I}}_{Ga} + \underline{B}_{a,p}\underline{\dot{I}}_p = 0 \in N_a x 1 \\ \dfrac{\partial L}{\partial \underline{\lambda}} = 0 \Rightarrow + \dfrac{\partial\left(\underline{\dot{I}}_{Ga}{}^T \underline{\lambda} \underline{\dot{I}}_{Ga}{}^*\right)}{\partial \underline{\lambda}} - \underline{I}_{GaMAX}{}^2 + \underline{\vartheta}^2 = 0 \in N_a x 1 \\ \dfrac{\partial L}{\partial \underline{\vartheta}} = 0 \Rightarrow 2\underline{\lambda}\underline{\vartheta} = 0 \in N_a x 1 \end{cases} \tag{2.45}$$

The resulting system has $3xN_a$ equations, and $3xN_a$ unknowns: the N_a active currents and the corresponding auxiliary variables λ and ϑ. Considering that each current has real and imaginary part, the total effective number of equation and unknowns is $4xN_a$. It is worth to observe that the last equation of the system imposes that when the j-th inequality constraint holds with < sign, the corresponding λ_j has to be zero. On the other side, when the constraint holds with equal sign, λ_j is different from zero and ϑ_j becomes zero. Therefore it is easy to understand how the complexity of an analytical solution grows with the increase of the distributed generation within the microgrid.

Moreover, another important consideration has to be made: trying to find a solution of a constrained minimization problem with the considered method, also the final state of the system in terms of saturated and non-saturated converters is unknown at the beginning of the procedure. This means that the problem has to be approached in an iterative way: assuming first that no saturated converters are in the microgrid, the ideal optimum currents are calculated from the unconstrained problem. The resulting currents are compared with the constraints to identify the saturated converters and the optimization is run again, now with the constraints, until no other generators saturate. For these reasons, in this chapter only the procedure for the example in Fig. 2.3 will be analytically presented based on (2.45). In the simulations chapter, the minimum loss condition with saturated converters will be numerically solved with Matlab.

Returning to the numeric example, to simplify the derivation the load current in node 2, $\dot{I}_{La2}$,is set to zero, and only the grid connected case is investigated. The new microgrid has two loads and two generators. The $\underline{B}$ matrices, describing the topology of the network remain the same. The new unconstrained optimum currents are:

$$\underline{\dot{I}}_{Ga,opt}^{grid} = \underline{B}_{a,a}^{-1}\,\underline{B}_{a,p}\,\underline{\dot{I}}_{p} + \underline{\dot{I}}_{La} = \begin{bmatrix} 3 & 1 \\ 1 & 4 \end{bmatrix}^{-1}\begin{bmatrix} 1 & 1 \\ 1 & 4 \end{bmatrix}\begin{bmatrix} 5+j5 \\ 15+j15 \end{bmatrix} = \begin{bmatrix} 1.3636+j1.3626 \\ 15.9091+j15.9091 \end{bmatrix} = \begin{bmatrix} \dot{I}_{Ga2} \\ \dot{I}_{Ga3} \end{bmatrix} \tag{2.46}$$

Assume now the introduction of current limits, expressed in terms of maximum squared module of the currents. For the first analysis, the converters have the same current rating with maximum squared module of:

$$\begin{bmatrix} \left|\dot{I}_{Ga2}\right|_{MAX}^{2} \\ \left|\dot{I}_{Ga3}\right|_{MAX}^{2} \end{bmatrix} = \begin{bmatrix} M_2 \\ M_3 \end{bmatrix} = \begin{bmatrix} 64 \\ 64 \end{bmatrix} A^2 \tag{2.47}$$

From the unconstrained optimization (2.46), the generator connected to node 2 respects the constraint, while the generator in node 3 saturates. The system of equations for the constrained optimization can now be written as:

$$\begin{cases} \dfrac{\partial L}{\partial \underline{\dot{I}}_{Ga}} = 0 \Rightarrow \left(-\begin{bmatrix} 3 & 1 \\ 1 & 4 \end{bmatrix} - \begin{bmatrix} \lambda_2 & 0 \\ 0 & \lambda_3 \end{bmatrix} \right)\begin{bmatrix} I_2 \\ I_3 \end{bmatrix} + \begin{bmatrix} 1 & 1 \\ 1 & 4 \end{bmatrix}\begin{bmatrix} 5+j5 \\ 15+j15 \end{bmatrix} = 0 \\ \dfrac{\partial L}{\partial \underline{\lambda}} = 0 \Rightarrow \begin{bmatrix} I_2 I_2^* \\ I_3 I_3^* \end{bmatrix} - \begin{bmatrix} M_2 \\ M_3 \end{bmatrix} + \begin{bmatrix} \vartheta_2{}^2 \\ \vartheta_3{}^2 \end{bmatrix} = 0 \\ \dfrac{\partial L}{\partial \underline{\vartheta}} = 0 \Rightarrow \begin{bmatrix} \lambda_2 & 0 \\ 0 & \lambda_3 \end{bmatrix}\begin{bmatrix} \vartheta_2 \\ \vartheta_3 \end{bmatrix} = 0 \end{cases} \tag{2.48}$$

Adding the information on the saturated generator 3: $\lambda_2 = 0$, $\vartheta_3 = 0$. The system can be rewritten as:

$$\begin{cases} \dfrac{\partial L}{\partial \underline{\dot{I}}_{Ga}} = 0 \Rightarrow \begin{bmatrix} -3 & -1 \\ -1 & -4-\lambda_3 \end{bmatrix} \begin{bmatrix} I_2 \\ I_3 \end{bmatrix} + \begin{bmatrix} 20+j20 \\ 65+j65 \end{bmatrix} = 0 \\ \dfrac{\partial L}{\partial \underline{\lambda}} = 0 \Rightarrow \begin{bmatrix} I_2 I_2^* \\ I_3 I_3^* \end{bmatrix} - \begin{bmatrix} 64 \\ 64 \end{bmatrix} + \begin{bmatrix} \vartheta_2{}^2 \\ 0 \end{bmatrix} = 0 \\ \dfrac{\partial L}{\partial \underline{\vartheta}} = 0 \Rightarrow \begin{bmatrix} 0 & 0 \\ 0 & \lambda_3 \end{bmatrix} \begin{bmatrix} \vartheta_2 \\ 0 \end{bmatrix} = 0 \end{cases} \tag{2.49}$$

That can be reordered in the set of equations:

$$\begin{cases} -3I_2 - I_3 + 20 + j20 = 0 \\ -I_2 - (4+\lambda_3) I_3 + 65 + j65 = 0 \\ I_2 I_2^* - 64 + \vartheta_2{}^2 = 0 \\ I_3 I_3^* - 64 = 0 \end{cases} \tag{2.50}$$

Defining now $I_2 = x_2 + jy_2$ and $I_3 = x_3 + jy_3$ the number of unknowns grows from four to six, and the same does the number of equations:

$$\begin{cases} -3x_2 - x_3 + 20 = 0 \\ -3y_2 - y_3 + 20 = 0 \\ -x_2 - (4+\lambda_3) x_3 + 65 = 0 \\ -y_2 - (4+\lambda_3) y_3 + 65 = 0 \\ x_2{}^2 + y_2{}^2 - 64 + \vartheta_2{}^2 = 0 \\ x_3{}^2 + y_3{}^2 - 64 = 0 \end{cases} \tag{2.51}$$

The system is clearly a non linear system, that can be analytically or numerically solved. Considering the overall complexity, the numerical solution is given, leading to:

$$\begin{cases} x_2 = 4.7810A \\ \mathrm{y}_2 = 4.7810A \\ x_2 = 5.6569A \\ \mathrm{y}_2 = 5.6569A \\ \vartheta_2 = 4.2759 \\ \lambda_3 = 6.6453 \end{cases} \Rightarrow P_d{}^{cons} = 2598\mathrm{W} \tag{2.52}$$

It can be easily shown that any other combination of active and non active constraints leads either to an unsolvable system or to a solution violating the constraints or with negative values of λ. The resulting minimum loss is 2598W. This value can be verified plotting the loss function (2.18) for the example under exam. For simplicity, the constrained current is assumed to be fixed at the value

obtained in (2.52). Fig. 2.4 reports the loss as a function of the real and imaginary part of $\dot{I}_2$, x_2 and y_2 respectively, confirming the obtained numbers. The case of islanded condition is omitted for simplicity, but the analytical derivation of the non linear system is similar.

In the next section a different approach is introduced, that approximates the theoretical loss minimization in case of converters saturation to offer a more practical and operative perspective on constrained minimization. A new function is introduced that is the weighted sum between the previous loss function and another term, representing the utilization of the current capability of the distributed generators.

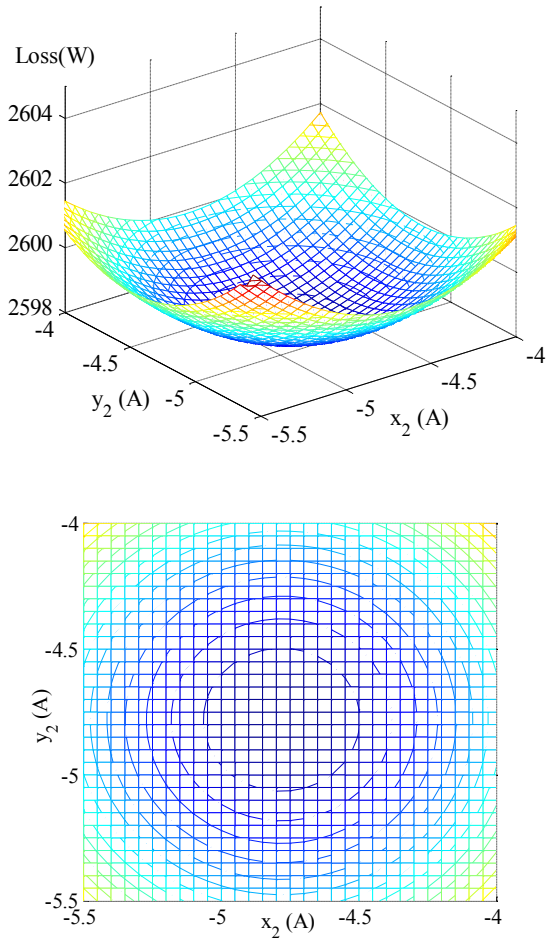

Fig. 2.4 Loss as a function of real and imaginary part of node current $\dot{I}_2$ for saturated $\dot{I}_3$ ($\dot{I}_2$ and $\dot{I}_3$ are expressed with load convention)

2.3.4. Simplified constrained minimization

The aim of this section is to offer a different perspective on the limit introduced by the converters saturation. In particular, the proposed solution gives an operative point of view that helps the investigation of the dependency of distribution loss on the current limits without involving a complex solution method. Of course the result will be sub-optimum, and the differences with respect to the previous approach will be investigated. The new objective function is:

$$\varphi = \varphi_p + \varphi_i \tag{2.53}$$

Where: $\varphi_p = \alpha P_d$ is the part depending on distribution loss, weighted with the positive constant α, while $\varphi_i = \beta\gamma$ depends on the utilization function γ weighted with the constant β. The utilization function is defined as:

$$\gamma = \frac{1}{N_a}\sum_{n=1}^{N_a}\left(\left|\dot{I}_{Gan}\right| / I_{Gan}^{rated}\right)^2 \tag{2.54}$$

γ is a function that increases as the generators increase their current reference with respect to the nominal value. The function is equal to one when all the generators are injecting their rated currents (but not only in this case, consider for example of two generators, one of them injecting zero current and the other one in overload operation, injecting $\sqrt{2}$ times its nominal value: the function is still equal to one. In the different case of no overload allowed for the generators, the maximum value of the function becomes one, and is reached if and only if all the generators are saturated). These considerations lead to the meaning of the proposed approach: trying to minimize the combined function is equivalent to trying to minimize the loss while keeping the generator utilization as low as possible, exactly as in the constrained minimization. Of course the choice of the weights α and β plays a role in the global minimization result, that will be investigated later. (2.54) can be rewritten as:

$$\begin{cases} \gamma = \dfrac{1}{N_a}\displaystyle\sum_{n=1}^{Na}\frac{\left|-\dot{I}_{an}+\dot{I}_{Lan}\right|^2}{\left(I_{Gan}^{rated}\right)^2} = \frac{1}{N_a}\sum_{n=1}^{Na}\frac{\left(-\dot{I}_{an}+\dot{I}_{Lan}\right)\left(-\dot{I}_{an}+\dot{I}_{Lan}\right)^*}{\left(I_{Gan}^{rated}\right)^2} \\ \underline{G} = \dfrac{1}{N_a}diag\left\{1/\left(I_{Gan}^{\max}\right)^2\right\}_{n=1}^{Na} \end{cases} \tag{2.55}$$

$$\Rightarrow \gamma = \left(-\dot{I}_a^T + \dot{I}_{La}^T\right)^T \underline{G}\left(-\dot{I}_a^* + \dot{I}_{La}^*\right)$$

And finally:

$$\gamma = \underline{\dot{I}}_a^T \underline{G}\, \underline{\dot{I}}_a^* - 2\Re\left(\underline{\dot{I}}_a^T \underline{G}\, \underline{\dot{I}}_{La}^* \right) + \underline{\dot{I}}_{La}^T \underline{G}\, \underline{\dot{I}}_{La}^* \tag{2.56}$$

Function γ is real, as it can be easily shown substituting in (2.56) the real and imaginary part of the load currents connected to the active node a $\underline{\dot{I}}_{La}$ and of the total absorbed current $\underline{\dot{I}}_a$. For the currents definitions and directions, the same convention of Fig. 2.3 has been used. Merging together the γ function (2.56) and P_d (2.18), the objective function is:

$$\begin{aligned} \varphi = & \alpha\left(\underline{\dot{I}}_a^T \underline{B}_{a,a}\, \underline{\dot{I}}_a^* + 2\Re\left(\underline{\dot{I}}_a^T \underline{B}_{a,p}\, \underline{\dot{I}}_p^* \right) + \underline{\dot{I}}_p^T \underline{B}_{p,p}\, \underline{\dot{I}}_p^* \right) \\ & + \beta\left(\underline{\dot{I}}_a^T \underline{G}\, \underline{\dot{I}}_a^* - 2\Re\left(\underline{\dot{I}}_a^T \underline{G}\, \underline{\dot{I}}_{La}^* \right) + \underline{\dot{I}}_{La}^T \underline{G}\, \underline{\dot{I}}_{La}^* \right) \end{aligned} \tag{2.57}$$

The minimum can be easily obtained setting to zero the gradient:

$$\begin{aligned} & \frac{\partial P_d}{\partial \underline{\dot{I}}_a} = \frac{\partial P_d}{\partial \underline{x}} + j\frac{\partial P_d}{\partial \underline{y}} \quad \Rightarrow \quad \frac{\partial P_d}{\partial \underline{\dot{I}}_a} = 2\underline{B}_{a,a} \underbrace{\left(\underline{x} + j\,\underline{y} \right)}_{\underline{\dot{I}}_a} + 2\underline{B}_{a,p} \underbrace{\left(\underline{a} + j\,\underline{b} \right)}_{\underline{\dot{I}}_p} = 0 \\ & \frac{\partial \gamma}{\partial \underline{\dot{I}}_a} = \frac{\partial \gamma}{\partial \underline{x}} + j\frac{\partial \gamma}{\partial \underline{y}} \quad \Rightarrow \quad \frac{\partial \gamma}{\partial \underline{\dot{I}}_a} = 2\underline{G} \underbrace{\left(\underline{x} + j\,\underline{y} \right)}_{\underline{\dot{I}}_a} - 2\underline{G} \underbrace{\left(\underline{c} + j\,\underline{d} \right)}_{\underline{\dot{I}}_{La}} = 0 \end{aligned} \tag{2.58}$$

Leading to the final optimum condition:

$$\frac{\partial \varphi}{\partial \underline{\dot{I}}_a} = \alpha\frac{\partial P_d}{\partial \underline{\dot{I}}_a} + \beta\frac{\partial \gamma}{\partial \underline{\dot{I}}_a} = 0 \quad \Rightarrow \quad \left(\alpha\underline{B}_{a,a} + \beta\underline{G} \right)\underline{\dot{I}}_a + \alpha\underline{B}_{a,p}\, \underline{\dot{I}}_p - \beta\underline{G}\, \underline{\dot{I}}_{La} = 0 \tag{2.59}$$

Defining $\underline{E} = \alpha\underline{B}_{a,a} + \beta\underline{G}$ and $\underline{\dot{F}} = -\alpha\underline{B}_{a,p}\, \underline{\dot{I}}_p + \beta\underline{G}\, \underline{\dot{I}}_{La}$ and solving for the set of total active currents $\underline{\dot{I}}_a$ absorbed by active nodes results:

$$\underline{\dot{I}}_{a,opt}^{grid} = \underline{E}^{-1}\, \underline{F} \tag{2.60}$$

From where the currents that the generators injects to minimize the objective function φ in grid connected operations are:

$$\underline{\dot{I}}_{Ga,opt}^{grid} = \underline{\dot{I}}_{La} - \underline{\dot{I}}_{a,opt}^{grid} \tag{2.61}$$

The set of optimum currents depends on the choice of the weights α and β. It is immediate to check that setting $\alpha \neq 0$ and $\beta = 0$ results in the optimum unconstrained currents already calculated in (2.21), that guarantees absolute minimum distribution loss. The other extreme case is $\beta \neq 0$ and $\alpha = 0$: the loss are no longer taken into account and only the utilization function γ is minimized,

leading to the condition of maximum loss, being all the generators set to zero current injection. Before presenting a deeper analysis on the α and β coefficients, the islanded case is presented. Only the final results are reported, being the derivation symmetrical to the one already presented in (2.31)-(2.38). The constraint on zero net absorption of current is (2.32). The constrained problem is again solved with the Lagrangian Multipliers method:

$$\begin{cases} \dfrac{\partial \varphi}{\partial \underline{\dot{I}}_a} + 2\lambda \dfrac{\partial \dot{I}_0}{\partial \underline{\dot{I}}_a} = 0 \\ \dot{I}_0 = 0 \end{cases} \Rightarrow \begin{cases} \underline{\underline{E}}\,\underline{\dot{I}}_a - \underline{\dot{F}} + \lambda \underline{1} = 0 \\ \underline{\dot{I}}_a^T \underline{1} = -\underline{\dot{I}}_p^T \underline{1} \end{cases} \tag{2.62}$$

Multiplying the first equation by $\underline{\underline{E}}^{-1}$, the problem is exactly in the same form of (2.36):

$$\underline{1}^T \underline{\dot{I}}_a - \underline{1}^T \underline{\underline{E}}^{-1} \underline{\dot{F}} - \lambda \underline{1}^T \underline{\underline{E}}^{-1} \underline{1} = 0 \tag{2.63}$$

And thus the resulting set of absorbed optimum active nodes currents is:

$$\underline{\dot{I}}_{a,opt}^{isle} = \underline{\underline{E}}^{-1} \underline{\dot{F}} + \lambda \underline{\underline{E}}^{-1} \underline{1} = \underline{\dot{I}}_{a,opt}^{grid} + \dot{I}_{0,opt}^{grid} \frac{\underline{\underline{E}}^{-1} \underline{1}}{\underline{1}^T \underline{\underline{E}}^{-1} \underline{1}} \tag{2.64}$$

Where it is worth to recall that $\dot{I}_{0,opt}^{grid} = \underline{1}^T \underline{\dot{I}}_p + \underline{1}^T \underline{\dot{I}}_{a,opt}^{grid}$. It is also important to observe that in islanded condition, setting $\alpha = 0$ leads to the active currents set that minimizes the stresses on the generators, being the losses neglected and being minimized only the utilization function γ

2.3.4.1. Choice of the weights for the objective function φ

As mentioned before, the position of the minimum, i.e. the set of active nodes currents $\underline{\dot{I}}_a$ that minimizes the objective function, depends on the objective function coefficients α and β. The two coefficients can be replaced by a single value μ, being the position of the minimum independent on a common gain in both the components of φ. In particular, it is worth to normalize the loss to the minimum achievable loss in the case of unconstrained minimization, thus leading to the new function:

$$\varphi = \frac{P_d}{P_{d\,\min}} + \mu\gamma \tag{2.65}$$

It becomes clear that $\mu = 0$ means loss minimization without constraints, $0 < \mu < 1$ weights loss and generators utilization in a balanced way ($\frac{P_d}{P_{d\,\min}}$=1 in the minimum loss, γ=1 in the condition of

full utilization of the generators, i.e. all the converters saturated to their nominal current) and $\mu > 1$ gives the priority to the minimization of the generators utilization, with the extreme limit of $\mu \to \infty$, meaning that all the generators are injecting zero current. The function φ is continuous, and thus between the two cases $\mu = 0, \mu \to \infty$, corresponding to minimum loss (maximum current stress in the generators) and maximum loss (zero current in the generators) respectively, there is also the minimum loss constrained to the saturation limits. For a given set of loads, the value of the optimum μ is a function of the saturation limits of the converters.

It is worth to observe that the optimum value for μ is generally far from the value that leads $\gamma = 1$. This happens because the definition of γ imposes a locus of current sets where the equality is satisfied. This means that whit N_a active nodes, one node could potentially inject N_a times his squared rated current, the other generators could be off, and γ function would be equal to one. In any case, in the direction of increasing μ, the microgrid will increase the loss and reduce the injected currents, until all the currents return within the limits. Moreover, the loss corresponding to the optimum μ is in general not the same of the constrained optimization reported in the previous paragraphs. Anyway, due to the regularity of the loss function and to the fact that the addition of a γ function weighted with μ tends to move the minimum of the resulting function from the unconstrained minimization to the origin, i.e. zero injected currents, it is reasonable to think that the point where this simplified optimum search technique stops, leading the generated currents within the limits, is not considerably far from the real optimum. Neglecting this inherent error, that is assumed to be small enough to be neglected, the latter approach is particularly simple, and it can also be solved graphically. In the next, to conclude the chapter, the example of Fig. 2.3 will be analyzed with this technique, and compared with the analytical solution of the constrained optimization for two different values of converters current ratings. The microgrid topology remains the one of Fig. 2.3 , while the values of active currents and loads are changed from complex values to real values, i.e. the microgrid can be considered either an AC microgrid with resistive cables and active power only both for loads and generators, or a DC microgrid. The impedances and currents are reported in Table 2.2 :

Branch impedances	
Z_1	1 Ω
Z_2	2 Ω
Z_3	3 Ω
Z_4	4 Ω
Load currents	
I_{Lp1}	10 A
I_{La2}	0 A
I_{Lp4}	15 A

Table 2.2 Modified values of impedances and currents for the microgrid in Fig. 2.3

The choice of real values has been made to be able to plot the objective functions in three dimensional plots. In fact, the only unknowns of the microgrid are the generators currents I_{La2} and I_{La3}. First of all, the unconstrained loss function is presented in Fig. 2.5 :

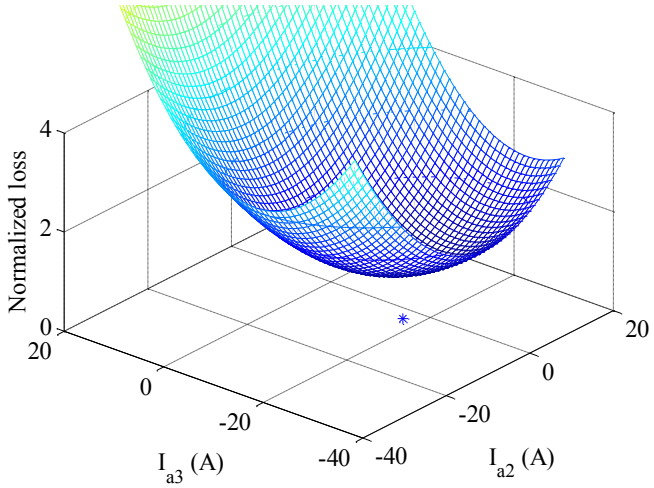

Fig. 2.5 Normalized loss function $P_d(I_{a2},I_{a3})$ for parameters in Table 2.2 .

The loss in Fig. 2.5 has been normalized to the minimum value, that is:

$$P_{d,\min} = 954.54\text{W} \quad \text{I}_{\text{a2,min}} = -2.7273\text{A} \quad \text{I}_{\text{a3,min}} = -16.8182\,\text{A} \tag{2.66}$$

In the next, the saturations of the power converters are added. To check the behaviour of the system is different conditions, two cases have been considered:

Case 1: $\left|\text{I}_{a2}\right|^2_{\max} = \left|\text{I}_{a3}\right|^2_{\max} = 100$. With these saturations, generator 2 is within the limits, while generator 3 saturates. First of all, the ideal solution of the constrained minimization problem is considered. The solution is found solving the following non-linear system (equivalent to system (2.51) apart from the values of load currents):

$$\begin{cases} -3I_{a2} - I_{a3} + 25 = 0 \\ -I_{a2} - (4+\lambda)I_{a3} + 70 = 0 \\ {I_{a2}}^2 - 100 + \vartheta^2 = 0 \\ {I_{a3}}^2 - 100 = 0 \end{cases} \tag{2.67}$$

The optimum current injection that optimize the constrained problem results:

$$P^{cons}_{d,opt} = 1125\text{W} \quad \text{I}^{cons}_{\text{a2,opt}} = -5\text{A} \quad \text{I}^{cons}_{\text{a3,opt}} = -10\,\text{A} \tag{2.68}$$

Now, the simplified method is applied, and compared with the ideal solution (2.68). A graphical solution is proposed, also to give a better idea of the behaviour of the system. It is worth to recall the objective function that has to be minimized is $\varphi = \frac{P_d}{P_{d\,\min}} + \mu\gamma$ with $P_{d,\min} = 954.54\text{W}$. The weight μ is varied from $\mu = 0$ to $\mu = 3$ with steps $\Delta\mu = 0.05$.

First of all, a plot of the objective function φ is reported for $\mu = 0$ and $\mu = 3$ in Fig. 2.6 :

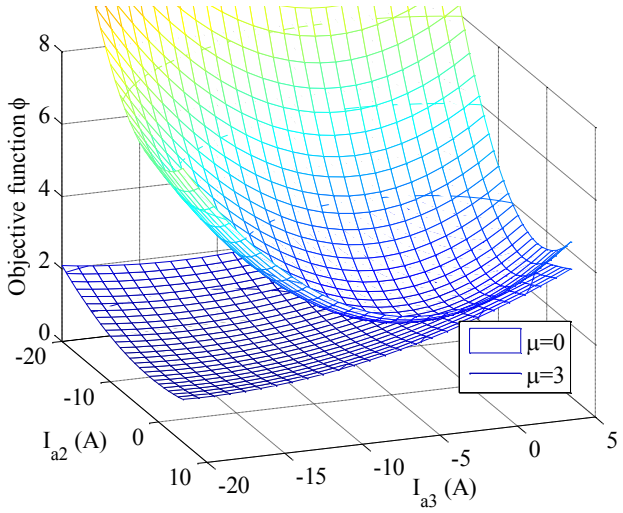

Fig. 2.6 Objective function for μ=0 (lower surface) and μ=3 (upper surface)

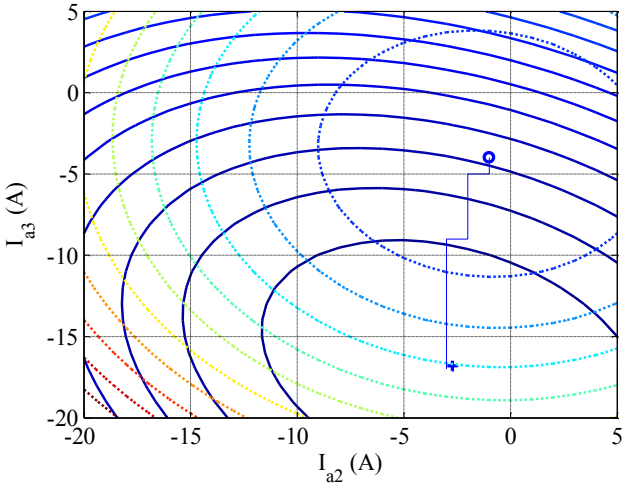

Fig. 2.7 Level curves for Fig. 2.6 and corresponding minimum points. μ=0 continuous lines and μ=3 dotted lines

Moreover, in Fig. 2.6 the level curves are reported, and the changing in the position of the objective function minimum can be appreciated. The original minimum, corresponding to loss function only, is indicated with the symbol "+", while the final minimum with "o". Increasing further the weight μ of the function γ, the minimum would converge in (0,0). Fig. 2.8 shows the

currents $I_{a2,\min}$ and $I_{a3,\min}$ corresponding to the minimum of function φ as a function of μ. The other figures, Fig. 2.9 and Fig. 2.10 respectively, report the values of the loss function P_d and of the utilization function γ corresponding to the minimum of φ. From the observation of the graphs it is immediate to derive the optimal μ that guarantees the best approximation of the ideal constrained optimization.

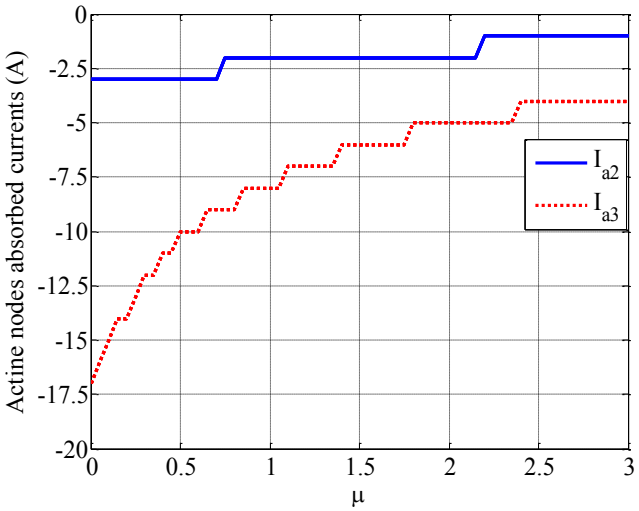

Fig. 2.8 Active nodes currents corresponding to the minimum of φ, as a function of μ

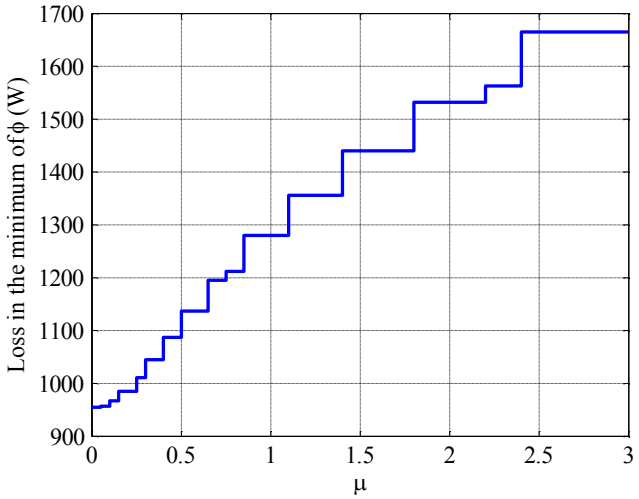

Fig. 2.9 Loss function P_d in the minimums of φ as a function of μ

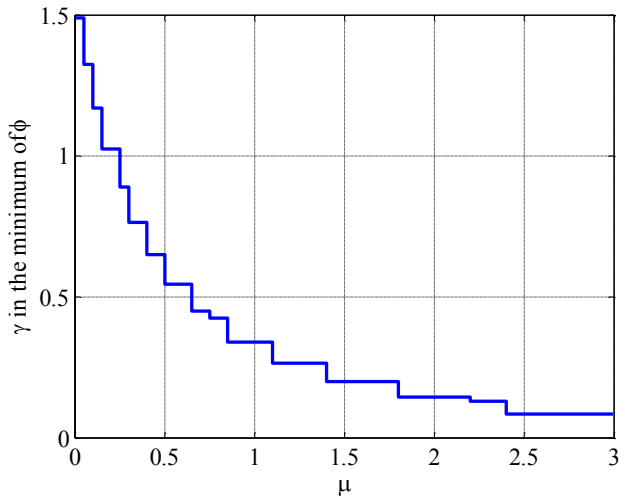

Fig. 2.10 Utilization function γ in the minimums of φ as a function of μ

From Fig. 2.8 , the saturation constrains are respected when $\mu \approx 0.5$, with a corresponding loss from Fig. 2.9 $P_d \approx 1137W$, that is reasonably closed to the ideal value in (2.68)., also considering the approximation introduced with a low resolution in μ.

Case 2: $|\mathrm{I}_{a2}|^2_{\max} = 100, |\mathrm{I}_{a3}|^2_{\max} = 10$: the same analysis of case 1 has been performed with different saturation limits. Without the repetition of all the waveforms, the ideal constrained solution is:

$$P_{d,opt}^{cons} = 1638\mathrm{W} \quad \mathrm{I}_{\mathrm{a2,opt}}^{cons} = -7.2792\,\mathrm{A} \quad \mathrm{I}_{\mathrm{a3,opt}}^{cons} = -3.1623\ \mathrm{A} \tag{2.69}$$

While the approximated solution is found for $\mu \approx 0.35$, corresponding to $P_d \approx 1671W$.

Before passing to the new chapter, it is worth to remind that all the reported analysis holds in the hypothesis of a microgrid with tree topology. This assumption strongly simplifies the matrices derivation, making the analysis particularly intuitive and with a direct physical meaning. The tree topology is dominant in low voltage distribution, and thus the hypothesis is consistent. Nevertheless, it could be necessary to consider the loss minimization of meshed microgrids, where for example some sensitive loads require a redundant feeding to increase the supply reliability. Moreover, this would be a more general approach: giving an instrument to derive the optimum loss of a meshed system, the solution of a tree topology would be a simpler case of the same method.

At the beginning of this chapter, the loss has been expressed as a function of the node currents, thanks to the invertibility of the incidence matrix $\underline{A}$, in equations (2.5)-(2.6) . In case of meshed network, the number of branches L is always greater than the number of nodes N, and thus the resulting $\underline{A}$ matrix is LxN and therefore non-invertible. As a consequence, the translation between

branch currents and node currents is not immediate. The solution can be found introducing the node voltage information as support variable. In particular, the Kirchhoff laws can be written as:

$$\begin{cases} \underline{A}^T \underline{\dot{J}} - \underline{\dot{I}} = 0 \\ \underline{A}\underline{\dot{U}} + \underline{R}\underline{\dot{J}} = 0 \end{cases} \tag{2.70}$$

Where $\underline{A}$ is the incidence matrix derived with the same definition of (2.2), but adding also node 0, $\underline{\dot{U}}$ is the vector of nodes voltages including node 0, $\underline{A}\underline{\dot{U}}$ are the branch voltages, $\underline{\dot{I}}$ the currents absorbed by the nodes and by node 0 and $\underline{R}$ an LxL matrix containing in the diagonal the resistance of branch L-th. This is true only if a purely resistive cable is considered, otherwise an impedances matrix $\underline{\dot{Z}}$ should be considered, considering only the real part in the calculation of the loss. The total distribution loss can therefore be written as:

$$P_d = \underline{\dot{J}}^T \underline{R}\underline{\dot{J}}^* = \underline{\dot{U}}^T \left(\underline{A}^T \underline{R}^{-1} \underline{A}\right)\underline{\dot{U}}^* = \underline{\dot{U}}^T \underline{L}\underline{\dot{U}}^* \tag{2.71}$$

Where $\underline{L}$ is an $(N+1)x(N+1)$ matrix, in general with complex values (non strictly resistive case). It can now be demonstrated that a symmetric matrix $\underline{X}$ exists such that:

$$\begin{cases} \underline{X}\underline{L} = I - \underline{1}\underline{1}_0^T \\ \underline{X}\underline{1}_0 = 0 \end{cases} \tag{2.72}$$

Where I is the identity $(N+1)x(N+1)$ matrix, $\underline{1}_0^T$ is a row vector with all zeros apart from the first element. Clearly, matrix $\underline{X}$ depends only on the microgrid topology. The meaning of definition of $\underline{X}$ could appear cryptic, but it can be explained based on (2.70):

$$\begin{cases} \underline{A}^T \underline{\dot{J}} = \underline{\dot{I}} \\ \underline{A}^T \underline{R}^{-1} \underline{A}\underline{\dot{U}} = -\underline{A}^T \underline{\dot{J}} \end{cases} \Rightarrow \underline{L}\underline{\dot{U}} = -\underline{\dot{I}} \tag{2.73}$$

Multiplying both sides of the last equation by $\underline{X}$:

$$\begin{aligned} &\underline{X}\underline{L}\underline{\dot{U}} = -\underline{X}\underline{\dot{I}} \Rightarrow \underline{\dot{U}} - \underline{1}\dot{U}_0 = -\underline{X}\underline{\dot{I}} \\ &\Rightarrow \underline{\dot{U}} = \underline{1}\dot{U}_0 - \underline{X}\underline{\dot{I}} \end{aligned} \tag{2.74}$$

The last equation can be substituted in (2.71), obtaining the desired expression of the loss as a function of the nodes currents:

$$P_d = \underline{\dot{I}}^T \Re(\underline{X})\underline{\dot{I}}^* \tag{2.75}$$

The construction of $\underline{X}$ for a given $\underline{L}$ follows from the definition: it can be shown that the sub-matrix obtained removing the first row and the first column of $\underline{L}$ is invertible: $\underline{X}$ is obtained adding to this inverse a first row of ones and a first column with the first element equal to one and the others equal to zero. Apart from the different dimensions, ((2.75) includes node 0 in the matrices definition, while (2.6) doesn't) the resulting equation has the same structure of (2.6) : the optimization can therefore be carried out similarly to the previous case. The analytical expression is not given for simplicity, leaving to the common solvers the search for the minimum loss condition for a given topology and a given set of loads and generators.

In the next section, the loss minimization problem in a meshed microgrid is solved in an alternative way, using networks theory, without the need for an explicit derivation of the Kirchhoff's laws.

2.4.Distribution Loss in meshed microgrids

As final generalization of the minimum loss condition, the ideal minimum loss configuration is here derived for the general case of a meshed microgrid. The hypotheses on the network are the same of the radial case, but no constraints are set on grid topology. In this general case, the incidence matrix (2.2) can be split in two different matrices A_t and A_l, respectively referred to the microgrid tree and to its complement, the cotree, containing the branches not included in the tree. Exactly like in the pure tree topology, A_t will be a NxN matrix with the nodes in the columns and the tree branches in the rows, where N is the total number of nodes (active and passive) excluding node 0, the PCC. The cotree incidence matrix, A_l will be a KxN matrix, where K is the number of branches belonging to the cotree. The total incidence matrix will be $A=\begin{bmatrix} A_t \\ A_l \end{bmatrix}$. The elements of the matrices are defined as in (2.2), after selecting an orientation for each branch. Similarly to the convention chosen for the tree topology, once a label number has been defined for each node, the branch connecting two nodes can be oriented from the node with lower label to the node with higher label. Of course this convention is arbitrary and can be changed without loss of generality. Moreover, in the definition of the tree and the cotree is not unique, again without any loss of generality.

The goal is now to obtain a result similar to the simpler tree topology, considering that the distribution loss always depends on the branch currents $\underline{\dot{J}}$ and on the branch resistances $\underline{R}$:

$$P_d=\underline{\dot{J}}^T\,\underline{R}\,\underline{\dot{J}}^*=\begin{vmatrix}\underline{\dot{J}}_t^T & \underline{\dot{J}}_l^T\end{vmatrix}\begin{vmatrix}\underline{R}_t & \underline{0}\\ \underline{0} & \underline{R}_l\end{vmatrix}\begin{vmatrix}\underline{\dot{J}}_t^*\\ \underline{\dot{J}}_l^*\end{vmatrix}=\underline{\dot{J}}_t^T\,\underline{R}_t\,\underline{\dot{J}}_t^*+\underline{\dot{J}}_l^T\,\underline{R}_l\,\underline{\dot{J}}_l^* \tag{2.76}$$

If the branch currents are expressed as a function of the node currents (active and passive, both with absorbed direction in this analysis), also the loss becomes function of the node currents and therefore the set of injected currents can be analytically found that minimizes the loss. To achieve this, it is observed that the currents in the branches belonging to the tree $\underline{\dot{J}}_t$ can be written as a function of the node currents $\underline{\dot{I}}$ and the cotree branches currents $\underline{\dot{J}}_l$. It is worth to remind that these currents have the same orientation defined for the branches in the definition of the incidence matrices. For linearity, the superposition of effects can be applied and therefore the contribution of $\underline{\dot{I}}$ will be:

$$\underline{\dot{J}}_t^{'} = \left(\underline{A}_t^{-1}\right)^T \underline{\dot{I}} = \underline{Q}_i \, \underline{\dot{I}} \tag{2.77}$$

While the contribution of $\underline{\dot{J}}_l$ is:

$$\underline{\dot{J}}_t^{''} = \left(\underline{A}_t^T\right)^{-1} \underline{A}_l^T \, \underline{\dot{J}}_l = \underline{Q}_l \, \underline{\dot{J}}_l \tag{2.78}$$

And finally:

$$\underline{\dot{J}}_t = \underline{\dot{J}}_t^{'} + \underline{\dot{J}}_t^{''} = \underline{Q}_i \, \underline{\dot{I}} + \underline{Q}_l \, \underline{\dot{J}}_l \tag{2.79}$$

The total distribution loss can be expressed as

$$\begin{aligned} P_d &= \left(\underline{\dot{I}}^T \, \underline{Q}_i^T + \underline{\dot{J}}_l^T \, \underline{Q}_l^T \right) \underline{R}_t \left(\underline{Q}_i \, \underline{\dot{I}}^* + \underline{Q}_l \, \underline{\dot{J}}_l^* \right) + \underline{\dot{J}}_l^T \, \underline{R}_l \, \underline{\dot{J}}_l^* = \\ &= \underline{\dot{I}}^T \underbrace{\underline{Q}_i^T \, \underline{R}_t \, \underline{Q}_i}_{\underline{S}_i} \underline{\dot{I}}^* + \underline{\dot{I}}^T \underbrace{\underline{Q}_i^T \, \underline{R}_t \, \underline{Q}_l}_{\underline{S}_i^l} \underline{\dot{J}}_l^* + \underline{\dot{J}}_l^T \underbrace{\underline{Q}_l^T \, \underline{R}_t \, \underline{Q}_i}_{\underline{S}_l^i} \underline{\dot{I}}^* + \underline{\dot{J}}_l^T \left(\underbrace{\underline{Q}_l^T \, \underline{R}_t \, \underline{Q}_l}_{\underline{S}_l} + \underline{R}_l \right) \underline{\dot{J}}_l^* \end{aligned} \tag{2.80}$$

That observing the symmetry of matrices $\underline{S}$, can be rewritten as:

$$P_d = \underline{\dot{I}}^T \, \underline{S}_i \, \underline{\dot{I}}^* + 2 \underline{\dot{I}}^T \, \underline{S}_i^l \, \underline{\dot{J}}_l^* + \underline{\dot{J}}_l^T \left(\underline{S}_l + \underline{R}_l \right) \underline{\dot{J}}_l^* = \underline{\dot{I}}^T \, \underline{S}_i \, \underline{\dot{I}}^* + 2 \underline{\dot{J}}_l^T \, \underline{S}_l^i \, \underline{\dot{I}}^* + \underline{\dot{J}}_l^T \left(\underline{S}_l + \underline{R}_l \right) \underline{\dot{J}}_l^* \tag{2.81}$$

In (2.80), the loss is still a function of both the node currents $\underline{\dot{I}}$ and the cotree branches currents $\underline{\dot{J}}_l$. To obtain the desired equation of the loss, a supplementary observation is required: in the hypothesis that all the branches have the same phase of the impedance, i.e. the same impedance per unit of length or equivalently the same cable section, for a given set of node currents $\underline{\dot{I}}$, the branch currents are the result of a natural repartition that automatically guarantees minimum loss (like in a

purely resistive network). Therefore, finding $\underline{\dot{J}}_l$ that minimizes (2.80) gives the desired relation between $\underline{\dot{J}}_l$ and $\underline{\dot{I}}$:

$$\frac{\partial P_d}{\partial \underline{\dot{J}}_l} = 0 \quad \Rightarrow \quad 2\,\underline{S}_l^i\,\underline{\dot{I}}^* + 2\left(\underline{S}_l + \underline{R}_l\right)\underline{\dot{J}}_l^* = 0 \quad \Rightarrow \quad \underline{\dot{J}}_l = -\left(\underline{S}_l + \underline{R}_l\right)^{-1}\underline{S}_l^i\,\underline{\dot{I}} \tag{2.82}$$

Substituting (2.82) in (2.81), the final loss results:

$$\begin{aligned} P_d &= \underline{\dot{I}}^T\,\underline{S}_i\,\underline{\dot{I}}^* - 2\,\underline{\dot{I}}^T\,\underline{S}_i^l\left(\underline{S}_l + \underline{R}_l\right)^{-1}\underline{S}_l^i\,\underline{\dot{I}}^* + \underline{\dot{I}}^T\,\underline{S}_i^l\left(\underline{S}_l + \underline{R}_l\right)^{-1}\left(\underline{S}_l + \underline{R}_l\right)\left(\underline{S}_l + \underline{R}_l\right)^{-1}\underline{S}_l^i\,\underline{\dot{I}}^* = \\ &= \underline{\dot{I}}^T\,\underline{S}_i\,\underline{\dot{I}}^* - 2\,\underline{\dot{I}}^T\,\underline{S}_i^l\left(\underline{S}_l + \underline{R}_l\right)^{-1}\underline{S}_l^i\,\underline{\dot{I}}^* + \underline{\dot{I}}^T\,\underline{S}_i^l\left(\underline{S}_l + \underline{R}_l\right)^{-1}\underline{S}_l^i\,\underline{\dot{I}}^* = \\ &= \underline{\dot{I}}^T\,\underline{S}_i\,\underline{\dot{I}}^* - \underline{\dot{I}}^T\,\underline{S}_i^l\left(\underline{S}_l + \underline{R}_l\right)^{-1}\underline{S}_l^i\,\underline{\dot{I}}^* \end{aligned} \tag{2.83}$$

Naming $\underline{B} = \underline{S}_i - \underline{S}_i^l\left(\underline{S}_l + \underline{R}_l\right)^{-1}\underline{S}_l^i$, the loss assumes the same form of (2.6) :

$$P_d = \underline{\dot{I}}^T\,\underline{B}\,\underline{\dot{I}}^* \tag{2.84}$$

$\underline{B}$ is again a symmetric matrix, and (2.83) represents a generalization of (2.6) that also includes the meshed networks. Therefore, for a given network, radial or meshed, once the matrix $\underline{B}$ has been built recalling:

$$\begin{aligned} &\underline{B} = \underline{S}_i - \underline{S}_i^l\left(\underline{S}_l + \underline{R}_l\right)^{-1}\underline{S}_l^i \\ &\underline{S}_i = \underline{Q}_i^T\,\underline{R}_t\,\underline{Q}_i \\ &\underline{S}_l = \underline{Q}_l^T\,\underline{R}_t\,\underline{Q}_l \\ &\underline{S}_i^l = \underline{Q}_i^T\,\underline{R}_t\,\underline{Q}_l \\ &\underline{S}_l^i = \underline{Q}_l^T\,\underline{R}_t\,\underline{Q}_i \\ &\underline{Q}_i = \left(\underline{A}_t^T\right)^{-1} \\ &\underline{Q}_l = \left(\underline{A}_t^T\right)^{-1}\underline{A}_l^T \end{aligned} \tag{2.85}$$

The corresponding loss minimization, constrained or unconstrained, has the same form of what has been shown in the radial network case.

Chapter 3

Distributed Loss Minimimization Techniques

3.1.Introduction

The theoretical loss minimization has been introduced in Chapter 2. Some simplifications about the microgrid topology have been done, deriving an analytical instrument able to explicitly compute the distribution loss in the microgrid as a function of loads and generators currents, both in the ideal unconstrained case and in the more realistic scenario of limited current injection from the distributed generators. The hypothesis on the topology is related with the assumption of a tree structure, that is functional to the explicit analytical derivation, but the approach can be extended to a generic topology. Consider now the case of a centralized controller, knowing all the electrical variables in the microgrid, the exact network topology and the branches impedances, and controlling all the distributed energy sources, interfaced with the grid through a current controlled inverter. Moreover, assume that no other strategies have in the microgrid a higher priority than the loss minimization, meaning that the only control objective is loss minimization. Of course this is an unrealistic assumption, because loss minimization can be reasonably applied to reactive power flows but not to active flows that are strictly controlled by the availability of energy and by economical or storage oriented strategies. Being loss minimization the goal of this work, the problem is therefore as simplified as possible to better focus the attention on the specific task. Such a centralized controller could measure the state of the network, and calculate the optimum current references for all the generators, that in a single control action drive the microgrid to the ideal minimum loss.

As a general approach, is preferable to avoid the presence of a centralized controller: the amount of information it should manage and the number of communication channels in the microgrid would become easily large, with increased costs and complexity of the infrastructure. Moreover, the reliability of a network controlled by a unique unit is strictly related with the reliability of the unit itself, and a failure in the controller would cause a blackout in the microgrid. These are among the reasons for the orientation toward distributed control solutions, already introduced in the previous

chapters. In a distributed solution, the control is demanded to the local power converters, with limited knowledge of the microgrid and limited communication capabilities with the other generators in the microgrid. Also a central controller can be introduced in the microgrid, but with limited capabilities as well, mainly relating with supervising tasks and alarm procedures management.

In this chapter, four different techniques for distributed loss minimization will be presented. As anticipated above, only the loss minimization is taken into account, even if it is normally an ancillary service provided with lower priority with respect to other control strategies. In any case, a full current injection, i.e. active and reactive, is first considered, to move then to an injection of reactive current, leaving the active part controlled by other microgrid management schemes. All the techniques will be simulated and compared in Chapter 4. Before starting with the distributed minimization techniques, some details are given about the assumptions made on the microgrid model, to better identify the operative conditions and limits of the algorithms.

3.2. Microgrid model

The same assumptions made in Chapter 2 are used also in the definition of distributed loss minimization techniques. In particular, the microgrid is single phase and distributed generators are modeled as AC current source. This approach is different from the traditional power flow analysis, normally used in power systems, where generators are modeled as active and reactive power sources. The reason of the simplification adopted in this work is that the microgrid can be linearly solved if and only if the generators are voltage or current sources. Basing the analysis of the network on powers, the resulting equations are nonlinear, with all the consequent increased complexity. Of course, the reduced computational and analytical effort by itself is not enough to justify the assumption.

The main reason that makes the current-source approach reasonable is the typical operating condition of a low voltage microgrid. As shown in Appendix A and consequent discussion, the power flow approach is normally required to guarantee the voltage and frequency stability of a network. Consider now a representative example of low voltage single phase (as part of a three phase system) microgrid, made of a single distribution line and an equivalent load at the end, depicted in Fig. 3.1 :

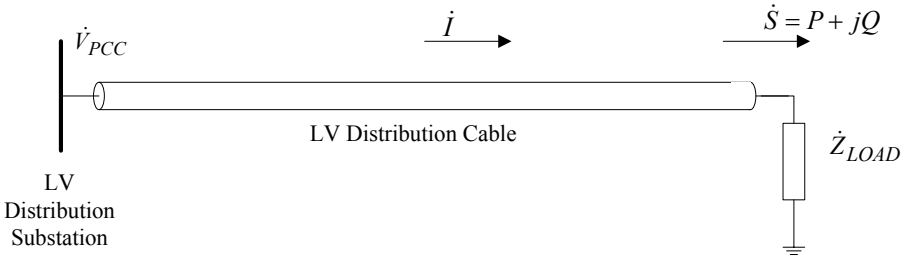

Fig. 3.1 Basic low voltage distribution system

Assume now a cable with the following electrical characteristics, derived from the commercial cables catalogue [121]:

$$S = 150mm^2 \quad \mathrm{r} = 0.13\frac{\Omega}{\mathrm{km}} \quad \mathrm{x} = 0.093\frac{\Omega}{\mathrm{km}} \tag{3.2.1}$$

The cable length is assumed to be $L = 200m$ and the total load power is $P_{LOAD} = 50kW$ with lagging $\cos\varphi = 0.9$, i.e. inductive load. Assuming a PCC voltage $\dot{V}_{PCC} = 230V$, the load impedance correspondent to these powers is:

$$\begin{cases} \dot{S} = P_{LOAD} + jQ_{LOAD} = \dot{V}_{LOAD}\dot{I}^*_{LOAD} = \dot{V}_{LOAD}\left(\dfrac{\dot{V}_{PCC} - \dot{V}_{LOAD}}{\dot{Z}_{LINE}}\right)^* \\ \dot{I}_{LOAD} = \dfrac{\dot{V}_{PCC} - \dot{V}_{LOAD}}{\dot{Z}_{LINE}} \end{cases} \Rightarrow \dot{Z}_{LOAD} = \frac{\dot{V}_{LOAD}}{\dot{I}_{LOAD}} \tag{3.2.2}$$

Substituting the real and imaginary part of $\dot{V}_{LOAD}$ and $\dot{I}_{LOAD}$, and solving with Matlab the resulting non linear system, the load impedance results:

$$\begin{cases} \dot{V}_{LOAD} = 222.116 - j1.297 \\ \dot{I}_{LOAD} = 224.46 - j110.34 \end{cases} \Rightarrow \dot{Z}_{LOAD} = 0.7947 + j0.3964\Omega \tag{3.2.3}$$

Considering that the line impedance is $\dot{Z}_{LINE} = 0.0260 + j0.0186\Omega$, the point of maximum transferable power shown in Appendix A is far from the operating condition. Moreover, in the considered situation, the voltage drop at the end of the feeder is already at the limits of the typical 3-5% range of voltage drop when the PCC is in nominal conditions, so that the possibility of an increase in the transferred power is not taken into account.

In these conditions it is easy to show that the PCC can be considered as reference for the definition of the active and reactive powers, i.e. instead of defining the loads and generators active and reactive powers referred to the load or generator connection point, they can be referred to the PCC introducing a reasonable error. With this approximation, the nodes voltages become known

variables, and active and reactive power can be defined without introducing non linearities in the system. It is worth to note that also the definition of a certain reference for the injected active and reactive currents from current controlled power converters ends up to be a non linear problem in a rigorous analysis. Considering that the proposed distributed loss minimization approaches are based on currents injection, and that a linear approach is preferred, this approximation becomes fundamental for the following analysis. It is important to clarify that this is functional only to the analysis and simulations, because in general, in a distributed approach, the available information is limited and usually excludes a synchronization with the PCC: if a node is demanded to inject a certain current waveform, e.g. derived from a distributed control strategy, the active and reactive parts of this current depend on the local voltage.

In the next paragraphs, the simplified microgrid of Fig. 3.2 will be used to explain the feasibility of the approximation. The considered network is the generic equivalent circuit seen by a current controlled generator connected to the microgrid. The equivalent voltage is assumed to be equal to the PCC voltage, for simplicity:

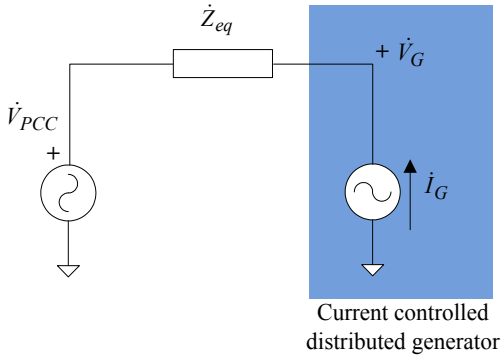

Fig. 3.2 Simplified microgrid seen by current generator $\dot{I}_G$

In the next, the analysis is carried out separating active and reactive currents injection, and considering the two cases of "local based injection" and "PCC based injection". Considering the case of "reactive local based injection" and "reactive PCC based injection", this means that a given module of the reactive current reference $\left|\dot{I}_G\right| = I_{REF}$ will be injected in (leading or lagging) quadrature with respect to voltage $\dot{V}_G$ in the first case and with respect to $\dot{V}_{PCC}$ in the second case.

Case 1: **Local based reactive injection**

In this case, the injected current is:

$$\dot{I}_G = I_{REF} e^{j\left(\varphi_{V_G} \pm \frac{\pi}{2}\right)} \tag{3.2.4}$$

Where φ_{V_G} is the phase of voltage $\dot{V}_G$ referred for convention to $\dot{V}_{PCC}$, assumed to be real. The $\pm$ sign indicates leading (+) or lagging (-) reactive current injection. Assume now the equivalent impedance to be $\dot{Z}_{eq} = Z_{eq} e^{j\varphi_{eq}}$. Moreover:

$$\dot{V}_{PCC} = \dot{V}_G - Z_{eq} e^{j\varphi_{eq}} I_{REF} e^{j\left(\varphi_{VG} \pm \frac{\pi}{2}\right)} = \dot{V}_G - Z_{eq} I_{REF} e^{j\left(\varphi_{eq} + \varphi_{VG} \pm \frac{\pi}{2}\right)} = \dot{V}_G - \Delta\dot{V} \tag{3.2.5}$$

Assuming the typical equivalent impedance for a low voltage cable, the phasorial diagram for the lagging reactive injection is reported in Fig. 3. If the cable is the same of Fig. 3.1 , in the hypothesis of current controlled generators and neglecting the PCC impedance, the equivalent impedance will have the same phase of the cable impedance, corresponding to $\varphi_{eq} = 0.62 rad$.

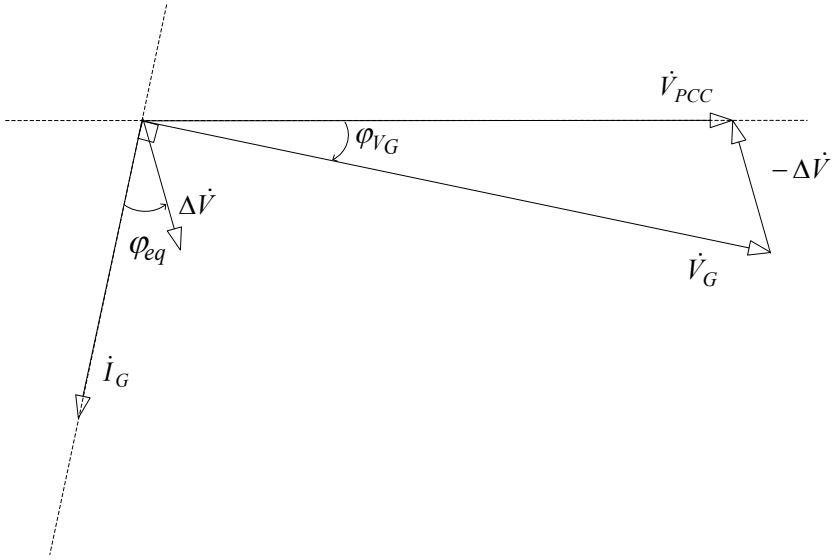

Fig. 3.3 Phasorial diagram for Case 1: "Local based reactive injection" for the particular case of lagging reactive current injection

From the figure, it is possible to calculate the phase difference φ_{VG} and the difference in the modules between $\dot{V}_{PCC}$ and $\dot{V}_G$, applying the Euler's sine theorem:

$$\begin{cases} \varphi_{VG} = -\arcsin\left(\dfrac{\Delta V \sin\left(\dfrac{\pi}{2} - \varphi_{eq}\right)}{V_{PCC}}\right) = -\arcsin\left(\dfrac{\Delta V \cos(\varphi_{eq})}{V_{PCC}}\right) \\ V_G = V_{PCC}\cos(\varphi_{VG}) + \Delta V \cos\left(\dfrac{\pi}{2} - \varphi_{eq}\right) = V_{PCC}\cos(\varphi_{VG}) + \Delta V \sin(\varphi_{eq}) \end{cases} \tag{3.2.6}$$

The case of leading reactive current injection can be derived symmetrically, and will give a symmetrical result, with φ_{VG} of opposite sign and $\dot{V}_G$ with module lower than $\dot{V}_{PCC}$. Considering that a compensation of loads reactive power normally requires a lagging injection, the attention is limited to that case. Equations (3.2.6) also shows the limits of a reactive current injection: it can be guaranteed only if $\left|\dot{I}_G\right| = I_{REF}$ is such that $\Delta V \cos(\varphi_{eq}) < V_{PCC}$ that is obviously respected, otherwise the load voltage would be under the acceptable voltage limits. Moreover, an idea of the dimension of equations (3.2.6) can be given substituting the parameters of the cable in Fig. 3.1 . Assume for example a reactive injection such that $\Delta V = 0.05 V_{PCC}$, the resulting angle and module of voltage $\dot{V}_G$ will be $\varphi_{VG} = -0.0407 rad$, $V_G = 1.028 V_{PCC}$. In these hypothesis about the module of ΔV, i.e. $\Delta V \ll V_{PCC}$, the angle φ_{VG} can be simplified, leading to the simplified equations:

$$\begin{cases} \varphi_{VG} = -\dfrac{\Delta V \cos(\varphi_{eq})}{V_{PCC}} \\ V_G = V_{PCC} \end{cases} \tag{3.2.7}$$

It can also be observed that in the case of a pure resistive cable, a reactive injection in the same hypothesis of (3.2.7), causes a maximized change in φ_{VG}, while the module V_G remains unchanged. Without going in further details, it can also be verified from (3.2.6), that injecting an arbitrary high (within the allowed limits) reactive power in a resistive cable, ends up in a drop in voltage V_G, both injecting lagging or leading reactive current (it can be easily verified with a phasorial diagram). This confirms that an injection of reactive power in a mostly resistive cable either barely modify the voltage level or decrease the voltage level. Trying to control the reactive current to increase the voltage would lead to instability.

Case 2: **PCC based reactive injection**

As anticipated before, this approach simplifies the analysis and the simulation, being the injected currents independent on the node voltage. In the next it will be shown that in a low voltage microgrid, the approximation can be accepted. The injection of a reactive current becomes now:

$$\dot{I}_G = I_{REF} e^{\pm j\frac{\pi}{2}} \tag{3.2.8}$$

The phasorial diagram of Fig. 3.2 is now:

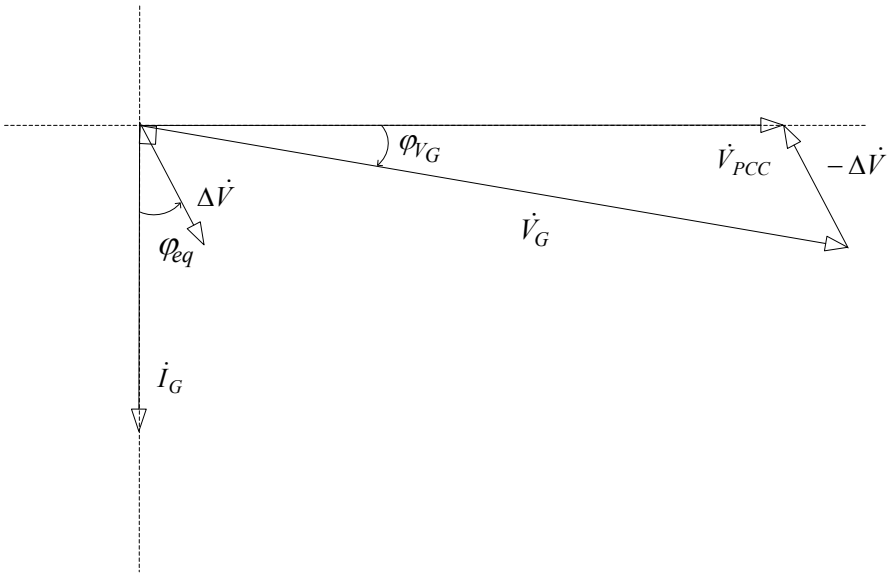

Fig. 3.4 Phasorial diagram for Case 2: "PCC based reactive injection" for the particular case of lagging reactive current injection

Similarly to equations (3.2.6) but applying now the Carnot's theorem:

$$\begin{cases} \varphi_{VG} = -\arctan\left(\dfrac{\Delta V \sin\left(\dfrac{\pi}{2}-\varphi_{eq}\right)}{V_{PCC}\left(1+\dfrac{\Delta V}{V_{PCC}}\cos\left(\dfrac{\pi}{2}-\varphi_{eq}\right)\right)}\right) = -\arctan\left(\dfrac{\Delta V\cos(\varphi_{eq})}{V_{PCC}\left(1+\dfrac{\Delta V}{V_{PCC}}\sin(\varphi_{eq})\right)}\right) \\ V_G = \sqrt{{V_{PCC}}^2 + \Delta V^2 + 2\Delta V V_{PCC}\sin(\varphi_{eq})} \end{cases} \quad (3.2.9)$$

Equations (3.2.9) can be simplified assuming $\Delta V \ll V_{PCC}$ as in the previous case, leading to:

$$\begin{cases} \varphi_{VG} = -\dfrac{\Delta V\cos(\varphi_{eq})}{V_{PCC}} \\ V_G = V_{PCC} \end{cases} \quad (3.2.10)$$

That is exactly the same system of equations (3.2.7), as it was clear also directly comparing Fig. Fig. 3.4 and Fig. 3.. Again, if $\Delta V \ll V_{PCC}$ the injection of reactive current, now referred to the PCC, leaves the generator voltage unchanged, while changing the phase. The maximum phase change is achieved with resistive cable. The behaviour is now different if the condition $\Delta V \ll V_{PCC}$ is no longer respected, i.e. increasing the amplitude of the current reference: considering again the resistive cable, module V_G is always higher than V_{PCC}, and independent on the sign of the reactive injection. In this case a voltage support can be guaranteed, but it is an unpractical approach: an injection of reactive current based on the PCC voltage means that the generator is supplying also an active power equal to the active power consumption of the line resistance, considering that the net power absorption at the PCC is purely reactive for hypothesis.

The other two cases of active injection referred to the PCC or to the generator node won't be taken into account, being their derivation and the consequent information complementary to the reactive case.

This preliminary analysis has been done to clarify the approach that will be presented later on in this chapter. In Chapter 2, the separation between active and reactive injected currents is not taken into account: for a given set of load currents, the optimum set of generator currents is derived that minimizes the distribution loss. This has been done assuming the ideal case where the generators are controlled with the only goal of minimizing the loss. This approach is completely decoupled from any energetic consideration: the current is injected independently on the node voltage, and therefore independently on the meaning of a certain current in terms of active and reactive power. In a real application, active power is related with generation, and thus with costs and investments, instead reactive power is included in the overrating of the power converters and can be controlled at zero cost. For this reason, in a grid connected operation of the microgrid the only controllable parameter is the reactive power. In islanded operation, respecting the power balance constraints, also the active current can be controlled to minimize the loss and therefore to extend the life of the microgrid energy storage.

In this work, only the grid connected case is considered for the distributed loss minimization. All the distributed approaches are first introduced in the unpractical case of fully controllable current injection and then reduced to the more realistic reactive injection. In this reduction, the modeling introduced before plays an important role. If the microgrid is properly designed and the voltage drops are limited compared with the PCC voltage, an injection of a current reference with a given module causes on the generator voltage phasor the same effects in the different cases of lagging injection with respect to the PCC or lagging injection at the generator node. This is enough to proceed with the analysis referring to the PCC (or to any other common reference), knowing that in a practical application the reference for each generator will be its own voltage . The net result will be a small error in the minimum loss condition when implementing the distributed controllers in a real application, compared to the simulated performances.

3.3. Plug and Play control

Before introducing the proposed distributed techniques for loss minimization, requiring measurements and communications, a first investigation has been carried out on a pure Plug and Play (P&P) control. Given a single phase low voltage microgrid with a number of distributed generators interfaced with the microgrid through power converters, the idea is to understand the possible improvement in the distribution loss if the generators are not equipped with communication infrastructure and can only perform local measurements on the network. The motivation of this

analysis is that the current regulations on the grid connected energy sources, e.g. [122], allow a pure active power injection, without any coordination and control among the different units, especially in the case of low power sources. In this technological background, the first step could be the introduction of a degree of local reactive power control, without the need for communication and with minimum updates to the converters control systems.

To clarify the notation adopted in the next paragraphs, and that has been already mentioned in the abstract, the distributed generation within the microgrid is demanded to distributed energy sources, with different power ratings and different nature: wind, photovoltaic, microturbines, diesel gensets, fuel cells, plus eventually an energy storage unit, are the most reasonable sources for a low voltage microgrid. The first requirement is that all the sources have to be interfaced with the microgrid through a power converter, i.e. a power conversion topology whose final stage is an inverter, to have a fully controllable power injection. Moreover, the inverter is current controlled. From now on, the energy source and its conversion system will be named Energy Gateway, (EG), using a nomenclature typically adopted in ICT systems: this is because the requirements for the EG to operate within the microgrid with a distributed control will create a scenario where power electronics and ICT merge together.

Focusing now on the Plug and Play technique, consider the generic node equipped with EG in the microgrid in Fig. 3.5 :

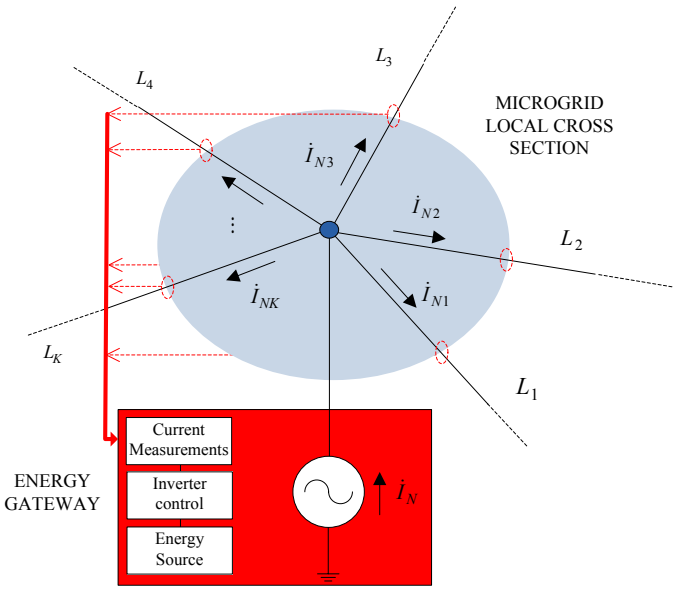

Fig. 3.5 Simplified representation of an EG and correspondent interface with the microgrid in case of Plug and Play control

From the figure, the active node N has access to a limited amount of information, represented by the measure of all the currents departing from the connection point. Moreover, node N measures its voltage. In these conditions any knowledge about the microgrid topology and about the other

generation units is excluded. Consider first the case where node N is fully controllable, meaning that the EG can inject both controlled active and reactive current.

3.3.1. Minimum Loss Plug and Play Control

In this first case, the driver for the definition of current references is the distribution loss. Considering the limited information, only a qualitative approach can be implemented: the basic observation is that, from the restricted point of view of node N, the distribution loss tends to be minimized if the sum of the modules of currents $\dot{I}_{N1}..\dot{I}_{NK}$ in the K surrounding branches is minimum, i.e. minimizing the function φ:

$$\varphi = \sum_{k=1}^{K} I_{Nk}^2 \tag{3.3.1}$$

The function could also include more information. For example knowing the local microgrid topology, and therefore knowing the impedance of each departing branch the objective function can be modified as follows:

$$\varphi_r = \sum_{k=1}^{K} R_k \, I_{Nk}^2 \tag{3.3.2}$$

Where R_k is the real part of branch k-th impedance. Considering that this additional information is generally not available, the analysis is limited to (3.3.1). To minimize (3.3.1), consider the application of a small perturbation $d\dot{I}_N$ to node current $\dot{I}_N$ and measure the corresponding current variations $d\dot{I}_{Nk}$ in each branch L_k. Define now the sharing coefficients $\dot{\chi}_{Nk}$ as:

$$\dot{\chi}_{Nk} = \left[\frac{d\dot{I}_{Nk}}{d\dot{I}_N} \right]_Q \tag{3.3.3}$$

where Q is the node status ($\dot{U}_N^0$, $\dot{I}_N^0$) before the perturbation is applied. Assuming that the network is linear, the coefficients $\dot{\chi}_{Nk}$ can be used to determine the current variations $\Delta\dot{I}_{Nk}$ corresponding to a larger perturbation $\Delta\dot{I}_N$ of the node current, i.e.:

$$\Delta\dot{I}_{Nk} = \dot{\chi}_{Nk} \, \Delta\dot{I}_N \tag{3.3.4}$$

In other words, $\dot{\chi}_{Nk}$ are the current dividers that indicate how the amount of current injected in node N is divided among the neighbour branches. Substituting in the objective function, and naming $\dot{I}^o_{Nk}$ the current in the k-th surrounding branch before the control action, results:

$$\varphi = \sum_{k=1}^{K} I_{Nk}^2 = \sum_{k=1}^{K} \left(\dot{I}^o_{Nk} + \Delta\dot{I}_{Nk}\right)\cdot\left(\dot{I}^o_{Nk} + \Delta\dot{I}_{Nk}\right)^* \tag{3.3.5}$$

Substituting (3.3.4) in equation (3.3.5):

$$\varphi = \sum_{k=1}^{K} I_{Nk}^2 = \sum_{k=1}^{K} \left(\dot{I}^o_{Nk} + \dot{\chi}_{Nk}\,\Delta\dot{I}_N\right)\cdot\left(\dot{I}^o_{Nk} + \dot{\chi}_{Nk}\,\Delta\dot{I}_N\right)^* \tag{3.3.6}$$

In equation (3.3.6), all the terms are known, and the only unknown is the current variation $\Delta\dot{I}_N$. The goal is to find the $\Delta\dot{I}_N$ that minimizes the cost function φ. The minimum is found setting to zero the derivatives of the function, calculated for the real and the imaginary part of $\Delta\dot{I}_N$. In particular, considering a generic element of the sum $\psi = \left(\dot{I}^o + \dot{\chi}\,\Delta\dot{I}\right)\left(\dot{I}^o + \dot{\chi}\,\Delta\dot{I}\right)^*$, and naming $\dot{I}^o = I_x + jI_y$, $\dot{\chi} = \chi_x + j\chi_y$, $\Delta\dot{I} = \Delta I_x + j\Delta I_y$ results:

$$\begin{cases} \dfrac{\partial\psi}{\partial\Delta I_x} = \left(\chi_x^2 + \chi_y^2\right)\Delta I_x + I_x\chi_x + I_y\chi_y = 0 \\ \dfrac{\partial\psi}{\partial\Delta I_y} = \left(\chi_x^2 + \chi_y^2\right)\Delta I_y + I_y\chi_x - I_x\chi_y = 0 \end{cases} \Rightarrow \left(\chi_x^2 + \chi_y^2\right)\Delta\dot{I} = -\dot{I}^o\dot{\chi}^* \tag{3.3.7}$$

Extending to the whole function φ:

$$\Delta\dot{I}_N = -\sum_{k=1}^{K}\dot{I}^o_{Nk}\cdot\dot{\chi}^*_{Nk} \Bigg/ \sum_{k=1}^{K}\chi^2_{Nk} \tag{3.3.8}$$

The node current which optimizes the cost function is finally given by:

$$\dot{I}_N = \dot{I}^o_N + \Delta\dot{I}_N \tag{3.3.9}$$

Of course, application of the solution (3.3.9) is possible only within the current capability of the EG connected at node N. In addition, it requires independent control of active and reactive current. If the active current is constrained to regulate the power flow from the energy source into the grid, solution (3.3.9) can be applied to determine reactive currents only. Clearly, controlling both active and reactive current performs better than controlling reactive current only, but this requires energy storage capability at node N. Moreover, observe that applying the above approach to a peripheral

node, (3.3.9) gives necessarily $\dot{I}_N = 0$. This means that the energy source located at node N should support only the local loads, without injecting power in the distribution grid.

The latter observation opens a discussion on the effectiveness of this technique and on its major limits. Consider the assumed microgrid model, where all the loads and generators are modeled as current sources, and a single generator, the PCC, is a voltage source. Consider for simplicity a tree topology. With these hypothesis, when a generic node N applies (3.3.9), the $\dot{\chi}$ coefficients for the surrounding branches will trivially end up to be zero for all the branches that are connecting node N only with other generators and loads, or clusters of them, while $\dot{\chi}$ will be equal to one for the only branch (the only one in the hypothesis of tree topology) that belongs to a path connecting node N and the PCC. The net result, assuming for simplicity un unlimited current capability for the EG, is that node N will inject the current required to feed all the equivalent loads in the surrounding branches, thus reducing to zero the current absorbed from the PCC.

When only the reactive current is taken into account, this means than node N and its surround will appear to the PCC an equivalent active load with unity power factor. The technique is therefore reduced to a simple power factor correction.

In the next paragraph, a simple example will be presented in different load vs. distributed generation configurations, to show how this technique can effectively reduce the loss but is generally different from the minimum loss condition, even if both active and reactive currents are injected and un unconstrained minimization is considered. Secondly, another limit will be highlighted, related with the constraints introduced by the EG power rating. The first case of the considered example is reported in Fig. 3.6 , while Table 3.1 resumes the main parameters. The distribution cable is the same already used in Fig. 3.1 .

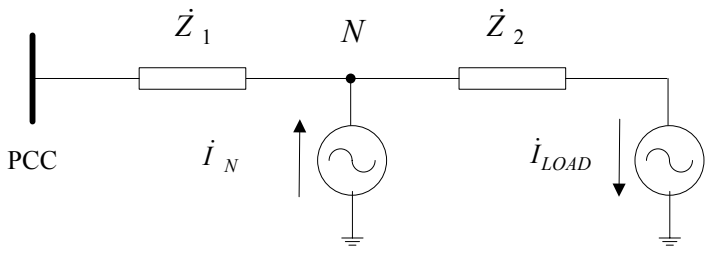

Fig. 3.6 Simplified microgrid with Plug and Play control. Case 1.

Distribution Cable	S=150mm^2, r=0.13Ω/km, x=0.093Ω/km
L_1=200m	$\dot{Z}_1 = 0.0260 + j0.0186\Omega$
L_2=50m	$\dot{Z}_2 = 0.0065 + j0.0047\Omega$
Load current	$\dot{I}_{LOAD} = 50 - j25\ A$

Table 3.1 Parameters for Case 1 in Fig. 3.6

Case 1 is the most simplified configuration, used to present the only situation where the Plug and Play approach is exactly matching the minimum distribution loss condition. Recalling the ideal unconstrained loss minimization in Chapter 2, it is immediate to verify:

$$\dot{I}_N^{opt} = \dot{I}_{LOAD} \tag{3.3.10}$$

Equation (3.3.9) for the Plug and Play control gives exactly the same expression. The result is trivial, because in the configuration proposed in Fig. 3.6 it is clear that the minimum loss are achieved if the load is completely supplied by the nearest source, in this case node N. When the complexity of the microgrid grows, this result continues to be locally true: the Plug and Play control minimizes the loss in the paths connecting a node equipped with Plug and Play control and all the peripheral loads reachable from the node. This is true in the hypothesis of no other EGs placed between the node and the peripheral loads.

Consider now Case 2, where the position of the load and the generator are swapped.

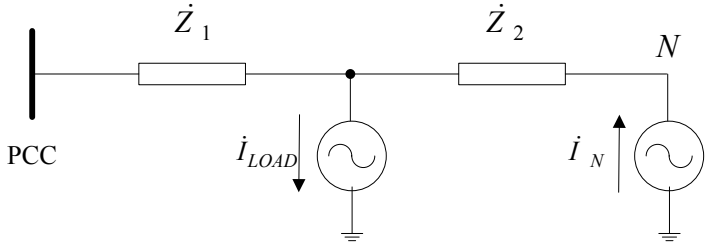

Fig. 3.7 Simplified microgrid with Plug and Play control. Case 2.

Again, Case 2 offers the other trivial condition where the Plug and Play control is totally ineffective: node N doesn't inject any current, even if the resistive part of impedance $\dot{Z}_2$ is much lower than the resistive part of $\dot{Z}_1$, and a feeding of the load from node N would be the most natural approach to minimize the distribution loss, whose minimum is a function of the currents and the resistive components of the paths. In Case 2, the optimum current injected by node N would be again equal to (3.3.10). It is possible to conclude that, for an arbitrary complex network, a generator connected to the extreme end of a peripheral branch is ineffective in reducing the distribution loss. With Case 1 and Case 2 the boundaries of the performances achievable with the Plug and Play

control have been set. In general, the Plug and Play approach guarantees a loss reduction between zero and the 100% of the initial loss. To highlight this general situation, consider Fig. 3.8 , where another branch and another load have been added to the microgrid. The additional parameters are described in Table 3.2 .

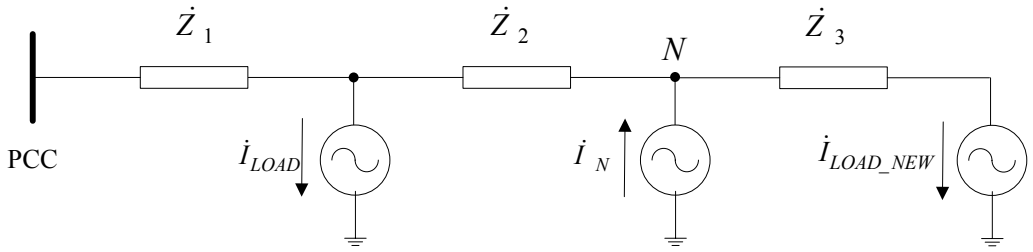

Fig. 3.8 Simplified microgrid with Plug and Play control. Case 3.

Distribution Cable	S=150mm^2, r=0.13Ω/km, x=0.093Ω/km
L_3=200m	$\dot{Z}_3 = 0.0260 + j0.0186\Omega = \dot{Z}_1$
Load current	$\dot{I}_{LOAD\_NEW} = 50 - j25\ A = \dot{I}_{LOAD}$

Table 3.2 Additional parameters for Case 3 in Fig. 3.8

Applying first the ideal unconstrained optimization, the optimum current injected by node N can be found. Recalling the analysis in Chapter 2, the matrices describing the microgrid in Fig. 3.8 are:

$$\begin{cases} \underline{A} = \begin{bmatrix} 1 & 0 & 0 \\ -1 & 1 & 0 \\ 0 & -1 & 1 \end{bmatrix} \\ \underline{R} = \begin{bmatrix} 0.026 & 0 & 0 \\ 0 & 0.0065 & 0 \\ 0 & 0 & 0.026 \end{bmatrix} \Omega \end{cases} \Rightarrow \underline{B} = \begin{bmatrix} 0.0260 & 0.0260 & 0.0260 \\ 0.0260 & 0.0325 & 0.0325 \\ 0.0260 & 0.0325 & 0.0585 \end{bmatrix} \tag{3.3.11}$$

The initial distribution loss, with generator N switched off is equal to:

$$P_d^{MAX} = \underline{I}_L^T \underline{B} \underline{I}_L^* = \begin{bmatrix} 50 - j25 & 0 & 50 - j25 \end{bmatrix} \begin{bmatrix} 0.0260 & 0.0260 & 0.0260 \\ 0.0260 & 0.0325 & 0.0325 \\ 0.0260 & 0.0325 & 0.0585 \end{bmatrix} \begin{bmatrix} 50 + j25 \\ 0 \\ 50 + j25 \end{bmatrix} = 426.56\text{W} \tag{3.3.12}$$

Naming $\underline{I}_a$ and $\underline{I}_p$ the currents absorbed by the active nodes, i.e. the generators, and the loads respectively:

$$\begin{cases} \underline{I}_a = \underline{K}_a \underline{I} = -I_N \rightarrow \underline{K}_a = \begin{bmatrix} 0 & 1 & 0 \end{bmatrix} \\ \underline{I}_p = \underline{K}_p \underline{I} = \begin{bmatrix} \dot{I}_{LOAD} \\ \dot{I}_{LOAD\_NEW} \end{bmatrix} \rightarrow \underline{K}_p = \begin{bmatrix} 1 & 0 & 0 \\ 0 & 0 & 1 \end{bmatrix} \end{cases} \tag{3.3.13}$$

$$\begin{aligned} \underline{B}_{a,a} &= \underline{K}_a \, \underline{B} \, \underline{K}_a^T \rightarrow \underline{B}_{a,a} = 0.0325 \\ \underline{B}_{a,p} &= \underline{K}_a \, \underline{B} \, \underline{K}_p^T \rightarrow \underline{B}_{a,p} = \begin{bmatrix} 0.0260 & 0.0325 \end{bmatrix} \end{aligned} \tag{3.3.14}$$

From where the current $\dot{I}_N$ that guarantees the minimum loss is:

$$\dot{I}_N^{opt} = \underline{B}_{a,a}^{-1} \, \underline{B}_{a,p} \, \underline{\dot{I}}_p = 90 - j45A \tag{3.3.15}$$

Corresponding to the minimum loss:

$$P_d^{\min} = \begin{bmatrix} 50 - j25 \\ -90 + j45 \\ 50 - j25 \end{bmatrix} \underline{B} \begin{bmatrix} 50 + j25 & -90 - j45 & 50 + j25 \end{bmatrix} = 97.5\text{W} \tag{3.3.16}$$

Apart from the matrices that formalize the problem, node N injects in the optimal case all the current $\dot{I}_{LOAD\_NEW}$ plus part of the current $\dot{I}_{LOAD}$ weighted by the current divider $\frac{\Re(\dot{Z}_1)}{\Re(\dot{Z}_1 + \dot{Z}_2)}$, whose physical meaning is immediate: the amount of current $\dot{I}_{LOAD}$ that has to be preferably supplied by node N instead of the PCC is as higher as the resistance of the path between $\dot{I}_{LOAD}$ and the PCC is higher than the resistance of the path between $\dot{I}_{LOAD}$ and node N. Observing now the behaviour of the Plug and Play control in the same condition, the injected current will be:

$$\dot{I}_N^{P\&P} = \dot{I}_{LOAD\_NEW} = 50 + j25A \tag{3.3.17}$$

Corresponding to the sub-optimum loss:

$$P_d^{P\&P} = \begin{bmatrix} 50 + j25 \\ -50 - j25 \\ 50 + j25 \end{bmatrix} \underline{B} \begin{bmatrix} 50 - j25 & -50 + j25 & 50 - j25 \end{bmatrix} = 162.5\text{W} \tag{3.3.18}$$

That is a worse performance compared with the optimum control but is still an improvement in the microgrid behaviour. All these analysis have been carried out assuming both active an reactive injection and with unconstrained current capability for the EG connected to node N. The presence of saturations simply worsen the achievable improvement.

The qualitative analysis carried out with the simplified cases 1…3, gives some hints on the potential use of a plug and play control of distributed energy resources in a low voltage microgrid with single PCC. The topology can be a tree topology or also, adding some hypothesis, a meshed topology. In low voltage distribution systems the topology is typically a tree topology, the introduction of meshes (more common in HV transmission) would require a different architecture for the fault protection schemes. On the other hand, it is worth to mention some visions that forecasts the change toward meshed systems in low voltage microgrids, to increase redundancy and reliability [109]. For these reasons, the extension to meshed architecture is mentioned in this work but not in deep details. Recalling the main features of Plug and Play control:

- An EG with Plug and Play control is ineffective if placed at the extreme of a peripheral branch without local load.

- An EG with plug and play control can be placed in peripheral branches loaded at the extreme end: in this case the EG locally feeds the load, instead of absorbing the current from the PCC, with longer distance and higher loss.

- From a microgrid design perspective, an EG with Plug and Play controller can either be placed near a specific peripheral load, for example to compensate the required reactive power, and consequently sized for the specific load, or in a central node of the network. In this second case, the size of the converter has to be properly chosen based on the load seen at the connection node. Another application could be to place the Plug and Play controlled EG at the PCC, to compensate the reactive power of the microgrid and therefore show a unity power factor to the main grid. In this case, the loss in the microgrid is unchanged.

In the specific case of single PCC and tree topology, the proposed approach is equivalent to a power factor correction (or a local supply if also active power is injected). The generalization to microgrids with generic topology, not only with strictly tree topology, is not straightforward. The basic problem is that the limited available information on the connection node has a direct meaning in terms of loss minimization in the tree topology, while in general the loss minimization applied to a local problem, such as the surrounding branches in (3.3.8), could lead to a global increase of the distribution loss. This concept will be clearer in the next sections when the distributed loss minimization with node to node communication will be presented. To introduce the problem, consider the example in Fig.3.9 , representing a simple one-load-one-generator microgrid including a mesh:

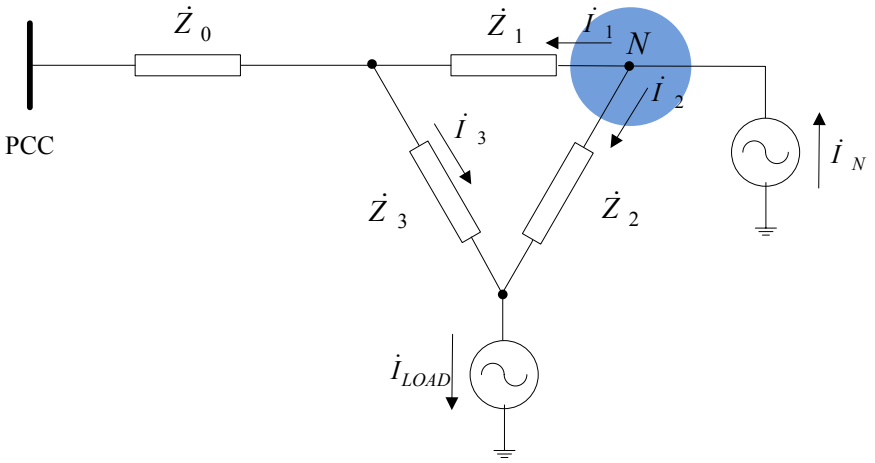

Fig.3.9 Plug and Play control. Example of meshed microgrid with single PCC

In the figure, the highlighted area reminds the limited knowledge that node N has about the microgrid. If the microgrid had a tree topology, it would be immediate for the EG to identify the surroundings simply measuring the $\dot{\chi}$ coefficients. Once the only branch that has a path to the PCC, i.e. the one with unity $\dot{\chi}$, is identified, its current is measured and set as reference for the EG. Assuming the additional simplification of resistive impedances, the injected current that locally minimizes the cost function φ in the braches $\dot{Z}_1$ and $\dot{Z}_2$ is found from (3.3.8):

$$\Delta\dot{I}_N = \frac{\dot{I}_{LOAD} R_3 (R_2 + R_3 - R_1)}{R_1^2 + (R_2 + R_3)^2} \tag{3.3.19}$$

Where node N initially injects zero current, and thus the current variation $\Delta\dot{I}_N$ is equal to the reference $\dot{I}_N$. From (3.3.19) it is worth to observe the sign of the requested current. When the sum $R_2 + R_3$ is greater than R_1, the injected current is a fraction of the current absorbed by the load. In this case, it is reasonable to suppose that the control action that minimizes φ is also reducing the distribution loss. In the opposite case of R_1 greater than $R_2 + R_3$, the generator behaves like a load, and therefore the loss increases. The trade-off between the two conditions depends on the specific network topology. A deeper investigation is required, and will be object of future developments of this work. In the particular case depicted in Fig.3.9 , a possible simplified control technique could be the addition of post-process conditions:

$$\begin{aligned} &if\left(\Re\left(\dot{I}_N\right) < 0\right) \rightarrow \Re\left(\dot{I}_N\right) = 0 \\ &if\left(\Im\left(\dot{I}_N\right) > 0\right) \rightarrow \Im\left(\dot{I}_N\right) = 0 \end{aligned} \tag{3.3.20}$$

Where the second condition assumes reactive loads only. Even without a formal analytical derivation, to conclude the section the microgrid in Fig.3.9 has been studied in simulation. In addition to the resistive nature of the distribution cable, active injection is considered, turning the

grid in a DC system. The advantage is the possibility of plotting the resulting loss as a function of the injected current I_N and the resistance R_1, fixing I_{LOAD}, R_2 and R_3. Moreover, $R_0 = 0$. The branch currents and the correspondent distribution loss are:

$$\begin{cases} I_1 = I_N \dfrac{R_2 + R_3}{R_1 + R_2 + R_3} - I_{LOAD} \dfrac{R_3}{R_1 + R_2 + R_3} \\ I_2 = I_N \dfrac{R_1}{R_1 + R_2 + R_3} + I_{LOAD} \dfrac{R_3}{R_1 + R_2 + R_3} \\ I_3 = -I_N \dfrac{R_1}{R_1 + R_2 + R_3} + I_{LOAD} \dfrac{R_1 + R_2}{R_1 + R_2 + R_3} \end{cases} \rightarrow P_d = R_1 {I_1}^2 + R_2 {I_2}^2 + R_3 {I_3}^2 \qquad (3.3.21)$$

The distribution loss P_d and the corresponding Plug and Play objective (3.3.6) have been plotted as function of R_1 and I_N in Fig. 3.10 . An important information can be extracted from the plots, observing the projection of the functions in the $P_d - I_N$ plane and in the $\varphi - I_N$ plane respectively, for different values of resistance R_1. The projections are reported in Fig. 3.11 . The arrows indicate the direction of change in the functions when R_1 increases.

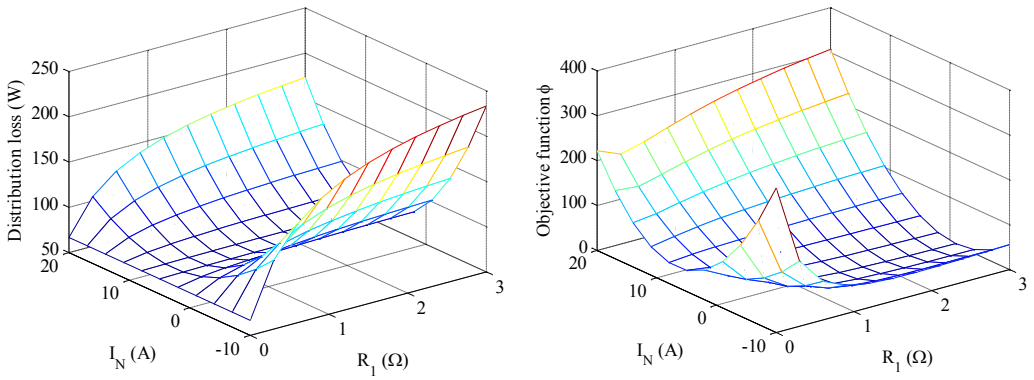

Fig. 3.10 Distribution loss and Plug and Play control objective function for the microgrid in Fig.3.9

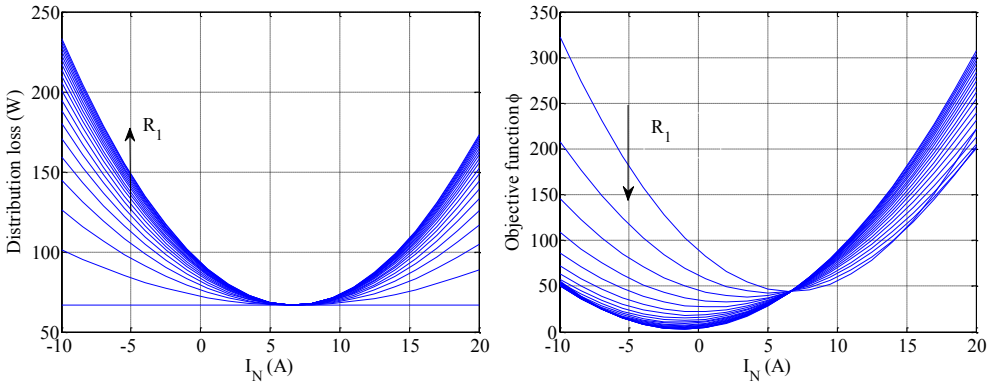

Fig. 3.11 Distribution loss and cost function for different values of resistance R_1

It is interesting to note how in the specific topology, the minimum of the loss is independent on the value of R_1, meaning that in the minimum the current through R_1 is zero. The behaviour is different for the objective function of Plug and Play control. The minimum moves as R_1 increases, and the required current I_N is progressively reduced, finally becoming less than zero. Therefore it can be validated, at least for Fig.3.9 , the heuristic approach of (3.3.21): for positive current injection, the minimum of the Plug and Play function corresponds to a current I_N that decreases, but not optimizes, the distribution loss.

3.3.2. Voltage Support Plug and Play Control

In case of weak grid, the EGs can perform voltage support too. This is a different topic compared to distribution loss minimization, especially because this service is needed when the microgrid scenario moves from the condition of voltage drops along the lines much smaller than the PCC voltage that has been so far considered. On the other hand, it is worth to mention this opportunity, that could become object o future analysis.

As a qualitative approach, within its current capability, each EG connected to a generic node N may be driven to minimize the difference between its actual RMS voltage U_N and the reference U_N^{ref}. The Thevenin equivalent circuit of the grid seen by node N, must be first determined measuring node voltage $\dot{U}_N$ and current $\dot{I}_N$ for different operating conditions. Let $\dot{Z}_N^{eq}$ be the equivalent impedance seen by node N, and $\dot{U}_N^0, \dot{I}_N^0$ be the node quantities at the instant of time when the Plug and Play voltage support detects a voltage sag and tries to reduce the voltage variation. Assuming for simplicity that $\dot{U}_N^0$ is purely real ($\dot{U}_N^0 = U_N^0$), and let $\dot{Z}_N^{eq} = R_N^{eq} + jX_N^{eq}$. The node voltage after a current variation $\Delta\dot{I}_N = \Delta I_N^{'} + j\,\Delta I_N^{''}$ becomes:

$$\dot{U}_N = U_N^o + \dot{Z}_{eq}\,\Delta\dot{I}_N = U_N^0 + \dot{Z}_{eq}\left(\Delta I_N^{'} + j\,\Delta I_N^{''}\right) \tag{3.3.22}$$

The real and imaginary components of the voltage are given by:

$$\begin{aligned} U_N^{'} &= U_N^0 + R\,\Delta I_N^{'} - X\,\Delta I_N^{''} \\ U_N^{''} &= X\,\Delta I_N^{'} + R\,\Delta I_N^{''} \end{aligned} \tag{3.3.23}$$

Thus the RMS value of the node voltage becomes:

$$U_N^2 = U_N^{02} + Z_{eq}^2\left(\Delta I_N^{'2} + \Delta I_N^{''2}\right) + 2U_N^0\left(R\,\Delta I_N^{'} - X\,\Delta I_N^{''}\right) \tag{3.3.24}$$

From (3.3.24) we may determine the current increments which cause voltage U_N to approach U_N^{ref} at the best. If the active current component $I_N^{'}$ is used to control the power flow, the voltage support can only be provided by regulating reactive current $I_N^{''}$. From (3.3.24) it can be noted that this solution works well if the line is inductive, while it is less effective in case of cabled grids, which are mostly resistive. This can be verified in the analysis carried out in this chapter in section 3.2. It is also important to recall how the definition of active and reactive injected currents should be referred to the injection node voltage. Saying that $I_N^{'}$ and $I_N^{''}$ are the active and reactive currents, the considered voltage is U_N^0, but in the meanwhile voltage $\dot{U}_N$ is no longer a purely real quantity.

Instead, if some energy storage capability is available at node N, both active and reactive current can be used to support the local voltage. The most effective way to do this is to impress a voltage increment which is proportional to the initial voltage, thus minimizing the current needed to approach voltage U_N^{ref}. Let:

$$\dot{U}_N = U_N^0 (1 + a) + j\,0 \tag{3.3.25}$$

By imposing the condition $U_N = U_N^{ref}$ and considering (3.3.22), we get:

$$a = \frac{U_N^{ref} - U_N^0}{U_N^0} = \frac{\dot{Z}_N^{eq}\,\Delta\dot{I}_N}{U_N^0} \tag{3.3.26}$$

The ideal current increments, which enforce voltage $\dot{U}_N$ to approach U_N^{ref}, are therefore given by:

$$\Delta\dot{I}_N = \frac{U_N^{ref} - U_N^0}{\dot{Z}_N^{eq}} = \frac{U_N^{ref} - U_N^0}{{Z_N^{eq}}^2}\left(R_N^{eq} - j\,X_N^{eq}\right) \tag{3.3.27}$$

Equation (3.3.27) confirms that the active current required for the regulation is as higher as the distribution line is resistive. Moreover, the higher is the line impedance, the smaller is the current needed for the regulation. Therefore the voltage support Plug and Play control technique can profitably be applied at remote peripheral nodes to support the local voltage during network transients.

3.4. Distributed algorithms for loss minimization

This section presents the first of the two main topics of this work. So far, the ideal loss minimization and the Plug and Play controllers have been investigated, introducing some assumptions on the microgrid model, that are reasonable in a low voltage distribution system, and that simplify both the theoretical analysis and the simulation model that will be introduced later. The same hypotheses are used in this section. As already said before in this chapter, normally a low voltage microgrid is based on a tree topology. This configuration is assumed as the reference structure of the microgrid. Nevertheless, sometimes the more general meshed architecture will be mentioned to evaluate the potential extension of the proposed techniques.

The main goal of the proposed distributed control solutions is to converge to a set of current references for the EGs that achieves a distribution loss in the microgrid as closed as possible to the ideal loss minimization, without the need for a central controller.

Moreover, with respect to the Plug and Play solutions, that have a minimal information from the microgrid, now a complete communication infrastructure is assumed to be available, at least able to guarantee a communication channel between each node and its neighbours. The communication requirements will be analyzed step by step while introducing the different control proposals. The analysis is limited to the functional behaviour of the communication, without going in the details of channel modelling or protocols. It is worth to recall that normally loss reduction is not the prime driver for the microgrid control: load power balance and power exchanges with the main grid have higher priority. Nevertheless, in this study the loss minimization is the only considered aspect of the microgrid management. In particular, the grid connected case is considered, leaving to future developments the extension to the islanded condition.

3.4.1. Current Based Surround Control

3.4.1.1. Introduction

In general, a microgrid can be divided in minimal subsystems represented by a distribution line branch and a number of loads connected along the branch. This cluster terminates when the topology has a ramification or if a distributed generator with EG is connected.

In this specific section, being the first investigation on a distributed approach to loss minimization, a simplification on the microgrid topology is introduced: all the branches terminate on a generator or on a line ramification, and in all the line ramifications are equipped with a distributed generator . The schematic microgrid reported in Fig. 3.12 shows an example of this kind of microgrids, where the clusters are highlighted with ellipses:

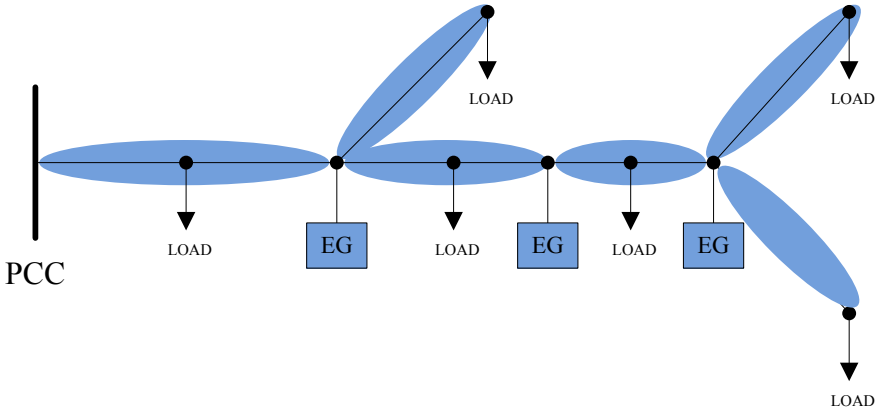

Fig. 3.12 Assumed microgrid topology and correspondent minimum clusters

In the figure, a single load is represented in each branch, with the meaning of equivalent load groping all the loads connected along the cluster. Consider now one of the clusters, connecting node A and B, generically represented in Fig. 3.13 :

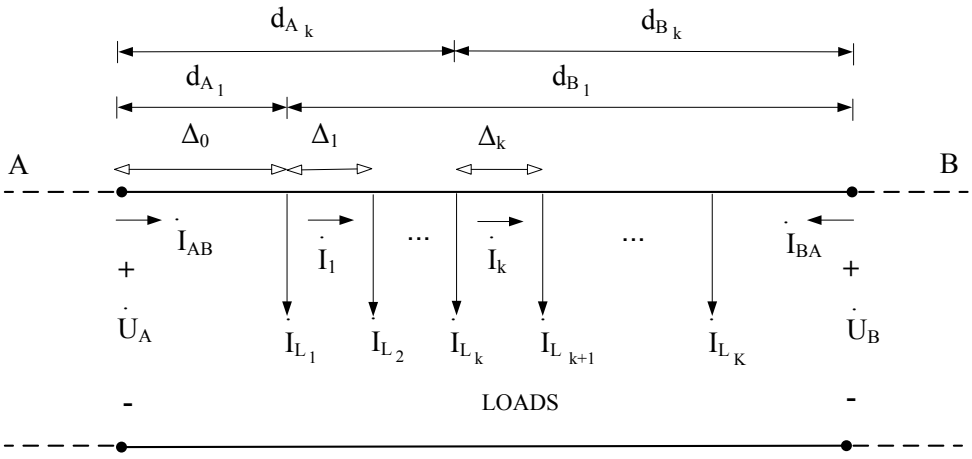

Fig. 3.13 Generic microgrid cluster connecting node A and B

To start with the investigation, Fig. 3.13 could be interpreted as single branch microgrid, with two current generators $\dot{I}_{AB}$ and $\dot{I}_{BA}$ connected at the extremes (as in the definition of the minimum cluster), K loads $\dot{I}_{L_1}..\dot{I}_{LK}$ and the PCC corresponding to node A. In node A the main grid and the generator $\dot{I}_{AB}$ are connected together to obtain a result of general value also for clusters located far from the PCC. The interest is to find the optimum references for $\dot{I}_{AB}$ and $\dot{I}_{BA}$ that minimizes the loss, with the condition that all the load currents have to be supplied locally, i.e. $\dot{I}_{AB} + \dot{I}_{BA} = \sum_{k=1}^{K} \dot{I}_{L_k}$.

Comparing with the analysis carried out in Chapter 2, this is equivalent to an unconstrained optimization of the microgrid in Fig. 3.13 assuming at the beginning no current generators connected

to node A. then, once node B optimum current is derived, the current $\dot{I}_0$ absorbed from the grid can be calculated and it is now possible to add the second current generator in node A setting $\dot{I}_{AB} = \dot{I}_0$. This because the minimum loss analysis is independent on the specific PCC voltage level, and the definition of generator $\dot{I}_{AB}$ makes the approach for the single branch extendable to all the branches.

Moving back to the figure, the minimum loss condition can also be calculated explicitly, without using the general approach introduced in Chapter 2. This is done considering from the beginning both the current generators at nodes A and B, and neglecting the PCC, that doesn't have any effect on the analysis. In a practical application, if the branch were actually connected to the PCC, only the generator at node B should be controlled with the calculated optimum reference, and as a consequence the PCC will inject the other optimum current "automatically".

3.4.1.2. Optimum current derivation

Let's proceed now toward the derivation of the optimum currents $\dot{I}_{AB}$ and $\dot{I}_{BA}$. The current $\dot{I}_k$ in the generic distribution path with length Δ_k is:

$$\dot{I}_k = \dot{I}_{AB} - \sum_{i=0}^{k} \dot{I}_{L_i} = \dot{I}_{AB} - \dot{I}_{\Sigma k} \tag{3.4.1}$$

Where $\dot{I}_{\Sigma k}$ is the sum of the currents absorbed by the first k loads and $\dot{I}_{L_0}$ is a load that could be directly connected to node A. The power loss in the path Δ_k depends on the squared rms value of current $\dot{I}_k$ and on the resistive component of the line impedance.

A fundamental assumption is now introduced on the line impedance. It is assumed that the line impedance per unit of length is constant in all the distribution lines within a cluster, and equal to $\dot{z} = r + j\,x \ (\Omega/km)$ i.e. the cable section is constant. This is not important for the derivation of the optimum currents but it will become relevant in the prosecution of the analysis, when the voltage corresponding to the optimum current reference will be considered.

The loss distribution loss can be written as:

$$P_{AB\,loss} = \sum_{k=0}^{K} r\,\Delta_k \dot{I}_k \dot{I}_k^* \tag{3.4.2}$$

Equation (3.4.2) is now rewritten as a function of the injected currents, and then derived to find the set of current references that minimizes the loss: $\dot{I}_{AB}$ and $\dot{I}_{BA}$

$$P_{AB\,loss} = r\sum_{k=0}^{K}\Delta_k\left(\dot{I}_{AB}-\dot{I}_{\Sigma k}\right)\left(\dot{I}_{AB}-\dot{I}_{\Sigma k}\right)^{*} \tag{3.4.3}$$

Separating the real and imaginary part of $\dot{I}_{AB} = I_{AB}^{'} + jI_{AB}^{''}$, deriving (3.4.3) with respect to both of them, and finally setting the derivatives to zero results:

$$\begin{cases}\dfrac{\partial P_{AB\,loss}}{\partial I_{AB}^{'}} = 0\\ \dfrac{\partial P_{AB\,loss}}{\partial I_{AB}^{''}} = 0\end{cases} \rightarrow r\sum_{k=0}^{K}\Delta_k\left(\dot{I}_{AB}^{opt}-\dot{I}_{\Sigma k}\right)=0 \rightarrow r\sum_{k=0}^{K}\Delta_k\dot{I}_{AB}^{opt} = r\sum_{k=0}^{K}\Delta_k\dot{I}_{\Sigma k}$$
$$\rightarrow \dot{I}_{AB}^{opt} = \frac{1}{d_{AB}}\sum_{k=0}^{K}\left(\Delta_k\sum_{i=0}^{k}\dot{I}_{L_i}\right) = \frac{1}{d_{AB}}\sum_{k=0}^{K}\dot{I}_{Lk}d_{Bk} \tag{3.4.4}$$

Where d_{AB} is the total length of the branch from node A to node B, while d_{Bk} is the distance between load k and node B. The lengths are expressed in km, if the line impedance is in Ω/km. Recalling that the sum of the injected currents has to balance the total load demand in the cluster:

$$\dot{I}_{AB} + \dot{I}_{BA} = \sum_{k=0}^{K}\dot{I}_{Lk} \tag{3.4.5}$$

Substituting the optimum current for node A (3.4.4) in (3.4.5), the optimum current in B can be calculated and the final optimum currents are:

$$\begin{aligned}\dot{I}_{AB}^{opt} &= \frac{1}{d_{AB}}\sum_{k=0}^{K}\dot{I}_{Lk}d_{Bk}\\ \dot{I}_{BA}^{opt} &= \frac{1}{d_{AB}}\sum_{k=0}^{K}\dot{I}_{Lk}d_{Ak}\end{aligned} \tag{3.4.6}$$

In case of variable cable section within the single cluster, equation (3.4.6) is still true but the distances d has to be substituted by the equivalent resistances R_{AB}, R_{Ak} and R_{Bk}. It is worth to note that (3.4.6) comprises both for the real and imaginary part of the optimum currents, that can therefore be controlled separately. This decoupling is fundamental for the practical application of the control. Even if this work investigates also the case of both active and reactive injection, the active current is normally defined by the availability of the energy source, while only the reactive current is available for loss minimization. The optimum currents depend only on the spatial distribution of the loads along the cluster, and on their current.

So far, the single cluster optimization has been done based only on the load currents. Another perspective on the distribution loss minimization is given observing the voltage drop along the line:

$$\dot{U}_{AB} = \dot{U}_A - \dot{U}_B = \sum_{k=0}^{K} \dot{z}\,\Delta_k \dot{I}_k = \sum_{k=0}^{K} \dot{z}\,\Delta_k \left(\dot{I}_{AB} - \dot{I}_{\Sigma k}\right) = \dot{z}\, d_{AB} \left(\dot{I}_{AB} - \dot{I}_{AB}^{opt}\right) \tag{3.4.7}$$

Voltage $\dot{U}_{AB}$ shows how the loss minimimization is equivalent to having node A and node B at the same potential, in fact $\dot{U}_{AB} = 0$ when $\dot{I}_{AB} = \dot{I}_{AB}^{opt}$. It can be observed that also this result is a consequence of using a constant cable section, so that if the sum of resistive voltage drops from A to B is equal to zero, the same happens for the voltage drops in the inductive components of the cable. In general, the minimum loss condition is different from the zero voltage drop condition. In fact, the optimum currents depends only on the resistive component of the cables, and if the inductive part is a degree of freedom, the voltage drop can also be different from zero. On the other hand, the hypothesis of constant section within a cluster is realistic and will be assumed in the prosecution of the work.

The minimum distribution loss corresponding to the optimum currents injection is:

$$\begin{aligned} P_d^{\min} &= r \sum_{k=0}^{K} \Delta_k \left(\dot{I}_{AB}^{opt} - \dot{I}_{\Sigma k}\right)\left(\dot{I}_{AB}^{opt} - \dot{I}_{\Sigma k}\right)^* = r \sum_{k=0}^{K} \Delta_k \left(I_{AB}^{opt2} - 2\,\Re\left(\dot{I}_{AB}^{opt} \dot{I}_{\Sigma k}{}^*\right) + I_{\Sigma k}{}^2 \right) = \\ &= r \left(d_{AB} I_{AB}^{opt2} - 2\, d_{AB} I_{AB}^{opt2} + \sum_{k=0}^{K} \Delta_k I_{\Sigma k}{}^2 \right) = r \left(\sum_{k=0}^{K} \left(\Delta_k I_{\Sigma k}{}^2\right) - d_{AB} I_{AB}^{opt2} \right) \end{aligned} \tag{3.4.8}$$

Where I_{AB}^{opt} and $I_{\Sigma k}$ are the modules of the correspondent phasors and the third part of the equation directly follows the definition of optimum current in (3.4.4) . When the minimum loss condition is not satisfied, the currents $\dot{I}_{AB}$ and $\dot{I}_{BA}$ can be rewritten in the general form:

$$\begin{aligned} \dot{I}_{AB} &= \dot{I}_{AB}^{opt} + \frac{\dot{U}_{AB}}{\dot{Z}_{AB}} = \dot{I}_{AB}^{opt} + \dot{I}_{AB}^{circ} \\ \dot{I}_{BA} &= \dot{I}_{BA}^{opt} - \frac{\dot{U}_{AB}}{\dot{Z}_{AB}} = \dot{I}_{BA}^{opt} - \dot{I}_{AB}^{circ} \end{aligned} \tag{3.4.9}$$

Where $\dot{I}_{AB}^{circ}$ is the circulation current, and has the meaning of the current flowing from A to B without any contribution in feeding the loads in the cluster between A and B. The concept of circulation current is schematically reported in Fig. 3.14 :

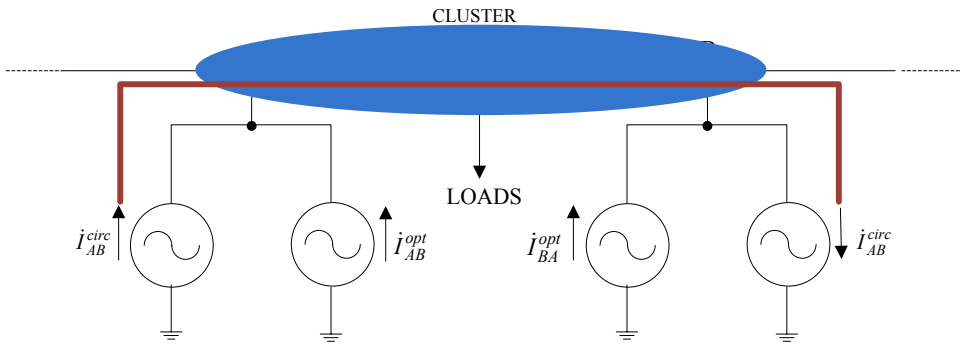

Fig. 3.14 Definition of circulation currents

In other words, the optimum current condition is equivalent to zero circulation current in the cluster. In the general case of non zero circulation current, the distribution loss (3.4.8) increases. Rewriting (3.4.8) for a general current $\dot{I}_{AB}$ and then substituting (3.4.9):

$$\begin{aligned} P_d &= r\sum_{k=0}^{K}\Delta_k\left(\dot{I}_{AB}-\dot{I}_{\Sigma k}\right)\left(\dot{I}_{AB}-\dot{I}_{\Sigma k}\right)^* = r\sum_{k=0}^{K}\Delta_k\left(I_{AB}{}^2+I_{\Sigma k}{}^2-2\Re\left(\dot{I}_{AB}\dot{I}_{\Sigma k}{}^*\right)\right)= \\ & rd_{AB}I_{AB}{}^2+r\sum_{k=0}^{K}\Delta_k I_{\Sigma k}{}^2-2r\Re\sum_{k=0}^{K}\left(\dot{I}_{AB}\dot{I}_{\Sigma k}{}^*\right)= rd_{AB}I_{AB}{}^2+r\sum_{k=0}^{K}\Delta_k I_{\Sigma k}{}^2-2rd_{AB}\Re\left(\dot{I}_{AB}\dot{I}_{AB}^{opt*}\right) \end{aligned} \tag{3.4.10}$$

Substituting now $\dot{I}_{AB}=\dot{I}_{AB}^{opt}+\dot{I}_{AB}^{circ}$:

$$\begin{aligned} P_d &= rd_{AB}\left(\dot{I}_{AB}^{opt}+\dot{I}_{AB}^{circ}\right)\left(\dot{I}_{AB}^{opt}+\dot{I}_{AB}^{circ}\right)^*+r\sum_{k=0}^{K}\Delta_k I_{\Sigma k}{}^2-2rd_{AB}\Re\left(\left(\dot{I}_{AB}^{opt}+\dot{I}_{AB}^{circ}\right)\dot{I}_{AB}^{opt*}\right)= \\ &= r\left(\sum_{k=0}^{K}\left(\Delta_k I_{\Sigma k}{}^2\right)-d_{AB}\left(I_{AB}^{opt2}-I_{AB}^{circ2}\right)\right)= P_d{}^{\min}+rd_{AB}I_{AB}^{circ2} \end{aligned} \tag{3.4.11}$$

Where the negative impact of circulation currents in distribution loss becomes evident. Moreover it is interesting to note how the superposition of effects can be applied in this particular case also to the loss: when only the optimum currents are injected, the loss correspond to $P_d{}^{\min}$, depending only on the optimum currents. When only the circulation current is injected, the second term $rd_{AB}I_{AB}^{circ2}$ depends only on that current. This will become useful later, in the next section.

Another interesting observation is that the definition of optimum currents can be used also to simplify the loads distribution in the cluster. In fact, for the theorem of momentum conservation, for the case of constant cable section it is possible to write:

$$\dot{I}_{AB}^{opt}=I_{AB}^{opt'}+jI_{AB}^{opt''}=\frac{1}{d_{AB}}\sum_{k=0}^{K}\left(I_{Lk}{}'+jI_{Lk}{}''\right)d_{Ak}=I_{LTOT}{}'\frac{d_{A\Phi\Re}}{d_{AB}}+jI_{LTOT}{}''\frac{d_{A\Phi\Im}}{d_{AB}} \tag{3.4.12}$$

Where $d_{A\Phi\Re}$ and $d_{A\Phi\Im}$ are the loads barycentre for the real and imaginary part of the load respectively and $\dot{I}_{LTOT}$ is the sum of all the loads in the cluster. The same equation holds for $\dot{I}_{BA}^{opt}$, with $d_{B\Phi\Re} = d_{AB} - d_{A\Phi\Re}$ and $d_{B\Phi\Im} = d_{AB} - d_{A\Phi\Im}$. Therefore, once the optimum current has been calculated, all the loads in the cluster can be substituted by an equivalent circuit with only two loads, positioned in the respective barycentre and corresponding to the real and the imaginary part of the total load $\dot{I}_{LTOT}$. In the particular case of coincident real and imaginary barycentre, the cluster is substituted by an equivalent circuits with two line impedances and the total load in the middle. The general case of different barycentre is depicted in Fig. 3.15 :

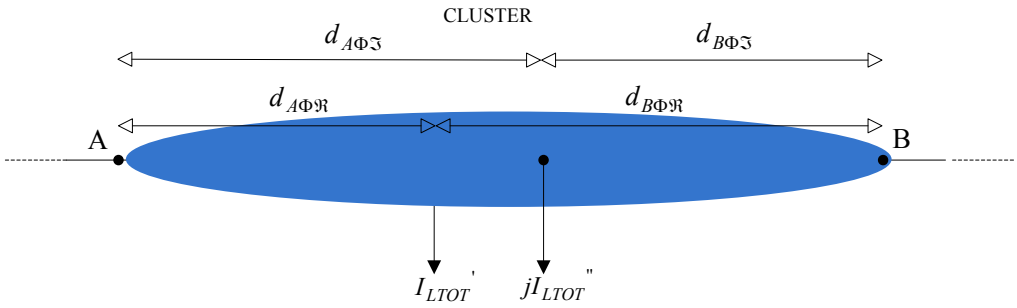

Fig. 3.15 Definition of load currents barycentre

3.4.1.3. Implementation details

The analysis so far presented on the single cluster loss minimization, can be extended to the whole microgrid to introduce the first, even if the most simplified, distributed control solution. The assumption under this solution are:

- The microgrid topology has to be consistent with the structure of Fig. 3.12 , with the modular repetition of clusters.
- A communication infrastructure has to be provided in the microgrid so that:
  - A Token Ring communication among the nodes can be implemented.
  - Each EG, corresponding to a grid node, has to be able to communicate in a bidirectional way with all the surrounding EGs and with the loads distributed in the surrounding clusters.
- Either reactive current only or both active and reactive currents can be injected by each EG.
- Initially, the EGs saturations are neglected

Going further in the details of the expected functionalities of the communication infrastructure, it is worth to observe that the two requirements mentioned above represent two different layers of the system.

The Token Ring is the higher level, and is motivated by the need for an authorization command that enables a specific EG to take the control, thus calculating and imposing its optimum current reference for the power converter control loop. This is a precaution, to guarantee minimum interactions between the different EGs output current controllers. The term Token Ring is therefore used in more general scenario with respect to the proper application standard [123]. For the application to a microgrid at this level of analysis the specific protocol is just a detail. The very basic requirement is that a message has to be continuously present in the microgrid, containing and updating the address of the EG that is authorized to locally apply the minimum loss control. Once a new EG is placed in the microgrid, only a node to node communication is sufficient for the Token Ring: the new EG is identified by a univocal physical address, and it will collect the address of its neighbours. The neighbourhood can be defined based on the physical distance, i.e. the neighbours of a generic node N are the set of nodes with a direct cable connection to node N, or based on the nodes located within a maximum distance from node N. Independently on this definition, once a node N knows its neighbours, it knows a table of addresses representing the possible destinations of the Token.

The Token delivery could be implemented as follows: the Token is first owned by an initial node, that could be the PCC (even if without EG, it is reasonable to assume that also the PCC has measurement and communication capabilities, that are necessary also to manage emergency situations such as faults or islanded operation control and synchronization). From the table of the surrounding addresses, the owner selects the node that has owned the Token for a lower number of times. If all the counters are at the same value, the destination is selected randomly among the candidates. The counter of the number of control actions is in the control system of each EG, and the number is sent to the querying node. Once the current owner has defined the next owner, a message is sent to the specified address, containing the authorization for the loss minimization control. As a result, the communication architecture is limited to node-to-node communication. When a node receives the Token, it performs the control action, i.e. definition of its optimum current reference, while all the other EGs in the microgrid remain in a hold state, keeping their previous current reference (in the hypothesis of current reference driven only by loss minimization). After a number o iterations, all the nodes in the microgrid receive the token and perform the control action required to minimize the distribution loss. Once all the nodes have received the Token and injected the optimum currents, the subsequent control actions will be ineffective, while maintaining the system able to respond to load transient, connection or disconnection of generators, etc. Such a system is easily

expandable and automatically adapts to changes in the microgrid. For the purpose of proving the effectiveness of loss minimization, the required bandwidth of the transmission can be slow, in the order of hundreds of milliseconds, to guarantee the microgrid stabilization between two consecutive control actions.

This is of course a qualitative behaviour required to the Token Ring approach, still far from a practical implementation, that should take into account communication errors such as lost Token and other security issues to guarantee the effectiveness of the technique. Other crucial aspects such as the identification of the neighbourhood, will be introduced later. This analysis will be object of future developments, related with the realization of a laboratory scaled microgrid.

The second communication layer is the one required for the final implementation of the distributed minimum loss control, and thus with all the operation that an authorized node, i.e. the node owning the Token, has to perform to calculate its optimum current. Fig. 3.16 reports a generic node N, owning the Token and applying the minimum loss control.

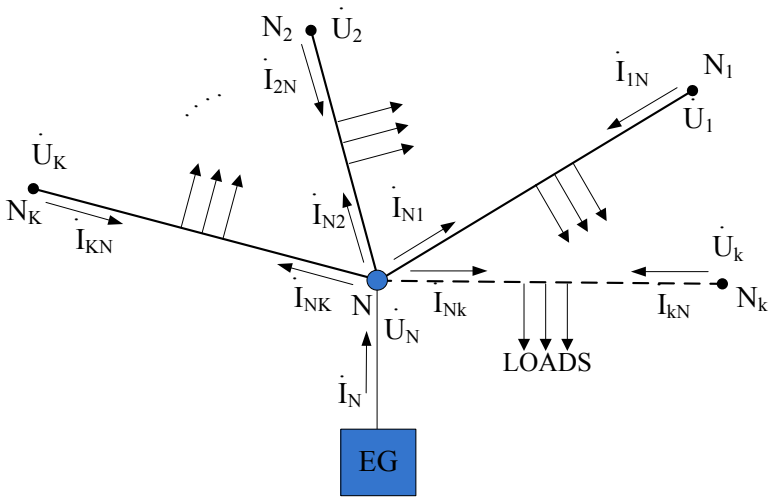

Fig. 3.16 Generic node N applying the minimum loss control to the correspondent cut-off section

Thanks to the hypothesis made on the microgrid topology, each cluster has minimum distribution loss if the currents injected at both the ends correspond to the optimum currents. This includes the action of the two EGs connected at the ends of the cluster. The single cluster optimization is naturally expandable to an arbitrary number of clusters converging in the same node, as in Fig. 3.16 . All the K surrounding clusters require from node N a specific optimum current and, in the ideal case of unconstrained injection, node N is able to inject the sum of all the required currents. As a consequence, if the microgrid is static, i.e. fixed loads and generation units, when all the nodes have received the token and injected the optimum currents, the global loss is minimized.

This is the main driver that will be applied also in the next analysis: iterating a local optimization all over the microgrid leads to a global loss minimization equivalent to the one achievable with a centralized controller.

Coming back to Fig. 3.16 , the current requested to node N is:

$$\dot{I}_N^{opt} = \sum_{k=1}^{K} \dot{I}_{Nk}^{opt} \tag{3.4.13}$$

Where the single $\dot{I}_{Nk}^{opt}$, required by the cluster connecting node N and the generic neighbour k is derived from (3.4.4) changing the variables:

$$\dot{I}_{Nk}^{opt} = \frac{1}{d_{Nk}} \sum_{h=0}^{H} \dot{I}_{Lh} d_{kh} \tag{3.4.14}$$

Where d_{Nk} is the total length of the cluster and H is the number of distributed loads along the cluster. Therefore, node N has to calculate all the optimum currents. For this reason, the following hypotheses are assumed:

- All the loads in the cluster are able to communicate their currents to the EGs at the extremes, using Phasors Measurement Units (PMU), with a common time synchronization (synchro-phasors). Considering that the loads is a distribution system are normally represented by residential or industrial buildings with power meter, this additional feature can be considered as a natural evolution of the current infrastructure.

- The distances between nodes N, k, and all the loads in the cluster can be assumed known, or better measured by using ranging techniques. It is worth to note that the also the identification of the EGs at the extremes of the cluster is a process requiring distance measurements done by each load. Ranging techniques will be briefly investigated in the next sections, as a valuable instrument to evaluate the electrical distance between two devices in the distribution line. These techniques were originally developed for wireless networks [124, 125] but an extension to PLC (Power Line Communication) is natural for the application of those techniques in Smart Grids environments. Also the development of PLC protocols to smart microgrids will be briefly introduced at the end of this chapter.

With these two powerful instruments, node N has all the information required for calculating its optimum current. It is worth to note that also these communications are node-to-node communications, without specific bandwidth requirements. The only strict requirement is the time

synchronization, meaning that the clocks of all the communication modules in the EGs have to be tightly synchronized, for example using GPS signal.

The name of *Current Based Surround Control* resumes the need for communication of each node with all the surroundings and the fact that the minimum loss condition is obtained exchanging only information on the currents absorbed by the loads along the cluster.

The Current Based Surround Control can be equivalently applied both to meshed and tree network topologies, if the initial hypothesis on the clusters division is satisfied. The technique can be defined as a feed-forward approach, because the optimum currents are measured and consequently injected in the microgrid. Any error in load currents measurements and in distances estimation is reflected in an increase of the loss with respect to the ideal minimization.

3.4.1.4. Saturations effect

So far, the *Current Based Surround Control* has been investigated in the ideal case of unconstrained optimization, where all the EGs where able to generate the required optimum currents. In a real application, it is likely to have a number of EGs saturating their current capability. In this case the loss increases, because a circulation current is required to fed the loads that cannot be locally fed by the EGs located at the ends of the clusters. It has to be noted that also the circulation current is a degree of freedom: assumed that in a specific cluster there is a circulation current, the system optimization becomes the identification of the nearest EG from where the required circulation current can be absorbed, to minimize the global loss due to circulation currents.

When a node N saturates, it automatically knows the amount of required circulation current. Knowing the distances between the node and the surrounding nodes, a request is sent to the nearest neighbour M, with the amount of required current $\dot{I}_{circ\_N}$. When M takes the control, two cases are possible: the node can satisfy the request of the saturated node, thus optimizing the circulation current dispatch, or can be saturated as well. In this second case, two sub-cases are possible: if the saturation of M is due to the extra demand coming from N, the amount of $\dot{I}_{circ\_N}$ that M cannot supply is sent back to N, that will try to send the required current to the other neighbours, in an iterative way. If the saturation of M is not caused by $\dot{I}_{circ\_N}$, the full $\dot{I}_{circ\_N}$ is sent back to N, and also node M will have a circulation current to be dispatched among the neighbours, excluding N. This simple saturations management ends up with the optimal constrained optimization of the system. The circulation current that cannot be injected by other EGs will be absorbed from the PCC.

The advantages of the *Current Based Surround Control* are the easy management of EGs saturations, and the inherent stability of the distributed control, being the current injection based on a

feed-forward control. On the other hands, the communication requirements are not trivial, and the applicability is restricted to microgrids that can be divided in clusters as in Fig. 3.12 .

3.4.2. Voltage Based Surround Control

3.4.2.1 Introduction

The *Voltage Based Surround Control* has been developed with the goal of reducing the amount of information required to achieve the distributed loss minimization. At the same time, also a relaxation in the hypothesis on the microgrid would help the definition of a more general technique. The Current Based technique can be applied either to tree or meshed topologies, but the microgrid has to be clustered and with constant cables section. The introduction of the Voltage Based approach starts from the same hypotheses, and is extended later. In equation (3.4.7) it has been verified that, for a single cluster, the minimum loss condition corresponds to have nodes A and B at the same potential. It is worth to recall that this is true if and only if the distribution cable has constant section along the cluster, i.e. $\dot{z} = r + j\,x \ (\Omega/km)$ with constant ratio r/x or equivalently constant phase of the line impedance.

In the Current Based approach, the information about the voltage is totally neglected, being the load currents sufficient to define the optimum current injection. If the load currents are no longer available, as it will be assumed from now on, the only residual information on the grid state is the voltage of the neighbours. When a generic node N receives the token, its surroundings can now be represented as:

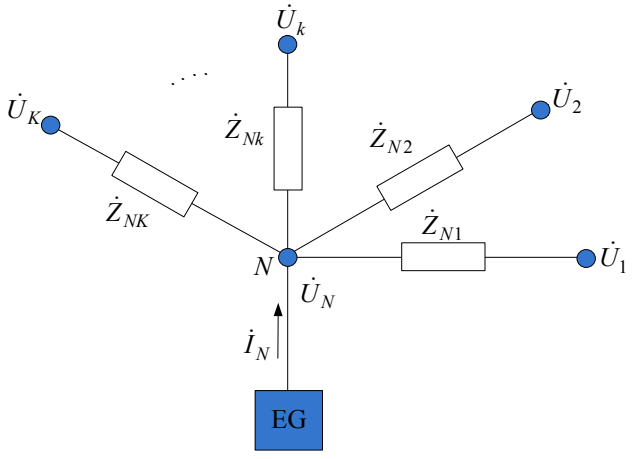

Fig. 3.17 Neighbour nodes representation for Voltage Based Surround Control

Fig. 3.17 is a representation of the neighbour nodes of node N that has to be interpreted as an "information oriented" equivalent circuit, and not an electrical equivalent circuit. This because the load currents along the clusters are not represented, while all the elements known by node N and

used during the control action, such as the neighbour nodes voltages and the clusters total line impedances are included. In other words, Fig. 3.17 a model of the surroundings, built by node N.

When node N receives the Token, the only control action oriented to loss minimization that can be done is to try to minimize the circulation currents in the considered microgrid cross section. To achieve this goal, an approximation has to be introduced on the equivalent circuit built by node N to model the surrounding nodes and used to define the optimum current reference $\dot{I}_N^{opt}$. The approximation will be investigated later in the details, but the main idea is to substitute all the surrounding nodes with voltage generators corresponding to the voltages that node N collects communicating with its neighbours. Therefore, the circuit used by node N is exactly the same as in Fig. 3.17 , adding the voltage generators in the surrounding nodes. It is important to point out that this is only the simplified model that node N adopts to model the microgrid and define the optimum current injection $\dot{I}_N^{opt}$.

3.4.2.2 Optimum current injection

Before calculating the optimum current reference, it is worth to clarify that the scenario represented by the microgrid cross section with voltage generators is different from the model used so far to define the optimum current injection of a generic node. In particular, with voltage sources it is more convenient to substitute optimum current with an optimum voltage source to be connected in N to minimize the loss. Once the voltage is calculated, the corresponding current is known and a current source $\dot{I}_N^{opt}$ can replace the voltage source $\dot{U}_N^{opt}$ using the substitution theorem. To clarify the definition of optimum voltage, assume now node N to be controlled as voltage source. In this way, the problem of loss minimization moves toward the definition of the voltage $\dot{U}_N$ that minimizes the global loss of the system. First, constant section of the cables within each cluster makes each cluster naturally absorbing the optimum currents from the voltage generators ($\dot{U}_N$ included), when their voltages are set to be equal, causing zero voltage drop along the clusters. This is also in the extreme case of voltage generators set to zero. Therefore, the superposition of effects can be applied to the loss, recalling (3.4.11). When voltage generators are set to zero while loads current generators are active, line currents are the optimum ones, and contribute to the first part of (3.4.11), the absolute minimum loss. When the voltage generators are activated and the current generators of the loads are off, the flowing currents are the circulation currents and contributes to the second part of (3.4.11). This decoupling between the currents and their effect on the loss is the base of the next analysis. Referring to Fig. 3.17 , the second term of (3.4.11)can be rewritten as:

$$P_{circ}^{loss} = \sum_{k=1}^{K} R_N^k \left| \dot{I}_N^k \right|^2 = \sum_{k=1}^{K} R_N^k \frac{\left| \dot{U}_N - \dot{U}_k \right|^2}{\left| \dot{Z}_N^k \right|^2} \tag{3.4.15}$$

Where R_N^k is the resistance of the distribution cable connecting N and k. For fixed surrounding voltages $\dot{U}_k$, the optimum voltage $\dot{U}_N$ can be found minimizing (3.4.15). In particular, the equation can be reordered as:

$$P_{circ}^{loss} = \sum_{k=1}^{K} \frac{R_N^k}{\left| \dot{Z}_N^k \right|^2} \left(\dot{U}_N - \dot{U}_k \right) \left(\dot{U}_N{}^* - \dot{U}_k{}^* \right) = \sum_{k=1}^{K} \frac{R_N^k}{\left| \dot{Z}_N^k \right|^2} \left(\dot{U}_N \dot{U}_N{}^* + \dot{U}_k \dot{U}_k{}^* - 2\Re\left(\dot{U}_N \dot{U}_k{}^* \right) \right) \tag{3.4.16}$$

Considering the single element $p = \left(\dot{U}_N \dot{U}_N{}^* + \dot{U}_k \dot{U}_k{}^* - 2\Re\left(\dot{U}_N \dot{U}_k{}^* \right) \right)$ substituting $\dot{U}_N = x + jy$ and $\dot{U}_k = a_k + jb_k$, and deriving with respect to x and y:

$$\begin{aligned} p &= x^2 + y^2 + a_k{}^2 + b_k{}^2 - 2xa_k - 2yb_k \\ \frac{\partial p}{\partial x} &= 2x - 2a_k \\ \frac{\partial p}{\partial y} &= 2y - 2b_k \end{aligned} \tag{3.4.17}$$

And thus:

$$\begin{cases} \dfrac{\partial P_{circ}^{loss}}{\partial x} = \displaystyle\sum_{k=1}^{K} \frac{R_N^k}{\left| \dot{Z}_N^k \right|^2} \left(2x - 2a_k \right) \\ \dfrac{\partial P_{circ}^{loss}}{\partial y} = \displaystyle\sum_{k=1}^{K} \frac{R_N^k}{\left| \dot{Z}_N^k \right|^2} \left(2y - 2b_k \right) \end{cases} \tag{3.4.18}$$

The optimum voltage is found setting (3.4.18) equal to zero:

$$\begin{cases} \displaystyle\sum_{k=1}^{K} \frac{R_N^k}{\left| \dot{Z}_N^k \right|^2} \left(2x - 2a_k \right) = 0 \\ \displaystyle\sum_{k=1}^{K} \frac{R_N^k}{\left| \dot{Z}_N^k \right|^2} \left(2y - 2b_k \right) = 0 \end{cases} \rightarrow \sum_{k=1}^{K} \frac{R_N^k}{\left| \dot{Z}_N^k \right|^2} \left(\dot{U}_N^{opt} - \dot{U}_k \right) = 0 \rightarrow \dot{U}_N^{opt} = \frac{\displaystyle\sum_{k=1}^{K} \frac{R_N^k}{\left| \dot{Z}_N^k \right|^2} \dot{U}_k}{\displaystyle\sum_{k=1}^{K} \frac{R_N^k}{\left| \dot{Z}_N^k \right|^2}} \tag{3.4.19}$$

Finally, the optimum current that a node N has to inject is:

$$\dot{I}_N^{opt} = \sum_{k=1}^{K} \dot{I}_{Nk}^{opt} + \sum_{k=1}^{K} \frac{\left(\dot{U}_N^{opt} - \dot{U}_k \right)}{\dot{Z}_N^k} \tag{3.4.20}$$

In the particular case of all the surrounding clusters with the same section $\dot{z} = r + j\,x \ (\Omega / km)$, (3.4.19) and (3.4.20) result simpler:

$$\dot{U}_N^{opt} = \frac{\sum_{k=1}^{K} \frac{rd_{Nk}}{|\dot{z}|^2 {d_{Nk}}^2} \dot{U}_k}{\sum_{k=1}^{K} \frac{rd_{Nk}}{|\dot{z}|^2 {d_{Nk}}^2}} = \frac{\sum_{k=1}^{K} \frac{\dot{U}_k}{d_{Nk}}}{\sum_{k=1}^{K} \frac{1}{d_{Nk}}} = \frac{\sum_{k=1}^{K} \frac{\dot{U}_k}{\dot{Z}_N^k}}{\sum_{k=1}^{K} \frac{1}{\dot{Z}_N^k}} \tag{3.4.21}$$

$$\begin{aligned} \dot{I}_N^{opt} &= \sum_{k=1}^{K} \dot{I}_{Nk}^{opt} \\ \sum_{k=1}^{K} \frac{\left(\dot{U}_N^{opt} - \dot{U}_k\right)}{\dot{Z}_N^k} &= 0 \end{aligned} \tag{3.4.22}$$

This means that in the case of constant section for all the surrounding clusters, the injection of the optimum current as sum of the surrounding optimum currents already minimizes also the loss due to the circulation currents. It is worth to repeat that this optimization is done on a fictitious network, that doesn't have a direct correspondence in the real microgrid.

Moreover, another approximation has to be introduced: once node N has computed $\dot{U}_N^{opt}$ using the information on the surrounding voltages and on the surrounding cables impedances (or simply distances in the simplified case), the voltage has to be translated in a current reference. Being the information on the microgrid limited, for example the optimum currents are unknown, the injected current $\dot{I}_N^{opt}$ is derived based on the real Thevenin's equivalent circuit seen by node N. In particular, naming $\dot{Z}_N^{eq}$ the total equivalent impedance seen from N, and $\dot{U}_N^0$ the voltage at node N before the control action (it has to be noted that the node could already be injection a non optimum current, whose effect is included in the measured $\dot{U}_N^0$), the current variation required to reach the optimum voltage is:

$$\Delta I_N^{opt} = \frac{\dot{U}_N^{opt} - \dot{U}_N^0}{\dot{Z}_N^{eq}} \tag{3.4.23}$$

If the microgrid surrounding node N were exactly coincident with the assumed equivalent circuit with voltage sources, this current would drive the system toward the optimum voltage, inherently taking into account also the optimum currents, that contribute to $\dot{U}_N^0$. In the real grid, with a topology different from the model, the loss are not minimized, but it will be shown that the system moves in the direction of loss reduction.

3.4.2.3 Discussion

The main point of this technique that requires a deeper explanation is the following: the definition of optimum voltage is done optimizing an equivalent neighbour network that doesn't correspond to the real system and finding a required voltage $\dot{U}_N^{opt}$. Then, on the real system, the current injection is found that drives the voltage to the desired value. But while that voltage can effectively be driven to $\dot{U}_N^{opt}$, assuming unconstrained current injection, the surrounding voltages are not voltage sources, and thus change as a consequence of the injection, invalidating the optimization that was supposed to take place. For these reasons the *Voltage Based Surround Control* is a feedback control, where the control action modifies the variables sampled by the controller itself, as schematically resumed in Fig. 3.18 :

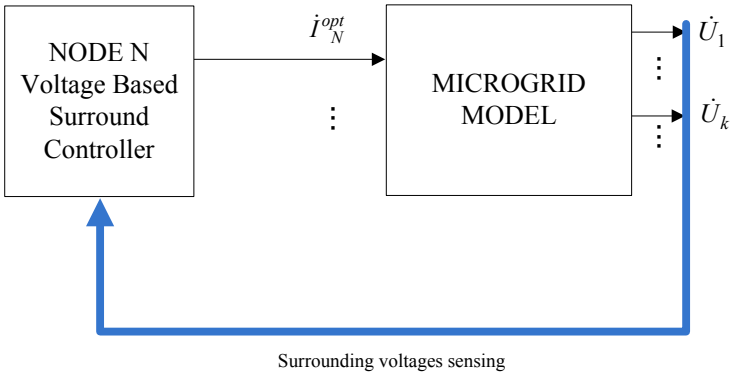

Fig. 3.18 Feedback scheme of the *Voltage Based Surround Control* applied to a generic node N

While a feed forward approach such as the *Current Based Surround Control* doesn't have any stability related issue, for a feedback system the stability is the first feature that has to be guaranteed. Moreover, in this distributed approach the stability should be verified both at local level, i.e. the surround control applied to a single node, and at system level, showing that the iteration of the Token, and therefore the repetition of the local control for the different EGs in the microgrid, drives the microgrid to converge to the global minimum loss condition as it has been verified for the *Current Based Surround Control.*

3.4.2.4 Stability analysis

Consider now the single EG connected to node N. Assume T_C to be the sample time of the controller. A phasor measurement unit calculates the phasors of the surrounding nodes voltages, based on a common reference. Every T_C the control samples the phasors, and calculates the injected current with (3.4.19) and (3.4.23). The microgrid model is now the real one, with a single voltage source in the PCC (point of common coupling) and all the distributed EGs modelled as current

sources. In general, directing the EGs currents as injected (as all the other currents, loads included), a microgrid can be described in sinusoidal regime as:

$$\underline{\dot{U}} = \underline{1}\dot{U}_0 + \underline{X}\underline{\dot{I}} \tag{3.4.24}$$

Where $\underline{\dot{U}}$ is the column vector of all the node voltages and $\underline{\dot{I}}$ the correspondent injected currents, loads or generators. $\underline{1}$ is a column of ones and $\dot{U}_0$ the PCC voltage. All the nodes of the microgrid are included, also the empty nodes (simple ramifications) and the loads. In the stability analysis only the current injected by node N is considered. Therefore all the other generators and loads are fixed AC current sources. Moreover, only voltages $\dot{U}_1..\dot{U}_K$ of the k nodes surrounding N are considered. $\underline{X}$ is a matrix of impedances, that has been introduced in Chapter 2, and whose elements are combinations of line impedances. Therefore, the generic element of $\underline{X}$ has the form $X_{ij} = \left(R_{ij} + j\omega L_{ij}\right)\Omega$. In the Laplace transform domain, this means that all the transfer functions between a current $\dot{I}_i$ and a voltage $\dot{U}_j$ are $G_{I_iU_j}(s) = \left(R_{ij} + sL_{ij}\right)$. From these observation, the block diagram of the controlled plant for node N local surround control is depicted in Fig. 3.19 :

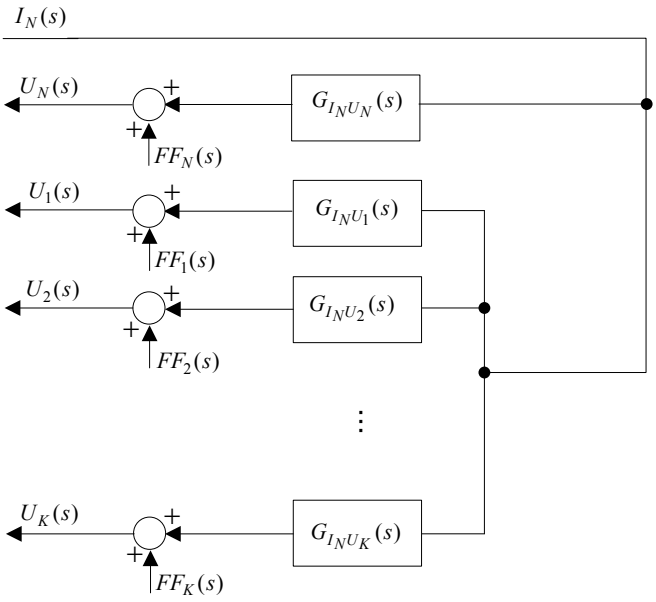

Fig. 3.19 Block diagram of the controlled plant for the Voltage Based Surround Control applied to node N

Where the terms $FF_i(s)$ are the components of the nodes voltages due to the combination of the PCC voltage and the other EGs behaving like AC current sources, and not involved in the dynamic of the controller. The scheme is in the continuous time domain because it is the general translation of (3.4.24).

In the implementation of the controller, the scheme has been translated in the discrete domain, being the controller acting on the phasors only when it receives the authorization from the Token. To simplify the scheme, a slow sampling frequency $f_C << f_{grid}$ is assumed, where $f_{grid} = 50Hz$, so that the dynamic of the measurements required for phasors real and imaginary part calculation can be neglected. Voltages and currents in the microgrid are sinusoidal but with amplitude and phase that are dynamically changed by the slow controller. Therefore the transfer functions can be rewritten as $G_{I_i U_j}(z) = R_{ij} + j\omega L_{ij} = |X_{ij}|e^{j\varphi_{ij}}$. The full scheme of the feedback control is now reported in Fig. 3.20 , where the simplified optimum voltage calculation (3.2.7) is considered, assuming all the microgrid made by the same distribution cable. The scheme neglects all the disturbances due to the other current generators, that are not influent for the stability study.

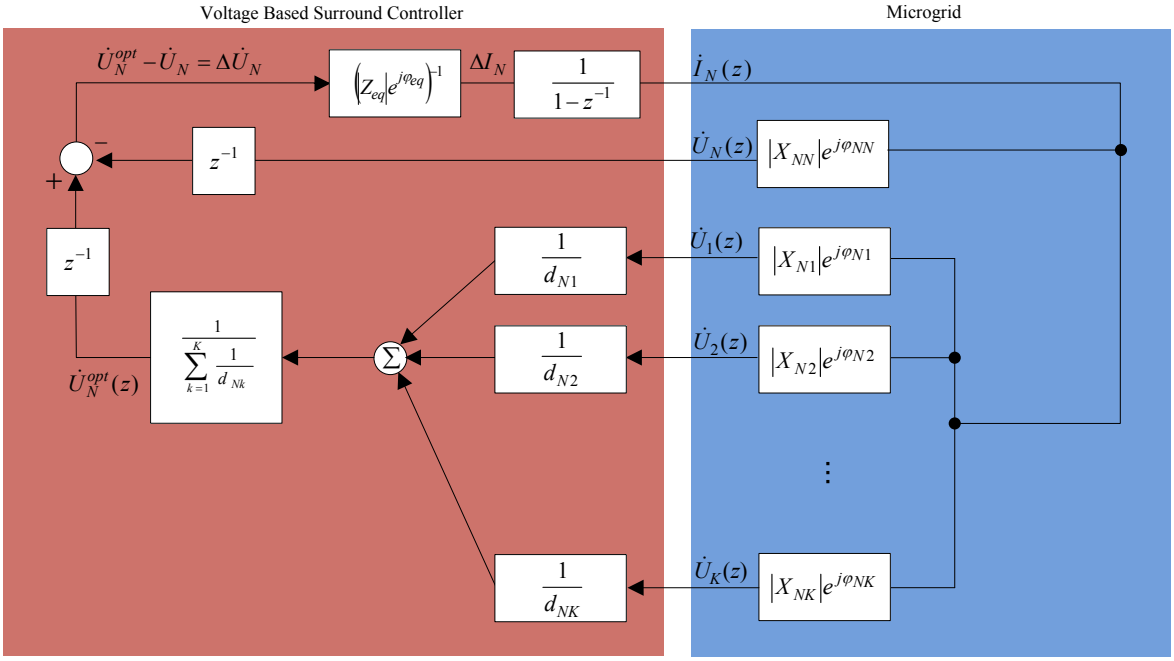

Fig. 3.20 Reduced block diagram for stability analysis of the Voltage Based Surround Controller

First of all, it is worth to simplify the block diagram. The blocks involving $\dot{U}_N^1 .. \dot{U}_N^K$ can be represented by a single equivalent impedance, therefore:

$$\dot{U}_N^{opt} = \frac{\sum_{k=1}^{K}\frac{\dot{U}_k}{d_{Nk}}}{\sum_{k=1}^{K}\frac{1}{d_{Nk}}} = \frac{\sum_{k=1}^{K}\frac{|X_{Nk}|e^{j\varphi_{Nk}}}{d_{Nk}}}{\sum_{k=1}^{K}\frac{1}{d_{Nk}}}\dot{I}_N = |Z_{TOT}|e^{j\varphi_{TOT}}\dot{I}_N \tag{3.4.25}$$

Moreover, it can be observed that:

$$|X_{NN}|e^{j\varphi_{NN}} = |Z_{eq}|e^{j\varphi_{eq}} \tag{3.4.26}$$

To study the stability of the closed loop system, it is important to remind the meaning of the complex gains present in the loop: they are due to the phasorial representation of the microgrid. The closed loop control goal is to control to zero the real and imaginary part of the error $\dot{U}_N^{opt} - \dot{U}_N^0$. Therefore, the system is equivalent to a double control loop, reported in Fig. 3.22 , where a continuous time controller is assumed, to simplify the analysis. Moreover, the total gain of the system between $\Delta\dot{I}_N$ and $\Delta\dot{U}_N$ is represented as:

$$\left|Z_{TOT}\right|e^{j\varphi_{TOT}} - \left|X_{NN}\right|e^{j\varphi_{NN}} = R + jX = R + j\omega L\Big|_{\omega=2\pi 50\frac{rad}{s}} \tag{3.4.27}$$

Before representing Fig. 3.22 , it is better to clarify the nature of the considered closed loop system, taking advantage of the simplification (3.4.27), and of the practical implementation of the controller. In fact, the measurement of the real and imaginary part of the voltages can be implemented with a DQ transformation, described in Appendix B. Fig. 3.21 represent the equivalent circuit, again omitting the effect of other current sources, and therefore without inputs:

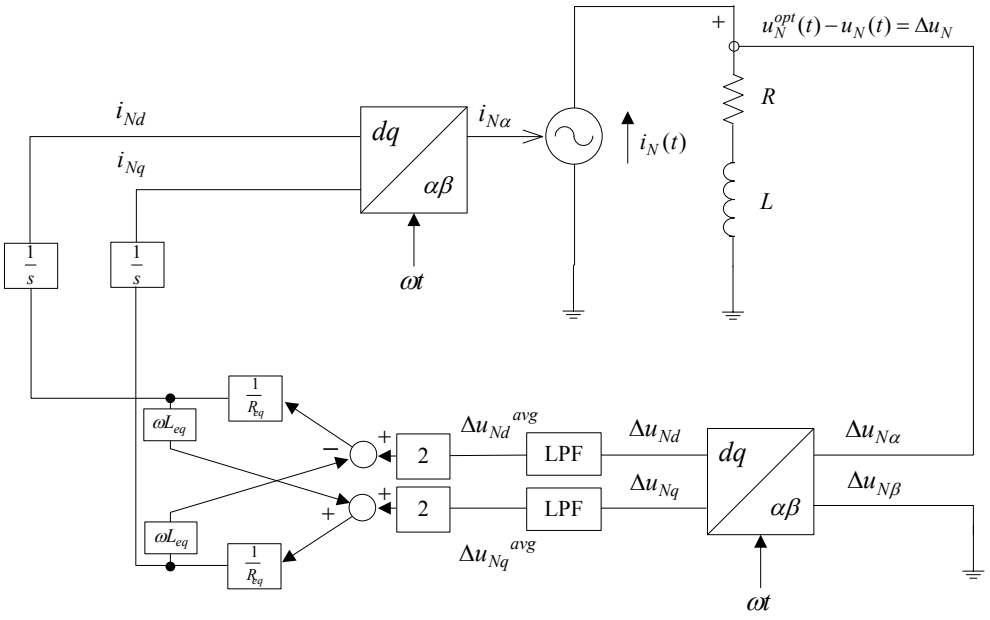

Fig. 3.21 Node N Voltage Based Surround Controller equivalent scheme for stability analysis

The blocks LPF are two low pass filters required to extract the mean value of the d and q components. In fact, with a single phase signal $\Delta u_{N\alpha}$ entering the alpha-beta to dq transformation block, the outputs will be oscillating signals at 2ω, around the mean value, corresponding to the projections of phasor $\Delta\dot{U}_{N\alpha}$ on the reference phasor $\dot{U}_{ref}$, assumed to be real, and on $\dot{U}_{ref\_q}$, leading in quadrature. It has to be specified that in the real case the dq transformation is made for each of the surrounding nodes, while here it is applied to Δu_N, to simplify the analysis without loss

of generality, being Δu_N a linear combination of the voltages. The gains 2 after the low pass filters guarantee the equivalence of the direct and reverse transformations. In fact, assuming $\Delta u_{N\alpha} = A\cos(\omega t + \varphi)$, the direct transformation is:

$$\begin{bmatrix} \Delta u_{Nd} \\ \Delta u_{Nq} \end{bmatrix} = \begin{bmatrix} \cos(\omega t) & \sin(\omega t) \\ -\sin(\omega t) & \cos(\omega t) \end{bmatrix} \begin{bmatrix} \Delta u_{N\alpha} \\ 0 \end{bmatrix} = \begin{bmatrix} \frac{A}{2}(\cos(\varphi) + \cos(2\omega t + \varphi)) \\ \frac{A}{2}(\sin(2\omega t + \varphi) + \sin(\varphi)) \end{bmatrix} \tag{3.4.28}$$

If now the LPF is applied, results:

$$\begin{bmatrix} \Delta u_{Nd}{}^{avg} \\ \Delta u_{Nq}{}^{avg} \end{bmatrix} = \begin{bmatrix} \frac{A}{2}\cos(\varphi) \\ \frac{A}{2}\sin(\varphi) \end{bmatrix} \tag{3.4.29}$$

Appling the reverse transformation without considering the 2 gains, results:

$$\begin{bmatrix} \Delta u_{N\alpha}{}^{avg} \\ \Delta u_{N\beta}{}^{avg} \end{bmatrix} = \begin{bmatrix} \cos(\omega t) & -\sin(\omega t) \\ \sin(\omega t) & \cos(\omega t) \end{bmatrix} \begin{bmatrix} \frac{A}{2}\cos(\varphi) \\ \frac{A}{2}\sin(\varphi) \end{bmatrix} = \begin{bmatrix} \frac{A}{2}\cos(\omega t + \varphi) \\ \frac{A}{2}\sin(\omega t + \varphi) \end{bmatrix} \tag{3.4.30}$$

While including the gains, the transformation becomes coherent. From another point of view, with the two gains the d and the q components correspond to the projections of the signal $\Delta u_{N\alpha} = A\cos(\omega t + \varphi)$ on the reference $\dot{U}_{ref} = \cos(\omega t)$ and on the corresponding axes leading in quadrature $\dot{U}_{ref\_q} = -\sin(\omega t) = \cos(\omega t + \frac{\pi}{2})$ in the phasorial representation. To finally study the stability, all the scheme has to be represented in the dq reference.

$$\begin{aligned} \Delta u_{N\alpha} &= Ri_{N\alpha} + L\frac{di_{N\alpha}}{dt} \\ \Delta u_{N\beta} &= 0 \end{aligned} \tag{3.4.31}$$

And transforming:

$$\begin{aligned} \Delta u_{Nd} &= \frac{1}{2}\left(Ri_{Nd} + L\frac{di_{Nd}}{dt} + L\omega i_{Nq} \right) \\ \Delta u_{Nq} &= \frac{1}{2}\left(Ri_{Nq} + L\frac{di_{Nq}}{dt} - L\omega i_{Nd} \right) \end{aligned} \tag{3.4.32}$$

Averaging over a period $T = \frac{\pi}{\omega}$, the output of the LPFs is:

$$\begin{aligned}\Delta u_{Nd}{}^{avg} &= \frac{1}{2}\left(Ri_{Nd} + L\omega i_{Nq}\right)\\ \Delta u_{Nq}{}^{avg} &= \frac{1}{2}\left(Ri_{Nq} - L\omega i_{Nd}\right)\end{aligned} \tag{3.4.33}$$

Therefore, Fig. 3.21 can be rearranged to the final equivalent blocks scheme of Fig. 3.22 :

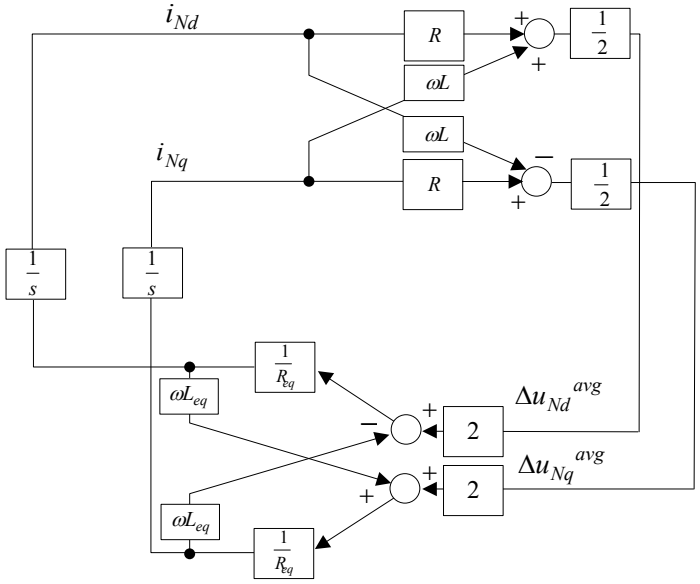

Fig. 3.22 Final equivalent scheme for the Voltage Based Surround Control applied to node N

The stability can be verified checking the eigenvalues of the A matrix in the state space model (with no inputs)

$$\frac{d\underline{x}}{dt} = A\underline{x} \tag{3.4.34}$$

The matrix results:

$$\begin{aligned}A &= \frac{1}{R_{eq}}\begin{bmatrix}1 & \frac{\omega L_{eq}}{R_{eq}}\\ -\frac{\omega L_{eq}}{R_{eq}} & 1\end{bmatrix}^{-1}\begin{bmatrix}R & \omega L\\ -\omega L & R\end{bmatrix} = \frac{1}{R_{eq}}\frac{1}{1+\left(\frac{\omega L_{eq}}{R_{eq}}\right)^2}\begin{bmatrix}1 & -\frac{\omega L_{eq}}{R_{eq}}\\ \frac{\omega L_{eq}}{R_{eq}} & 1\end{bmatrix}\begin{bmatrix}R & \omega L\\ -\omega L & R\end{bmatrix}\\ &= \frac{1}{R_{eq}}\frac{1}{1+\left(\frac{\omega L_{eq}}{R_{eq}}\right)^2}\begin{bmatrix}R+\frac{\omega^2 LL_{eq}}{R_{eq}} & \omega L-\frac{R\omega L_{eq}}{R_{eq}}\\ -\left(\omega L-\frac{R\omega L_{eq}}{R_{eq}}\right) & R+\frac{\omega^2 LL_{eq}}{R_{eq}}\end{bmatrix}\end{aligned} \tag{3.4.35}$$

The eigenvalues s are roots of the polynom $\det(sI - A)$, where I is the identity matrix. Naming $K = \frac{1}{R_{eq}} \frac{1}{1 + \left(\frac{\omega L_{eq}}{R_{eq}} \right)^2}$, $H = R + \frac{\omega^2 L L_{eq}}{R_{eq}}$ and $G = \omega L - \frac{R \omega L_{eq}}{R_{eq}}$:

$$A = K \begin{bmatrix} H & G \\ -G & H \end{bmatrix} \rightarrow \det(sI - A) = \det \begin{bmatrix} s - KH & -GK \\ GK & s - KH \end{bmatrix} = (s - KH)^2 + (GK)^2 \rightarrow$$
$$s = KH \pm jGK \tag{3.4.36}$$

Therefore the system is stable if and only if $KH < 0$, where $K > 0$. Checking the terms in H, $\frac{\omega^2 L_{eq}}{R_{eq}} > 0$, and thus the stability depends on the signs of R and L. These two values come from equation (3.4.27). In case of a tree topology, the frequency response between an injected current $\dot{I}_N$ and the surrounding voltages are always either equal to or with both the real and the imaginary part lower than the one of the frequency response between $\dot{I}_N$ and $\dot{U}_N$, i.e. the equivalent impedance. Hence, linearly combining the surrounding transfer functions to obtain $|Z_{TOT}|e^{j\varphi_{TOT}}$, it will always be:

$$|Z_{TOT}|e^{j\varphi_{TOT}} = |X_{NN}|e^{j\varphi_{NN}} - r - j\omega l \tag{3.4.37}$$

Thus guaranteeing the local stability of the Voltage Based Surround Control. A similar result can be proved also in case of a meshed microgrid topology, simply formulating (3.4.37) in a more general way. Therefore, it can be concluded that the Voltage Bases Surround Control is locally stable for every microgrid topology. This analysis guarantees that leaving the control acting on node N (or in other words leaving the Token in N for an infinite time), the steady state condition corresponds to the current injection $\dot{I}_N^{opt}$ guaranteeing $\dot{U}_N^0 = \dot{U}_N^{opt}$. In general this doesn't mean that all the surrounding nodes are at the same potential, because of the offsets terms reported in Fig. 3.19 , and omitted for the stability analysis.

In the next, with a simplified example adopting the usual hypotheses on the microgrid, it is shown that when a Token Ring based distributed control is running on the microgrid the only possible steady state configuration for all the nodes is with equal voltages in all the EGs, in particular equal to the PCC voltage, that is fixed. In general, this condition correspond to minimum loss only if the cable section is constant within a cluster (or group of clusters in case of ramifications without EG). In the definition of Token Ring based surround control (either current based or voltage based) it has been specified that once a node receives the Token, it performs a single control action, then sending the Token to another EG. In the current based approach, it means that in a number of

Token iterations equal to the number of nodes the distributed algorithm converges to the minimum loss (in the hypotheses made on microgrid structure). In the voltage based approach, that is no longer true, because a single control action based on (3.4.23) changes the surround voltages according to the feedback scheme in Fig. 3.20 .

In the next paragraphs, the convergence of the distributed controller to the minimum loss condition will be demonstrated adopting a simplified approach: again, the microgrid has a tree topology, with single PCC and constant section. Moreover, the clustered structure of Fig. 3.12 is assumed. With these hypotheses, the minimum loss condition correspond to all the nodes with EGs at the same potential, and thus zero circulation currents in all the clusters. To demonstrate that this is the steady state condition when a Token iteratively activates all the EGs in the microgrid, the behaviour of the distributed control can be analyzed in an effective way starting from the most peripherals EGs: consider the case where only one of these EGs, node P, is implementing the Voltage Based Surround Control. The node will measure the voltage of its only neighbour M, and will implement (3.4.23). Without loss of generality, assume that no loads are connected after node P (there is no loss of generality because the fixed load current generators after P can be modelled as an offset current for P). The equivalent circuit of the microgrid is in Fig. 3.23 :

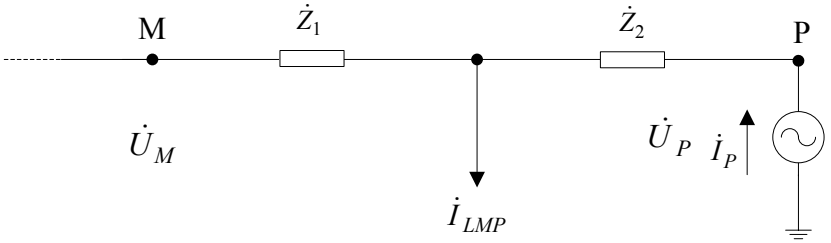

Fig. 3.23 Equivalent circuit for the Voltage Based Surround Control applied to the peripheral node P

The equivalent circuit seen by node M is deliberately left unknown, because this is the key for the easy proof of convergence to the minimum loss. The scheme of the Voltage Based Surround Control applied to node P is reported in Fig. 3.24 . In the figure, $\left|Z_{eq}\right|e^{j\varphi_{eq}}$ is the total impedance seen by node P, including the unknown impedance seen by M. Knowing that the closed loop system is stable, from the figure follows the only possible steady state condition:

$$\dot{U}_P = \dot{U}_M \tag{3.4.38}$$

That is the condition required to minimize the loss in the cluster. It is also worth to note that, once the controller is in steady state, any change in the voltage $\dot{U}_M$ doesn't have any effect on the required current $\dot{I}_P$, that for $k \to \infty$, where k is the iterations number, becomes a fixed AC current source.

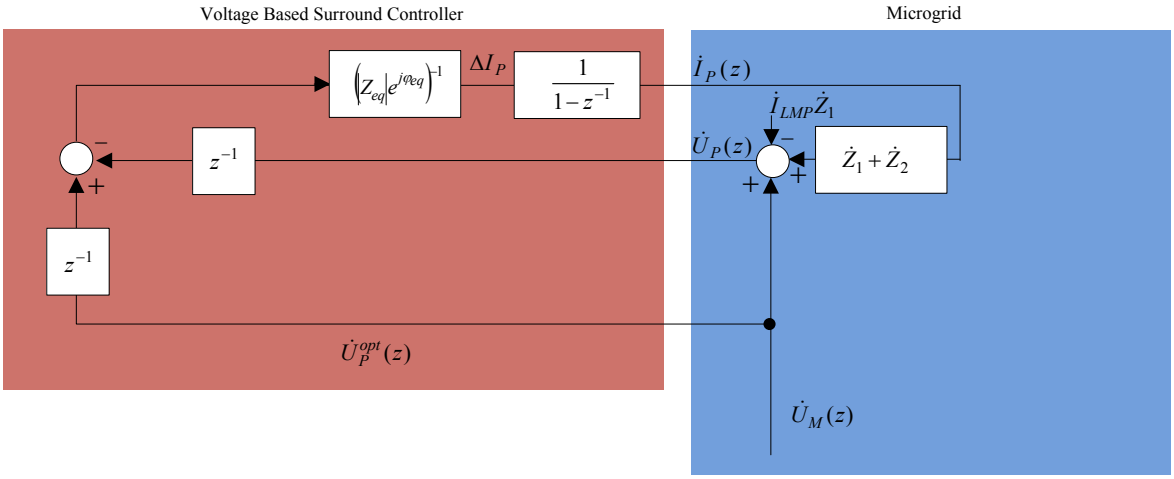

Fig. 3.24 Discrete time Voltage Based Surround Controller for peripheral node P

The same controller is now sequentially applied to all the peripheral nodes, waiting for each of them the achievement of the steady state condition. A threshold on the error can be set, so that the steady state is considered achieved after a finite number of iterations T. In other terms, each peripheral node keeps the Token until it reaches the steady state, then passing it to another peripheral node. Once all the nodes are in steady state, they become fixes current sources, and the control is passed to the upper level in the tree. Level by level, all the voltage drops along the lines are set to zero, leading to a final convergence where the loss is minimum and all the voltages are equal, and in particular equal to the PCC voltage.

Of course in the desired distributed approach is not possible to identify the different levels in the microgrid topology, but the Token is continuously exchanged among the nodes to guarantee that all the nodes continuously update their current reference according to the Voltage Based Surround Control. Therefore, the control actions will be distributed. But the independence of the control of peripheral nodes on the voltage of their neighbours, guarantees that the distributed control converges to the same microgrid state as the case of sequential turning on of the controllers described above.

With this simplified analysis, the convergence to the minimum loss of the Voltage Based Surround Control is proved in the specific case of a microgrid with clustered tree topology and constant section cables. It is worth now to spend few words on the case where the hypotheses are not respected. The behaviour remains the same with tree topology but clusters with different cable sections, because for the convergence each cluster can be optimized alone, starting from the peripheral nodes up to the PCC. Keeping the tree topology but assuming a non-clustered structure, i.e. not all the nodes are equipped with an EG, but there are also free ramifications, the behaviour depends on the cables: if the section is the same within the ramified cluster, it can be proved the minimum loss condition is again when all the terminations of the ramified cluster are at the same

voltage. From the definition of the control action (3.4.19) it is clear that an equilibrium of the closed loop system in steady state is guaranteed if all the voltages in the microgrid are equal, in particular equal to the PCC voltage. In presence of ramifications without EGs, the simplified analysis that decouples the control loops and easily demonstrates the convergence cannot be presented. The same scenario appears in case of meshed microgrids.

In general it has to be kept in mind that this distributed control aims at levelling all the voltages to the value of the PCC voltage. The demonstration of the overall stability is simple in a clustered tree microgrid, where the stability of a local control becomes the stability of the whole distributed control, and it is also easy to demonstrate the convergence to equal voltages. This will correspond to minimum loss when the section is constant within a cluster.

The extension of stability and convergence to the general case of non clustered structures or even meshed microgrids is not immediate and easy to demonstrate in a general case. This because the system becomes a MIMO system with feedback control. Assuming now the whole system to be stable, from system theory, being each voltage controllable and the whole system linear and time invariant, the only possible convergence point is with all the voltages equal to the PCC, guaranteeing zero error in the input of all the integrators.

A proof of stability for the control with all loops acting contemporarily can be given in the simpler case of a microgrid with resistive cables and real currents only, referred to the PCC voltage, to avoid the cross-coupled loops appearing with the decomposition in real and imaginary part. Moreover, all the microgrid is assumed to be made of generators only, meaning that all the node currents are controllable, excluding the PCC. This simplifies the matrices required for the stability study. Moreover, the analysis is reported for a specific network, including a mesh, reported in Fig. 3.25 . The cable section is generic, therefore no relations are assumed between distances and resistances.

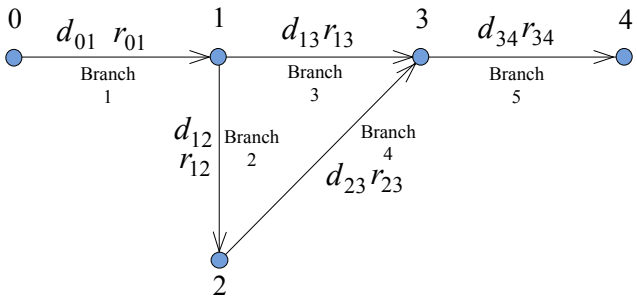

Fig. 3.25 Resistive microgrid for simplified stability analysis

The incidence matrix is:

$$A=\begin{bmatrix} -1 & 1 & 0 & 0 & 0 \\ 0 & -1 & 1 & 0 & 0 \\ 0 & -1 & 0 & 1 & 0 \\ 0 & 0 & -1 & 1 & 0 \\ 0 & 0 & 0 & -1 & 1 \end{bmatrix} \tag{3.4.39}$$

From the theoretical analysis in Chapter 2, the matrix of branches impedances is:

$$R=\begin{bmatrix} r_{01} & 0 & 0 & 0 & 0 \\ 0 & r_{12} & 0 & 0 & 0 \\ 0 & 0 & r_{13} & 0 & 0 \\ 0 & 0 & 0 & r_{23} & 0 \\ 0 & 0 & 0 & 0 & r_{34} \end{bmatrix} \tag{3.4.40}$$

$$L=A^T R^{-1} A=\begin{bmatrix} \frac{1}{r_{01}} & -\frac{1}{r_{01}} & 0 & 0 & 0 \\ -\frac{1}{r_{01}} & \frac{1}{r_{01}}+\frac{1}{r_{12}}+\frac{1}{r_{13}} & -\frac{1}{r_{12}} & -\frac{1}{r_{13}} & 0 \\ 0 & -\frac{1}{r_{12}} & \frac{1}{r_{12}}+\frac{1}{r_{13}} & -\frac{1}{r_{23}} & 0 \\ 0 & -\frac{1}{r_{13}} & -\frac{1}{r_{23}} & \frac{1}{r_{13}}+\frac{1}{r_{23}}+\frac{1}{r_{34}} & -\frac{1}{r_{34}} \\ 0 & 0 & 0 & -\frac{1}{r_{34}} & \frac{1}{r_{34}} \end{bmatrix} \tag{3.4.41}$$

Where the submatrix required for the calculation of $\underline{X}$ is:

$$L^s=\begin{bmatrix} \frac{1}{r_{01}}+\frac{1}{r_{12}}+\frac{1}{r_{13}} & -\frac{1}{r_{12}} & -\frac{1}{r_{13}} & 0 \\ -\frac{1}{r_{12}} & \frac{1}{r_{12}}+\frac{1}{r_{13}} & -\frac{1}{r_{23}} & 0 \\ -\frac{1}{r_{13}} & -\frac{1}{r_{23}} & \frac{1}{r_{13}}+\frac{1}{r_{23}}+\frac{1}{r_{34}} & -\frac{1}{r_{34}} \\ 0 & 0 & -\frac{1}{r_{34}} & \frac{1}{r_{34}} \end{bmatrix} \tag{3.4.42}$$

Is non singular, being the rank equal to the number of rows and columns. Therefore, the inverse can be calculated. Without loss of generality in the stability analysis, a specific set of resistances is considered: $r_{01}=0.5\Omega$ $r_{12}=1\Omega$ $r_{13}=0.75\Omega$ $r_{23}=0.25\Omega$ $r_{34}=0.1\Omega$, therefore:

$$L^s=\begin{bmatrix} \frac{13}{3} & -1 & -\frac{4}{3} & 0 \\ -1 & 5 & -4 & 0 \\ -\frac{4}{3} & -4 & \frac{46}{3} & -10 \\ 0 & 0 & -10 & 10 \end{bmatrix} \tag{3.4.43}$$

And finally matrix $\underline{X}$ is:

$$\underline{X} = \begin{bmatrix} 1 & 1 & 1 & 1 & 1 \\ 0 & 0.5 & 0.5 & 0.5 & 0.5 \\ 0 & 0.5 & 1 & 0.875 & 0.875 \\ 0 & 0.5 & 0.875 & 0.9688 & 0.9688 \\ 0 & 0.5 & 0.875 & 0.9688 & 1.9688 \end{bmatrix} \tag{3.4.44}$$

It is now easier to interpret the meaning of each term in $\underline{X}$, remembering that $\underline{\dot{U}} = \underline{1}\dot{U}_0 + \underline{X}\underline{\dot{I}}$, where $\underline{\dot{I}}$ is the vector of the injected currents, including the PCC, with $\dot{I}_0 = -\sum_{i>0} \dot{I}_i$. $\dot{I}_i$ are the currents injected by the current generators in nodes 1,2,3,4 in Fig. 3.25 . Skipping the first row that represents the currents balance of the PCC, for any other row i, the term $\underline{X}(i,j)$ represent the effect of each injected current j in the $i-th$ voltage. It can be observed that the coefficients are all positive, and that:

$$\underline{X}(i,i) \geq \underline{X}(i,j) \quad \forall j \neq i \tag{3.4.45}$$

Moreover, the elements $\underline{X}(i,i)$ are the equivalent resistances seen by node i. Appling now the feedback surround control to all the EG nodes in the microgrid, excluding node 0, the resulting state space model, assuming the input $\dot{U}_0 = 0$ is:

$$\frac{d\underline{i_g}}{dt} = \underline{K}' \underline{X}' \underline{i_g} \tag{3.4.46}$$

Where $\underline{X}'$ is matrix $\underline{X}$ without the first row and column, being $\dot{U}_0$ and the corresponding current, non influent for the stability. $\underline{K}'$ is the matrix with the linear combinations of the surround voltages for the Voltage Based Surround Control. $\underline{i_g}$ is the vector of the injected currents, excluding node 0. Therefore:

$$\underline{X}' = \begin{bmatrix} 0.5 & 0.5 & 0.5 & 0.5 \\ 0.5 & 1 & 0.875 & 0.875 \\ 0.5 & 0.875 & 0.9688 & 0.9688 \\ 0.5 & 0.875 & 0.9688 & 1.9688 \end{bmatrix} \tag{3.4.47}$$

In particular:

$$\underline{K}^{'}=\begin{bmatrix} \dfrac{-1}{\underline{X}(2,2)} & \dfrac{\left(\dfrac{\dfrac{1}{d_{12}}}{\dfrac{1}{d_{01}}+\dfrac{1}{d_{12}}+\dfrac{1}{d_{13}}}\right)}{\underline{X}(2,2)} & \dfrac{\left(\dfrac{\dfrac{1}{d_{13}}}{\dfrac{1}{d_{01}}+\dfrac{1}{d_{12}}+\dfrac{1}{d_{13}}}\right)}{\underline{X}(2,2)} & 0 \\ \dfrac{1}{\underline{X}(3,3)} & \dfrac{-1}{\underline{X}(3,3)} & 0 & 0 \\ \dfrac{\left(\dfrac{\dfrac{1}{d_{13}}}{\dfrac{1}{d_{13}}+\dfrac{1}{d_{23}}+\dfrac{1}{d_{34}}}\right)}{\underline{X}(4,4)} & \dfrac{\left(\dfrac{\dfrac{1}{d_{23}}}{\dfrac{1}{d_{13}}+\dfrac{1}{d_{23}}+\dfrac{1}{d_{34}}}\right)}{\underline{X}(4,4)} & \dfrac{-1}{\underline{X}(4,4)} & \dfrac{\left(\dfrac{\dfrac{1}{d_{34}}}{\dfrac{1}{d_{13}}+\dfrac{1}{d_{23}}+\dfrac{1}{d_{34}}}\right)}{\underline{X}(4,4)} \\ 0 & 0 & \dfrac{1}{\underline{X}(5,5)} & \dfrac{-1}{\underline{X}(5,5)} \end{bmatrix} \tag{3.4.48}$$

Assuming all the distances to be equal to the corresponding resistances and substituting the values, (3.4.48) becomes:

$$\underline{K}^{'}=\begin{bmatrix} -2 & 0.4615 & 0.6154 & 0 \\ 1 & -1 & 0 & 0 \\ 0.0898 & 0.2693 & -1.0323 & 0.6732 \\ 0 & 0 & 0.5079 & -0.5079 \end{bmatrix} \tag{3.4.49}$$

It is worth to note that all the rows, apart from the first row, corresponding to the node seeing the PCC as neighbour, sum to zero. Now that both $\underline{X}^{'}$ and $\underline{K}^{'}$ are known, the stability depends on the eigenvalues of the product, resulting:

$$\underline{K}^{'}\underline{X}^{'}=\begin{bmatrix} -0.4616 & 0 & 0 & 0 \\ 0 & -0.5 & -0.375 & -0.375 \\ 0 & 0 & -0.0673 & 0.6059 \\ 0.0355 & 0.0622 & 0.0689 & -0.4390 \end{bmatrix} \tag{3.4.50}$$

Corresponding to the eigenvalues $\lambda=[-0.0432\ -0.3857\ -0.4615\ -0.5774]$. Being all the eigenvalues λ_i with $\Re(\lambda_i)<0$, the closed loop MIMO system is stable. Despite the specific considered case, the result is of general value for a microgrid controlled with the Voltage Based Surround Control. If the system is stable in continuous time, the stability is guaranteed also with the distributed approach with Token ring.

3.4.2.5 Reactive current injection only

As already said in the previous chapters, the reported analysis investigates the distribution loss minimimization starting from un unconstrained problem, assuming the EGs in the microgrid to be able to inject all the required active and reactive current to reach the goal of loss minimization. In some practical applications, excluding the presence of energy storage, the only available current is

the reactive current. It is clear that in this new scenario, the steady state equilibrium point depends on the loads. Consider the case of a purely resistive cable: if all the loads were purely reactive, the voltage Based Surround control would converge to the same condition of a full injection, with all the voltages equal to the PCC. When also active loads are in the microgrid, the control can compensate only the drops due to the reactive loads, and therefore the voltages will depend on the active current flows. Referring to the clustered microgrid hypothesis, this means that the Voltage Based Surround control would converge to the voltages corresponding to the injection of the reactive part of the cluster optimum currents. This is the only possible stable point, where none of the controllers acts, and being the system stable this is also the convergence of the distributed algorithm. Referring the definitions of active and reactive to the PCC, this brief analysis can be summarized in Fig. 3.26 , where constant cable section is assumed, and therefore constant phase φ_{eq} of the impedance seen by each EG.

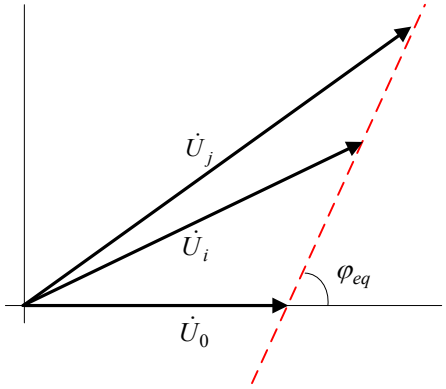

Fig. 3.26 Phasorial diagram for th steady state condition during reactive only injection from EGs

When all the voltage phasors of the EGs are in the position of Fig. 3.26 , the control action of the Voltage Based surround Control in each node N, $\Delta I_N^{opt} = \frac{\dot{U}_N^{opt} - \dot{U}_N^0}{\dot{Z}_N^{eq}}$ would require a real current injection, that is not available, stopping the algorithm.

3.4.2.6 EGs Saturations

As in the Current Based Surround Control, the main limitation to the optimum condition is represented by the EGs saturations, both in the case of full current injection and in the case of reactive only injection. When the converter at node N can't inject the required current variation ΔI_N^{opt}, the EG is saturated. The only possible action for the distribute controller is to transform the node from an active node to an equivalent load. A saturated node will receive the Token as the non saturated ones, but only to check if the saturation condition is changed. If it is still saturated, the Token is passed by without any action. When another node receives the Token, it will inquire the surrounding nodes. If one of those nodes is saturated, it will communicate its condition, and instead

of communicating its voltage to the active node, it will become a “bridge”, connecting the active node to the part of the saturated node neighbours that are not in common with the active node. Connecting means communicating voltages and distances (or line impedances). With this strategy, each node has to know only its neighbourhood, possibly becoming a bridge in case of saturation. The implementation of this saturation management is fundamental for the performances of the control. To give a comprehensive example, consider the simple microgrid in Fig. 3.27 :

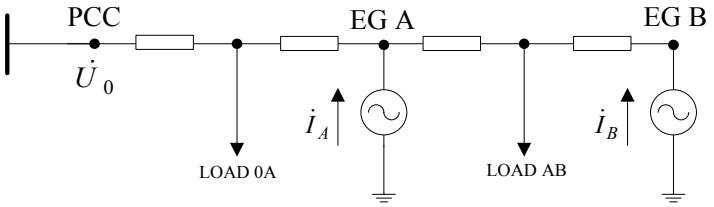

Fig. 3.27 Effect of EG current saturation

Assume EG A to have a very low power rating, and thus low current saturation levels, while EG A to have much higher current capability. This case reflects the topology used for the first simplified convergence analysis. Applying the distributed control, node B easily set to zero (in case of active and reactive injection) the voltage drop with respect to A, optimizing the cluster AB. But when node A controls , the current limit is too low and it can’t guarantee to set A voltage equal to the PCC. Therefore the cluster 0A is not optimized. Instead, bypassing the saturated node A, node B communicates with the PCC and sets its voltage equal to the PCC, guaranteeing global lower loss.

3.4.2.7 Implementation requirements

With this simplified analysis, the theoretical study of the distributed control is considered completed. Of course other studies should be done to investigate for example the convergence rate, but their analysis is left to future developments. To approach the conclusion of the Voltage Based Surround Control, some implementation issues are described in this section. In particular, the attention is focused on the basic architectural requirements in terms of measurement and communication. The main actions required to implement the distributed control are:

- Neighbourhood identification
- Bidirectional communication with the surround nodes
- Distance or impedance measurement, to calculate the optimum voltage (3.4.21)
- Total equivalent impedance, for (3.4.23)
- Synchronized voltage measurement

Among these, the equivalent impedance estimation is a local technique, that can be implemented using conventional techniques, correlating an injected current disturbance with the consequent voltage perturbation. The synchronized voltage measurement requires the embedding in each EG of a PMU, Phasor Measurement Unit, adopting a common time reference, tightly synchronized, to be able to exchange coherent phasors.

The other three points are strictly related with the communication architecture of the system. From the need for surround nodes identification follows that the communication channel has to coincide with the distribution cable. Therefore, only two options can be considered: a dedicated line, built in parallel to the distribution cable, or the use of the cable as communication channel through PLC, Power Line Communication. Based on the simple hypothesis that any action to modify the grid has to optimize the microgrid behaviour while minimizing the investment cost, the second option is the most realistic for a practical implementation. Some details on the PLC state of art and on distance measurement techniques will be presented in two dedicated sections at the end of this chapter. Given the communication standard and the distance measurement, or ranging technique, when a node N receives the Token, it can identify the neighbourhood. In particular:

- It broadcasts an inquiry via PLC and collects the addresses of all responding nodes (corresponding nodes), that will be the nodes located within a maximum distance from the active node.

- Then, according to a suitable ranging technique, it determines the distance from each corresponding node and sets up a distance table, which contains address and distance of each corresponding node. This is done for all the corresponding nodes, so that the output will be a squared distances matrix relating all the corresponding nodes and node N.

- If the microgrid has a tree topology, the neighbor nodes are finally identified by considering that they are the only nodes for which the direct path is shorter than any other connecting path.

- Instead, the more general case of meshed microgrids has to take into account the effect of multiple path propagation during the ranging, and more complex algorithms are required to extract the information. This study is left to future developments of the work.

3.4.2.8 Comment

As a final comment on the Voltage Based Surround Control, it is reminded that in the ideal condition of unconstrained current injection, the algorithm drives all the microgrid nodes to the PCC voltage. This is equivalent to minimum distribution loss, if the distribution cable section is constant,

i.e. the line impedance has constant phase, otherwise the condition is a sub-optimum. Therefore it can be observed that any other stable control, defining the current reference of the EGs based on the error between the node voltage and a weighted mean of the surrounding voltages, would converge to the same steady state. The contribution of this specific controller is the effort in defining the weights of the voltages with an orientation to local loss minimization. This is to try to minimize the duration of the loss minimization transient, and thus to save as much energy as possible during the transient.

3.4.3. Cooperative Distributed Control

3.4.3.1. Introduction

From the analysis of distributed solutions so far presented in the previous sections, it can be observed that the architectural requirements are strict, in terms of synchronization for phasors measurement, and identification of neighbour nodes. Moreover, the approaches are based on a number of hypotheses on the microgrid topology and cables section making the application involved when the possible use of the controllers and their performance have to be studied in a specific real case. For these reasons, in this last section a simplified approach will be introduced, independent on the microgrid topology. The basic idea is: the Token owner, i.e. the active EG, defines its current reference starting from the knowledge of the load currents, transmitted to the EG via PLC, and of the distances of these loads. The result is of course a sub-optimum loss, because the topology is neglected, but a loss reduction is guaranteed, being the loads fed mainly from the closer EG. The technique is named “Distributed Cooperative Control”.

3.4.3.2. Simplified approach to loss minimization

Considering a generic microgrid, each of the N_a load currents is divided among the N_p EGs, based on the absolute distance. Therefore, the quote of the $m-th$ load current demanded to the $n-th$ energy gateway is:

$$\dot{I}_m^n = \frac{\dot{I}_m}{d_m^n}\left(\sum_{i=0}^{Na}\frac{1}{d_m^i}\right)^{-1} \tag{3.4.51}$$

Where d_m^i is the distance of load m from EG i. Note that also the PCC is weighted in the sum, exactly like in the optimum current injection studied in section 3.4.1 the PCC participates with a quote of current to minimize the distribution loss. From (3.4.51) it is immediate to verify:

$$\sum_{n=0}^{Na}\dot{I}_m^n = \dot{I}_m \tag{3.4.52}$$

Consequently, the current injection demanded to the generic EG n is the sum of the fractions required by the different loads:

$$\dot{I}_p^n = \sum_{m=1}^{Np} \dot{I}_m^n \tag{3.4.53}$$

From these basic definitions follow that in grid connected operation the PCC voltage, corresponding to node 0, has to be included in the definition of the loads currents demands, while in islanded operation the node has to be excluded, being its current equal to zero. It is worth to remind that in islanded operation a backup generator is assumed to substitute the main grid voltage as voltage generator, but without injecting power into the microgrid. The loads balance is therefore demanded to the current controlled EGs.

The implementation is very simple: each load communicate with all the EGs, measuring the distances. Once it knows the distances, the load computes the fraction of current requested to each EG. Each fraction is finally sent to the EGs excluding the PCC, whose fraction is automatically absorbed once fixed the other current references. The control sequence is again managed with a Token Ring technique.

The resulting loss is in general different from the minimum loss condition. It is easy to verify that the Distributed Cooperative Control leads to minimum loss in case of a microgrid made by a single cluster in the form presented in the Current Based Surround Control, where for a single cluster between node A and B at the extremes and k distributed loads, results:

$$\begin{aligned} \dot{I}_{AB}^{opt} &= \frac{1}{d_{AB}} \sum_{k=0}^{K} \dot{I}_{Lk} d_{Bk} \\ \dot{I}_{BA}^{opt} &= \frac{1}{d_{AB}} \sum_{k=0}^{K} \dot{I}_{Lk} d_{Ak} \end{aligned} \tag{3.4.54}$$

Running the Cooperative Control, the current demanded to node A would be:

$$\dot{I}_{AB}^{coop} = \sum_{k=0}^{K} \dot{I}_{Lk} \frac{\frac{1}{d_{Ak}}}{\frac{1}{d_{Ak}} + \frac{1}{d_{Bk}}} = \sum_{k=0}^{K} \dot{I}_{Lk} \frac{\frac{1}{d_{Ak}}}{\frac{d_{Ak} + d_{Bk}}{d_{Ak} d_{Bk}}} = \sum_{k=0}^{K} \dot{I}_{Lk} \frac{d_{Bk}}{d_{AB}} \tag{3.4.55}$$

That corresponds exactly to equation (3.4.54). If the single cluster is extended to other clusters to form the clustered microgrid used for the Current Based Surround Control, the injection is no longer optimum, because each load should theoretically absorb current only from the EGs connected at the extremes of the cluster, while now a current request is sent also to the farer EGs. Nevertheless it is

intuitive that the latter portion of current is weighted by a larger distance, and thus with less effects on the loss. Therefore, at least in tree topologies, the Distributed Cooperative Control would reasonably approximate the optimum current injection. In a meshed topology the approximation similar, but the worsening of the loss results less straightforward. On the other hand, the principle of the injection of current as close as possible to the utilization point is in general a good behavioural approach for loss reduction.

It has to be reminded that in this distance-based approach the only hypothesis is the constant section of the distributed cables, to guarantee the proportional relation between distance and loss.

3.4.3.3. Saturations management

Despite the reduction of performances in terms of distribution loss, the Distributed Cooperative Control guarantees a much easier management of converters saturations, that in the other proposed approaches requires complex modifications to the communications between the nodes.

The idea is very simple: once an EG saturates, because the aggregation of currents demanded by the different loads is over its ratings, the EG communicates back to the loads that it is not able to provide their current demand, or the maximum available current. This communication is done starting from the farer nodes, until the total demand returns within the limits. The loads receiving this communication will recalculate the quotes of current demanded to the generators, taking into account the saturated node. In this way, iteration after iteration, the load current demand is properly shared among the generators, depending on distances and saturations.

Another consistent advantage of this technique is the possibility of avoiding the PMU (phasor measurement units): being the approach essentially a current feed forward as the Current Based Surround Control, each load m can calculate a power demand instead of a current demand, and send to the $n-th$ node, with $n \in [0, N_a]$ the conservative information represented by the complex power $\dot{S}_m^n = P_m^n + jQ_m^n$. Therefore, recalling that $\dot{S} = \dot{U}\dot{I}^*$, the generic load m will send to generator n the complex power reference:

$$\dot{S}_m^n = \dot{U}_m \left(\dot{I}_m^n\right)^* = \dot{U}_m \left(\frac{\dot{I}_m}{d_m^n} \left(\sum_{i=0}^{Na} \frac{1}{d_m^i} \right)^{-1} \right)^* \tag{3.4.56}$$

And generator n will inject the current:

$$\dot{I}_p^n = \left(\frac{\sum_{m=1}^{Np} \dot{S}_m^n}{\dot{U}_n} \right)^* \tag{3.4.57}$$

In the hypothesis of negligible voltage drop between the nodes, the current injection is closed to the result obtainable sending the complete current phasors information.

3.4.3.4. Discussion

This latter methods guarantees minimum architectural requirements: neither neighbourhood identification nor time synchronization are needed. Only distance measurements are required, together with transmission of constant power signals via PLC. The performances in terms of loss minimization are generally worse than the other techniques, but the expectation is an acceptable error, also considering the lower number of hypothesis behind the technique and the immediate management of the energy gateways saturations. In Chapter 4 a comparison between this techniques and the other two will be reported in different conditions, showing the good performances of the simplified approach.

3.4.4. Ranging techniques

The measurement of distances between nodes, required in all the proposed distributed controls, can be estimated by extending to PLC some methods used in wideband wireless standards, where several ranging techniques have recently been proposed. The most interesting approaches can be grouped in the following two categories.

- Signal strength based ranging

Received signal strength indication (RSSI) techniques are based on the rationale that there is a relation between distance and attenuation. RSSI methods have small computational complexity but are strongly affected by channel dynamics, which affect the accuracy of measurement even in presence of a large communication bandwidth.

- Time of arrival (TOA) based ranging

More accurate results can be obtained by time-domain techniques which take advantage of the large bandwidths available nowadays. The underlying basic idea is illustrated in Fig. 3.28 , showing a two-way handshaking where:

- Node A sends at time 0 a message to node B

- Node B receives the message at time T_B
- Node B sends a packet back to A after a known time T
- Node A receives the packet at time $T_A = 2T_B + T$.

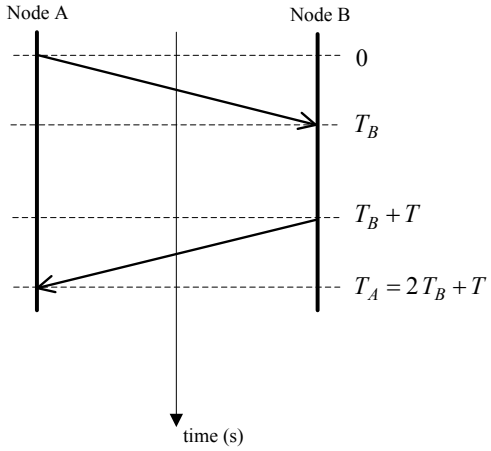

Fig. 3.28 Two way handshake for ranging

As T_B is related to the distance d_{AB} between A and B by the speed of light c, such distance can be derived as:

$$d_{AB} = c\,T_B = c\frac{T_A - T}{2} \tag{3.4.58}$$

Note that the above process requires a TOA estimate for the round trip time T_A. This method is highly accurate for wideband transmissions which provide high synchronization accuracy. The best performance is obtained with UWB systems (30 cm accuracy) [124, 125], for which the method is standardized in IEEE 802.15.4a.

Both RSSI and TOA techniques can be applied to distance measurements in smart microgrids. However the TOA approach is preferred because of the higher accuracy and robustness. The expected accuracy of TOA-based ranging in the context of state-of-the-art PLC standards and techniques is of some meters, confirming PLC as a viable candidate for ranging measurements. The proposed ranging methods are well known in wireless sensors networks, but nowadays there are no commercial devices able to implement the techniques in PLC. Nevertheless, considering the massive interest in PLC solutions for smart grids, it is reasonable to assume that these measurement units will be available in a relatively short time.

3.4.5. Power Line Communication

Considering the importance of PLC for the implementation of the three proposed distributed control algorithms, this section briefly resumes the main features of this communication technique, highlighting the limits and the performances. For any further specific detail, refer to the literature. In this analysis, the time synchronization of the phasors measurement units is assumed. This can be based on GPS signal, wireless broadcast time reference for the microgrid, or clock synchronization algorithms acting on the EGs within the microgrid [126, 127]. Therefore the specifications of the required communication channel only depend on the distributed loss minimization algorithms requirements. In the proposed techniques, the transmission of Token and measured signals for the distributed control can be slow, considering that loss minimization is achieved in steady state condition. On the other hand, a large bandwidth is needed to achieve accuracy in distance measurement with ranging techniques. Apart from the reduced investments due to the use of the power cable as communication channel, when an electrical distance has to be measured, PLC is the only possible choice. PLC standards can be divided in [94]:

- Ultra Narrow Band (UNB) PLC: The data rate is low, typically <100bps, transmitting in the Ultra Low Frequency band, between 0.3 and 3kHz. This technology is typically used for substation to meters bidirectional communication. In particular, the substation to meter communication is based on voltage disturbance, reversely the meter to substation transmission disturbs the current. Examples of UNB PLC are the RCS (Ripple Carrier System) used for load control, transmitting several bps with ASK modulation and the TWAC system, transmitting 60bps and able to cover distances over 150km. An extreme case is represented by the Turtle System, with few bits per hour but covering distances over 200km without regeneration.

- Narrow Band (NB) PLC: operating in the VLF/LF/MF bands, between 3 and 500kHz. Standards Cenelec A,B,C and D operate in the band 10-148.5kHz. The data rate ranges from few kbps for the standards ISO/IEC 14908-3 LonWorks, ISO/IEC14543-3-5 KNX, CEA-600.31 CEBus, IEC 61334-3-1, IEC 61334-5-1 to 0.1-1Mbps for ITU-T G.hnem, IEEE 1901.2. Other non standardized NB PLC systems are Insteon, X10, HomePlug C&C, ArianeControls, BacNet, PRIME and G3-PLC.

- Broad Band (BB) PLC: operates at HF/VHF frequencies, 1.8-250MHz, leading to bit rates between Mbps to 10^2 Mbps. Among the standardized systems there are TIA-1113, IEEE 1901, ITU-T G.hn with capability up to 200Mbps. Similar performances are achieved by non standardized solutions such as HomePlug 1.0, HomePlug AV (Extended), HD-PLC, UPA Powermax, and GigleMediaXtreme.

In general, the higher the bit rate, the lower the transmission range without regeneration. This is in contrast with the ideal behaviour required by distance measurement, that would need high accuracy, i.e. high bandwidth, and covered distance as large as possible. On the other hand, a low voltage microgrid rated for few hundreds of kVA is reasonably expected to have limited extensions, around few hundreds of meters, that are easily covered by NB and BB solutions. In the whole smart grid scenario, PLC is being applied at all the power system levels, from high voltage transmission to low and medium voltage distribution. At transmission levels, the power line is a good channel for communication, where long distances can be covered. Nowadays, few experiments are running in BB PLC over HV lines, especially for fault detection and protection. Similarly, in MV and LV distribution PLC can be efficiently used to upgrade the protection systems and to reduce the fault recovery procedures. Another application is the islanding detection capability of PLC, particularly relevant in smart microgrids. Moreover PLC is the basis of any other ancillary service provided within the microgrid, such as loss minimization, load control, demand response. When using PLC in distribution systems, one of the issues is related with transformers: UNB PLC is able to pass through transformers, while NB and BB require dedicated devices to be able to bypass the transformers. As a matter of facts, BB PLC is seen as an in-home PLC technique, not suitable for application in the distribution grid, where NB is preferred for the less attenuation and therefore the higher coverage. On the other hand the required bit rate for smart grids and smart microgrids applications will most probably rise soon, requiring the technology to approach the bit rates currently available with BB PLC. Nowadays an established and standardized PLC technology is still far to come, even if the scientific and industrial community is investing in PLC development.

Chapter 4

Simulation Results - Loss Minimization

4.1. Introduction

In this chapter, the proposed distributed loss minimization techniques will be tested in simulation. Due to the unconventional approach to the low voltage microgrid control, the simulation software has been completely developed for this work in Matlab environment. The adopted approach is simplified but guarantees a reasonable approximation of the real microgrid while keeping the flexibility required for developing the distributed control solutions. The microgrid has been simulated using a phasorial representation, and therefore assuming all the currents and voltages to be sinusoidal and with the same frequency. The advantage of this steady state approach is a shorter simulation time, the main disadvantage is that none of the distributed generators control loops can be modeled. A current controlled distributed generator is in this representation an ideal current source. When, during the optimization algorithms, the current references are modified, the resulting behavior in time domain is a sequence of steady states, that neglects all the local dynamics. In the future development of the work related with the implementation of the algorithm in a laboratory scale microgrid, the complete control system will be modeled and simulated. For now, the phasorial representation is a simple tool to test and validate the distributed controllers.

From a network point of view, the simulated microgrid is here considered as a single phase belonging to a balanced three-phase low voltage system, so that only the loss in the phase cable is considered, being the neutral current equal to zero. Therefore, when defining the microgrid load and loss, they will be one third of the whole system. The power cable is modeled with its series equivalent impedance, using the specifications in [121]. The loads are modeled as the series between a resistor and an inductor. The model is different from the constant current sources used in the theoretical analysis, but is more suitable for representing real loads. On the other hand, if the line voltage can be considered constant, the two models are equivalent in a large signals phasorial representation. All the distributed generators are constant currents sources. The reference for the phasors has been chosen to be the PCC voltage, assumed to be unique (single substation feeding the microgrid) and on the real axis of the complex plane. As already introduced in Chapter 2, if the

voltage drop along the power line can be considered negligible, the real part of the generators currents can be associated with the active power, and therefore it is named active current, and the imaginary part is the reactive current. In the real implementation, active and reactive currents will be determined by local voltage measurements. Of course the voltage drop is negligible in terms of the impact on the active and reactive components of the currents, but is not neglected in the analysis, being the Voltage Based Surround Control developed on the voltage measurement and variation. To simplify the approach, the simulated microgrid has the form of a "clustered" microgrid, made of the repetition of modular blocks, the T-quadripoles line-load-line. If a "clustered" microgrid is used, as assumed in part of Chapter 3, at both the ends of each cluster a generator will be connected, leading to the most simplified microgrid topology. In a more general case, the ports of the quadripoles will be simply connected to other ports, for example to form a series of distributed loads, or a grid ramification.

From a control point of view, in the developed software each node has access to the required information for the specific implemented control (Plug and Play, Voltage Based Surround, Current Based Surround, Cooperative). Moreover a Token is defined as the authorization of executing the control action. At a specified time instant, only one of the generators in the microgrid owns the Token. This is not an absolute requirement, but at this stage of the research it is considered reasonable to separate the different control phases. Once the Token owner has executed its control, it modifies the field of the Token containing the recipient, writing the address of the next token owner, and sends the new message. The next recipient is chosen among the neighbors of the actual owner, selecting the node that in the past has owned the Token for the lower number of times. For this purpose, each generator will maintain a counter of the control actions already taken. The Token is initially owned by the PCC. In fact, the PCC is a fundamental node of the microgrid, managing all the power exchanges with the main grid. Therefore it is reasonable to assume that the Token will start from there. Moreover, the PCC will be the master of the Token communication, supervising the Token state and managing the errors such as lost or corrupted Token. In this work no further details have been considered about the Token communication. Of course a complete protocol should be defined, also taking into account all the possible critic aspects, such as for instance the fault of the master, to guarantee the prosecution of the control action. In the simulations, the time is measured in terms of "Token iterations". This because the simulation is a sequence of steady states, and the time interval required between a control action and the other is the time taken by the current control and network dynamics to reach the new steady state after a generator current reference variation. Neglecting these dynamics it makes no sense to define now a duration, that will be reasonably in the order of few line cycles, but will be determined only in a more detailed model.

The next sections are organized as follows: first, the simulation software will be briefly described, without lingering on the details of the functions, but presenting the overall approach; then the microgrid used as testbench will be introduced; finally, the simulation results for the four control techniques, i.e. Plug and Play, Current Based Surround Control, Voltage Based Surround Control and Cooperative control will be presented. The loss minimization techniques will be compared in three different microgrid configurations, described later, and in three operative conditions of the distributed Energy Gateways: ideal active and reactive current injection (unconstrained optimization), active and reactive current injection limited by the power ratings, reactive current only, limited by the power ratings. For all the cases, the correspondent theoretical minimum loss will be used as a reference to validate the effectiveness of the proposed algorithms.

4.2.Simulation Software

The proposed simulation software consists of a set of Matlab functions, written in Matlab programming language, building a set of matrices describing the microgrid and solving the resulting linear system in different operative conditions, i.e. with different current references injected by distributed generators. The global inputs are the microgrid topology and its parameters, the outputs are all the voltages and currents of the network, and any other required function of these variables, for example the distribution loss. The software has been developed to offer an intuitive and simplified approach to the analysis of distributed control strategies for smart microgrids, with a number of distributed generators interfaced with the main grid through power converters with communication capabilities, the Energy Gateways. The problem of simulating grids with a large number of Energy Gateways and different types of loads is in general a complex problem, traditionally solved with the power flow equations, ending up in a non linear system that is numerically solved. The complexity can be widely reduced accepting some approximations and setting some constraints in the grid topology, finally obtaining a linear system.

The basic approach followed in the development of this Matlab software has been to define a “grid quantum”, assumed to be a T-quadripole, and to build up the grid connecting the single quadripoles as described in a set of simple source files containing the information about connections and grid parameters. With this approach, the structure of the matrices required to solve the grid results perhaps non optimized, but more intuitive because of its modularity. The T-quadripole offers a generalized approach for describing the grid, as reported in the next paragraphs. Also the assumed hypothesis and approximations are described hereafter. Fig. 4.1 reports the basic scheme of the considered quadripole:

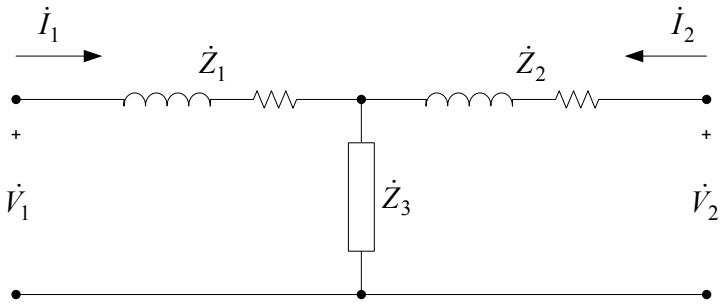

Fig. 4.1 microgrid basic element

The figure represents a generic portion of the microgrid, connecting port 1 (left side in figure) and port 2 (right side). Ports 1 and 2 are identified as "nodes" in the prosecution of this analysis. The only difference is that a node is generally made by a number of ports greater or equal than one, for the connection to the other quadripoles forming the grid. Also the connection point of the load within a quadripole is technically speaking a node, but in this software it is assumed that nodes are only the accessible points of the quadripoles, i.e. where a current or voltage generator can be placed. Impedance $\dot{Z}_3$ is the load, while $\dot{Z}_1$ and $\dot{Z}_2$ are the models of distribution cables between node 1 and 2. It is worth to observe that with such a structure, any topology of interest can be implemented between node 1 and 2: for example the load can become an open circuit, transforming the quadripole in a pure connection, or setting to zero $\dot{Z}_1$ or $\dot{Z}_2$ the load can be placed directly at node 1 or 2, or finally node 1 and 2 could be collapsed in a single node with a load, of course obtaining in the latter case a redundant representation. The portion of network represented by Fig. 4.1 has been model with Y parameters. Therefore the equations of the model are:

$$\begin{cases} \dot{I}_1 = \dot{y}_{11}\dot{V}_1 + \dot{y}_{12}\dot{V}_2 \\ \dot{I}_2 = \dot{y}_{21}\dot{V}_1 + \dot{y}_{22}\dot{V}_2 \end{cases} \tag{4.1}$$

That can be rewritten in a compact form as:

$$I = MV \tag{4.2}$$

Or in the homogeneous form:

$$MV - I = 0 \tag{4.3}$$

Where

$$V = \begin{bmatrix} \dot{V}_1 \\ \dot{V}_2 \end{bmatrix} \quad I = \begin{bmatrix} \dot{I}_1 \\ \dot{I}_2 \end{bmatrix} \quad M = \begin{bmatrix} \dot{y}_{11} & \dot{y}_{12} \\ \dot{y}_{21} & \dot{y}_{22} \end{bmatrix} \tag{4.4}$$

The values of y_{ij} can be easily found applying the superposition of effects in the model, the derivation is omitted for simplicity.

The Y-Parameters representation is used to build up the linear system required to solve the grid, i.e. to obtain al the complex voltages and currents of all the quadripoles. The main idea is first to define the desired microgrid, obtained connecting N quadripoles. Therefore, the unknown in the system will be $4N$, represented by the voltages and currents at the port of each quadripole. Of course there is a redundant information, for example the ports connected together could have just a single unknown, represented by the common voltage. On the other hand the used approach is not optimized in terms of matrices dimensions and computation efficiency, but the global complexity remains very low, considered the basic calculations required to solve a linear system. Nevertheless, representing the grid as a sum of basic quadripole blocks is helpful to give a clearer structure to the grid solver and to the functions required to control the smart microgrid. All the unknowns have been grouped in a single column vector, where the first half contains the port voltages pairs, the second half the correspondent port currents. The order of appearance depends on how the microgrid has been described in the source files. The final goal is to obtain a linear system in the form $Ax = b$, where x is the $4Nx1$ unknowns column vector, A is the $4Nx4N$ system matrix and b the $4Nx1$ input vector. With the quadripoles equations (4.3), only $2N$ equations can be built. Moreover these $2N$ equations are homogeneous for construction. The remaining $2N$ equations come from the connections and the inputs definition. In particular, part of them (the number depends on the microgrid specific topology, anyway the software automatically identifies the required equations) are still homogeneous equations, describing the connection between couples of quadripoles. The remaining equations will be derived from the inputs, represented either by nodes voltages or injected currents. In this work, only one node, the PCC, is defined as voltage source, while all the other nodes are current sources. At the end matrix A will have full rank, and for a given set of inputs a solution of the network is found solving the linear system.

To summarize, the main hypotheses on which the software is based are:

- The microgrid has been previously modelled as connections of quadripoles
- The loads are RL impedances, while the generators are either current or voltage sources, therefore the network is linear. Constant current loads can be modelled as negative generators, while constant power loads or generator cannot be modelled.
- The line is represented with a concentrated parameters model, taking into account only the series resistance and the series inductance (parallel capacitance is neglected).

- The simulations are carried out in the phasorial domain, hence the calculated voltages and currents of the quadripoles are steady state values, referred to the PCC voltage, assumed to be real. The only information of time is related with the evolution of the steady state voltages and currents when the control slot changes, i.e. one of the energy gateways changes its current reference.

In the next paragraphs, the description of the three main routines is reported, with

- **NET_BUILD:**

Builds the first part of the linear system required to solve the grid, i.e. to find out voltages and current of all the quadripoles. These first equations come from the interpretation of the source files *rete.txt*, *gen.txt* and *Z.txt*, and are the part of the system independent on the generators status at the nodes, relying only on grid topology.

- **NET_SOLVER**

Adds to the partial matrices the equations related with the possible current and voltage generators connected to the quadripoles terminals. The assumed model is a generalized generator, that is a parallel between a voltage and a current generator, with complementary enable signals (If a generator is set as voltage source, the possible current reference is ignored). The current generator is off when its current is zero, the voltage generator is off when its voltage is labelled as "undef", being the voltage a variable imposed by the rest of the grid, and therefore still an unknown at this stage. The outputs of the function NET_SOLVER are the voltages and currents of the whole grid. Actually, NET_SOLVER is a nested function, always contained in RUN_SOLVER, that prepares the remaining parts of matrix A starting from the information about the inputs, i.e. the generators status (V or I source) and value.

- **RUN_SOLVER**

This function called to solve the grid. It receives the voltage controlled nodes (normally only the PCC) and their voltage reference, plus the vector of the current references for the remaining current controlled sources. The latter vector is $Nx1$ long and the current references contained in positions corresponding to nodes operating as voltage sources are ignored by the control. The output is a column vector VI, containing in the first half the voltages at the ports of each quadripole, and in the second half the currents with the same convention.

Beyond these main routines, a number of other functions has been developed to meet all the requirements of distributed controls implementation.

4.3. Microgrid Testbenches

To validate the proposed loss minimization algorithms and to compare the different solutions, a realistic even if approximated microgrid testbench has been defined. The goal is to recreate a residential settlement with a limited number of loads and generators. There are three load types, representing small houses, consuming 2.5 kW, larger houses with 5kW and workshops consuming 10kW and two possible energy gateways interfacing distributed energy sources: 3kW with converter rated for 5kVA and 10kW with converter rated for 15kVA, installed in residential buildings and workshops respectively. Cables are low voltage distribution cables with useful section $S = 240mm^2$, assumed to be constant in all the microgrid.

The microgrid has been analyzed in two configurations. The first is a radial network, with total length of the conductors equal to $1.8km$, total load equal to $P_{RL} = 52.5kW$ and power factor $\cos\varphi_{RL} = 0.857$, divided among nine loads. The total distributed generation is $P_{RG} = 55kW$ and maximum power factor at the rated power equal to $\cos\varphi_{RG} = 0.6476$. It is worth to note that being all the generators fully controllable, neglecting for now any energetic constraint i.e. photovoltaic power that has to be injected in the grid, the power factor of the injected power is actually arbitrary, within the maximum total rating of $S_{RG} = 85kVA$. The second configuration is a modification of the first, with the addition of another load, forming a mesh in the microgrid. The total extension becomes $2.2km$ in this second case. The total load is now $P_{ML} = 62.5kW$ with $\cos\varphi_{ML} = 0.848$, made by ten distributed loads, while the generation set remains the same. The test of a meshed microgrid has been added to complete the analysis, even if a low voltage distribution system is typically radial. On the other hand, specific requirements could ask for a double feeding of some critic loads, that have to be inserted in a mesh. It is worth to remind that in this case the traditional cascaded protections of the grid has to be modified for the meshed part. The loading and generation conditions, the selection of the cable and the corresponding geographic distances are believed to represent a realistic case of residential low voltage microgrid. The design has been done to guarantee in any node a voltage drop <5% of the PCC voltage, and nominal currents in each bus within the limits indicated in [121] for the chosen cable. This details will be presented in the next two subsections, where the configurations will be presented and analyzed. First, the case of nominal currents and voltages without generation is considered, showing the initial loss condition. Then the optimum current injection from the distributed energy gateways that guarantees minimum loss is analytically derived using the equations in Chapter 2.

4.3.1. Radial microgrid testbench

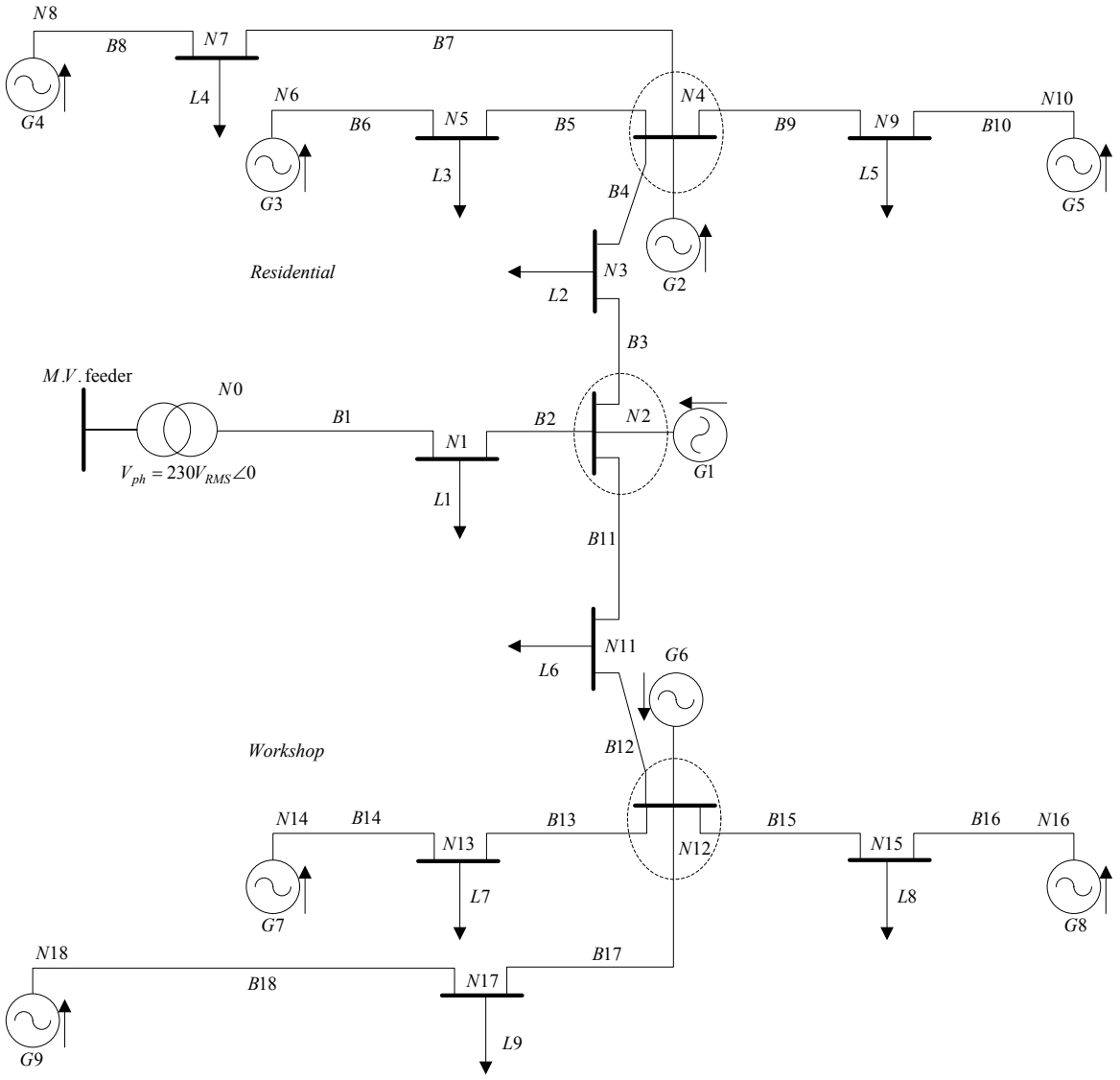

Fig. 4.2 Radial microgrid testbench

Fig. 4.2 reports the first configuration of the microgrid testbed. The system is a 18-bus low voltage distribution network, with nine distributed generators and nine loads. Table 4.1 ,Table 4.2 and Table 4.3 summarize the relevant information about the microgrid. It is worth to note that the loads are assumed to be series of resistors and inductors. In the theoretical loss analysis shown in Chapter 2, the loads are assumed to be constant current sources. Therefore, a first approximation is made, assuming the loads here to be constant sources absorbing the current correspondent to the nominal voltage. In the matched simulation that will be shown later on testing the minimization techniques, the loads will be modelled as RL, and therefore the resulting loss will be slightly lower than the theoretical one, due to the line voltage drop caused by loads absorbing a lagging current over the line cables.

Bus	Length (m)	Impedance (Ω) r=0.08Ω/km l=255μH/km
B1	100	(8+j8)e-3
B2	50	(4+j4) e-3
B3	50	(4+j4) e-3
B4	50	(4+j4) e-3
B5	100	(8+j8)e-3
B6	100	(8+j8)e-3
B7	200	(16+j16) e-3
B8	100	(8+j8)e-3
B9	100	(8+j8)e-3
B10	100	(8+j8)e-3
B11	100	(8+j8)e-3
B12	50	(4+j4) e-3
B13	100	(8+j8) e-3
B14	100	(8+j8) e-3
B15	100	(8+j8) e-3
B16	100	(8+j8) e-3
B17	100	(8+j8) e-3
B18	200	(16+j16)e-3

Table 4.1 bus lengths and impedances – radial microgrid

Load Z=R+jωL	R(Ω)	L(mH)	Power @ $230V_{RMS}$
L1	8.76	12.7	5kW cosφ=0.91
L2	8.76	12.7	5kW cosφ=0.91
L3	19.5	18.1	2.5kW cosφ=0.96
L4	19.5	18.1	2.5kW cosφ=0.96
L5	19.5	18.1	2.5kW cosφ=0.96
L6	8.76	12.7	5kW cosφ=0.91
L7	3.39	8.1	10kW cosφ=0.80
L8	3.39	8.1	10kW cosφ=0.80
L9	3.39	8.1	10kW cosφ=0.80

Table 4.2 Load resistances and inductances, and corresponding power at the nominal voltage – radial microgrid

Distributed Generator (Energy Gateway)	P_{MAX}(kW)	S_{MAX}(kVA)
G1	3	5
G2	3	5
G3	3	5
G4	3	5
G5	3	5
G6	10	15
G7	10	15
G8	10	15
G9	10	15

Table 4.3 distributed generators active and absolute power ratings – radial microgrid

4.3.1.1. Theoretical loss analysis

The goal of this section is to analytically find the initial loss in the microgrid when all the distributed generators are off, and then to derive the optimum set of injected currents that minimizes the loss, finding the correspondent loss value. This ideal optimum condition will be used to validate the loss minimization algorithms. Moreover, being this analysis completely independent on the developed simulation software, it is useful also as a testbench for the correctness of the developed software (within the approximation made here assuming constant current sources). All the following considerations are based on the analysis made in Chapter 2. Being the number of buses relatively large for an explicit calculation, the matrices of the microgrid will be omitted, reporting only the two relevant ones, that are the incidence matrix A_R and the bus resistances matrix R_R. In the construction of A_R, the branches have been oriented in the direction from the node with lower label to the node with higher label number. The result is reported in (4.5) , where the rows represent the branches, numbered as in Fig. 4.2 , and the columns represent the nodes, with the same ordering convention. The result is an $18x18$ matrix. Matrix R_R has the same dimensions, is diagonal.

An important observation is that with the specific choice of labels in Fig. 4.2 , the column vector of node currents (loads and generators) results to be the alternation of a load and a generator, as reported in (4.7), where only the first two elements are shown. The currents $\dot{I}_{L_i}$ and $\dot{I}_{G_i}$ are considered with the convention of Fig. 4.2 , and that is why the sign is changed for the generator currents, because all the developed theoretical analysis assumes absorbed currents both in the loads and in the generators nodes.

$$A_R = \begin{bmatrix}
1 & 0 & 0 & 0 & 0 & 0 & 0 & 0 & 0 & 0 & 0 & 0 & 0 & 0 & 0 & 0 & 0 & 0 \\
-1 & 1 & 0 & 0 & 0 & 0 & 0 & 0 & 0 & 0 & 0 & 0 & 0 & 0 & 0 & 0 & 0 & 0 \\
0 & -1 & 1 & 0 & 0 & 0 & 0 & 0 & 0 & 0 & 0 & 0 & 0 & 0 & 0 & 0 & 0 & 0 \\
0 & 0 & -1 & 1 & 0 & 0 & 0 & 0 & 0 & 0 & 0 & 0 & 0 & 0 & 0 & 0 & 0 & 0 \\
0 & 0 & 0 & -1 & 1 & 0 & 0 & 0 & 0 & 0 & 0 & 0 & 0 & 0 & 0 & 0 & 0 & 0 \\
0 & 0 & 0 & 0 & -1 & 1 & 0 & 0 & 0 & 0 & 0 & 0 & 0 & 0 & 0 & 0 & 0 & 0 \\
0 & 0 & 0 & -1 & 0 & 0 & 1 & 0 & 0 & 0 & 0 & 0 & 0 & 0 & 0 & 0 & 0 & 0 \\
0 & 0 & 0 & 0 & 0 & 0 & -1 & 1 & 0 & 0 & 0 & 0 & 0 & 0 & 0 & 0 & 0 & 0 \\
0 & 0 & 0 & -1 & 0 & 0 & 0 & 0 & 1 & 0 & 0 & 0 & 0 & 0 & 0 & 0 & 0 & 0 \\
0 & 0 & 0 & 0 & 0 & 0 & 0 & 0 & -1 & 1 & 0 & 0 & 0 & 0 & 0 & 0 & 0 & 0 \\
0 & -1 & 0 & 0 & 0 & 0 & 0 & 0 & 0 & 0 & 1 & 0 & 0 & 0 & 0 & 0 & 0 & 0 \\
0 & 0 & 0 & 0 & 0 & 0 & 0 & 0 & 0 & 0 & -1 & 1 & 0 & 0 & 0 & 0 & 0 & 0 \\
0 & 0 & 0 & 0 & 0 & 0 & 0 & 0 & 0 & 0 & 0 & -1 & 1 & 0 & 0 & 0 & 0 & 0 \\
0 & 0 & 0 & 0 & 0 & 0 & 0 & 0 & 0 & 0 & 0 & 0 & -1 & 1 & 0 & 0 & 0 & 0 \\
0 & 0 & 0 & 0 & 0 & 0 & 0 & 0 & 0 & 0 & 0 & -1 & 0 & 0 & 1 & 0 & 0 & 0 \\
0 & 0 & 0 & 0 & 0 & 0 & 0 & 0 & 0 & 0 & 0 & 0 & 0 & 0 & -1 & 1 & 0 & 0 \\
0 & 0 & 0 & 0 & 0 & 0 & 0 & 0 & 0 & 0 & 0 & -1 & 0 & 0 & 0 & 0 & 1 & 0 \\
0 & 0 & 0 & 0 & 0 & 0 & 0 & 0 & 0 & 0 & 0 & 0 & 0 & 0 & 0 & 0 & -1 & 1
\end{bmatrix} \tag{4.5}$$

$$R_R = \begin{bmatrix}
8 & 0 & 0 & 0 & 0 & 0 & 0 & 0 & 0 & 0 & 0 & 0 & 0 & 0 & 0 & 0 & 0 & 0 \\
0 & 4 & 0 & 0 & 0 & 0 & 0 & 0 & 0 & 0 & 0 & 0 & 0 & 0 & 0 & 0 & 0 & 0 \\
0 & 0 & 4 & 0 & 0 & 0 & 0 & 0 & 0 & 0 & 0 & 0 & 0 & 0 & 0 & 0 & 0 & 0 \\
0 & 0 & 0 & 4 & 0 & 0 & 0 & 0 & 0 & 0 & 0 & 0 & 0 & 0 & 0 & 0 & 0 & 0 \\
0 & 0 & 0 & 0 & 8 & 0 & 0 & 0 & 0 & 0 & 0 & 0 & 0 & 0 & 0 & 0 & 0 & 0 \\
0 & 0 & 0 & 0 & 0 & 8 & 0 & 0 & 0 & 0 & 0 & 0 & 0 & 0 & 0 & 0 & 0 & 0 \\
0 & 0 & 0 & 0 & 0 & 0 & 16 & 0 & 0 & 0 & 0 & 0 & 0 & 0 & 0 & 0 & 0 & 0 \\
0 & 0 & 0 & 0 & 0 & 0 & 0 & 8 & 0 & 0 & 0 & 0 & 0 & 0 & 0 & 0 & 0 & 0 \\
0 & 0 & 0 & 0 & 0 & 0 & 0 & 0 & 8 & 0 & 0 & 0 & 0 & 0 & 0 & 0 & 0 & 0 \\
0 & 0 & 0 & 0 & 0 & 0 & 0 & 0 & 0 & 8 & 0 & 0 & 0 & 0 & 0 & 0 & 0 & 0 \\
0 & 0 & 0 & 0 & 0 & 0 & 0 & 0 & 0 & 0 & 8 & 0 & 0 & 0 & 0 & 0 & 0 & 0 \\
0 & 0 & 0 & 0 & 0 & 0 & 0 & 0 & 0 & 0 & 0 & 4 & 0 & 0 & 0 & 0 & 0 & 0 \\
0 & 0 & 0 & 0 & 0 & 0 & 0 & 0 & 0 & 0 & 0 & 0 & 8 & 0 & 0 & 0 & 0 & 0 \\
0 & 0 & 0 & 0 & 0 & 0 & 0 & 0 & 0 & 0 & 0 & 0 & 0 & 8 & 0 & 0 & 0 & 0 \\
0 & 0 & 0 & 0 & 0 & 0 & 0 & 0 & 0 & 0 & 0 & 0 & 0 & 0 & 8 & 0 & 0 & 0 \\
0 & 0 & 0 & 0 & 0 & 0 & 0 & 0 & 0 & 0 & 0 & 0 & 0 & 0 & 0 & 8 & 0 & 0 \\
0 & 0 & 0 & 0 & 0 & 0 & 0 & 0 & 0 & 0 & 0 & 0 & 0 & 0 & 0 & 0 & 8 & 0 \\
0 & 0 & 0 & 0 & 0 & 0 & 0 & 0 & 0 & 0 & 0 & 0 & 0 & 0 & 0 & 0 & 0 & 16
\end{bmatrix} 10^{-3}(\Omega) \tag{4.6}$$

$$\underline{\dot{I}} = \begin{bmatrix} \dot{I}_{L_1} & -\dot{I}_{G_1} & \dot{I}_{L_2} & -\dot{I}_{G_2} \ldots \end{bmatrix}^T \tag{4.7}$$

The resulting initial loss, when all the generators are switched off:

$$P_{R_{\max}} = 1.277\text{kW} \tag{4.8}$$

Searching for the minimum loss condition, the generators injected currents set corresponding to minimum loss is:

$$\underline{\dot{I}}_{R_{Ga}}^{opt} = \begin{bmatrix} 32.6174-14.8559\text{j} \\ 25.3664-9.1785\text{j} \\ 5.4352-1.5849\text{j} \\ 7.2470-2.1133\text{j} \\ 5.4352-1.5849\text{j} \\ 86.8214-60.8929\text{j} \\ 21.6975-16.2871\text{j} \\ 21.6975-16.2871\text{j} \\ 14.4650-10.8581\text{j} \end{bmatrix} (A) \tag{4.9}$$

Where the reference for the phasorial representation is the PCC voltage (node $N0$ in Fig. 4.2), assumed to be purely real. The corresponding minimum distribution loss are:

$$P_{R_{\min}} = 45.15\text{W} \tag{4.10}$$

This result is achieved assuming to control both the active and reactive part of the injected currents, without constraints. It is now interesting to observe the achievable performances limiting the injection to reactive currents only, while keeping the unconstrained injection. Recalling the derivation of the optimum current set, it can be shown that active and reactive currents can be optimized separately, due to the orthogonality of the components. The active part of the optimum current considers only the active part of load currents, and reversely for the reactive. Therefore the optimum current set in case of reactive only injection corresponds to (4.9) where the all the real parts are set to zero. The resulting minimum loss is:

$$P_{R_{\min}}^{react} = 918.7\text{W} \tag{4.11}$$

While the full optimum current injection reduces the loss to the 3.5% of the initial loss, the reactive only injection reduces the loss to the 71.95% of the initial value. Therefore 96.5% of loss reduction versus 28.05% of loss reduction. The origin of these numbers can be analyzed from a qualitative point of view observing that a load with a $\cos\varphi = 0.80$ has a ratio between active and reactive current equal to $\kappa = \tan(\cos^{-1}(\varphi)) = 0.75$. Therefore, in the same resistor, the percentage of loss due to the active current will be (remembering the orthogonality) $\nu_a = \frac{1}{1^2 + 0.75^2} = 64\%$, while the reactive current contributes with $\nu_a = \frac{0.75^2}{1^2 + 0.75^2} = 36\%$. Therefore, the resulting numbers are coherent with the considered microgrid.

4.3.1.2. Initial State Simulation

In this section, the radial microgrid is simulated with the developed software. The initial loss will be shown, together with the node voltages and branch currents, to verify their position with respect to the maximum allowable values. The same simulation is then carried out applying the optimum currents to the generators. Being the microgrid a "clustered microgrid", as defined in Chapter 3, the minimum loss corresponds to all the generators at the same voltage, equal to the PCC voltage. Therefore, the voltage seen by the load impedances will be approximately equal to the nominal value, and the resulting loss are the same obtained minimizing in the assumption of loads modelled as current sources. Reversely, in the initial condition, with all the generators switched off, the simulated loss are lower, due to the lower power absorbed by the load impedances under the line voltage drop. The resulting initial loss are:

$$P_{R_{MAX},sim} = 1.202k\text{W} \tag{4.12}$$

The difference of $75W$ with respect to (4.8) is justified by the load voltage drops, whose RMS values, in per unit with respect to the PCC voltage $V_{ph} = 230V_{RMS}$, and phases are reported in Fig. 4.3 and Fig. 4.4 respectively:

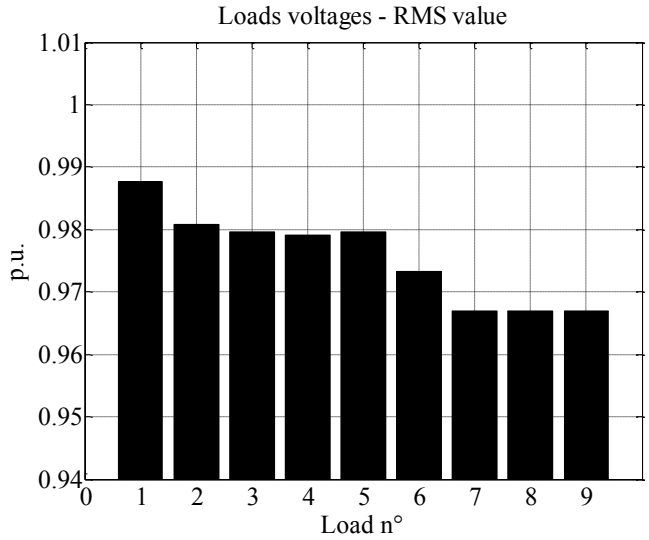

Fig. 4.3 RMS values of the initial voltages on loads $L_1..L_9$ - radial testbench

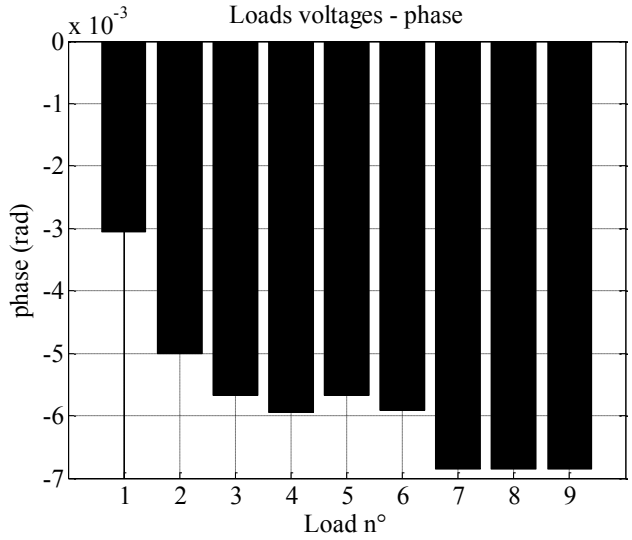

Fig. 4.4 Phases of the initial voltages on loads $L_1 \ldots L_9$ - radial testbench

Similarly, Fig. 4.5 and Fig. 4.6 report the RMS value in p.u. and the phase of the voltages at the generators nodes. In the figures, the generator number 0 is the PCC.

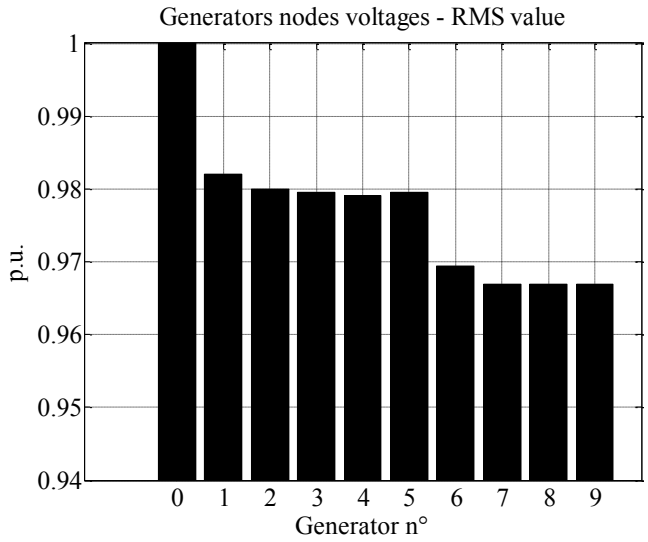

Fig. 4.5 RMS values of the initial voltages on generators $G_1 \ldots G_9$ -radial testbench

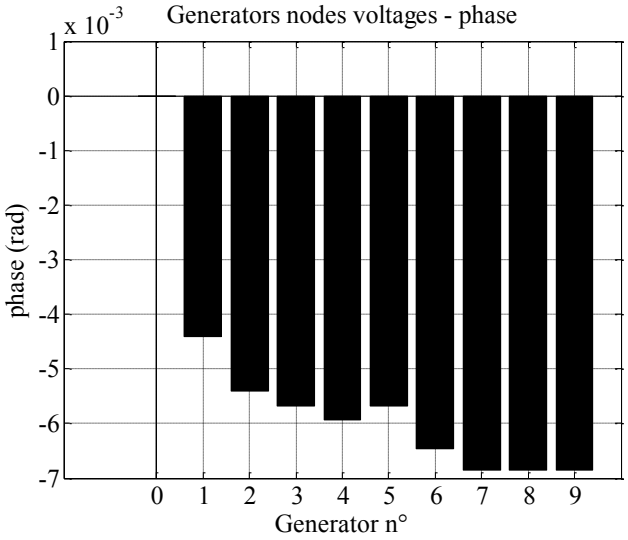

Fig. 4.6 Phases of the initial voltages on generators $G_1 \ldots G_9$ - radial testbench

From the figures it is confirmed that all the RMS voltages in the microgrid are within the maximum allowed drop of 5%. The next two figures, Fig.4.7 and Fig. 4.8 , reports the RMS values and phases of the bus currents. The currents are identified with the labels Bij , with the meaning that the current is exiting the node corresponding to G_i in Fig. 4.2 , and is directed toward G_j . "0" refers to the PCC. This notation comes from the modular structure of the developed simulation routines.

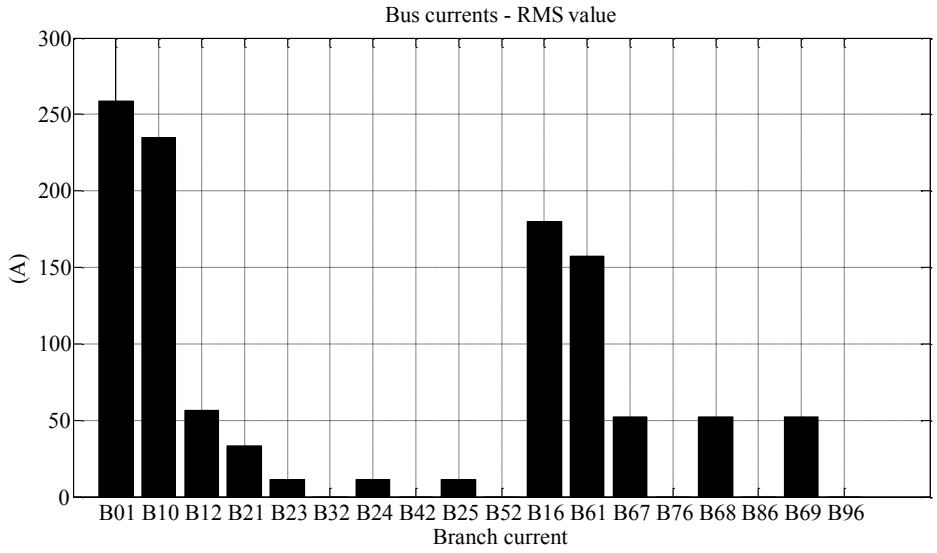

Fig.4.7 Initial bus RMS currents – radial testbench

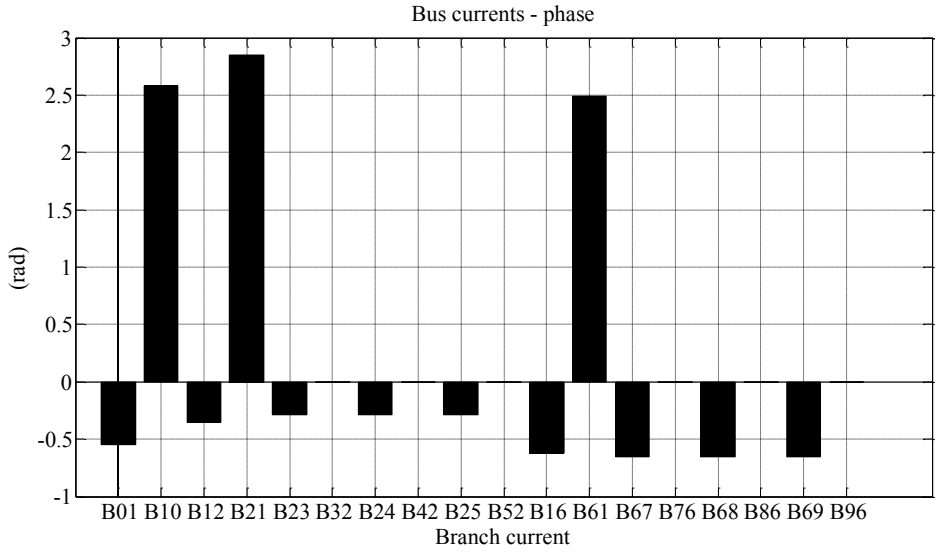

Fig. 4.8 Initial bus currents phase – radial testbench

Without any support from distributed generation, the first bus, connecting the PCC to the first load L_1 has the highest current stress, equal to $I_{MAX} = 258.5\text{A}_{\text{RMS}}$. This current corresponds to a current density $d = 1.07\frac{\text{A}}{\text{mm}^2}$, still far from the limits in [121].

4.3.1.3. Optimum State Simulation

In the previous section the microgrid design has been validated, deriving the initial loss, voltages and currents in the radial microgrid with all the generators switched off. The same simulation is now carried out turning on the generators and assigning their optimum injected currents references calculated in (4.9). In this second case the loss is minimized and results:

$$P_{R_{\min},sim} = 45\text{W} \tag{4.13}$$

The resulting loss corresponds to (4.10) with minimum error. In fact the error due to the presence of loads impedances instead of current generators is minimized because the optimum current injection corresponds to have all the generators voltages at the same value. The voltage drop at loads connection points is limited to the effect of loads currents in the local line impedances between the loads and the nearest generators. This can be appreciated in Fig. 4.9 and Fig. 4.10 reporting generators and loads p.u. voltages respectively in the optimum current injection condition:

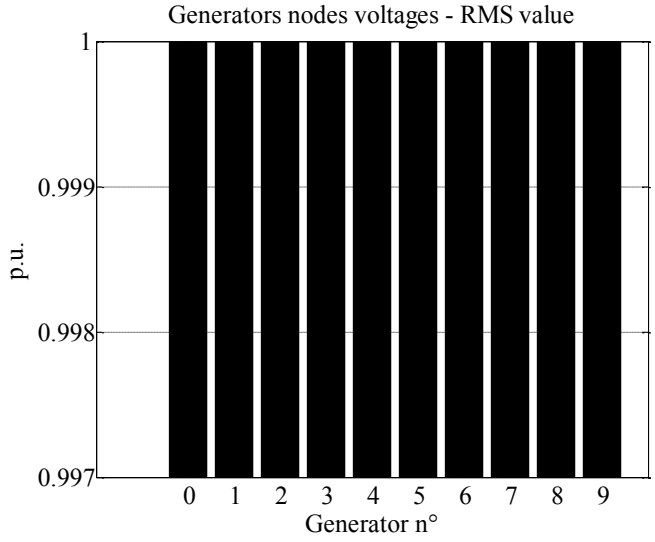

Fig. 4.9 RMS values of the voltages on generators $G_1 \ldots G_9$ after optimum currents injection – radial testbench

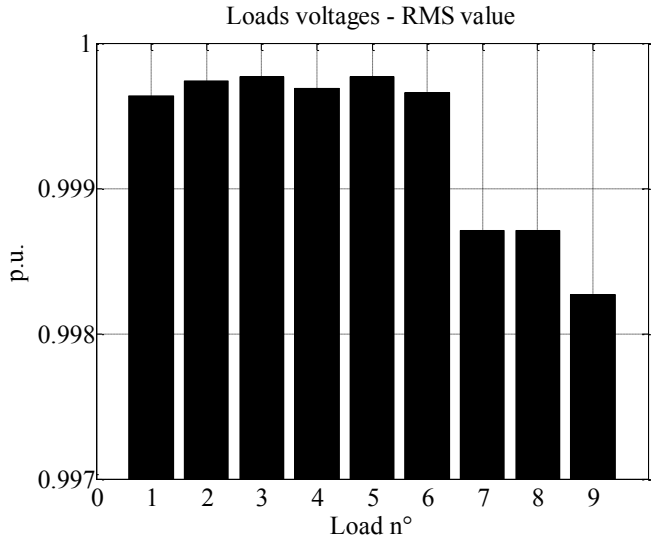

Fig. 4.10 RMS values of the voltages on loads $L_1 \ldots L_9$ after optimum currents injection – radial testbench

It is also interesting to compare the resulting distribution of the currents. Fig. 4.11 and Fig. 4.12 report the RMS values of the injected currents and consequent bus currents respectively. It is immediate to verify how the currents are now more homogenous in the buses, including the most peripheral buses, while before the current was concentrated in the buses close to the PCC. Also the peak current is strongly reduced, passing from $I_{MAX} = 258.5\text{A}_{\text{RMS}}$ to $I_{MAX}^{opt} = 36\text{A}_{\text{RMS}}$. Of course this comes at the cost of high currents demands from the generators, with a peak of $I_{G,MAX}^{opt} = 106\text{A}_{\text{RMS}}$ demanded to generator G_6, connected to the node collecting the buses where all the largest loads in the microgrid L_7, L_8 and L_9 are connected.

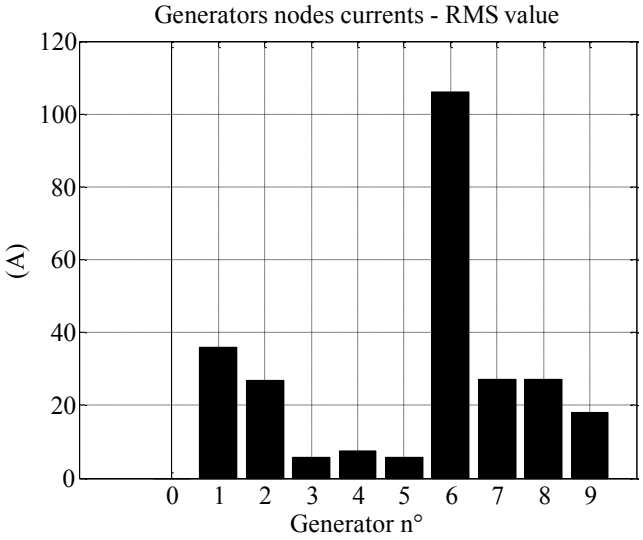

Fig. 4.11 Optimum injected RMS currents – radial testbench

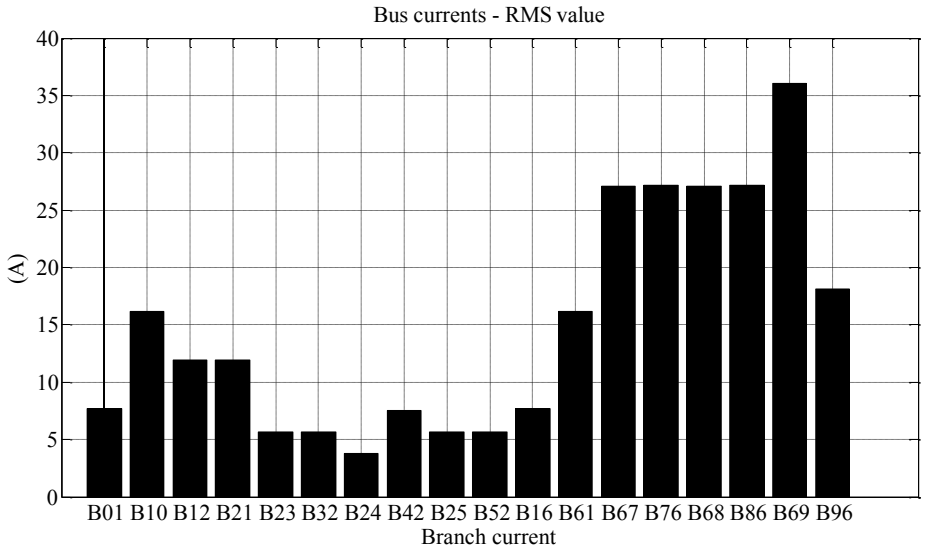

Fig. 4.12 Bus RMS currents during optimum currents injection – radial testbench

In the next section, the second considered configuration of the microgrid is introduced, with a lightly meshed structure. A symmetrical analysis has been done, but only the most significant results are reported, being the topology very similar to the previous one.

4.3.2. Meshed Microgrid Testbench

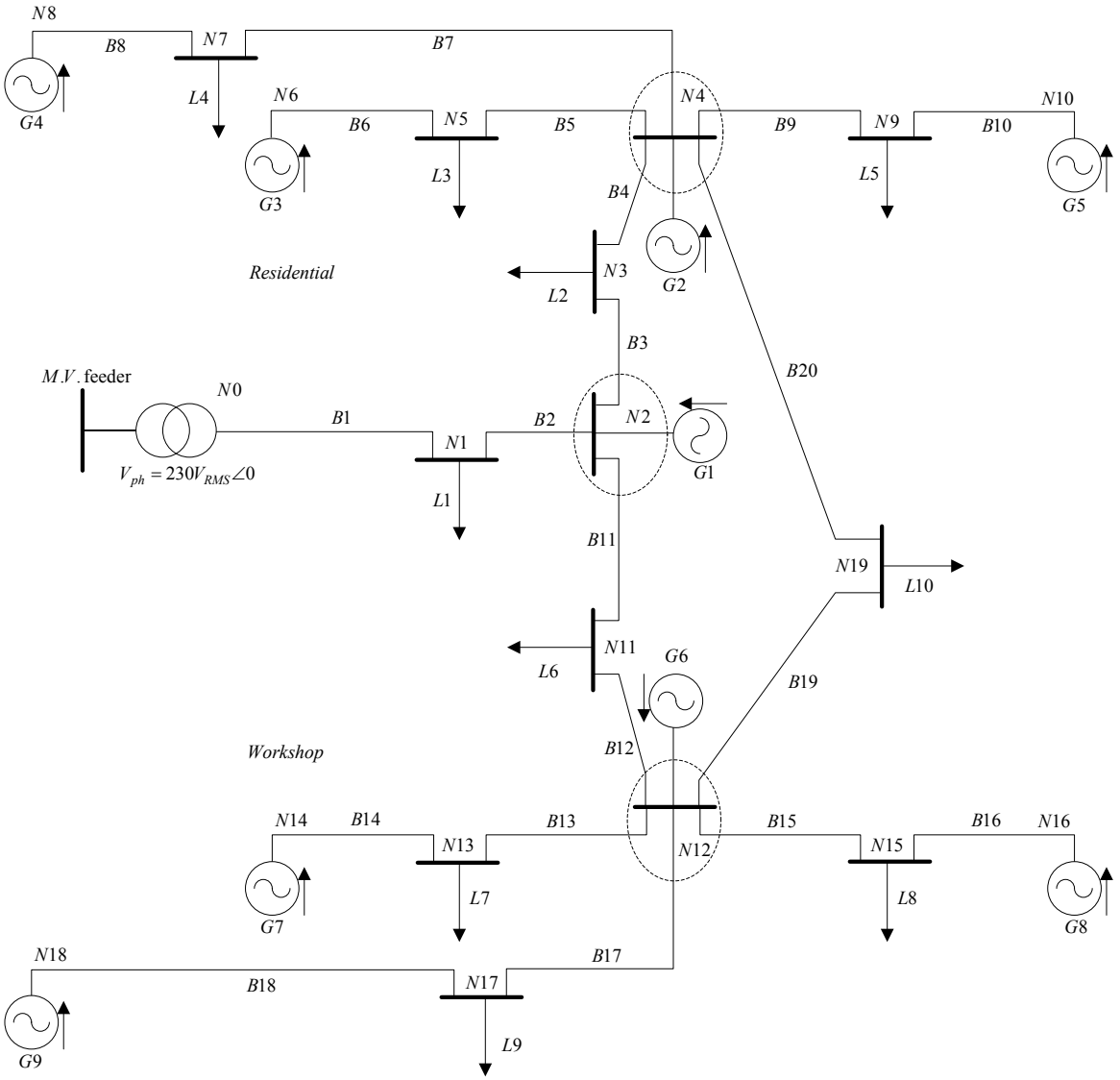

Fig. 4.13 Meshed microgrid testbench

Fig. 4.13 reports the considered meshed system. The microgrid is a simple variation on the radial case, adding the buses B_{19} and B_{20} and the load L_{10} between nodes N_4 and N_{12}. To derive the set of injected currents required for loss minimization, the general approach proposed at the end of Chapter 2 has to be applied. Table 4.4 , Table 4.5 and Table 4.6 summarize the microgrid parameters in terms of buses length, loads and generators respectively.

Bus	Length (m)	Impedance (Ω) r=0.08Ω/km l=255μH/km
B1	100	(8+j8)e-3
B2	50	(4+j4) e-3
B3	50	(4+j4) e-3
B4	50	(4+j4) e-3
B5	100	(8+j8)e-3
B6	100	(8+j8)e-3
B7	200	(16+j16) e-3
B8	100	(8+j8)e-3
B9	100	(8+j8)e-3
B10	100	(8+j8)e-3
B11	100	(8+j8)e-3
B12	50	(4+j4) e-3
B13	100	(8+j8) e-3
B14	100	(8+j8) e-3
B15	100	(8+j8) e-3
B16	100	(8+j8) e-3
B17	100	(8+j8) e-3
B18	200	(16+j16)e-3
B19	150	(12+j12)e-3
B20	250	(20+j20)e-3

Table 4.4 bus lengths and impedances – meshed microgrid

Load Z=R+jωL	R(Ω)	L(mH)	Power @ 230V_{RMS}
L1	8.76	12.7	5kW cosφ=0.91
L2	8.76	12.7	5kW cosφ=0.91
L3	19.5	18.1	2.5kW cosφ=0.96
L4	19.5	18.1	2.5kW cosφ=0.96
L5	19.5	18.1	2.5kW cosφ=0.96
L6	8.76	12.7	5kW cosφ=0.91
L7	3.39	8.1	10kW cosφ=0.80
L8	3.39	8.1	10kW cosφ=0.80
L9	3.39	8.1	10kW cosφ=0.80
L10	3.39	8.1	10kW cosφ=0.80

Table 4.5 resistive and inductive part of the loads, and corresponding power at the nominal voltage – meshed microgrid

Distributed Generator (Energy Gateway)	P_{MAX}(kW)	S_{MAX}(kVA)
G1	3	5
G2	3	5
G3	3	5
G4	3	5
G5	3	5
G6	10	15
G7	10	15
G8	10	15
G9	10	15

Table 4.6 distributed generators active and absolute power ratings – meshed microgrid

4.3.2.1. Theoretical loss analysis

First of all the incidence matrix is presented, as the concatenation between the tree incidence matrix A_t and the cotree one A_l. Being the definition of tree and cotree not unique, the choice has been to include bus B_{19} in the tree, and therefore the cotree is just made by bus B_{20}.

$$A_M = \begin{bmatrix} A_t \\ A_l \end{bmatrix} \tag{4.14}$$

Where:

$$A_t = \begin{bmatrix}
1 & 0 & 0 & 0 & 0 & 0 & 0 & 0 & 0 & 0 & 0 & 0 & 0 & 0 & 0 & 0 & 0 & 0 & 0 \\
-1 & 1 & 0 & 0 & 0 & 0 & 0 & 0 & 0 & 0 & 0 & 0 & 0 & 0 & 0 & 0 & 0 & 0 & 0 \\
0 & -1 & 1 & 0 & 0 & 0 & 0 & 0 & 0 & 0 & 0 & 0 & 0 & 0 & 0 & 0 & 0 & 0 & 0 \\
0 & 0 & -1 & 1 & 0 & 0 & 0 & 0 & 0 & 0 & 0 & 0 & 0 & 0 & 0 & 0 & 0 & 0 & 0 \\
0 & 0 & 0 & -1 & 1 & 0 & 0 & 0 & 0 & 0 & 0 & 0 & 0 & 0 & 0 & 0 & 0 & 0 & 0 \\
0 & 0 & 0 & 0 & -1 & 1 & 0 & 0 & 0 & 0 & 0 & 0 & 0 & 0 & 0 & 0 & 0 & 0 & 0 \\
0 & 0 & 0 & -1 & 0 & 0 & 1 & 0 & 0 & 0 & 0 & 0 & 0 & 0 & 0 & 0 & 0 & 0 & 0 \\
0 & 0 & 0 & 0 & 0 & 0 & -1 & 1 & 0 & 0 & 0 & 0 & 0 & 0 & 0 & 0 & 0 & 0 & 0 \\
0 & 0 & 0 & -1 & 0 & 0 & 0 & 0 & 1 & 0 & 0 & 0 & 0 & 0 & 0 & 0 & 0 & 0 & 0 \\
0 & 0 & 0 & 0 & 0 & 0 & 0 & 0 & -1 & 1 & 0 & 0 & 0 & 0 & 0 & 0 & 0 & 0 & 0 \\
0 & -1 & 0 & 0 & 0 & 0 & 0 & 0 & 0 & 0 & 1 & 0 & 0 & 0 & 0 & 0 & 0 & 0 & 0 \\
0 & 0 & 0 & 0 & 0 & 0 & 0 & 0 & 0 & 0 & -1 & 1 & 0 & 0 & 0 & 0 & 0 & 0 & 0 \\
0 & 0 & 0 & 0 & 0 & 0 & 0 & 0 & 0 & 0 & 0 & -1 & 1 & 0 & 0 & 0 & 0 & 0 & 0 \\
0 & 0 & 0 & 0 & 0 & 0 & 0 & 0 & 0 & 0 & 0 & 0 & -1 & 1 & 0 & 0 & 0 & 0 & 0 \\
0 & 0 & 0 & 0 & 0 & 0 & 0 & 0 & 0 & 0 & 0 & -1 & 0 & 0 & 1 & 0 & 0 & 0 & 0 \\
0 & 0 & 0 & 0 & 0 & 0 & 0 & 0 & 0 & 0 & 0 & 0 & 0 & 0 & -1 & 1 & 0 & 0 & 0 \\
0 & 0 & 0 & 0 & 0 & 0 & 0 & 0 & 0 & 0 & 0 & -1 & 0 & 0 & 0 & 0 & 1 & 0 & 0 \\
0 & 0 & 0 & 0 & 0 & 0 & 0 & 0 & 0 & 0 & 0 & 0 & 0 & 0 & 0 & 0 & -1 & 1 & 0 \\
0 & 0 & 0 & 0 & 0 & 0 & 0 & 0 & 0 & 0 & 0 & -1 & 0 & 0 & 0 & 0 & 0 & 0 & 1
\end{bmatrix} \tag{4.15}$$

And

$$A_l = \begin{bmatrix} 0 & 0 & 0 & -1 & 0 & 0 & 0 & 0 & 0 & 0 & 0 & 0 & 0 & 0 & 0 & 0 & 0 & 0 & 1 \end{bmatrix} \tag{4.16}$$

The rest of the matrices is omitted for simplicity. The resulting initial loss, when all the generators are off, results:

$$P_{M_{\max}} = 1.765\text{kW} \tag{4.17}$$

Compared with (4.8), the loss is increased. Normally, the introduction of meshes reduces the loss, due to the paralleling of cables. Of course this is true if the total load remains constant, while in this

example an additional load is also included in the mesh. Applying the ideal loss minimization, the theoretical optimum injected currents set results:

$$\underline{\dot{I}}_{M_{Ga}}^{opt} = \begin{bmatrix} 32.62-14.86j \\ 41.64-21.39j \\ 5.44-1.58j \\ 7.25-2.11j \\ 5.44-1.58j \\ 113.94-81.25j \\ 21.70-16.29j \\ 21.70-16.29j \\ 14.46-10.86j \end{bmatrix} (A) \tag{4.18}$$

Corresponding to a distribution loss:

$$P_{R_{\min}} = 67.23\text{W} \tag{4.19}$$

This loss is achieved assuming a fully controllable active and reactive currents injection, without power ratings constraints. Also in this case, the minimization has been done injecting only reactive current as well, obtaining a minimum loss:

$$P_{M_{\min}}^{react} = 1.263\text{kW} \tag{4.20}$$

Corresponding to the 71% of the initial loss. The maximum achievable reduction with reactive only injection is therefore the 29% of the initial loss.

Again, these values have been double checked comparing the results obtained with the simulation software, solving the whole microgrid (all the currents and voltages are calculated) and from them obtaining the loss, instead of doing the direct calculation of the loss. In this way it is also possible to check the microgrid design in terms of bus currents and voltage variations.

4.3.2.2. Initial State Simulation

With the developed simulation software, using load impedances instead of current sources, the initial loss with all the generators switched off results:

$$P_{M_{MAX,sim}} = 1.649k\text{W} \tag{4.21}$$

Again, the difference with respect to the value in (4.17) is related with the line voltage drops, for which the load impedances absorb a lower current.

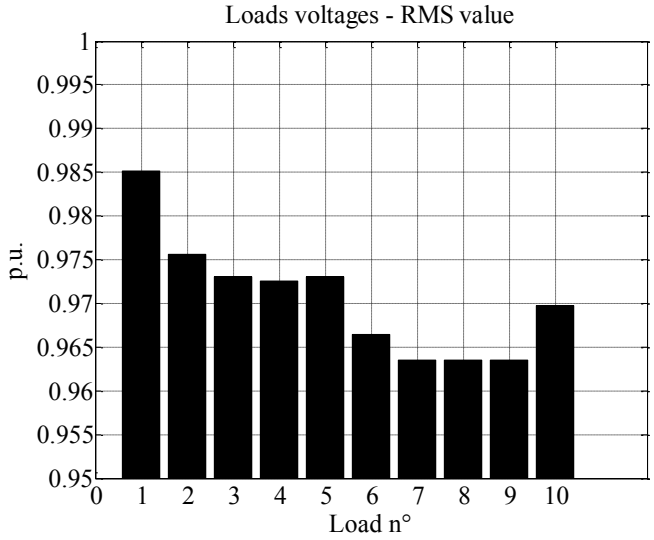

Fig. 4.14 RMS values of the initial voltages on loads $L_1 \ldots L_{10}$ - meshed testbench

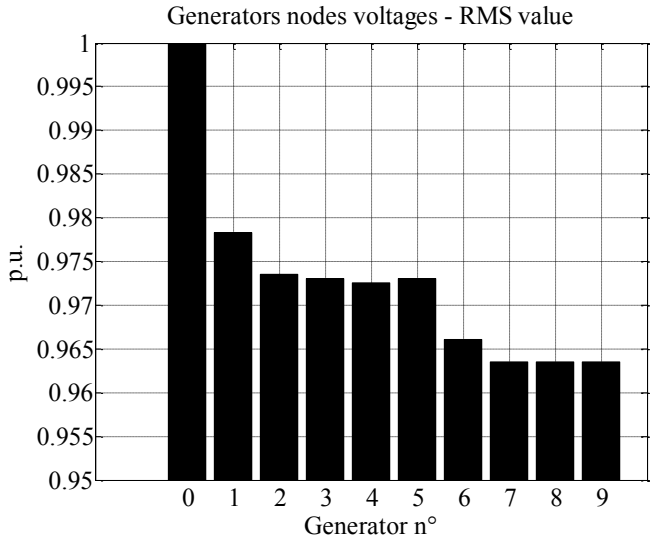

Fig. 4.15 RMS values of the initial voltages on generators $G_1 \ldots G_9$ - meshed testbench

Fig. 4.14 , Fig. 4.15 and Fig. 4.16 report the p.u. values of loads and generators voltages and bus RMS currents.

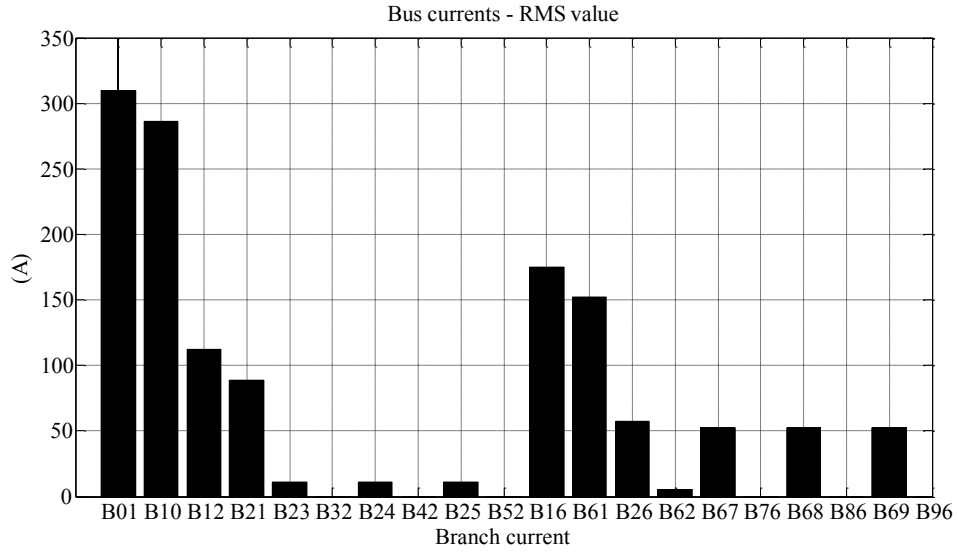

Fig. 4.16 Initial bus RMS currents – meshed testbench

All the RMS voltages are over the minimum limit of $0.95p.u.$. The maximum current, again in bus connecting the PCC to the rest of the microgrid, is now $I_{MAX} = 309.7\text{A}_{\text{RMS}}$, still acceptable for the $240mm^2$ cables.

4.3.2.3. Optimum State Simulation

The simulation software is now run applying as input the optimum injected currents (4.18) as references for generators $G_1 \ldots G_9$. The resulting minimum loss is:

$$P_{M_{\min,sim}} = 67\text{W} \tag{4.22}$$

Therefore, the data found in (4.19) is confirmed. To complete the analysis, Fig. 4.17 , Fig. 4.18 and Fig. 4.19 report node voltages, generators voltages and branch currents in this optimum loss configuration. The generators voltages become equal to the PCC voltage, while the drop at the loads nodes is only due to the current supplied to the local loads. Comparing the branch currents in Fig. 4.19 with the initial values in Fig. 4.16 , the improved current sharing among the buses can be appreciated. Of course this comes at the cost of high currents injection demanded to the generators, as it can be seen in (4.18), where G_6 is injecting $140A_{RMS}$ with $\cos\varphi = 0.8142$ and therefore at the nominal PCC voltage $V_{ph} = 230V_{RMS}$ its energy gateway should be rated for $S_{6,MAX} = 32.2kVA$ and equipped with an energy source rated at least for $P_{6,MAX} = 26.22kW$.

With the meshed microgrid, testbenches analysis is completed. The results have first of all confirmed the correctness of the theoretical minimum loss analysis based on incidence matrices, loads and impedances and of the different approach proposed with the developed simulation

software, leading to the same results. This is a fundamental check when dealing with simulation results in a complex system. The other important part is the definition of the theoretical minimum loss in the microgrids, that will be used as reference to evaluate the performances of distributed algorithms. The loss has been minimized in the case of full (unconstrained) active and reactive current injection and in the reactive only (unconstrained) injection. Of course the most practical case is the one including energy gateways saturations, and therefore it will be considered in one the next sections. Moreover, before moving to the constrained optimization, a third testbench will be defined, as a simple variation of the radial microgrid, but removing some of the generators.

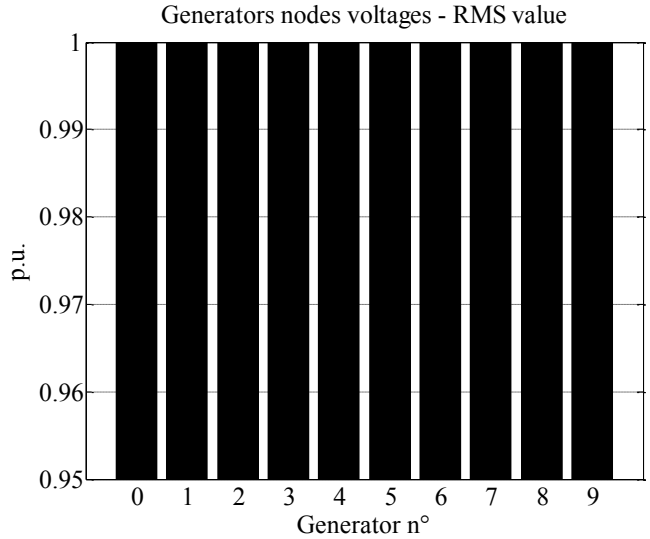

Fig. 4.17 values of the voltages on generators $G_1..G_9$ after optimum currents injection – meshed testbench

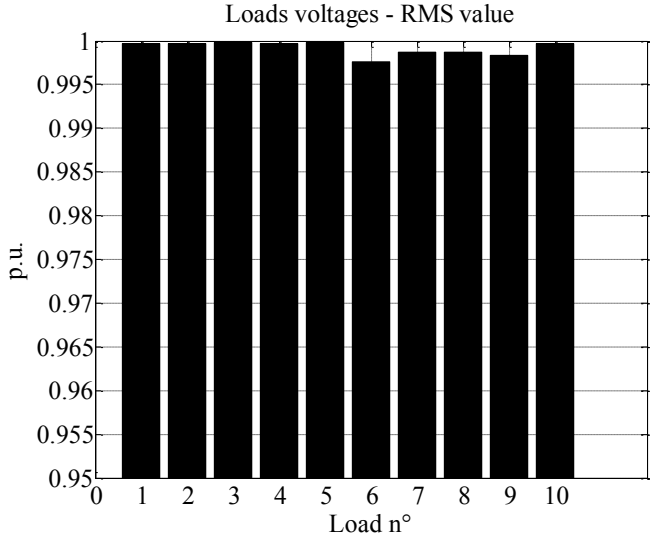

Fig. 4.18 RMS values of the voltages on loads $L_1..L_{10}$ after optimum currents injection – meshed testbench

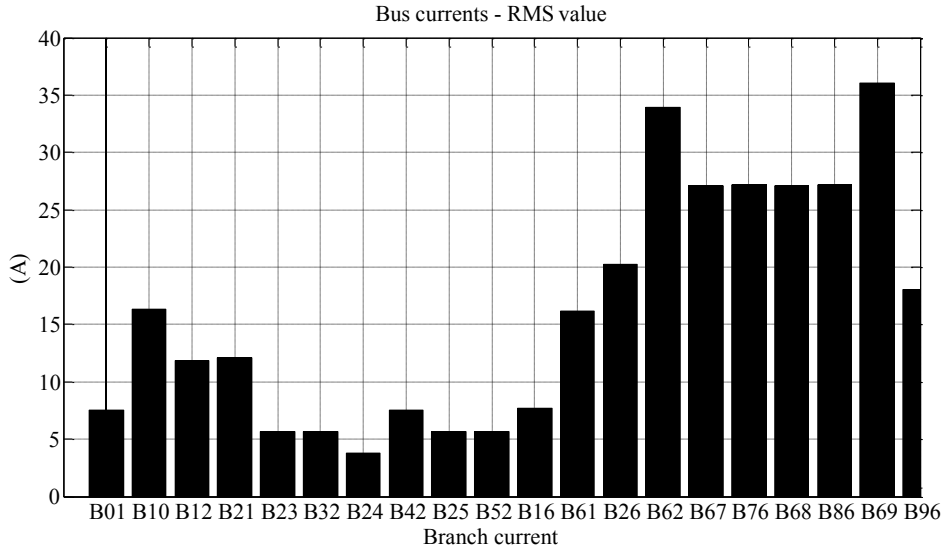

Fig. 4.19 Bus RMS currents during optimum currents injection – meshed testbench

4.3.3. Variant on Radial Microgrid Testbench

The microgrids considered in Fig. 4.2 and Fig. 4.13 are modular structures, where the cluster generator-bus-load-bus-generator is repeated, to form the "clustered microgrid" already used in Chapter 3. For a more general analysis, another configuration is considered for the case of radial microgrid in Fig. 4.2 , removing generators G_2 and G_6. For simplicity, the analysis is reported only with the theoretical loss minimization proposed in Chapter 2, without reporting the comparative results from the developed software for microgrid steady state simulation. The initial loss are of course the same of the original radial microgrid (4.8):

$$P_{Rv\max} = 1.277\text{kW} \tag{4.23}$$

The ideal optimization with full (unconstrained) active and reactive current injection leads to the theoretical minimum loss corresponding to:

$$P_{Rv\min} = 92.63\text{W} \tag{4.24}$$

The minimum loss is obtained with the following set of injected currents from the generators. G_2 and G_6 are kept in the vector, with zero current reference. It is interesting to compare current set (4.25) with the radial microgrid with all the generators in (4.9). In that case G_6 was the generator with the higher current request. Now, that request is divided among the active generators, and the interesting result is that the minimum loss is about twice the previous case, that is a minimum difference considering the reduced amount of generation and the overall loss reduction.

$$\underline{\dot{I}}_{Rv_{Ga}}^{opt} = \begin{bmatrix} 72.4257 - 39.0853j \\ 0 \quad 0 \\ 10.8728 - 3.5529j \\ 10.8692 - 3.4231j \\ 10.8728 - 3.5529j \\ 0 \quad 0 \\ 43.4035 - 31.5106j \\ 43.4035 - 31.5106j \\ 28.9346 - 21.0065j \end{bmatrix} (A) \tag{4.25}$$

The observation gives an important hint for future developments of this work: for a given set of generators, that normally are not sized specifically for loss minimization, also an optimum placement of the generators exists that minimizes the distribution loss even if the theoretical minimum can't be achieved for current limitations. This aspect will be verified also in the following section, where minimization constrained by energy gateways current limits is considered.

In case of unconstrained reactive current injection and active current set to zero, the minimum achievable loss is:

$$P_{Rv\min}^{react} = 933.8\text{W} \tag{4.26}$$

Again, not far from the case with all the generators activated. It is reminded that due to the orthogonality of active and reactive currents, the corresponding loss components are independent, and therefore the required current injection in this case corresponds to (4.25) where the real part is set to zero. In case of a constrained optimization with active power and maximum power constraints, this property is no longer true, for the amplitude dependence of the currents when the saturation limits are active.

4.3.4. Constrained Loss Minimization

As anticipated above, the practical effectiveness of the proposed methods has to be tested in presence of power converters saturations. In Chapter 2 it has been shown how the complexity of the minimum loss problem grows in case of inequality constraints like current saturations. The solution is no longer the solution of a simple linear system obtained by the derivation of the loss quadratic form, but becomes a complex non linear system, with difficult explicit analytical formulation. A graphical approximated solution has been proposed in Chapter 2, but its value is more practical than theoretic, and a strictly theoretical result is preferred here. On the other hand, the distribution loss is a quadratic form, and the nonlinear system resulting from the addition of constraints is easily solved by any numeric solver without particular critic aspects on convergence and precision.

The choice has been to solve the constrained loss problem using *fmincon* function in Matlab. The formulation is particularly simple, because the loss is defined as usual:

$$P_d = \underline{\dot{I}}_a^T \underline{B}_{a,a} \underline{\dot{I}}_a^* + 2\Re\left(\underline{\dot{I}}_a^T \underline{B}_{a,p} \underline{\dot{I}}_p^* \right) + \underline{\dot{I}}_p^T \underline{B}_{p,p} \underline{\dot{I}}_p^* \tag{4.27}$$

Where the matrices $\underline{B}_{i,j}$ depends on the topology and bus resistances, $\underline{\dot{I}}_p$ is the vector of load currents phasors and $\underline{\dot{I}}_a$ is the vector of the unknowns, i.e. currents at generators nodes (directed as absorbed). All the details of the formulation can be found in Chapter 2.

The *fmincon* function easily permits the addition of linear and nonlinear equality or inequality constraints. Linear constraints are used to set the maximum active current limits, while non linear constraints are required for global current limits. If $\underline{I}_{aSAT\_VA}$ and $\underline{I}_{aSAT\_P}$ are the full current rating and the active current rating respectively, the constraints will be:

$$\begin{cases} \Re\left(\underline{\dot{I}}_a\right) < \underline{I}_{aSAT\_P} \\ \left|\underline{\dot{I}}_a\right| < \underline{I}_{aSAT\_VA} \end{cases} \tag{4.28}$$

The adopted constraints are derived from Table 4.3 and Table 4.6 . The power ratings are translated in current ratings at the nominal voltage, being (4.27) dependent only on the loads and generators currents, assumed to be AC current sources. Table 4.7 reports the result of the constrained minimization for the three considered microgrids and for the two cases of active and reactive constrained injection and reactive only constrained injection.

	Loss A/R (W)	Loss R (W)
Radial microgrid	61.14	918.7
Meshed microgrid	114.1	1263
Radial microgrid with G_2, G_6 off	120.53	935

Table 4.7 Constrained minimum distribution loss: Loss A/R if active and reactive currents are injected, Loss R if reactive current only is injected

4.4.Distributed algorithms for loss minimization

This final section presents the simulation results obtained applying the different proposed distributed control solutions for loss minimization to the previously described testbenches. Plug and Play technique is included even if it cannot be properly defined “distributed”, but is useful as term of comparison. Among the distributed solutions, Voltage Based Surround Control and Cooperative

Control are presented, while Current Based Surround Control is omitted. The reason is that the value of the control is purely theoretic, because its definition strictly requires a microgrid with a clustered structure, as shown in Chapter 3. If the hypothesis is not satisfied there is apparently no way of defining a reasonable even if sub optimum solution, due to the lack of knowledge on microgrid topology. Assuming the distributed loads to be able to identify the exact topology of a microgrid section, a generalization of a single cluster could be proposed, but the solution seems to be involved and of limited practical value. On the other hand, Cooperative Control could reasonably be considered a sub optimal extension of the Current Based Surround control, and therefore the attention is focused on that solution. The comparison is therefore between a "voltage based" solution, the Voltage Based Surround Control and a "current based" solution, the Cooperative Control, plus the communication-less Plug and Play.

The section is organized as follows: the three loss minimization techniques will be tested in the three microgrid testbenches, and in four conditions of current injection from the energy gateways: unconstrained injection first of both active and reactive current and then only of reactive current, and then constrained injection, adding the power converters saturation, again in the two conditions of full current injection and reactive current only injection.

The simulations are carried out using the simplified linear solver implemented in the developed Matlab software. The software implementation exactly tests the distributed control equations reported in Chapter 3. The obtained results will be compared with the analytical derived ideal optimum conditions presented in the previous sections. Before passing to the results, some details about the simulations are given.

4.4.1. Token management and communications

In Chapter 3, the authorization of controlling, i.e. current reference updating, is given to a specific Energy Gateway using a Token. When an energy gateway owns the Token, it is the only distributed generator in the network acting on loss minimization, calculating and applying a new current reference (assuming for simplicity the condition where no other controllers are acting on the currents, that is reasonable for reactive currents but quite unrealistic for active currents, apart from the case where energy storage is present in the microgrid, where loss minimization could be used as a way of minimizing the amount of current imported from the PCC), while the others are holding the previous reference.

Being the simulation a sequence of steady states, the time duration of each control slot, i.e. the sampling period of the distributed control, is not taken into account. Of course in a practical implementation it has to be as short as possible, to have a microgrid able to react to load changes or connection-disconnection of energy gateways. This transients are not particularly relevant for the

distribution loss, because a slower convergence simply means a higher energy lost during the transient. More relevant are the possible under or over voltages that could happen changing loads or generators while other generators are in hold state. Similarly, the periodic repetition of load steps could be critic if the distributed control doesn't guarantee fast convergence, thus keeping the microgrid in an average condition. All these aspects are neglected in this study and will be part of future developments, related with the implementation in a real microgrid.

In the simulations, the Token is emulated simply defining a random variable, with uniform distribution, that chooses the energy gateway authorized to control. Similarly, all the required node to node communications are neglected, having the software a direct access to all the required information. Nevertheless, all the communication and measurement requirements will be highlighted in the simulation results.

4.4.2. Saturations

The most interesting results for a future practical implementation, are related with the constrained loss minimization, where the current injection is limited by power converters and energy source power ratings. The $i-th$ energy source is identified by its active power rating (considering a single phase):

$$P_i^{MAX} = V_{i,NOM} I_{iA} \tag{4.29}$$

While the corresponding energy gateway is identified by the total power rating:

$$S_{EGi}^{MAX} = V_{i,NOM} I_{EGi} \tag{4.30}$$

Assuming the microgrid voltage RMS value to be equal to the nominal value $V_{i,NOM}$, the active power and apparent power constraints are translated into RMS active current and RMS total current I_{iA}^{MAX} and I_{EGi}^{MAX}. Of course, $I_{EGi}^{MAX} > I_{iA}^{MAX}$. Therefore, when a current reference $\dot{I}_i = I_{iA} + jI_{iB}$ is demanded to the energy gateway by the distributed control, different situations are possible:

- If $I_{iA} > I_{iA}^{MAX}$, I_{iA} is set equal to the limit, and then the total current limit is checked: if the current demand $I_{iEG} = \sqrt{I_{iA}^{MAX\,2} + I_{iB}^{\;2}}$ is greater than I_{EGi}^{MAX}, I_{iB} is reduced to meet the limits, leading to $I_{iB,SAT1} = \sqrt{I_{EGi}^{MAX\,2} - I_{iA}^{MAX\,2}}$.

- $I_{iA} < I_{iA}^{MAX}$ but $I_{iEG} > I_{EGi}^{MAX}$: in this case two options are reasonable, among the infinite combinations able to move the current vector within the limits. The total current vector can

be reduced keeping the same phase, and thus reducing active and reactive components, or the active component can be held constant and the reactive one reduced accordingly. The adopted solution is the latter, and therefore $I_{iB,SAT2} = \sqrt{I_{EGi}^{MAX\,2} - I_{iA}^{2}}$. This is mainly because in general the active current could be set by energetic reasons (for instance photovoltaic power availability), and therefore the reactive injection has to adapt to the fixed active component. On the other hand, also the active power could be controlled by the minimum loss control: consider the scenario of energy storage availability, and the need for a minimization of active and reactive currents absorbed from the PCC, for economical reasons. A loss minimization algorithm is a good candidate for this goal, guaranteeing minimum currents in the branches, while supplying the load demand. For a reasons of costs, is more convenient to deliver as much active power as possible (thus subtracting it from the PCC) while leaving to the reactive component to respect the system limits.

4.4.3. Plug and Play control

The Plug and Play approach has been tested first in the radial microgrid testbench. As observed in Chapter 3, with tree topology the plug and play control becomes equivalent to a control that sets to zero the current of the surrounding branches that have a path to the PCC. Injecting reactive power only, this is equivalent to a power factor correction of the equivalent load seen by the PCC.

Fig. 4.20 reports the distribution loss obtained with unconstrained active and reactive current injection. It is immediately clear that a number of iterations are ineffective in loss reduction. They are the control slots where the Token is owned by the peripheral nodes, that are completely ineffective in the Plug and Play control. Therefore, referring to Fig. 4.2 , only G_1, G_2 and G_6 are cooperating to the control. The final loss are consistently reduced to $85.74W$, close to the ideal theoretic optimum $P_{R\min} = 45.15\text{W}$, considering the initial loss $P_{R_{MAX,sim}} = 1.202k\text{W}$. As expected, this comes at the cost of high current injection, as reported in Fig. 4.21 ,Fig. 4.22 and Fig.4.23 .

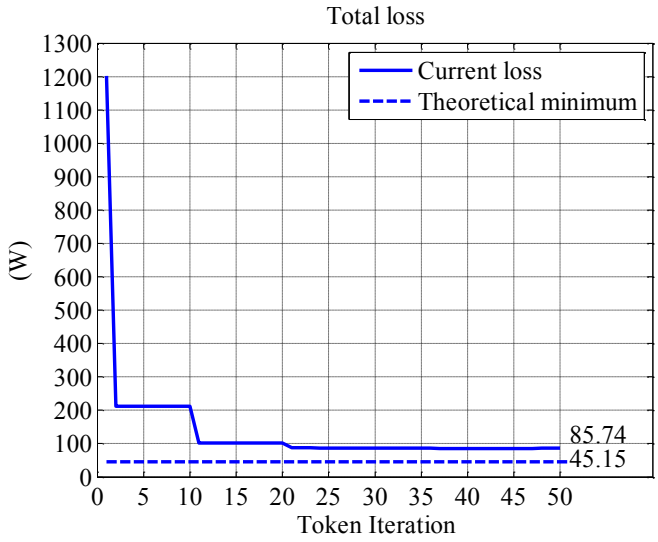

Fig. 4.20 Distribution loss - unconstrained Plug and Play control - radial testbench

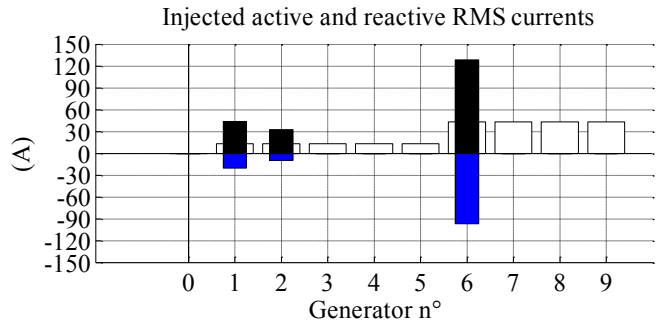

Fig. 4.21 Injected currents - unconstrained Plug and Play control - radial testbench - active (black bars) and reactive (coloured bars) injection

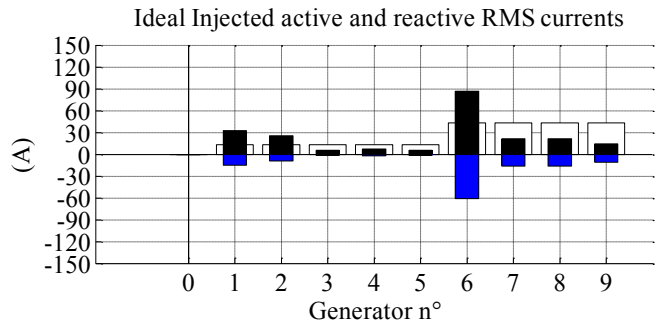

Fig. 4.22 Ideal unconstrained injected currents for loss minimization in radial testbench - active (black bars) and reactive (coloured bars)

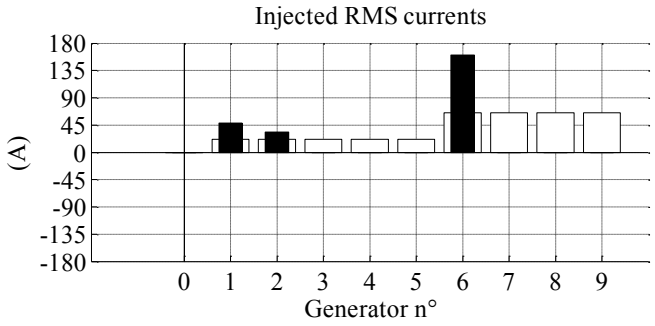

Fig.4.23 RMS injected currents - unconstrained Plug and Play control - radial testbench

Fig. 4.21 and Fig. 4.22 reports the injected currents and the corresponding theoretical optimum injection. Considering that the loads absorbs active current and lagging reactive current, the bar representation has this meaning: the upper bars are the real part of the injected current phasor, the lower bars are the imaginary part. The amplitude is always the RMS value. The reported generator number is coherent with the numbers in Fig. 4.2 . As anticipated, only G_1, G_2 and G_6 are injecting current, while all the other generators are off. In particular, generator G_6 has the highest current demand as shown also in Fig.4.23 , being located in a node where all the heavy loads of the microgrid, L_7, L_8 and L_9 are connected. In all the figures, the white bars represent the saturation limits that will be applied later. For the Plug and Play approach, G_6 has to feed all these loads, to set to zero the current of the branch connecting G_6 with the PCC. This can be easily seen comparing the testbench topology in Fig. 4.2 with Fig. 4.24 , reporting the RMS value of bus currents. The bus is named Bij with the meaning of bus connecting node N_i with node N_j in Fig. 4.2 . Black bars represent the initial currents, when all the distributed energy gateways are switched off. The grey bars represent the steady state, when all the generators have received the Token. The final currents in buses $B10$, $B21$ and $B61$ are set to zero, meaning that in Fig. 4.2 the microgrid becomes equivalent to three different microgrids where G_1 feeds only L_1, L_2 and L_6, G_2 feeds only L_3, L_4 and L_5 and finally G_6 feeds L_7, L_8 and L_9.

The large reduction of bus currents justify the correspondent distribution loss reduction. To conclude, Fig. 4.25 shows the RMS value of load voltages before and after the control, showing the voltage support resulting by the localized supply load currents. In the figure, load numbers are coherent with the numbers in Fig. 4.2 .

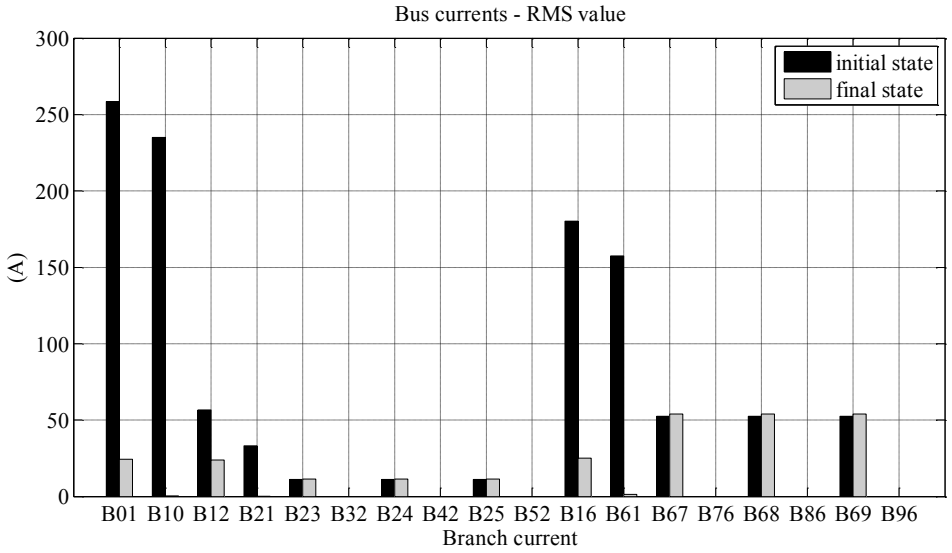

Fig. 4.24 Bus currents - unconstrained Plug and Play control - radial testbench

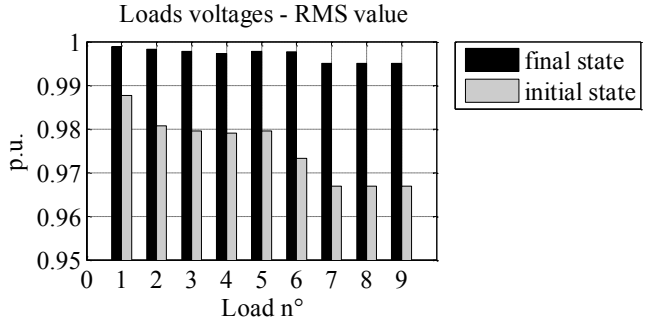

Fig. 4.25 Load RMS voltages- unconstrained Plug and Play control applied to radial testbench

The injection is now switched to reactive current only. Fig. 4.26 reports the distribution loss in this second case, compared with the theoretical optimum.

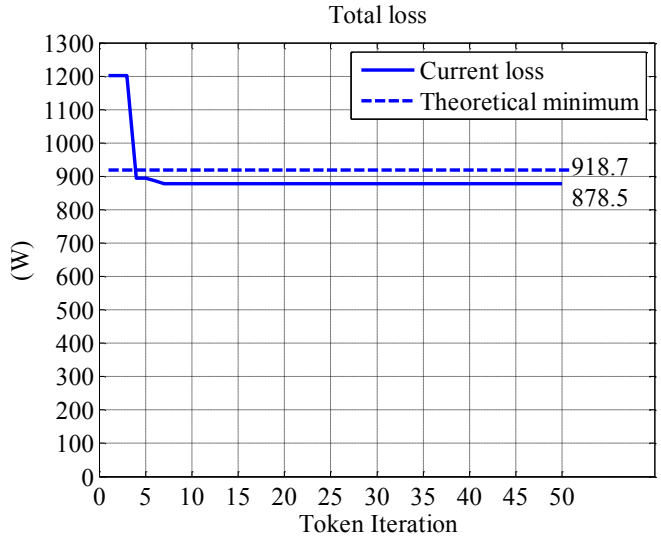

Fig. 4.26 Distribution loss - unconstrained Plug and Play control - radial testbench – reactive only injection

The final distribution loss is lower than the theoretical optimum. This inconsistency is due to the different conditions of theoretical optimum calculation and simulations: in the first case the loads are current sources, while in the latter constant impedances. The two cases are equivalent only when the voltages are closed to their nominal value, condition verified with good approximation only in the Voltage Based Surround Control with unconstrained injection, as it will be shown in the next sections. On the other hand, the relative error due to this approximation is acceptable, considered the overall loss reduction. The generator currents are omitted in this case, because the injected reactive current corresponds to the imaginary part of the currents in Fig. 4.21 and the corresponding ideal injection to the imaginary part in Fig. 4.22 . This because in absence of saturations the loss components corresponding to active and reactive currents are independent. Fig. 4.27 reports the loads RMS voltages, showing the reduced support effect obtained compensating only the reactive current. The reason is the resistive component of the cables.

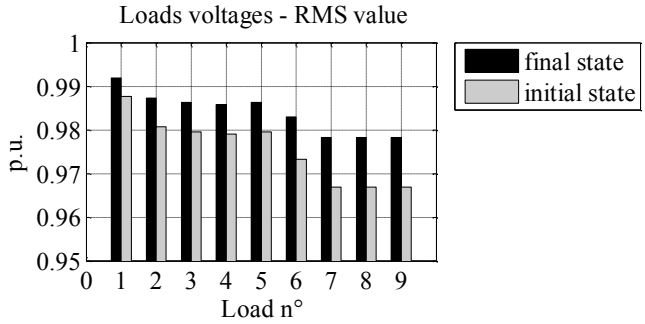

Fig. 4.27 Load RMS voltages- unconstrained Plug and Play control - radial testbench - reactive only injection

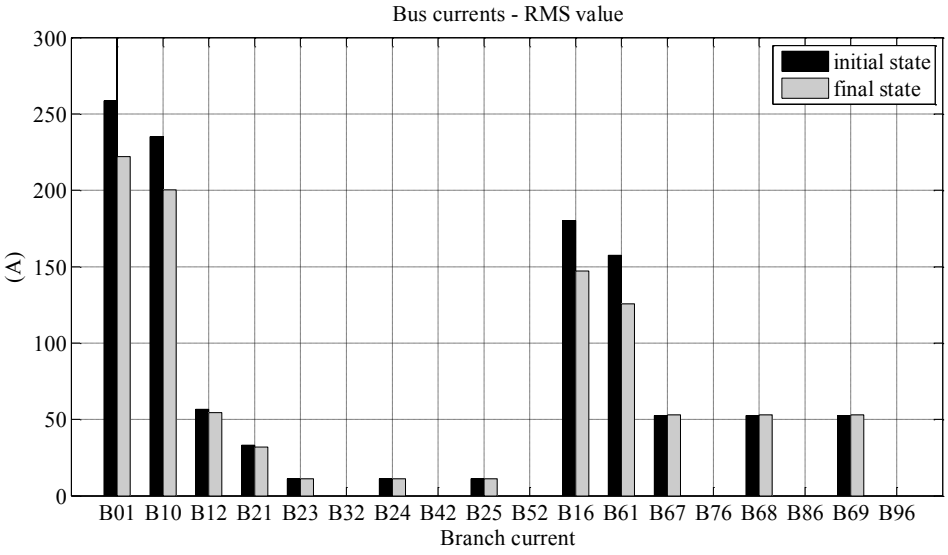

Fig. 4.28 Bus currents - unconstrained Plug and Play control - radial testbench – reactive only injection

Observing also Fig. 4.28 , with the bus currents RMS values, a consideration follows on voltage drop over line cables. Consider the first bus, $B01$, connecting the microgrid with the PCC. Initially,

when none of the generators is supplying current, the absorbed current at this bus is (assuming constant current loads):

$$\dot{I}_{01}^{init} = 228.03\text{-}136.94\text{j} = 265.99\text{e}^{\text{j}0.54}\text{A} \tag{4.31}$$

Causing the voltage the voltage ad node N_1 to be:

$$\Delta\dot{V}_{N1}^{init} = 230 - \dot{V}_{N1}^{init} = \dot{Z}_{01}\dot{I}_{01}^{init} = 2.9198 + 0.7287\text{j} = 3.0094e^{\text{j}0.2446}\text{V} \tag{4.32}$$

Compensating the reactive component, the current becomes:

$$\dot{I}_{01}^{fin} = 228.03\ \text{A} \tag{4.33}$$

Corresponding to a voltage on N_1:

$$\Delta\dot{V}_{N1}^{fin} = 230 - \dot{V}_{N1}^{fin} = \dot{Z}_{01}\dot{I}_{01}^{fin} = (1.824 + 1.824\text{j}) = 2.5799\,e^{\text{j}0.7854}\text{V} \tag{4.34}$$

Therefore, setting to zero the reactive current slightly modifies the module of the voltage drop over the line cable, while the phase is almost three times, becoming equal to the line impedance phase $\varphi_{line} = \frac{\pi}{4}$ for the cable used in the testbench. As a result, the voltage $\dot{V}_{N1}^{fin}$ slightly increases in module. The reason is that in a cable impedance with phase $\varphi_{line} = \frac{\pi}{4}$, the active and reactive currents (defined with respect to the PCC, for simplicity) equally contributes to voltage drops, differently from a traditional inductive line, where the voltage amplitude is controlled by the reactive component. In the specific example, it is easy to write the module of line voltage as a function of active and reactive currents:

$$\dot{V}_{N1} = \dot{V}_{PCC} - \dot{Z}_{01}\dot{I}_{01} = 230 - \frac{\left|\dot{Z}_{01}\right|}{\sqrt{2}}\left(I_{01}^{A} - I_{01}^{B} + j\left(I_{01}^{A} + I_{01}^{B}\right)\right) \tag{4.35}$$

Where $\dot{I}_{01} = I_{01}^{A} + jI_{01}^{B}$. Assuming for simplicity $\left|\dot{Z}_{01}\right| = \sqrt{2}$, the corresponding module and phase are:

$$\begin{aligned} \left|\dot{V}_{N1}\right| &= \sqrt{\left(230 - I_{01}^{A} + I_{01}^{B}\right)^2 + \left(I_{01}^{A} + I_{01}^{B}\right)^2} \\ \angle\dot{V}_{N1} &= \tan^{-1}\left(\frac{I_{01}^{A} + I_{01}^{B}}{230 - I_{01}^{A} + I_{01}^{B}}\right) \end{aligned} \tag{4.36}$$

It is therefore clear that if the active and reactive components have the same amplitude, setting to zero one or the other leads to the same module and phase variation in the considered case, where is $I_{01}^{A} > 0$ and $I_{01}^{B} < 0$, being the load inductive.

From now on, the saturations constraints are added to the Plug and Play control. The expected result is an increased loss, due to the impossibility of generating all the required currents. For simplicity, only the active and reactive injection is considered. The reason is that observing Fig. 4.22 , the required reactive currents for the unconstrained reactive only injection are within the saturation limits reported in Fig.4.23 . Therefore no additional information would be given by the analysis. Fig. 4.29 reports the resulting loss, much larger than the minimum but still with a reduction equal to the 66% of the initial loss, acting with only three of the nine generators in the microgrid. The correspondent currents injections are reported in Fig. 4.30 , Fig. 4.31 and compared with the ideal constrained loss minimization in Fig. 4.32 .

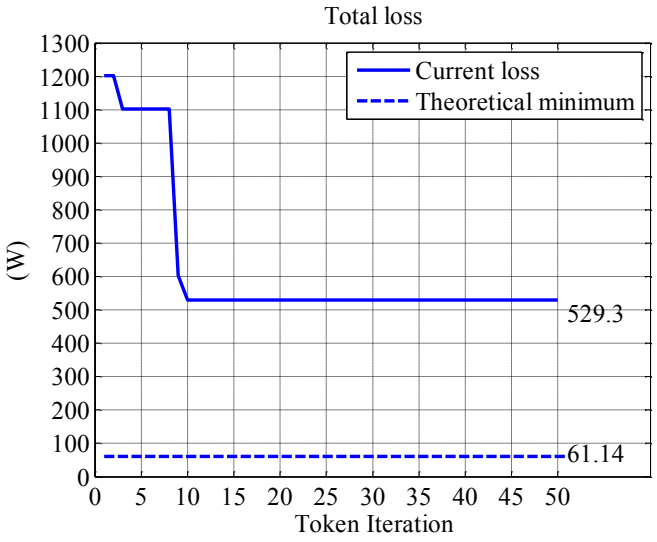

Fig. 4.29 Distribution loss - constrained Plug and Play - active and reactive injection - radial testbench

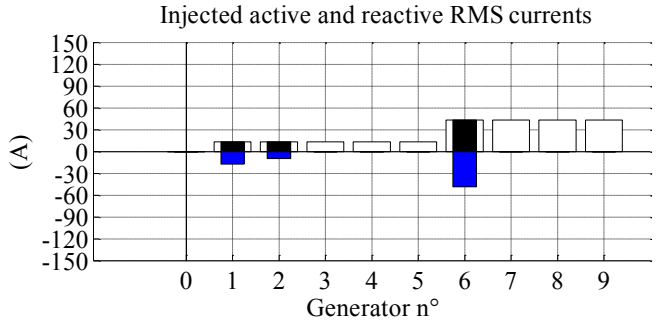

Fig. 4.30 Injected currents - constrained Plug and Play – active (black bars) and reactive (coloured bars) injection - radial testbench

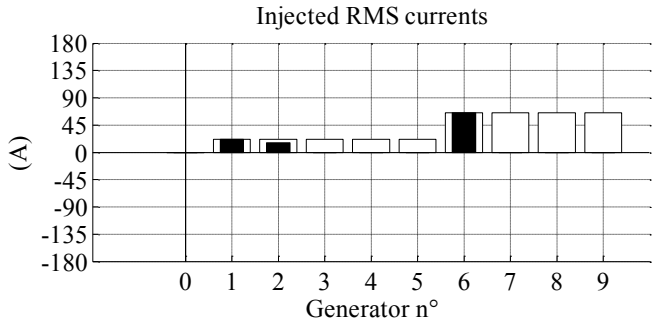

Fig. 4.31 Injected RMS currents - constrained Plug and Play - active and reactive injection - radial testbench

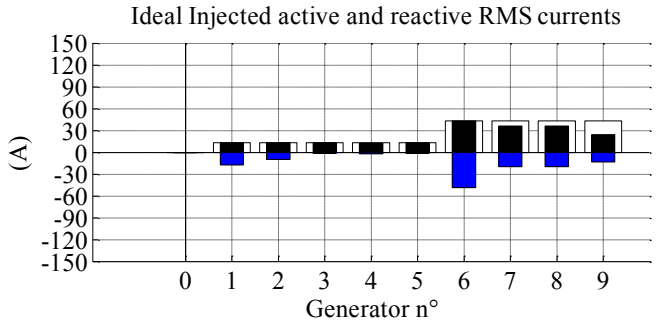

Fig. 4.32 Ideal constrained injected currents for loss minimization in radial testbench - active (black bars) and reactive (coloured bars)

Only the constrained active and reactive case is reported for the meshed testbench. Fig. 4.33 shows the resulting loss, compared with the ideal theoretical minimum loss. Fig. 4.34 and Fig. 4.35 report the correspondent generators injection and the ideal injection that minimizes the loss.

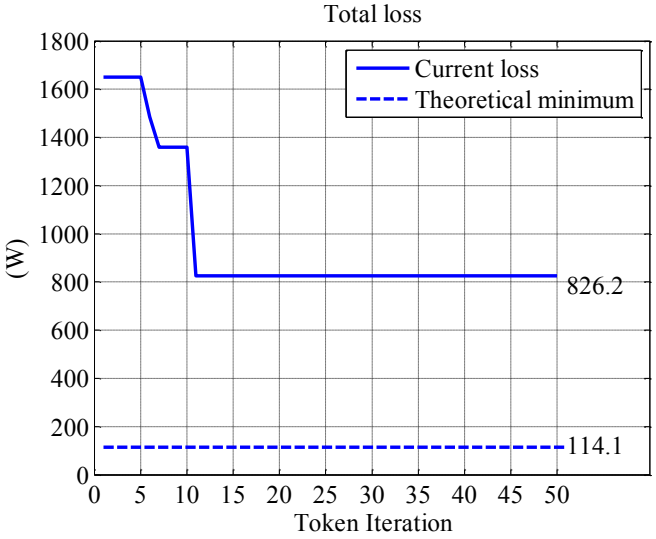

Fig. 4.33 Distribution loss - constrained Plug and Play - active and reactive injection - meshed testbench

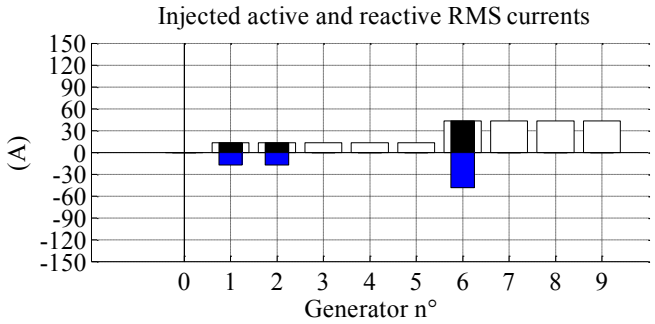

Fig. 4.34 Injected currents - constrained Plug and Play - active (black bars) and reactive (coloured bars) injection - meshed testbench

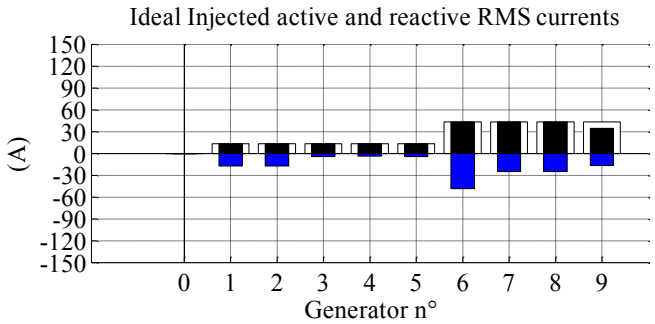

Fig. 4.35 Ideal constrained injected currents for loss minimization in meshed testbench - active (black bars) and reactive (coloured bars)

The test in a meshed topology is important to confirm that the proposed Plug and Play technique is a generalization of the simple approach that sets to zero the current in the branches connected to a generator that form a path to the PCC.

As a general comment, the Plug and Play approach is particularly simple, being based only on local current measurements. At least for the proposed testbenches, the performances in terms of loss reduction are consistent. The main limitation is that the peripheral nodes are not involved in the optimization, and therefore their potential contribution to loss minimization is not considered. As a result, the power rating required to the energy gateways placed in non peripheral nodes has to be increased.

4.4.4. Voltage Based Surround Control

Voltage Based Surround Control is the first considered distributed loss minimization technique. It will be tested in the same condition of the Plug and Play control, to enable a direct comparison. An additional condition is then tested, using the radial testbench but switching off generators G_2 and G_6, thus obtaining a more general topology and not a clustered microgrid made of repetitions of the same section. As in Chapter 3, when a node receives the Token it is assumed to be able to identify the neighbours and to measure the corresponding distances (equivalent to impedances if the

distribution cable has constant section as in these testbenches), as well as to gather measured voltage phasors from the all the neighbours.

Starting from unconstrained active and reactive current injection, Fig. 4.36 reports the resulting distribution loss. A first comparison is immediate: while the Plug and Play control requires a number of iterations equal to the number of active generators, the Voltage Based Surround takes a larger number of iteration to converge, due to the feedback nature of the approach. The advantage is that the resulting loss matches the theoretical data with minimum deviation.

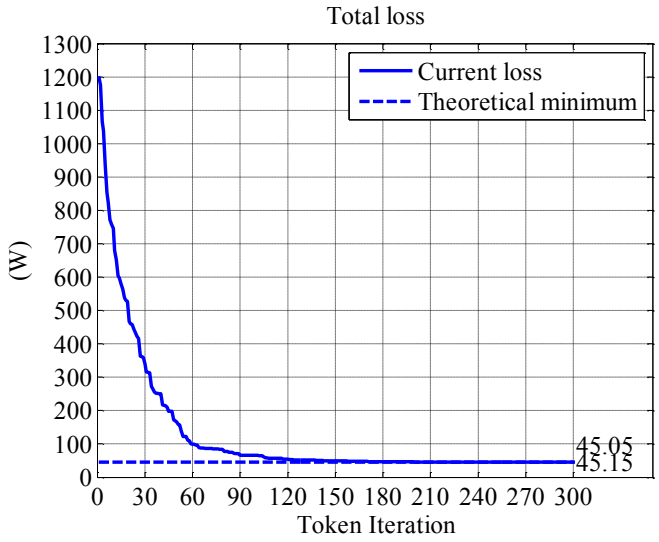

Fig. 4.36 Distribution loss - unconstrained Voltage Based Surround Control - radial testbench

It is worth to remind that during the iterations the Token is randomly exchanged among the energy gateways in the network, and that only one of the nine distributed generators is controlling in each control slot. Fig. 4.37 reports the injected currents when Token Iteration=300 and the system is considered in steady state, while Fig. 4.38 reports the theoretical set of currents required to minimize the loss (again calculated with the constant current loads approximation).

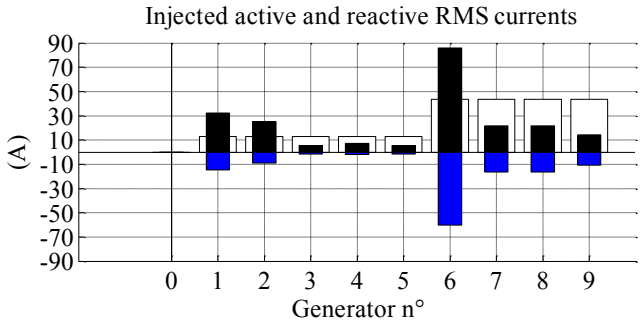

Fig. 4.37 Injected currents - unconstrained Voltage Based Surround Control - active (black bars) and reactive (coloured bars) injection - radial testbench

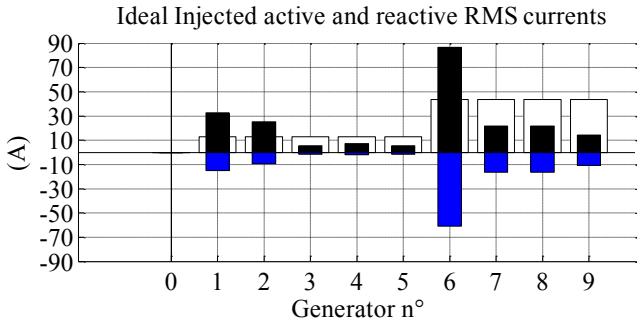

Fig. 4.38 Ideal unconstrained injected currents for loss minimization in radial testbench - active (black bars) and reactive (coloured bars)

Comparing the figures it can be observed that almost all the generators are injecting the ideal current. Only G_6 doesn't exactly match the ideal reference. Considering that the loss can be considered minimized, the error is only due to the limited observation interval of 300 token iterations. The relevance of the error can be checked on the generators voltages. In fact, the steady state condition of Voltage Based Surround would require all the generators voltages to be equal.

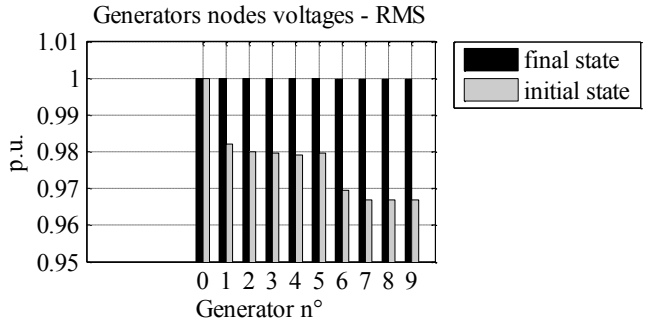

Fig. 4.39 Generators RMS voltages- unconstrained Voltage Based Surround Control - radial testbench

Fig. 4.39 , showing the RMS values of generators voltages, confirms the convergence of the surround control to the theoretical minimum loss for the radial testbench. The corresponding phase is omitted for simplicity, being equal to zero or all the generators. Finally, the bus currents are reported in Fig. 4.40 , showing that now none of the bus currents is set to zero, but they are set to the optimum value required by each cluster of the microgrid, as already described in Chapter 3. A fist comparison with the Plug and Play approach can be done, observing that first the Voltage Based Surround Control guarantees the convergence to the optimum currents, minimizing the loss. This is achieved with lower current stresses on the generators, being the loads supply shared among all the distributed energy gateways, as it can be noticed comparing Fig. 4.37 and Fig. 4.21 .

The same analysis is now done for the unconstrained reactive current injection, remembering that the same results holds in the constrained reactive current injection. Fig. 4.41 shows the obtained distribution loss. The result is again slightly lower than the theoretical optimum, for the constant current loads approximation.

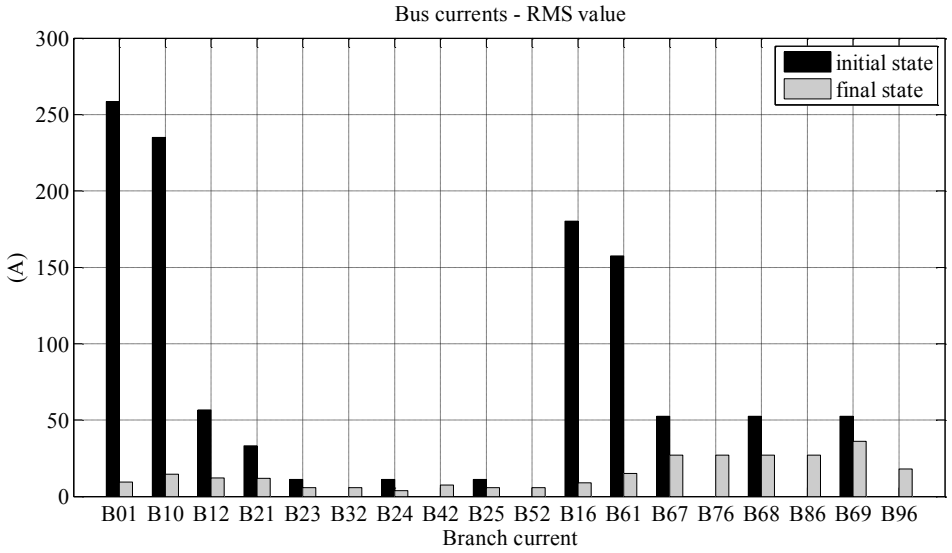

Fig. 4.40 currents - unconstrained Voltage Based Surround Control - radial testbench

Moreover, the final loss is very close to the one obtained with the Plug and Play control. The reason is only that the main component of the losses due to reactive currents (active and reactive currents have independent contributions on the loss) is related with the heavy loads L_7, L_8 and L_9. The Plug and Play control guarantees in this case the local supply of the reactive current, and due to the relatively balanced bus lengths, the result is similar to the surround control. If for example $B12 \gg B14, B15 \gg B16, b17 \gg B18$, the behaviour of the surround would be much better than the Plug and Play, thanks to the use of peripheral generator. Fig. 4.42 reports the injected currents. The ideal ones are the imaginary components of Fig. 4.38 . To confirm the respect of saturation limits, and therefore the absence of information analyzing the constrained reactive injection, Fig. 4.43 reports the injected RMS values compared with saturation limits.

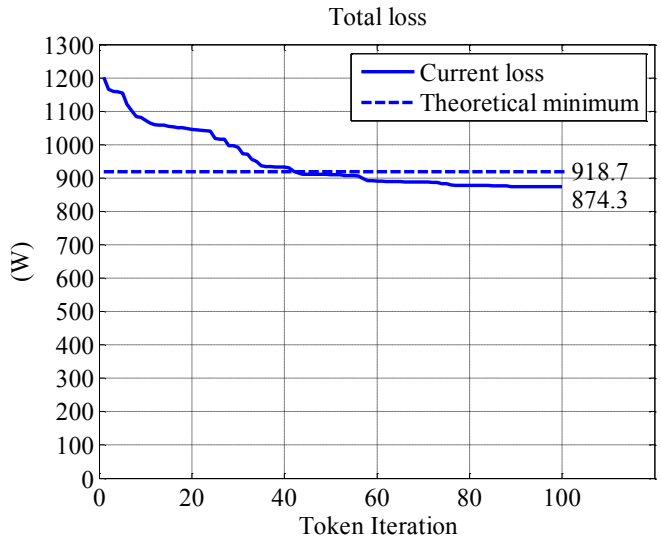

Fig. 4.41 Distribution loss - unconstrained Voltage Based Surround Control - reactive only injection - radial testbench

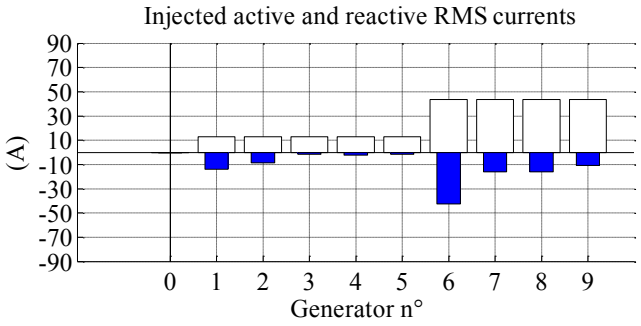

Fig. 4.42 Injected currents - unconstrained Voltage Based Surround Control - reactive only injection (coloured bars)- radial testbench

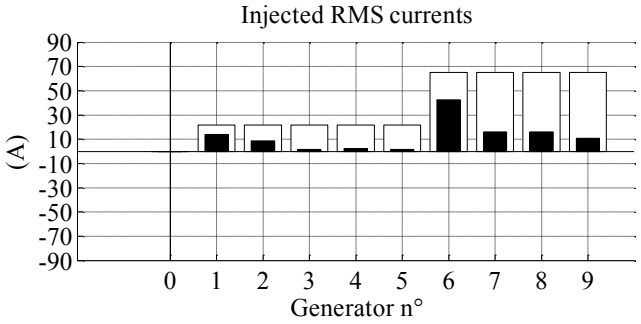

Fig. 4.43 RMS currents – Voltage Based Surround Control - reactive injection - radial testbench

Another important observation is related with voltages in steady state during reactive only injection. Recalling the origin of the surround approach, when injecting reactive currents the technique converges to the condition where all the nodes have zero voltage drop caused by reactive load currents. Therefore the voltages are expected to depend only on the active load currents, as seen in Chapter 3. In particular, the phase of the voltage drops $\dot{V}_{PCC} - \dot{V}_{Gi}$, where $\dot{V}_{Gi}$ is the $i-th$ generator, is supposed to be the same as the line impedance, shifted of π for the is flowing from the PCC to the loads. This is confirmed in Fig. 4.44 :

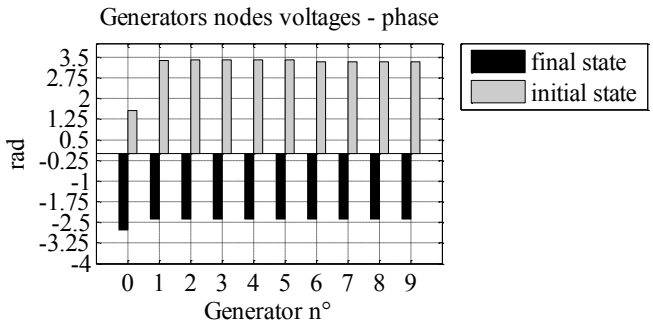

Fig. 4.44 Phase of generators voltage phasors - Voltage Based Surround Control - reactive injection - radial testbench

An interesting result is obtained in the case of saturated active and reactive current injection. In the same case, Plug and Play approaches fails in reducing the loss, due to the lack of information that excludes the peripheral nodes and the limited rating of the active ones. Instead, Voltage Based

Surround Control, succeed in driving the microgrid to the theoretical minimum loss. It has to be observed that the constrained minimum is very closed to the theoretical unconstrained optimum because power ratings of the energy gateways have been chosen so that the load demand is fully balanced by distributed generators (that in general is not enough to guarantee that constrained and unconstrained optimum are similar, because the result depends on the distribution of saturation limits among the energy gateways).

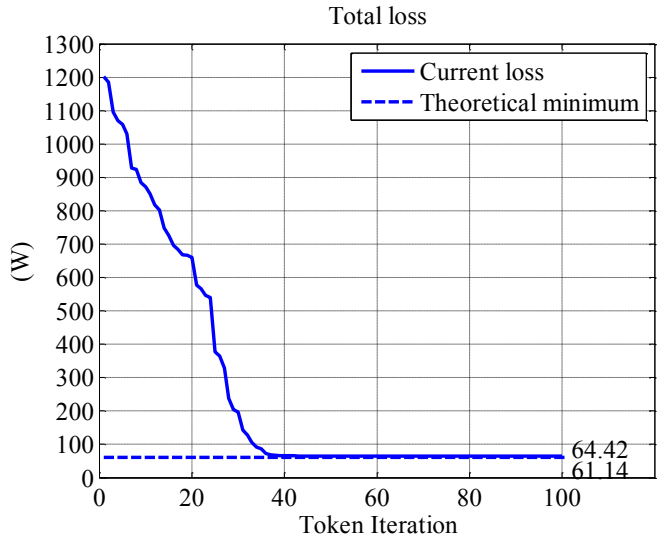

Fig. 4.45 Distribution loss - constrained Voltage Based Surround Control - active and reactive current injection - radial testbench

Fig. 4.45 reports the distribution loss in this condition, compared with the theoretical value. Fig. 4.46 and Fig. 4.47 shows the injected and ideal current references, while in Fig. 4.48 it is shown that only the active current is saturating, while the global injection is below the saturation limit for all the generators. The saturation limits are identified by white bars, and corresponds to active current limits in Fig. 4.46 and Fig. 4.47 and to global current limit in Fig. 4.48 .

As described in Chapter 3, when a node saturates it behaves in a different manner: when questioned by other nodes belonging to its surrounding, instead of communicating its voltage phasor, it communicates the voltages of its other neighbours not seen by the questioning node, thus extending the surround section seen by the Token owner. A saturated node receives the token normally, to check if its condition can be changed.

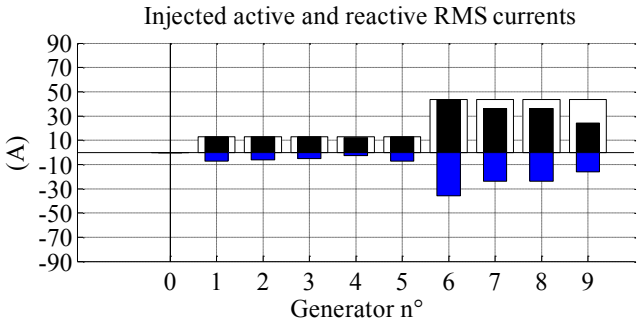

Fig. 4.46 Injected currents - constrained Voltage Based Surround Control – active (black bars) and reactive (coloured bars) injection – radial testbench

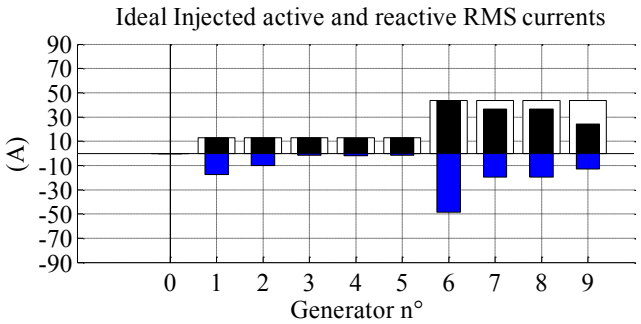

Fig. 4.47 Ideal constrained injected currents for loss minimization in radial testbench - active (black bars) and reactive (coloured bars) injection

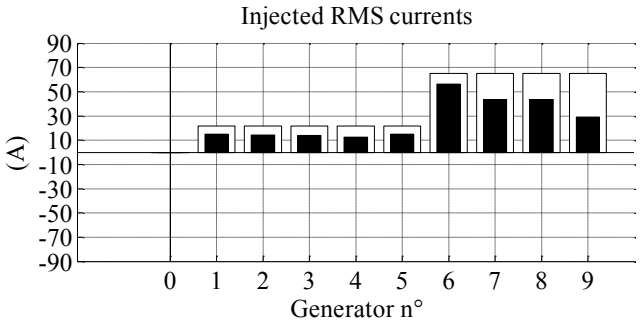

Fig. 4.48 RMS currents - Voltage Based Surround Control – active and reactive injection - radial testbench

To prove the general effectiveness of the technique, the analysis is now performed in the modified radial microgrid, where G_2 and G_6 are removed from the network. Doing so, the microgrid has no longer a clustered structure. Being this case simply a validation of a theoretic aspect, only the unconstrained case will be considered, proving the convergence of Voltage Based Surround Control to the theoretical minimum. The only required hypothesis is constant section of distributed cables, as assumed here. Fig. 4.49 reports the resulting loss compared to the theoretical minimum loss in the modified testbench:

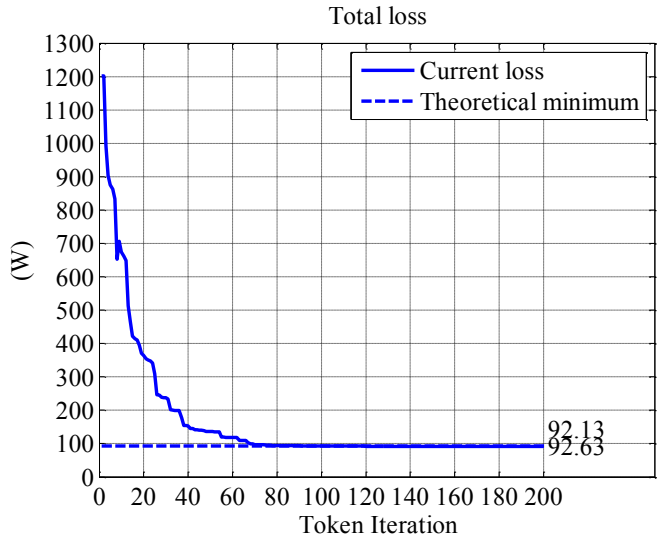

Fig. 4.49 Distribution loss - unconstrained Voltage Based Surround Control - active and reactive current injection – modified radial testbench

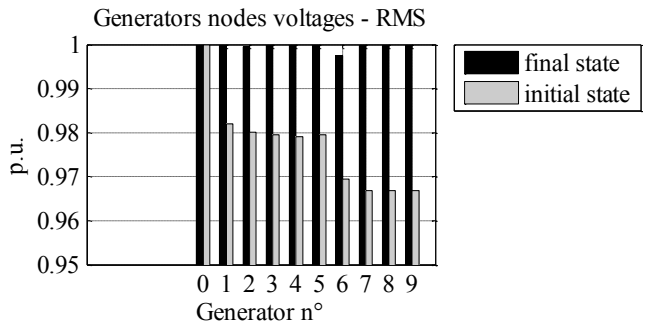

Fig. 4.50 Generators RMS voltages- unconstrained Voltage Based Surround Control - radial modified testbench

Fig. 4.50 show the initial and final (token iteration >100) RMS value of generators voltages. It is interesting to note how the voltages are equal to the PCC voltage (also the phase, omitted for simplicity) apart from G_2 and G_6, with lower RMS values, belonging the nodes to the internal part of a section that can be optimized only acting on the external nodes.

The final simulations for Voltage Based Surround Control investigates the behaviour of the control in the mashed testbench. From a theoretical point of view, the technique can be applied to any topology, and if the section is constant it is expected to drive the microgrid toward the minimum loss, corresponding to equal voltage phasors in all the generators, and equal to the PCC voltage phasor, that is assumed to be purely real. For these reasons no substantial differences are expected from this latter test. The saturated case with both active and reactive current injection has been considered. The loss are reported in Fig. 4.51 , together with the theoretical minimum, and confirms the effectiveness of the method.

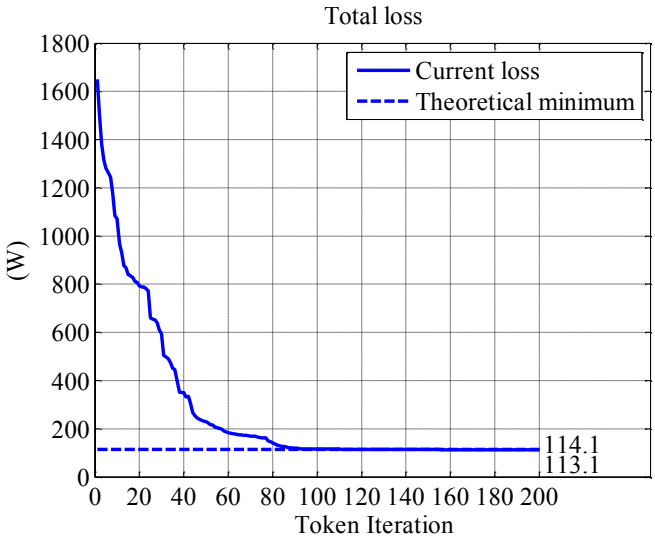

Fig. 4.51 Distribution loss - constrained Voltage Based Surround Control - active and reactive current injection - meshed testbench

4.4.5. Distributed Cooperative Control

The final results are presented for the Cooperative Control. The main idea behind the technique is that the distribution loss minimization corresponds to local supply of load currents: the closer is the generator supplying a load current, the lower are the losses, with the limit case of having all the loads directly supplied by generators, with zero current in all the distribution line, that in this extreme case would become a simple voltage reference for generators and loads. Following this idea, each load could measure the absolute distance with respect to all the generators in the microgrid, and then send to each of them a quote of current demand, inversely dependent on the distance.

As already seen in Chapter 3, this approach cannot be considered an optimum approach. In fact, only in the case of single microgrid cluster (as defined in Chapter 3) the corresponding injected currents are the optimum currents, and therefore the Cooperative Control becomes equivalent to the Current Based Surround Control. In any other case, i.e. with multiple clusters, the solution is suboptimum, because a generator connected between two clusters should in the optimum case inject the two optimum currents for the loads in the surrounding branches, while in the Cooperative Control it injects a quote of all the load currents. Nevertheless this quote is dominated by the two surrounding nodes, and the whole resulting loss is reasonably expected to be closer to the optimum case.

This analogy with the Current Based Surround Control is the reason for analyzing only the Cooperative Control. In fact, the Current Based Surround is applicable only in a clustered microgrid. In any other topology, an additional information on the grid structure would be required to be able to compute the optimum currents, leading to an unpractical technique. Instead, Distributed Cooperative Control gives a sub optimum result but without any information on microgrid topology, apart node

to node (load to generator) distance measurement, that can be implemented in PLC using ranging techniques.

Another interesting feature of Cooperative Control is the simplified management of energy gateways saturations, that has been implemented and tested in simulations. Again, the main driver is the physical distance. All the loads measure the distance with respect to all the generators, and define the quote of current demanded to each of them. When a generator receives the Token, it will enquire all the loads, thus building a “table of current demands”, where at each load correspond a distance and a current demanded by the specific load. Once a generator saturates because the aggregated current demand is over the limits, it can autonomously decide to reduce the current demand, starting from the farer demanding loads, until the limits are respected. A new table is therefore filled, with the references that have been modified by the generator and sent back to the loads whose current demand cannot be fully satisfied. These loads will change the repartition of the portion of current demand that cannot be satisfied, trying to charge with it other generators. Of course the system has to be sensitive to changes in loads and generators, and therefore the “updated table” has to be reset to the original one (purely dependent on distances) if one of the loads or generators is disconnected or changes its available rating. In case of load change, the “original table “ has to be built ex-novo.

Being this algorithm a feed forward solution, the speed of detection of this changes is fundamental for the microgrid to avoid misbehaviours, and in particular the required timeslot has to be faster than the interval between two Token iterations.

As in the previous techniques, the Cooperative Control has been tested in the radial and meshed testbench. To better focus on the control behaviour and on the saturation management technique, only the case of full current injection will be considered, comparing for each testbench the three following situations: unconstrained current injection, saturated current injection without saturation management and finally saturated injection with saturation management. Starting from the radial microgrid, the loss with unconstrained injection is in Fig. 4.52 :

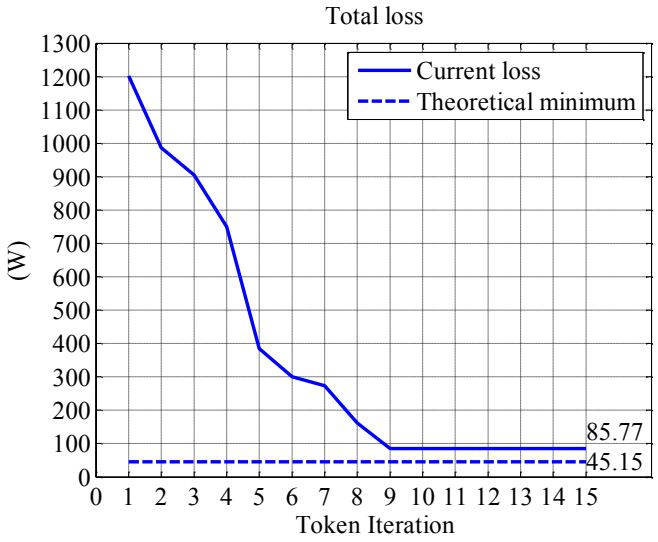

Fig. 4.52 Distribution loss - unconstrained Cooperative Control - active and reactive current injection - radial testbench

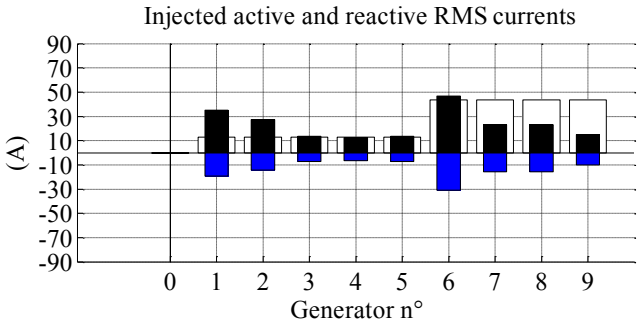

Fig. 4.53 Injected currents - unconstrained Cooperative Control – active (black bars) and reactive (coloured bars) injection – radial testbench

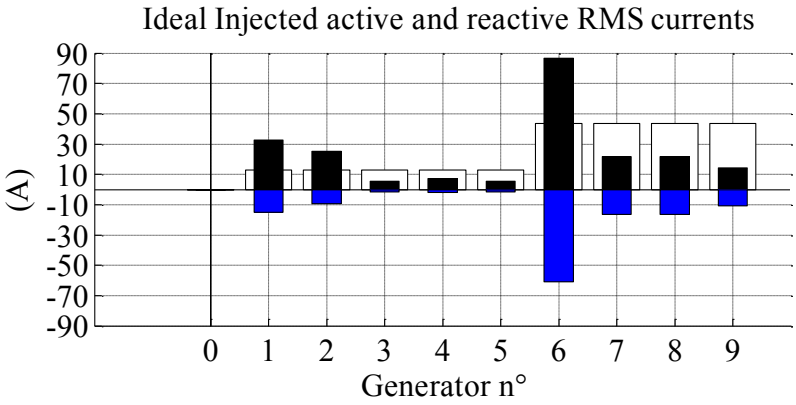

Fig. 4.54 Ideal unconstrained injected currents for loss minimization in radial testbench - active (black bars) and reactive (coloured bars)

Moreover, Fig. 4.53 and Fig. 4.54 show the correspondent injected currents and the theoretical optimum current set. Observing the loss, the final result is very close to the one obtained with Plug and Play control. The main advantage here is that the current demand from the generators required to reduce the loss is shared among the energy gateways. Comparing the set of injected currents with

the theoretical optimum of the testbench, the origin of the non optimized loss becomes evident: in the ideal set, G_6 is the most loaded generator, and the reason is that it has to feed all the heaviest loads of the network, L_7, L_8, L_9, generating most of their current demand. In the Cooperative Control, part of this current is also divided among the farer generators (PCC included even if not reported, being its current not controlled), resulting in a more shared demand even compared to the ideal case. This current partition can be better appreciated comparing the ideal bus currents and the bus currents after Cooperative control, in Fig. 4.55 . In the ideal case $B16$ and $B61$ have much lower current, being most of the heavy loads current coming from G_6.

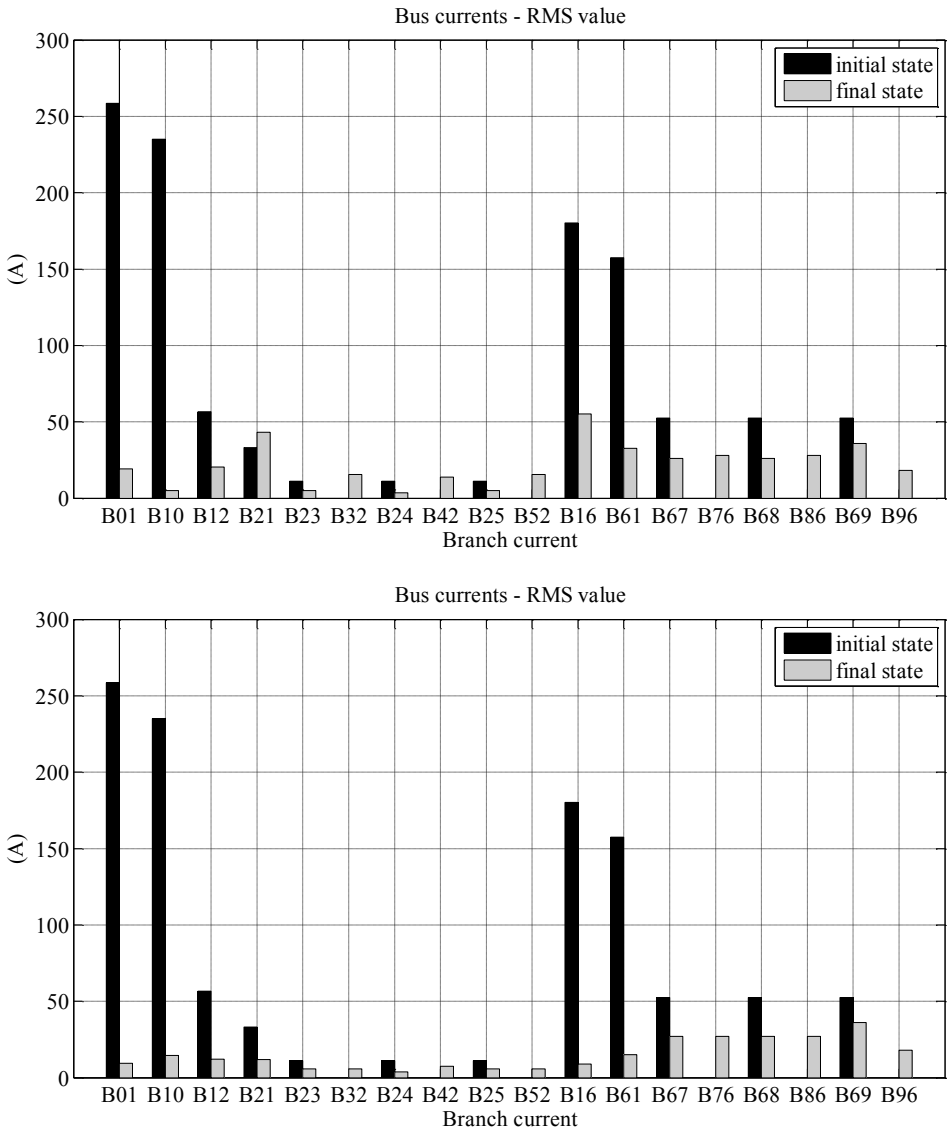

Fig. 4.55 Comparison between unconstrained Cooperative Control bus currents (top figure) and ideal unconstrained bus currents (bottom figure) – active and reactive injection – radial testbench

Therefore, a first main advantage of the technique is that accepting a sub optimum loss, a consistent reduction of generators current stresses is possible. This is true also comparing with

Voltage Based Surround, that in the unconstrained case corresponds in steady state with the ideal injection.

Introducing the energy gateways saturations, the results are presented in parallel for the unmanaged saturations and the proposed management technique, both compared with theoretical minimum. For a more practical comparison, the sequence of Token owners is the same in the two simulations, and not randomized. Fig. 4.56 reports the loss in the two cases:

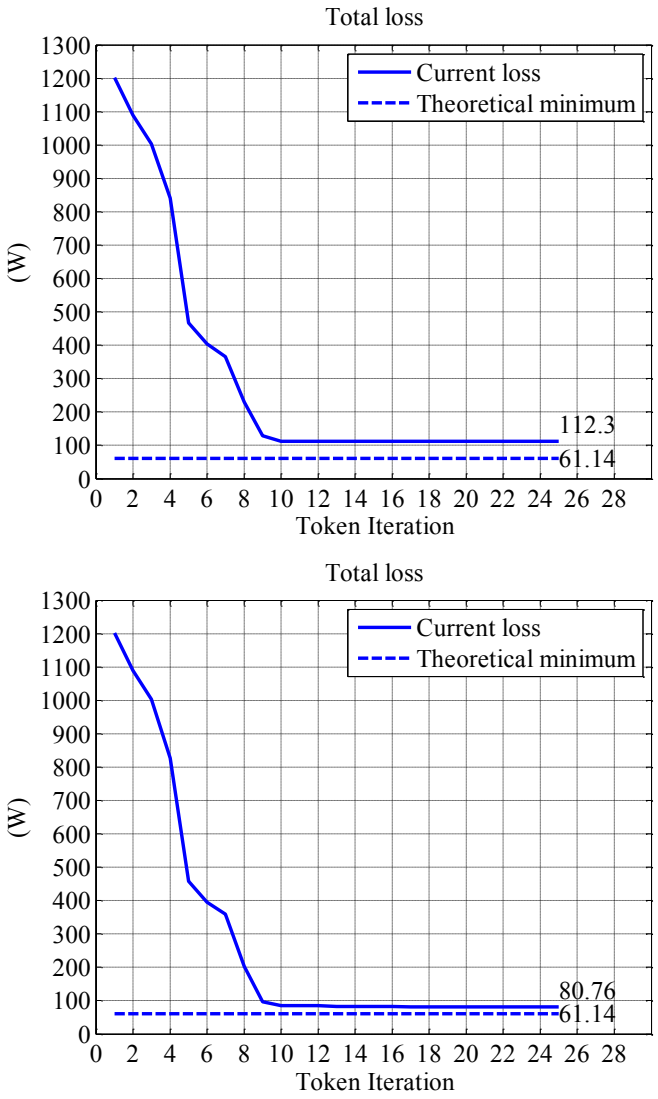

Fig. 4.56 Distribution loss – constrained Cooperative Control – active and reactive current injection -.radial testbench – comparison between unmanaged saturations (top figure) and proposed management technique (bottom figure)

From the figure it is evident how the proposed saturations control improves the performances of Cooperative Control, further reducing the loss. This is due to the very basic principle of dividing the currents demanded by the loads and that a saturated generator is not able to inject among the other generators. The behaviour can be appreciated comparing in Fig. 4.57 the injected currents in the two

conditions, reported together with Fig. 4.53 , recalling the currents that the Cooperative Control tries to inject in the unconstrained case.

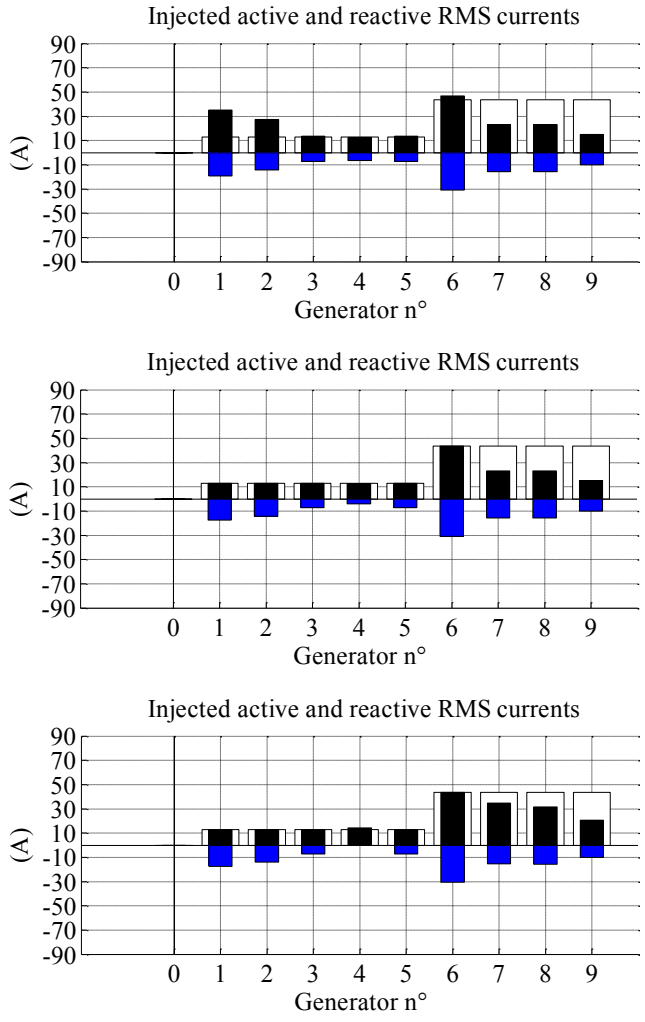

Fig. 4.57 Injected currents – a) unconstrained, b) constrained, c) constrained with saturations management Cooperative Control - active (black bars) and reactive (coloured bars) injection - radial testbench

From figure b) it can be appreciated how the original saturated version of the Cooperative Control simply clamps the current references demanded by the loads, limiting the injection to the available capacity. In particular, this can be seen in G_1 and G_2, while the other generators are all within the limits or very close to, like G_6. The specific testbench is not the most significant to highlight differences between the saturation managements, as shown in Fig. 4.56 from the slight loss improvement. Anyway, figure c) shows how the currents that cannot be given by G_1 and G_2 are partitioned among the unsaturated generators G_7, G_8 and G_9. A smaller power rating of G_6 would better highlight the improvement, also in terms of loss.

Only to give a comparison to the previous results, Fig. 4.58 reports the loss with Cooperative Control and reactive only constrained current injection, with saturation management. In this specific

condition, none of the saturations is active, as reported in the total injected RMS currents in Fig. 4.59 (that being the injection purely reactive correspond to minus the reactive components of injected currents phasors).

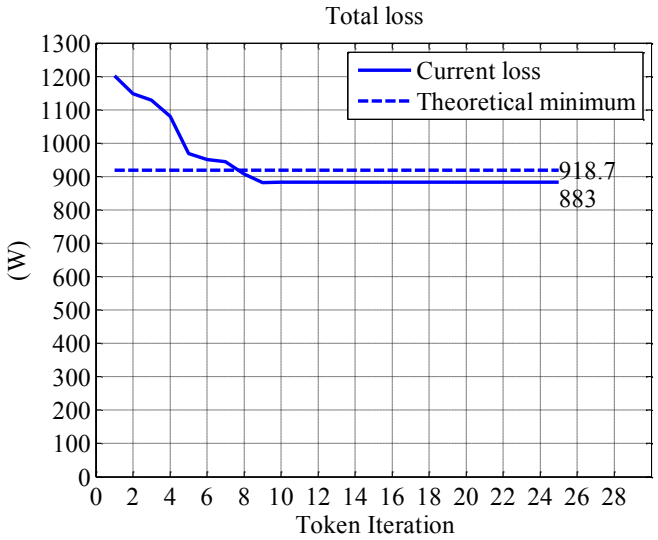

Fig. 4.58 Distribution loss - constrained Cooperative Control - radial testbench – reactive only injection

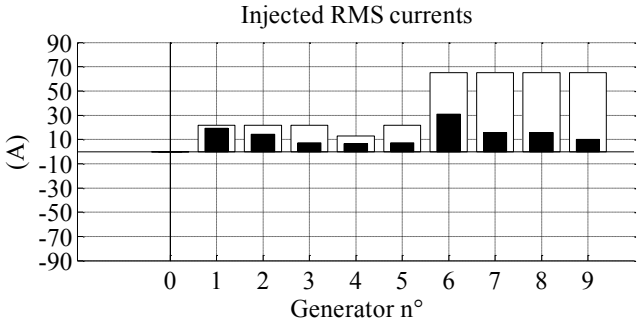

Fig. 4.59 RMS currents – unconstrained Cooperative Control–reactive only injection - radial testbench

The results in the meshed testbench are omitted for simplicity, being their information content quite limited. In fact, the technique doesn't suffer particular variations on system topology.

As a conclusion, the proposed loss minimization techniques have been tested in simulation using a Matlab based software to solve an approximated model of a microgrid. The microgrid has been designed to represent a possible testbench for a practical implementation of the controllers, that will be developed in the prosecution of this work. As expected, the Plug and Play approach is effective only if the power converters are strategically placed in the microgrid, and rated for the compensation of a relevant percentage of the loads. The limited performances are due to the availability of local information only. Voltage Based Surround Control guarantees convergence to the theoretical optimum both in the unconstrained and in the constrained case. This is true in the hypothesis of constant cable section, otherwise additional information on the network would be required. Even in the ideal case, the amount of data required by a generator when it receives the Token and has to

perform the control action is not negligible: neighbourhood identification and distance measurements, as well as communication of voltage phasors in a synchronized reference frame. Therefore the good performances come at the cost of complex communication, measurement and data exchange requirements. The final method, the Cooperative Control has been developed to significantly simplify all the system, thanks to the fact that only distance measurement is required, and current references can be sent to the generators in form of power signals, in the hypothesis of negligible voltage variations. From an infrastructural point of view, Cooperative Control requires communication capability also in the loads, while Voltage Based Surround Control only on energy gateways. The global simplification is obtained accepting as a drawback a non optimal loss, that is still close to the theoretical minimum and appears to be a reasonable compromise.

In the future developments of this work, the three distributed loss minimization solutions will be tested in a laboratory scale microgrid, implementing the testbenches proposed here.

PART II

Use of a STATCOM with Energy Storage for Frequency Stability Enhancements in Microgrids

Chapter 5

Microgrid Frequency Stabilization during Load Transients

5.1. Introduction

The aim of this part of the work is to address a specific problem, that is the frequency stability in microgrids fed by synchronous machines with a combustion diesel or gas powered engine as prime mover [128, 129, 130, 131, 132, 133, 134, 135]. This project has been developed during the period spent with the PEMC group at the University of Nottingham, UK.

Specifically, the simplified scenario of a single synchronous machine is considered, to avoid the effects of machine to machine interactions in case of multiple generators. First observing the problem from a qualitative perspective, the slow dynamic of the combustion engine is unable to follow fast active power variations in the load. In case of a sudden load power increase, the energy required to supply the load is not instantaneously released by the combustion process but has to be subtracted by the mechanical energy of the system: the net result is a drop in the generator speed, meaning a drop in the generated output frequency. The opposite holds for steps down in the active load demand, causing over-frequency. Both the events are hazardous for the utilities that require a tight frequency regulation and for the stability of grid frequency regulation. For these reasons, the national and international regulations such as IEEE 1547 [122] for connection of distributed generators, impose specific limits to the allowed frequency variation of the generated power. When these limits are overcome by a distributed generator, it has to be disconnected from the grid. The problem exists in any power system where generation is demanded to synchronous machines. Therefore the result of this work is potentially applicable to a generic power systems.

Following the analysis on microgrids carried on in the first part of this thesis, the choice has been to focus the attention on that specific power system. In particular, a microgrid can be equipped with a number of small power distributed synchronous generator. When the microgrid is in grid connected operation, the power that the distributed generators, for their slow dynamic, cannot

provide during load transients is absorbed by the main utility, from the PCC (Point of Common Coupling). Being the main grid a stiff source, the frequency is expected to be stable. What can happens instead is a voltage transient due to the current peak absorbed from the main grid during the transient, until the distributed generators reaches their steady state, with the Automatic Voltage Regulators leading the voltage to the nominal value (normally through droop control for reactive power sharing). The voltage transient is due to the drop on the PCC equivalent impedance caused by the absorbed current peak, as shown in [128]. On the contrary, when the microgrid is operating in islanded conditions, the risk is a chain reaction leading to a black out: when a generator experiences a load step and is disconnected after a frequency limit breaking, its disconnection appears to the other generator as another load step variation, that may cause other disconnections, in a process that could eventually turn off all the generators, interrupting the supply of the loads. The problem is amplified in microgrids, where synchronous machines have normally small power, in the order of tens of kW, and therefore low inertia and less stored kinetic energy.

This latter condition is investigated in this work, analyzing a simple microgrid, fed by a single synchronous machine. The simplification has been chosen to better focus on load transient effects on a single machine, avoiding interactions with other machines. Future developments will consider the extension to a generic microgrid.

The proposed solution is the combination of a synchronous generator and a STATCOM (STATic COMpensator) with energy storage capabilities. The storage can be realized with supercapacitors or batteries, but can be extended to any other energy source, the only requirement is a fast dynamic response, to be able to inject consistent amount of energy in few line cycles. The combined system is schematically represented in Fig. 5.1 :

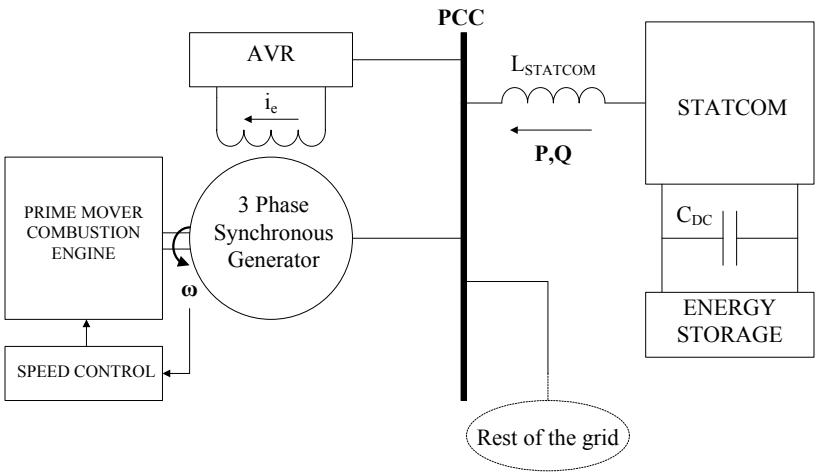

Fig. 5.1 Synchronous generator and STATCOM with energy storage

In Fig. 5.1 , on the left of the PCC (Point of Common Coupling) the three phase synchronous generator is shown, together with the prime mover endothermic engine with its speed controller, and the AVR (Automatic Voltage Regulator), controlling the generator field excitation current i_e to keep constant the voltage at the PCC. The choice of using a STATCOM is at this stage of the project an arbitrary choice, mainly related with possible future application of the system to higher power generators (>1MW). For the small power that will be processed here (10kW), the power converter could be better defined an active power filter (APF). Nevertheless, the term STATCOM will be adopted to keep in mind the general value of the approach.

Before moving to the specific system, it is worth to remind the possible generation structures in a microgrid. In fact, distributed generation can be classified in two categories: synchronous machines and electronically interfaced sources, as in Fig. 5.2 :

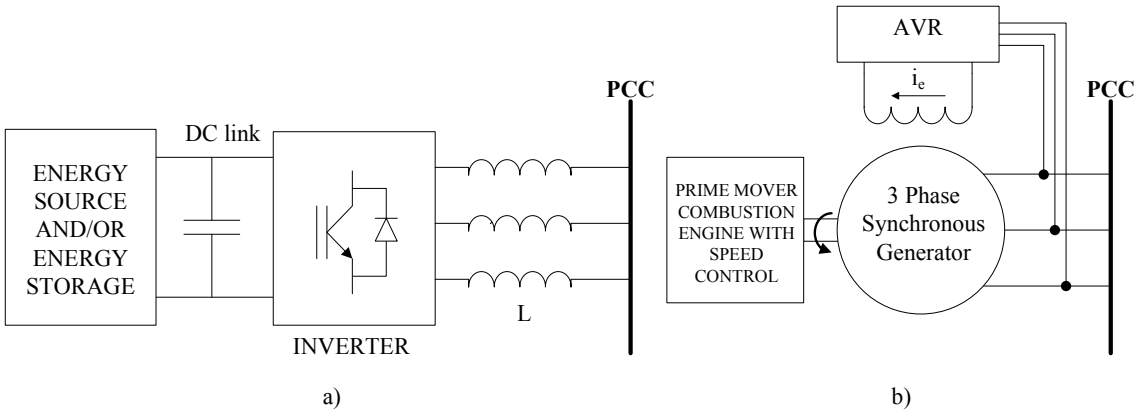

Fig. 5.2 Distributed Generators classification: a) Power electronics interfaced distributed generator, b) Synchronous-generator

In Fig. 5.2 a) the power electronics interfaced system is presented with its basic components: the energy source, that could be renewable like wind turbines, photovoltaic systems, fuel cells, gas turbines or diesel generators. Moreover, the energy source can be substituted by or coupled with an energy storage, like batteries or supercapacitors, as a backup or to improve the transient responses. The energy source has to be interfaced with a DC link, and thus a first stage is required to provide a suitable link voltage. The topology of the first stage depends on the nature of the energy source: alternated sources require an AC/DC converter, typically a controlled rectifier, while DC sources require a DC/DC converter to optimize the voltage levels. The second stage is a DC/AC converter, to fully control the power injected in the PCC.

Fig. 5.2 b) represents the distributed generation based on synchronous machines, that is historically one of the most common generation system, both for big power plants, rated for MW, and for small backup generators rated for few kW. A prime mover, that for large power application is a steam or water turbine, while for the small system is often an endothermic engine, run at fixed

speed through a speed controller. The rotor of the synchronous generator is coupled with the output shaft. The generated frequency depends on the speed of the prime mover, while the voltage amplitude is controlled by an AVR (automatic Voltage Regulator), defining the excitation current for the rotor and therefore the magnetic field of the machine. The output of the generator is directly connected to the PCC. The main advantages of these machines are related with the intrinsic robustness of the construction that increases the reliability of the power generation.

In recent years, with the improvements in power electronics solutions, most of the small power production has moved toward the solution a). In fact, especially for engine driven synchronous generators, improvements in efficiency can be achieved decoupling the prime mover speed and the output frequency of the generated voltage: in that way the engine can be run at its maximum efficiency speed, that is a function of the generated power, without the limits imposed by the grid frequency. Nevertheless, the topology represented in b) is still widespread for many applications, and this work proposes a solution that could results in an upgrade of the existing plants to improve their performances.

For any power system, the most important requirements are to keep the synchronization of all the generators, meaning that the frequency has to be as constant as possible for all the generators, and the voltage level has to stay within the under voltage and over voltage limits for all the loads. In large synchronous generators powered grids, this is mostly related with load transient events causing acceleration or deceleration of the prime mover, before recovering the nominal frequency. The problem is usually solved designing the power system with large stability tolerances. Moreover, the inertia of large power machines helps the reduction of the speed variations, being the inertia increasing faster than the power rating.

In the next sections, the analysis of frequency stability issues during load step changes in active power will be presented. Finally, a coordinated control of the STATCOM plus energy storage coupled with the synchronous generator is proposed to ride through load steps keeping the required tight frequency regulation band. The proposed technique has been validated through simulations in Matlab Simulink and building a scaled experimental rig, rated for 10kW, confirming the effectiveness of the proposed solution. Simulations and experimental will be shown in Chapter 6 and 7 respectively.

5.2. Description of the considered system

The final goal of the project is to demonstrate, both theoretically and experimentally, the improvements in frequency stability of a synchronous generator fed microgrid, using a STATCOM with energy storage to support the generator during the transient that follows a load step change in the absorbed active power. To focus the attention on the basic compensation principle, a very simple three-phase isolated micro-grid is assumed, as schematically reported in Fig. 5.3 :

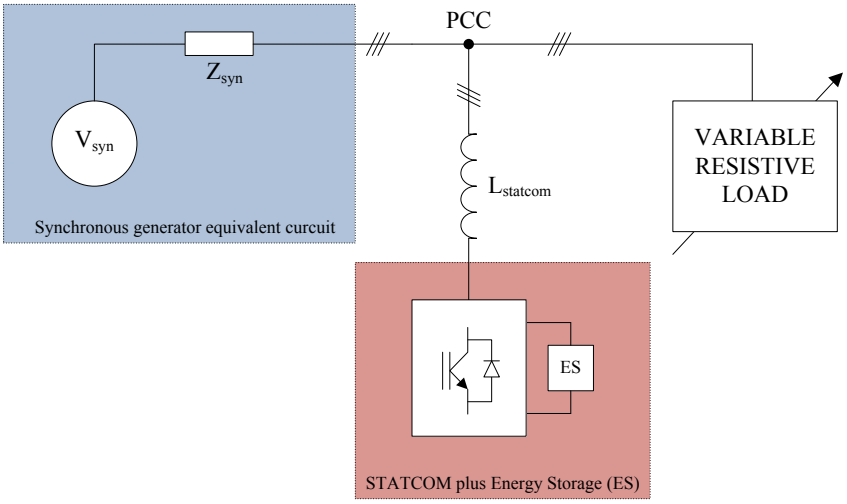

Fig. 5.3 Considered three-phase micro-grid

In addition, some other simplifications have been done:

- The module of the generator internal impedance Z_{syn} is assumed to be negligible if compared with the minimum resistive load, meaning that the voltage sag at the PCC is negligible, and the voltage can be considered equal to the generator voltage V_{syn}, regulated by the AVR. The synchronous machine model is not considered.

- The STATCOM is used just as active power compensator, being the load a pure resistive load. The injected active power comes from an Energy Storage, that in this first study is an infinite energy source. In this way, the analysis and the compensation can be done without the constraints of a limited amount of stored energy, that would be a more realistic scenario in case of a SuperCaps and batteries based energy storage.

- No distribution line impedances are considered.

- The prime mover for the synchronous generator is assumed to be a diesel engine.

5.2.1. Origin of the frequency variation during load power transients

The frequency variation under load active power steps is due to the slow dynamic of the prime mover speed control loop, mainly limited by the prime mover energy conversion transfer function. In a diesel engine this transfer function is the one between the throttle demand coming from the speed regulator and the generated torque after the chemical to mechanical energy conversion process operated by the engine. Fig. 5.4 reports the block diagram of the prime mover speed control, with the main considered parts, without STATCOM plus Energy Storage.

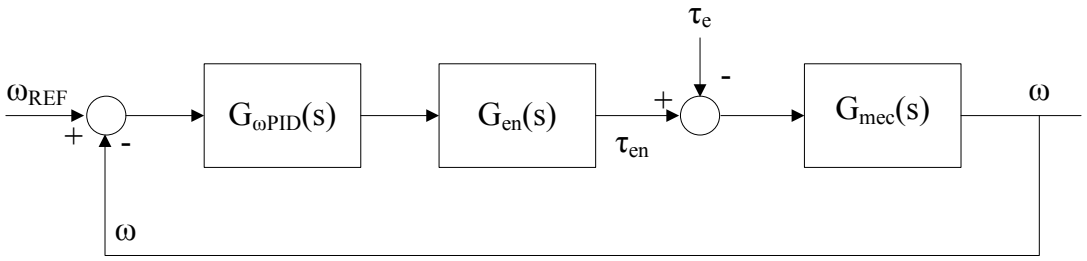

Fig. 5.4 Prime mover speed control loop

Where $G_{\omega PID(s)}$ is the PID regulator transfer function, $G_{en}(s)$ the throttle to torque transfer function for the diesel engine, $G_{mec}(s)$ the mechanical load, and τ_e the load torque due to the resistive loads, representing a disturbance for the regulation loop. The prime mover is connected to the synchronous generator, and then the only load torque is the electric torque related with the generator loading. The analysis neglects the exact diesel engine transfer function $G_{en}(s)$, for different reasons. First because the behaviour of a diesel engine is strongly nonlinear, making difficult to do assumptions about the transfer functions without a real diesel engine in the experimental rig. In fact, in the experimental part in Chapter 7, an induction motor has been used to emulate the prime mover dynamic. Second because the structure of the experimental setup with the induction is flexible enough to permit future developments and refinements of the diesel engine modelling. In this analysis, the diesel engine has been modelled in the most simple way as a first order transfer function, with time constant T_{en} taking into account the combustion system delays, assumed to be of the order of few hundreds of milliseconds. After these considerations, the transfer functions in Fig. 5.3 are:

$$
\begin{aligned}
G_{\omega PID}(s) &= K_{P\omega} + \frac{K_{I\omega}}{s} + K_{D\omega}s \\
G_{en}(s) &= \frac{1}{1+T_{en}s} \\
G_{mec}(s) &= \frac{1}{B+Js}
\end{aligned}
\qquad (5.1)
$$

From another perspective, Fig. 5.3 represent the linearization of the system around the nominal speed. With this approximation, the mechanical power generated by the engine and the electrical active power absorbed by the load can be represented by the correspondent torques. In equations (5.1), $K_{P\omega}$, $K_{I\omega}$ and $K_{D\omega}$ are the coefficients of the PID regulator, B is the friction factor of the mechanical load and J is the inertia of the coupled system diesel engine plus synchronous generator. With the approximation assumed for the engine transfer function, the derivative action is not necessary to close a stable control loop, being the maximum phase lag of the plant $G_P(s) = G_{en}(s)G_{mec}(s)$ equal to $-\pi$, but is required if the bandwidth has to be increased keeping a desired phase margin. For simplicity, the next analysis is carried out assuming that a PI regulator is enough to fulfil the closed loop design requirements. In this conditions, the effect of a load torque on the mechanical speed is described by the transfer function:

$$G_{\tau\omega}(s) = -\frac{G_{mec}(s)}{1 + G_{mec}(s)G_{en}(s)G_{\omega PI}(s)} \tag{5.2}$$

Where:

$$\begin{aligned} G_{\omega PI}(s) &= \frac{K_{I\omega}}{s}(1 + sT_{I\omega}) \\ T_{I\omega} &= \frac{K_{P\omega}}{K_{I\omega}} \end{aligned} \tag{5.3}$$

Substituting all the transfer functions in (5.2) results:

$$\begin{aligned} G_{\tau\omega}(s) = -\frac{s(1 + sT_{I\omega})}{(B + Js)(1 + sT_{en})s + K_{I\omega}(1 + sT_{I\omega})} = \\ -\frac{s^2 T_{I\omega} + s}{\tau_{en} J s^3 + (J + BT_{en})s^2 + (B + K_{I\omega}T_{I\omega})s + K_{I\omega}} \end{aligned} \tag{5.4}$$

The result is a band-pass transfer function, responding to a step input with an impulsive output. A simplified expression of the speed disturbance in the time domain can be derived assuming to design the PI controller with time constant $T_{I\omega} = T_{en}$. With this assumption, the transfer function becomes:

$$G_{\tau\omega}(s) = -\frac{1}{J}\frac{s}{s^2 + \frac{B}{J}s + \frac{K_{I\omega}}{J}} \tag{5.5}$$

The response to a step change in the load torque with amplitude A is, in the Laplace domain:

$$\Omega(s) = -\frac{A}{J}\frac{1}{s^2 + \frac{B}{J}s + \frac{K_{I\omega}}{J}} \tag{5.6}$$

The poles of $\Omega(s)$ are:

$$p_{1,2} = \frac{B}{J}\left(-1 \pm \sqrt{1 - \frac{4K_{I\omega}J}{B^2}}\right) \tag{5.7}$$

Assuming the PI designed to give a non oscillatory response, the poles will be real, meaning that:

$$\frac{4K_{I\omega}J}{B^2} < 1 \tag{5.8}$$

With all these hypothesis, equation (5.6) can be rewritten as:

$$\Omega(s) = -\frac{A}{J(p_1 - p_2)}\left(\frac{1}{s - p_1} - \frac{1}{s - p_2}\right) \tag{5.9}$$

Whose inverse Laplace transform is

$$\begin{aligned}\omega(t) &= -\frac{A}{J(p_1 - p_2)}\left(\exp(p_1 t) - \exp(p_2 t)\right) = \\ &-\frac{A}{2B\sqrt{1 - \frac{4K_{I\omega}J}{B^2}}}\left(\exp\left(\frac{B}{J}\left(-1 + \sqrt{1 - \frac{4K_{I\omega}J}{B^2}}\right)t\right) - \exp\left(\frac{B}{J}\left(-1 - \sqrt{1 - \frac{4K_{I\omega}J}{B^2}}\right)t\right)\right)\end{aligned} \tag{5.10}$$

Equation (5.10) represents the speed component due to the load torque disturbance, that has to be added to the steady state component due to the input ω_{REF}. Hence, for a positive step, A>0, (5.10) will be a negative function, meaning a reduction in the generator speed, while the opposite holds for a negative step, A<0.

The time derivative of equation (5.10) permits to find the minimum or maximum of the speed variation, defining the maximum acceptable load torque step amplitude A for a given system, to fulfil the frequency regulation requirements. Using the implicit representation of (5.10):

$$\frac{d\omega(t)}{dt} = 0 \rightarrow \left(p_1 \exp(p_1 t^*) - p_2 \exp(p_2 t^*)\right) = 0 \rightarrow p_1 \exp(p_1 t^*) = p_2 \exp(p_2 t^*) \rightarrow t^* = \frac{\ln\left(\frac{p_1}{p_2}\right)}{p_2 - p_1} \tag{5.11}$$

$$\omega_{\min,\max} = \omega(t^*) = -\frac{A}{J(p_1 - p_2)}\left(\exp\left(p_1\frac{\ln\left(\frac{p_1}{p_2}\right)}{p_2 - p_1}\right) - \exp\left(p_2\frac{\ln\left(\frac{p_1}{p_2}\right)}{p_2 - p_1}\right)\right) \tag{5.12}$$

As previously stated, the load torque τ_e is the equivalent electric torque due to the loading of the synchronous generator, derived from the electromechanic power balance. Assuming a three phase synchronous generator with symmetric voltages, with concatenated RMS value V_{c_RMS} and balanced star-connected resistive load R:

$$P_{mec}(t) = P_{el}(t) \rightarrow \omega\tau_e = \frac{V_{c\_RMS}^{\ 2}}{R} \rightarrow \tau_e = \frac{V_{c\_RMS}^{\ 2}}{\omega R} \tag{5.13}$$

Comparing equation (5.13) with Fig. 5.3 , it can be observed that the electric load equivalent torque is not an independent input as it has been so far considered, but is related with the mechanical speed through the nonlinear equation (5.13). In general this is solved stating that the system has to be designed to have a minimum speed variation, such that the ω in (5.13) can be considered $\omega \approx \omega_{REF}$.

5.3. Optimum response to large load step transients

Actually, the analysis in the previous section is implicitly assuming a small signal perturbation in the load torque, so that the regulation loop remains closed and all the equations (5.5)-(5.13) are valid. In general, for large load power variations, the speed PI controller saturates, giving to the output speed response a different behaviour, becoming the system an open-loop transfer function, at least for some intervals during the transient.

To avoid the transients that affect the integral part of the PI after the saturation, a theoretical optimum management of the PI controller during large load steps is now proposed, that minimizes the amplitude of the speed variation and the duration of the correspondent transient: when a load power step from an initial value P_1 to $P_2 < P_{MAX}$ is detected (assuming to have access to all the required information and measurements), the PI regulator is saturated, to zero or to the maximum throttle, depending on the load step direction. After that, the duration of the maximum throttle phase is computed, together with the following minimum throttle phase, in a MAX-MIN impulsive action that restores the nominal speed. The obtained response is the fastest achievable dynamic with the existing system. That dynamic will be strongly improved with the addition of the STATCOM plus energy storage, as it will be shown in the next sections.

It is worth to note that normally the throttle should be expressed as a 0-1 saturated value. In this initial analysis the throttle is assumed to be between zero and the maximum torque, without loss of generality.

In this large-signals control management, the PI can be considered instantaneously saturated to the maximum or minimum value, so that the control system becomes the open loop one depicted in Fig. 5.5 , where a step up load power transient is considered and the mechanical plant is assumed to be lossless (B=0), so that in steady state the diesel engine torque exactly matches the load torque. After the optimum control action, the PI control is restored to maintain the close loop regulation

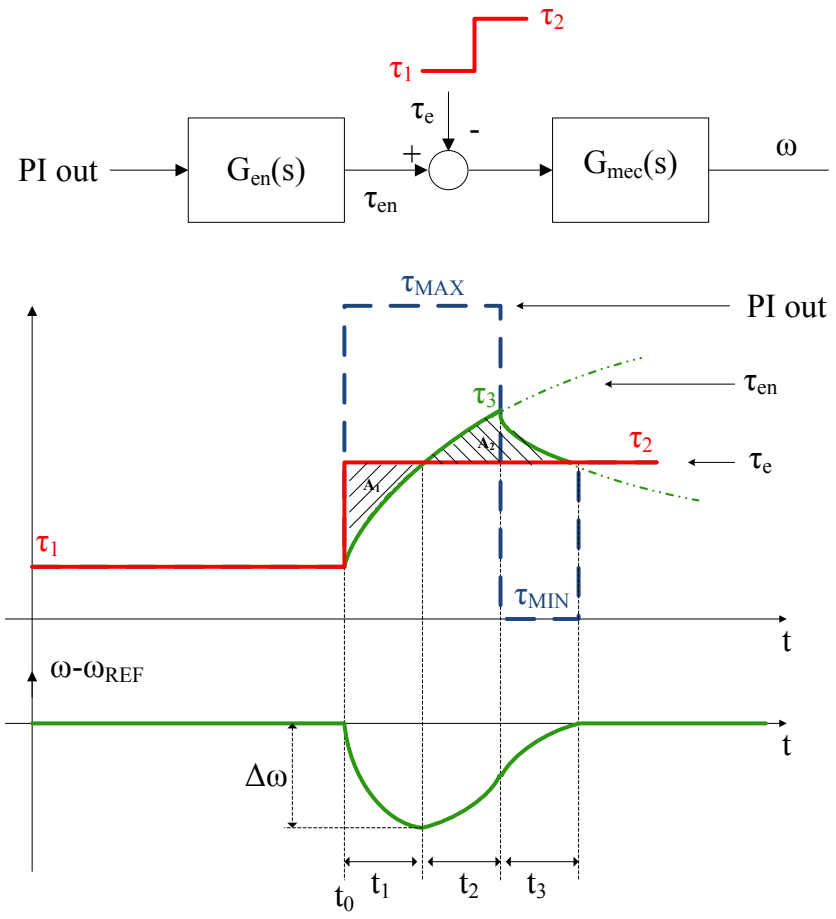

Fig. 5.5 Optimum transient response to a load torque step up transient

The application of the optimum algorithm consists on the calculation of the time intervals t_1, t_2 and t_3, to finally calculate the duration of the τ_{MAX} phase $T_{\tau MAX}= t_1+ t_2$ and the τ_{MIN} phase $T_{\tau MIN}= t_3$. The very basic principle behind the calculation is the balance of the two positive areas A_1 and A_2.during the transient. In the next equations, the steps to find the intervals are schematically reported, supposing instantaneous detection of the load torque variation and measurement of the load torque, so that the values τ_1 and τ_2 are known.

Step 1: Calculation of A_1 and t_1

Remembering that $G_{en}(s)$ is assumed to be a first order transfer function with time constant T_{en}, the waveform of the diesel engine generated torque τ_{en} is known from the load transient instant t_0=0:

$$\tau_{en}'(t) = \tau_1 + (\tau_{MAX} - \tau_1)\left(1 - e^{-\frac{t}{T_{en}}}\right) \quad t_0<t<(t_1+ t_2) \tag{5.14}$$

The positive area A_1 is now derived integrating the positive function $\tau_2(t)$-$\tau_{en}(t)$ for the time interval [0 t_1]. Before calculating the integral, the interval t_1 is required, and can be simply derived observing that:

$$\tau_{en}'(t_1) = \tau_1 + (\tau_{MAX} - \tau_1)\left(1 - e^{-\frac{t_1}{T_{en}}}\right) = \tau_2 \tag{5.15}$$

Hence:

$$t_1 = -T_{en}\ln\left(1 - \frac{\tau_2 - \tau_1}{\tau_{MAX} - \tau_1}\right) \tag{5.16}$$

And the area A_1:

$$A_1 = \int_0^{t_1}\left(\tau_2 - \tau_{en}'(t)\right)dt = (\tau_2 - \tau_{MAX})t_1 + T_{en}(\tau_{MAX} - \tau_1)\left(1 - e^{-\frac{t_1}{T_{en}}}\right) \tag{5.17}$$

Both in equation (5.16) and (5.17), all the variables are known, so t_1 and A_1 are known.

Step 2: Calculation of A_2, t_2 and t_3

Naming τ_3 the maximum torque generated by the engine at the time t_1+t_2, and observing that the engine torque during the τ_{MIN} phase is:

$$\tau_{en}''(t) = \tau_3 e^{-\frac{t-(t_1+t_2)}{T_{en}}} \quad (t_1+t_2)<t<(t_1+t_2+t_3) \tag{5.18}$$

$$\begin{aligned} A_2 &= \int_{t_1}^{t_1+t_2}\left(\tau_{en}'(t) - \tau_2\right)dt + \int_{t_1+t_2}^{t_1+t_2+t_3}\left(\tau_3 e^{-\frac{t-(t_1+t_2)}{T_{en}}} - \tau_2\right)dt = \\ &(\tau_{MAX} - \tau_2)t_2 - \tau_2 t_3 + \tau_3 T_{en}\left(1 - e^{-\frac{t_3}{T_{en}}}\right) + T_{en}(\tau_{MAX} - \tau_1)\left(e^{-\frac{t_1+t_2}{T_{en}}} - e^{-\frac{t_1}{T_{en}}}\right) \end{aligned} \tag{5.19}$$

Moreover, setting $\tau_{en}' = \tau_{en}''$ in $t=t_1+t_2$:

$$\begin{cases} \tau_3 = \tau_2 e^{-\frac{t_3}{T_{en}}} \\ \tau_3 = \tau_1 + (\tau_{MAX} - \tau_1)\left(1 - e^{-\frac{t_1+t_2}{T_{en}}}\right) \end{cases} \tag{5.20}$$

Equations (5.20) give a relation between the time intervals t_2 and t_3.

Step 3: $T_{\tau MAX}$ and $T_{\tau MIN}$ calculation

Substituting (5.20) into (5.19), equation (5.19) can be rewritten as a function of a single unknown time interval t_2 or t_3. The unknown can now be calculated introducing the areas balance between A_1 and A_2:

$$A_1 = A_2 \tag{5.21}$$

Where A_1 is already known from (5.17). Once the intervals t_2 and t_3 have been calculated, the intervals $T_{\tau MAX}$ and $T_{\tau MIN}$ can be derived from Fig. 5.5 . The full calculation is omitted for simplicity, being simply a combination of the reported equations.

It is interesting to calculate the minimum achievable speed deviation $\Delta\omega$ adopting the optimum controller. Assuming a mechanical load with friction B=0:

$$|\Delta\omega| = \frac{1}{J} A_1 \tag{5.22}$$

Equation (5.22) represents the minimum speed deviation under a load torque step up variation from τ_1 to τ_2. The same analysis can be carried out for a step down transient, with symmetric results.

Unfortunately, the value of this technique is purely theoretic, being required the knowledge of the transfer function $G_{en}(s)$, that in a real case would be highly nonlinear. The next section, another theoretic analysis is proposed, adding the STATCOM with energy storage.

5.4. Speed loop with the addition of the STATCOM with Energy Storage

The addition of the STATCOM modifies the speed loop block diagram of Fig. 5.5 in the one of Fig. 5.6 , where an additional torque input is depicted. In fact, the presence of an energy storage makes the STATCOM able to inject active power into the system. The normal use of a STATCOM

as reactive power compensator, wouldn't generate any instantaneous total power in the system, and thus no contribution on the mechanical torque (assuming a balanced and symmetric injection).

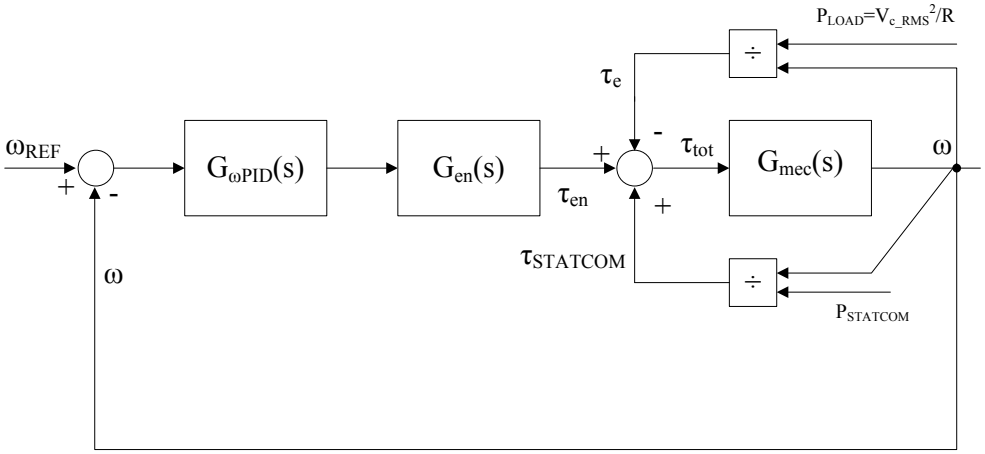

Fig. 5.6 Speed loop control adding STATCOM with energy storage

In Fig. 5.6 , the torque τ_e is a load torque, and thus represented with the minus sign in the adding node, while the STATCOM torque $\tau_{STATCOM}$ is a generated torque, contributing with a positive sign.

With an infinite-energy storage connected to the STATCOM, it could potentially compensate all the load power demand, without any effect in the speed regulation loop. Nevertheless, this scenario is not realistic because the synchronous generator should just generate a constant power, and once in steady state all the additional power demand should be given by the STATCOM.

In the real application, the energy storage has limited energy, that could come from batteries and/or SuperCaps. For this reason, the active power injection from the STATCOM has to be a time-limited power profile, with impulsive waveform. In the next paragraphs a close loop and an open loop compensation based on active power injection from the STATCOM are briefly introduced, to understand the potential use of the system.

5.4.1. Closed loop achievable improvements

Keeping the closed loop regulation, in the hypothesis of a load power step small enough to avoid the PI saturation, the only action that the STATCOM can take is to slow down the total equivalent load torque transient $\tau_{load\_eq}=\tau_e-\tau_{STATCOM}$, shaping for example the load torque variation as depicted in Fig. 5.7 :

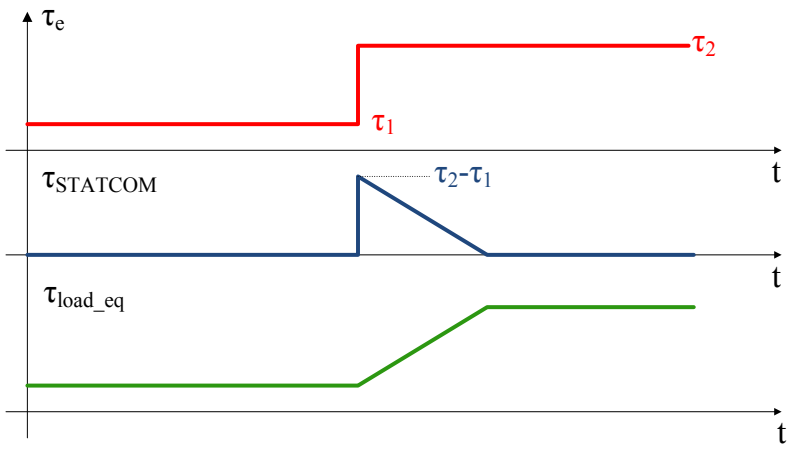

Fig. 5.7 Possible closed loop action of the SATCOM with energy storage

In this case, the advantage is a reduction in the output speed variation, that however can't be totally eliminated, due to the closed loop control structure. Better results can be achieved combining the optimum load step transient described in the previous section and the STATCOM.

5.4.2. Open loop optimum transient with STATCOM and Energy Storage

In this section, the optimum load transient response achievable combining an open loop action on the engine and the STATCOM with energy storage is presented. The action is taken only during the load transient, while before and after the load step, the control is left to the speed loop PI regulator. The advantage of the proposed controller is the theoretical capability of keeping the speed totally unchanged during all the load power transients. Moreover, the same result can be achieved also with any other shapes of the load variation (ramp, exponential, etc). The solution will be presented here in an ideal scenario, where the knowledge of all the transfer functions is assumed, together with the load power (torque). Being the load torque known, the load transient detection is instantaneous, avoiding non-idealities in the control due to detection delays. It is worth to remember that in the analysis, "load torque step" and "load power step" are referred as the same phenomenon, both meaning the change of active power absorbed by the resistive load connected to the synchronous generator output. In fact, with the hypotheses of constant PCC voltage and negligible speed variation, the two values are proportional.

From Fig. 5.6 , the very basic observation is that the speed is kept constant if and only if after reaching the steady state speed the total torque τ_{tot} applied to the mechanical load is kept constant. That means that the generated torque $\tau_{gen}=\tau_{en}+\tau_{STATCOM}$ has to instantaneously match the electrical load torque τ_e. Moreover, the best response that the engine controller can guarantee, is to set the maximum throttle, or equivalently to set the maximum torque demand, as soon as the transient is

detected. In this way, the speed loop becomes open, and the instantaneous torques match is possible, as in Fig. 5.8 , where the electrical torque τ_e step is supposed to be a step up variation from τ_1 to τ_2 occurring at the time instant t^*. Between t^* and t^{**} the PI output is saturated to τ_{MAX}, and the STATCOM injects $\tau_{STATCOM}=\tau_e-\tau_{en}$, so that the total steady state torque τ_{tot} is equal to zero, and the speed doesn't have any variation. The total steady state torque is zero in the hypothesis of a lossless mechanical load, with friction B=0. When the torque generated by the engine τ_e becomes equal to the final load torque τ_2, in t^{**}, the control returns to the PI, without any transient, being the speed error equal to zero. Of course the integral part of the PI has to be set to the new steady state τ_2.

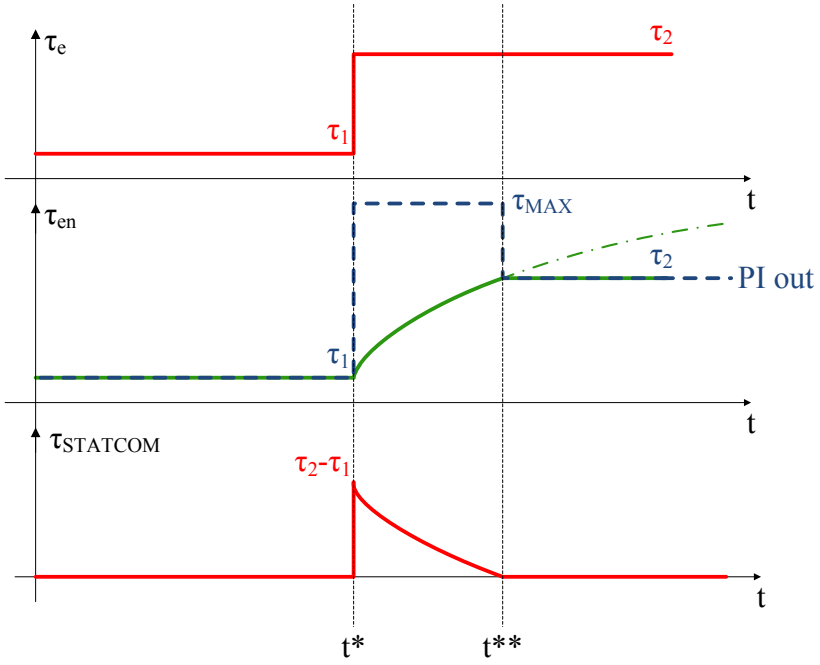

Fig. 5.8 Zero speed variation load step up transient

With the transfer functions described in (5.1), the engine torque τ_{en} during the interval $[t^*, t^{**}]$ is:

$$\tau_{en}(t) = \tau_1 + (\tau_{MAX} - \tau_1)\left(1 - e^{-\frac{t-t^*}{T_{en}}}\right) \tag{5.23}$$

And thus the STATCOM equivalent torque $\tau_{STATCOM}$:

$$\tau_{STATCOM}(t) = \begin{cases} \tau_2 - \tau_1 - (\tau_{MAX} - \tau_1)\left(1 - e^{-\frac{t-t^*}{T_{en}}}\right) = (\tau_2 - \tau_{MAX}) - (\tau_1 - \tau_{MAX})e^{-\frac{t-t^*}{T_{en}}} & \text{for } t \in [t^*, t^{**}] \\ 0 \text{ elsewhere} \end{cases} \tag{5.24}$$

Being the speed ω constant, $\omega=\omega_{REF}$, the active power injected by the STATCOM is:

$$P_{STATCOM}(t) = \begin{cases} \omega_{REF}\left((\tau_2 - \tau_{MAX}) - (\tau_1 - \tau_{MAX}) e^{-\frac{t-t^*}{T_{en}}} \right) & \text{for } t \in [t^*, t^{**}] \\ 0 \text{ elsewhere} \end{cases} \tag{5.25}$$

The instant t^{**}, corresponding to the end of the STATCOM injection, is the instant when (5.23) becomes equal to τ_2:

$$t^{**} = t^* - T_{en} \ln\left(1 - \frac{\tau_2 - \tau_1}{\tau_{MAX} - \tau_1}\right) \tag{5.26}$$

The total energy subtracted from the energy storage to compensate the transient corresponds to the integration of (5.25) over the interval $[t^*, t^{**}]$.

$$\begin{aligned} \varepsilon_{ES} &= \omega_{REF} \int_{t^*}^{t^{**}} \left((\tau_2 - \tau_{MAX}) - (\tau_1 - \tau_{MAX}) e^{-\frac{t-t^*}{T_{en}}} \right) dt = \\ &= \omega_{REF} (\tau_2 - \tau_{MAX}) \Delta T + T_{en} (\tau_1 - \tau_{MAX}) \left(e^{-\frac{\Delta T}{T_{en}}} - 1 \right) \\ \Delta T &= t^{**} - t^* \end{aligned} \tag{5.27}$$

In the analysis and in the experimental results in Chapter 7, the energy storage is assumed to be an infinite energy source, but in general the amount of energy is limited and has to be properly managed. This study is left to the future development of the project. With a more general approach, (5.25) can be rewritten as:

$$P_{STATCOM}(t) = \begin{cases} \omega_{REF}\left(\tau_2 - \left(\tau_1 + L^{-1}\left(\frac{\tau_{MAX} - \tau_1}{s} G_{en}(s) * e^{-st^*} \right) \right) \right) & \text{for } t \in [t^*, t^{**}] \\ 0 \text{ elsewhere} \end{cases} \tag{5.28}$$

Some important considerations follow (5.28), that is the instantaneous power reference for the STATCOM to guarantee a zero speed variation during the load power transient:

- A load torque measurement is needed to know τ_1 and τ_2 and to detect the load step.
- The knowledge of the diesel engine transfer function $G_{en}(s)$ is mandatory, or equivalently the diesel engine output torque has to be measured.

- Equation (5.28) is based on the assumption that the transient is an ideal step. For other shapes it's sufficient to modify (5.28) substituting τ_2 with $\tau(t)$. This is another reason for which the load torque has to be measured.

- The control technique guarantees in these ideal conditions a zero speed variation. For this reason, there is no need for a particular strategy to re-synchronize the PI controller after the load step management, apart from setting the new steady state torque τ_2 in the integral part.

- The knowledge of the diesel engine transfer function is a critic requirement, being the overall diesel system quite complex and with a non-linear behaviour. The measure of the load torque is less difficult, being easy to measure the load electric power with voltage and current transducers at the PCC.

In the next section, the approximated optimum controller for frequency support proposed in this project is presented, guaranteeing a more flexible and less parameters-sensitive approach, while maintaining a flat speed transient after load active power steps.

5.5. Proposed load step controller using STATCOM with Energy Storage

In this section, an approximated optimum controller is proposed to guarantee a minimum speed variation during load step transients. The controller has been developed to approximate the zero speed variation transient presented in the last paragraphs of the previous section, overcoming its main limitations, like the need for the knowledge of the diesel engine transfer function and torque measurement. The proposed controller architecture is very simple but effective in minimizing the speed variation. Further investigations will be carried out in the future developments of this project, to refine and optimize the controller. In this work, the complexity has been deliberately kept as low as possible, to optimize the limited available research period being also able to built the experimental setup that validates the proposed technique.

The main consideration behind the proposed architecture is that the large speed variations in a system without STATCOM, even using the optimum τ_{MAX}-τ_{MIN} sequence, is basically due to the slow dynamic of the power source, in this case the diesel engine. Even when, with the optimum control without STATCOM, the throttle is set to the maximum, the power generation has the slow dynamic of the $G_{en}(s)$ transfer function, that for a 10kW engine (power rating used later for the simulations and for the experimental rig) can be approximated in a first order time constant of hundreds of milliseconds, corresponding to a bandwidth of few Hz.

The transfer function $G_{en}(s)$ and the mechanical load $G_{mec}(s)$ are the main limitations to the increase of the speed loop bandwidth, that would strongly attenuate the effect of a load torque step transient, increasing the loop gain and the correspondent immunity to load disturbances. If the mechanical load can't be changed, the rest of the speed loop can be modified during the load transient event, as proposed in Fig. 5.9 , that summarizes the new developed technique.

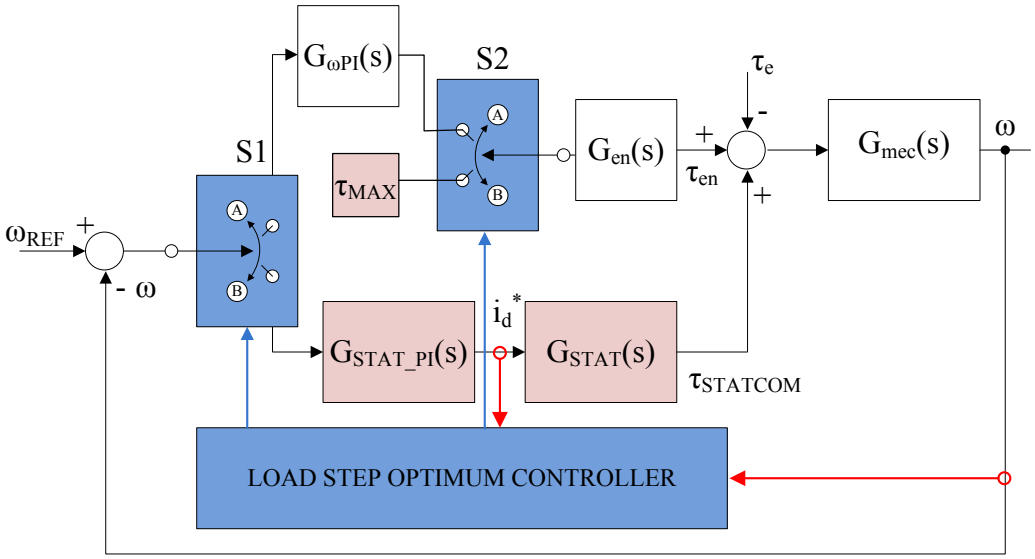

Fig. 5.9 Proposed approximated optimum controller using STATCOM with energy storage

In the open loop compensation, proposed at the end of the previous section, the speed PI was set to its maximum value τ_{MAX} and at the same time the STATCOM power reference was set, assuming the knowledge of the engine transfer function $G_{en}(s)$ or measuring the engine output torque, to compensate for the difference between the load power and the engine generated power.

In Fig. 5.9 , the reference for the STATCOM doesn't require any knowledge or measurement. After the transient detection, based for simplicity on a speed threshold, the two switches pass from position A to position B: the engine torque demand becomes τ_{MAX}, while the STATCOM power reference (or equivalently i_d current reference in the synchronous frame dq control, as stated in Fig. 5.9) is defined by a new speed loop, where the speed is controlled by the STATCOM, that can inject power with a much faster dynamic (current control bandwidth around $f_{SW}/10$ where f_{SW} is the switching frequency) than the diesel engine.

From another point of view, the new speed loop is controlling the speed and has to respond to an equivalent load torque transient equal to the difference between the load torque and the diesel generated torque with maximum torque reference. This equivalent torque corresponds to the STATCOM torque reference that should be followed by the STATCOM for the ideal compensation in Fig. 5.8 .

This control configuration lasts until this equivalent torque disturbance reaches zero, meaning that the diesel engine torque reaches the electrical load torque. At that instant the two switches are moved back to the A position. With instantaneous detection and instantaneous response both for the STATCOM controlled speed loop and for the inner STATCOM current controller (infinite bandwidth for both), the behaviour of this structure is exactly the same of Fig. 5.8 , with zero speed variation. Actually, the detection has a delay, and the regulation loops (speed and current) have limited bandwidth, meaning that a speed variation is always present. Assuming a detection threshold tight enough, and control fast control loops (qualitatively, at least with bandwidth higher than the mechanical load cut-off frequency), the introduced error can be reasonably considered negligible, for the preliminary goals of this project. In this way, also the re-synchronization with the PI that controls the diesel engine can be approximated deriving the amplitude of the load step change from the maximum amplitude of the injected i_d current (or equivalently electrical torque or power). Fig. 5.10 reports a simple flow chart to summarize the behaviour of the controller, while Fig. 5.11 shows the active control loops during the different intervals of the control action.

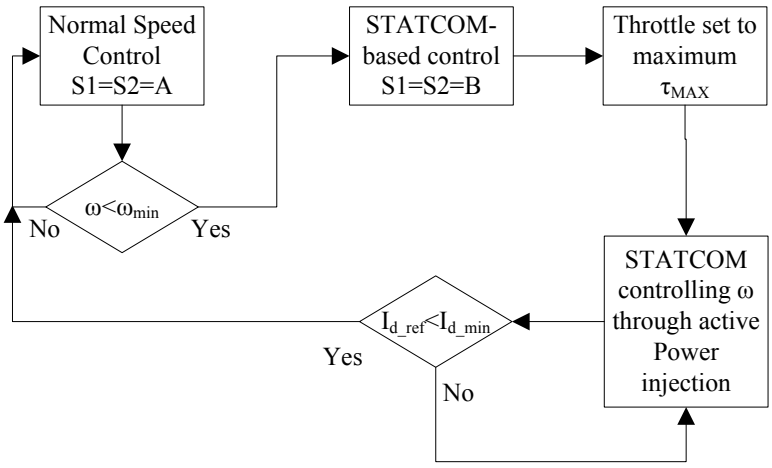

Fig. 5.10 Simplified control algorithm

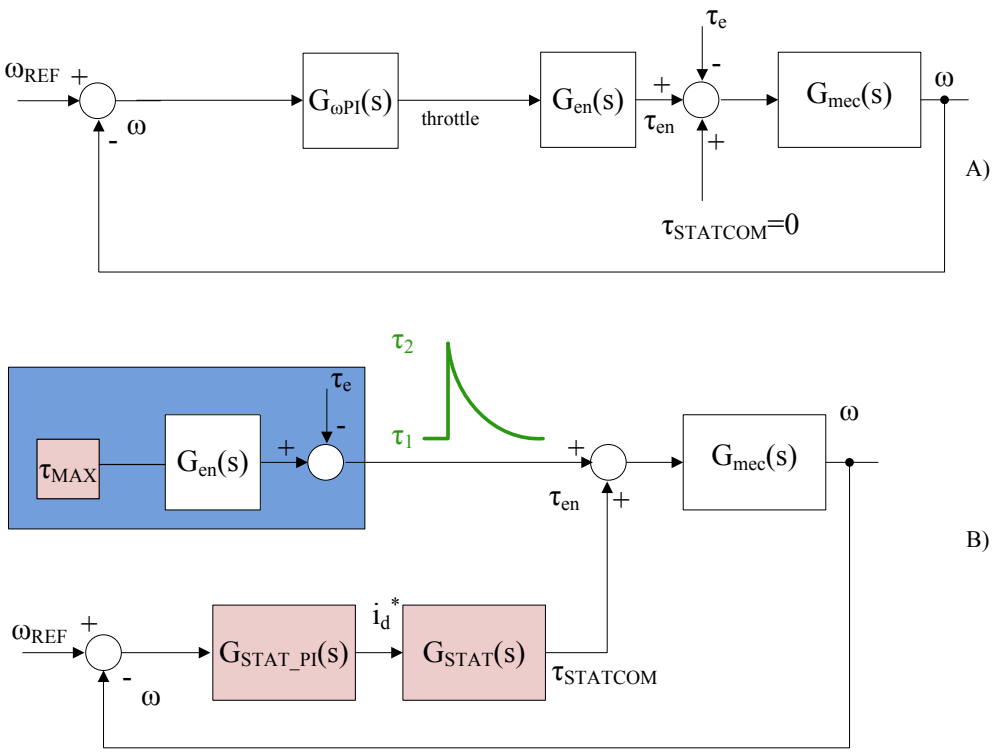

Fig. 5.11 Equivalent speed control loops during A) normal operation and B) during optimum control of the load torque step from τ_1 to τ_2

In the next chapter, the simulation results for the proposed approximated optimum controller will be presented, together with the preliminary schemes of the speed control of the induction motor emulating the diesel engine in the experimental rig presented in Chapter 7.

Chapter 6

Simulation Results - Frequency Stabilization

6.1.Introduction

This section presents the simulation results for the proposed approximated optimum control to load active power steps using a STATCOM with energy storage to stabilize the frequency of a synchronous generator feeding an autonomous microgrid. Before simulating the whole system, the simulation models for the STATCOM DQ current control (see Appendix B) and for the induction motor speed loop have been developed. As anticipated in the previous sections, an induction motor is used to emulate the diesel engine prime mover. As a result, all the parts the final experimental setup have been investigated separately, thus permitting an easier final hardware and software implementation.

Being at this point of the project the design specifications not completely defined yet, in the next paragraphs some assumptions about system parameters and control specifications have been arbitrarily made, with the goal of obtaining a system that will be reasonably near the real setup.

6.2.STATCOM DQ Current Control

Based on the derivation in Appendix B, the DQ current control has been modelled in Matlab Simulink using simscape blockset for the electrical part. The main parts of the schematic are the electrical model of the simulated three-phase three-wires microgrid, with the synchronous generator and its internal impedance, the PCC with the SATCOM coupling inductors and the variable resistive load. The STATCOM is modelled with an average approach, thus neglecting the commutations and obtaining a faster simulation, and its output voltages are derived from the DQ controller. A three phase PLL has been implemented, locked on the PCC voltage, to get the angle required for the DQ transformation. The PI regulators for the DQ current loops, together with the PLL regulator have been designed using approximated transfer functions, in the continuous time domain, neglecting the

digital modulator delay and the computation delay and assuming a linearized model for the PLL. The resulting coefficients have been discretized using a Forward Euler discretization, and used in the digital controllers in the simulations in Simulink. Table 6.1 reports the parameters of the system, while Table 6.2 reports the design specifications for the control loops.

Parameter	Value
Synchronous generator frequency	f_{REF}=50Hz
Line to line generator rms voltage	V_{GEN}=200V
Generator internal inductances	L_{GEN}=1mH
STATCOM coupling inductors	L_S=5mH
Maximum STATCOM rms line to line voltage	V_{S_MAX}=280V (SVM modulation with V_{DC}=400V)
Load before load step	R_{LA}=10Ω (P=4kW)
Load after step	R_{LB}=5Ω (P=8kW)

Table 6.1 :Simulated current control parameters

Parameter	Value
Sampling frequency	f_M=5kHz
DQ current loops bandwidth	B_I=450Hz
DQ current loops phase margin	$m_{\phi I}$=80°
PLL bandwidth	B_{PLL}=10Hz
PLL phase margin	$m_{\phi PLL}$=60°

Table 6.2 Current control design specifications

In the next, the results are reported both for the controllers design in the frequency domain and for the system behaviour in the time domain. In particular, Fig. 6.1 Fig. 6.2 report the loop gain and the closed loop step response for the PLL, while Fig. 6.3 and Fig. 6.4 reports the same quantities for the DQ current controllers, for both D and Q components. All these plots have been derived from the design scripts in Matlab implanting the continuous time transfer functions. Fig. 6.5 and Fig. 6.6 will finally show the STATCOM currents and PCC voltages under a 10 to 15A D-current reference step change in the Simulink model, to evaluate the dynamic performances of the loops.

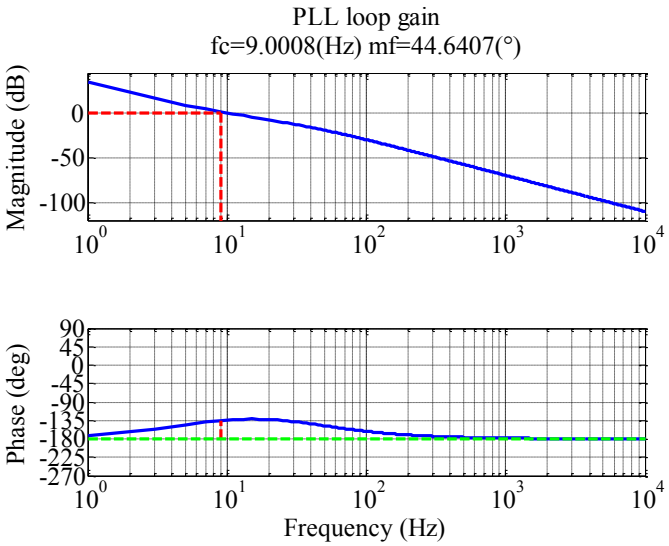

Fig. 6.1 Three phase DQ PLL loop gain -

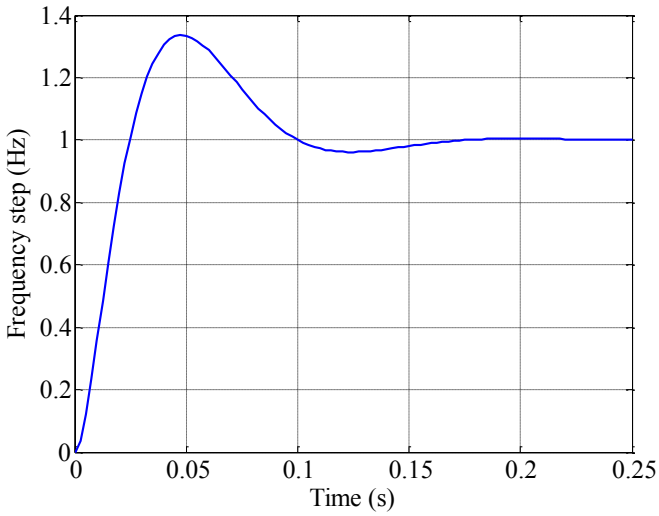

Fig. 6.2 PLL frequency step response

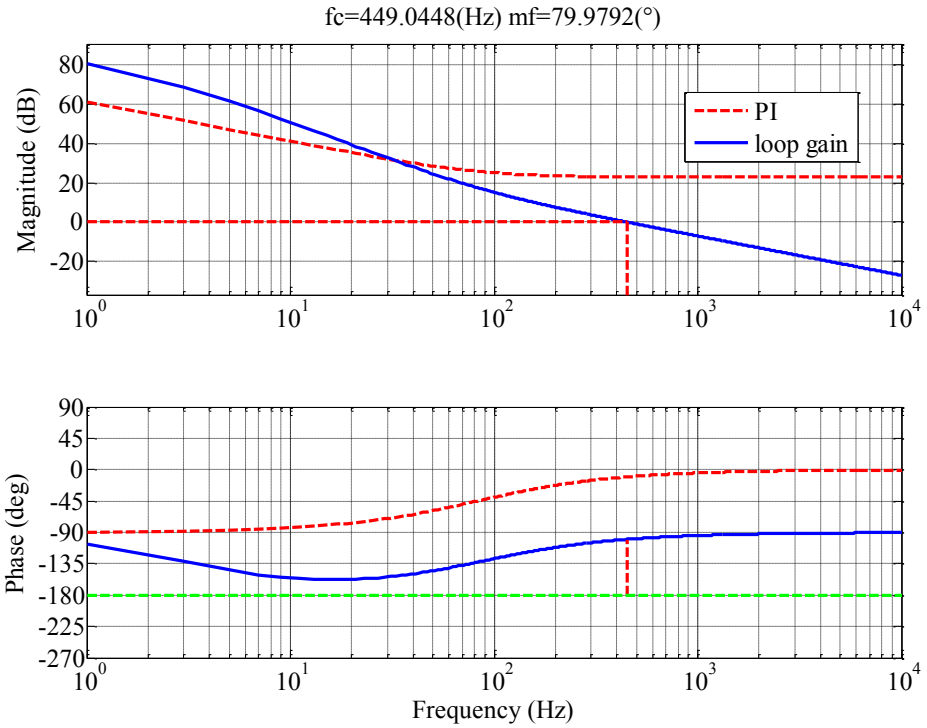

Fig. 6.3 DQ current control loop gain and PI regulator – from design scripts

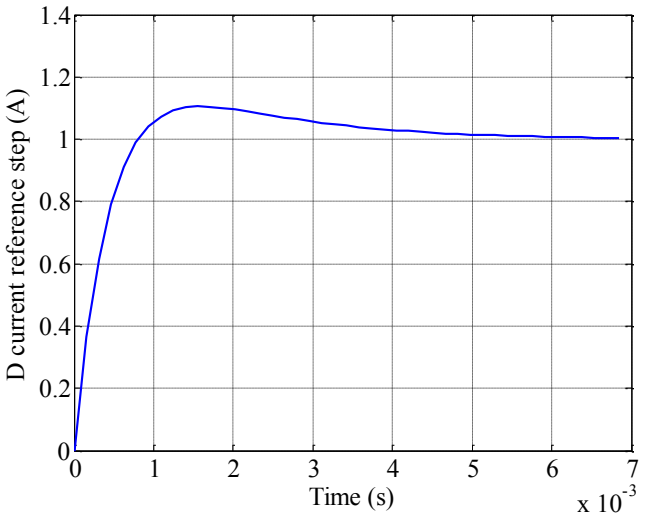

Fig. 6.4 D current reference step response– from design scripts

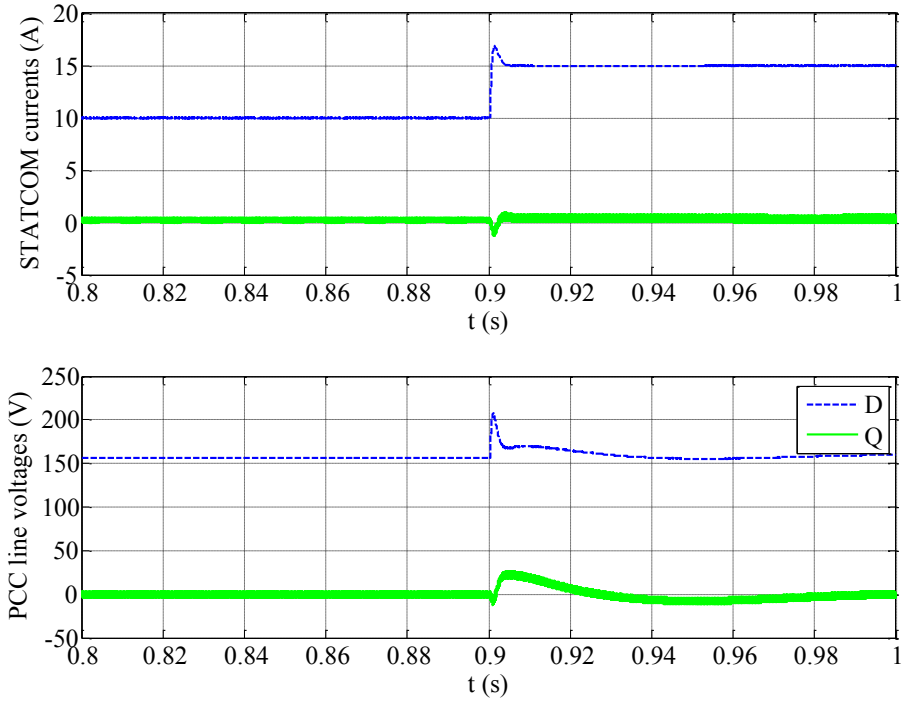

Fig. 6.5 D current reference10 to 15A step – Simulink model

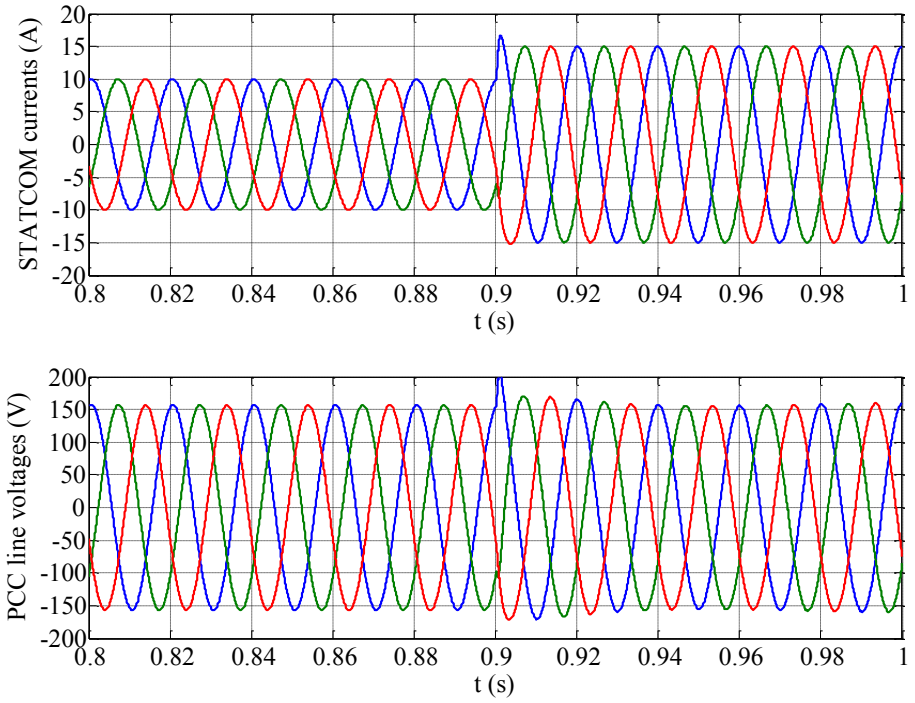

Fig. 6.6 STATCOM currents and PCC line star voltages during a 10 to 15A D current reference step

6.3.Induction motor speed control

The second part of the simulations is dedicated to the induction motor speed control, that is fundamental to implement the optimum load step control. In fact, the induction motor will emulate in the experimental rig the behaviour of a diesel engine. Considering that in the experimental implementation the electrical drive will be a commercial unit, the attention has been focused here in the pure control section, assuming ideal the induction motor with Field oriented control and its internal DQ current loops. Therefore, the induction motor model and its power conversion stage are included in the Simulink model but considered a black box in the controllers design, approximately represented by the constant gain transfer function between the Q current demand and the generated torque:

$$\tau = \frac{3}{2} p \frac{L_m{}^2}{L_r} i_{sd} i_{sq} \tag{6.1}$$

Where the D current i_{sd} is the magnetizing current, i.e. the flux producing current, and is assumed to be constant. The Q current i_{sq} is the torque producing current, and is controlled by the speed PI controller through the throttle to torque delay that emulates the diesel engine. Moreover, the magnetizing inductance L_m and the rotor inductance L_r are assumed to be equal for simplicity, so that equation (6.1) is rewritten as an equivalent gain:

$$G_{q\tau} = \frac{\tau}{i_{sq}} = \frac{3}{2} p L_m i_{sd} \tag{6.2}$$

Parameter	Value
Nominal Speed	1500 RPM
Nominal Power	16 kW
Nominal Torque	102 Nm
Nominal Voltage	340VRMS line to line
Nominal Current	38 A
Magnetizing current	16 A
Nominal Frequency	51.5 Hz
Maximum speed	7000RPM
Phase resistance	0.1721 Ω
Leakage inductance	3.025 mH
Magnetic inductance	32.31 mH
Rotor resistance	0.153 Ω

Table 6.3 Magnetic MA 133 K F1 plate data

To obtain realistic data from the design, the motor that will be used in the experimental setup has been considered for the simulations. The machine is a Magnetic MA 133 K F, a two poles 16kW machine, with plate data reported in Table 6.3 .

Referring to the speed loop scheme presented in Chapter 5 and reported in Fig. 6.7 , the PI regulator sets the fraction of Q current demand for the drive, or throttle fraction of the emulated diesel engine. To achieve the diesel engine emulation, this reference is filtered through a first order transfer function, corresponding to $G_{en}(s)$ in Chapter 5, emulating the throttle to torque response of a diesel engine. The output is the percentage of torque producing current reference sent to the induction motor drive becoming generated torque percentage after (6.2), representing the drive. This torque percentage is multiplied by the maximum torque producing current i_{sq_NOM} to obtain the actual torque applied to the mechanical load. Therefore, the resulting approximated speed loop will have four main transfer functions: PI regulator, $G_{en}(s)$, (6.2) and the mechanical load $G_{mec}(s)$, as resumed in Fig. 6.7 .

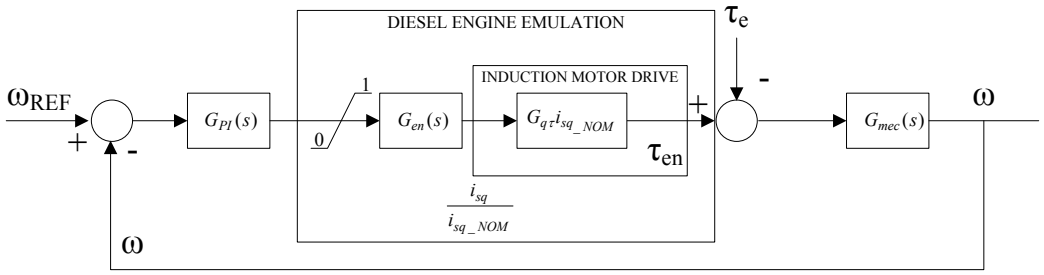

Fig. 6.7 Simulated speed loop

The choice of this control structure, with specific scale factors, has been made to obtain a system as close as possible to what will be the experimental setup, with the drive receiving a torque reference as a percentage of its maximum rated value.

Table 6.4 and Table 6.5 report the simulated system parameters and the control requirements respectively. The data have been used in Matlab scripts to design the digital controllers and simulate the system in Simulink. The choice of the of the sampling frequencies for the current and speed loops has been based on preliminary hypotheses on the future experimental setup.

Parameter	Value
Induction motor	Magnetic MA 133 K F1
Speed reference	1500 RPM
Mechanical inertia Jm	0.2 Kg*m2
Mechanical friction Bm	0.05 Nms/rad
Drive DC link	400 V
Maximum Iq current	17 A
Maximum power	8kW
Magnetizing current Id	14 A
Drive current control sampling frequency	5kHz
Speed control sampling frequency	250Hz
Diesel throttle to torque delay cutoff frequency (firs order transfer function)	5Hz

Table 6.4 Speed loop system parameters

Parameter	Value
Drive DQ current loop bandwidth	500Hz
Drive DQ current loop phase margin	60°
Speed loop bandwidth	2.5Hz
Speed loop phase margin	45°

Table 6.5 Speed loop control design specifications

Fig. 6.8 reports the final speed loop gain, Fig. 6.9 the initial loop gain and the designed PI regulator, while Fig. 6.10 the closed loop speed step response. Fig. 6.11 shows the diesel engine emulated throttle to torque transfer function $G_{en}(s)$. It is worth to remind that $G_{en}(s)$ has been named "throttle to torque transfer function" in chapter 5, where the scale factors where arbitrary. In the scheme of Fig. 6.7 $G_{en}(s)$ is the transfer function between the throttle and the fraction of current demand sent to the induction motor drive. All these figures have been derived from Matlab design scripts. From the Simulink model, Fig. 6.12 presents a 50 RPM speed reference step and the consequent response of the speed, the throttle demand from the PI regulator and the fraction of torque producing current demand out of $G_{en}(s)$, that will become torque after the block $G_{q\tau}(s)i_{sq\_NOM}$.

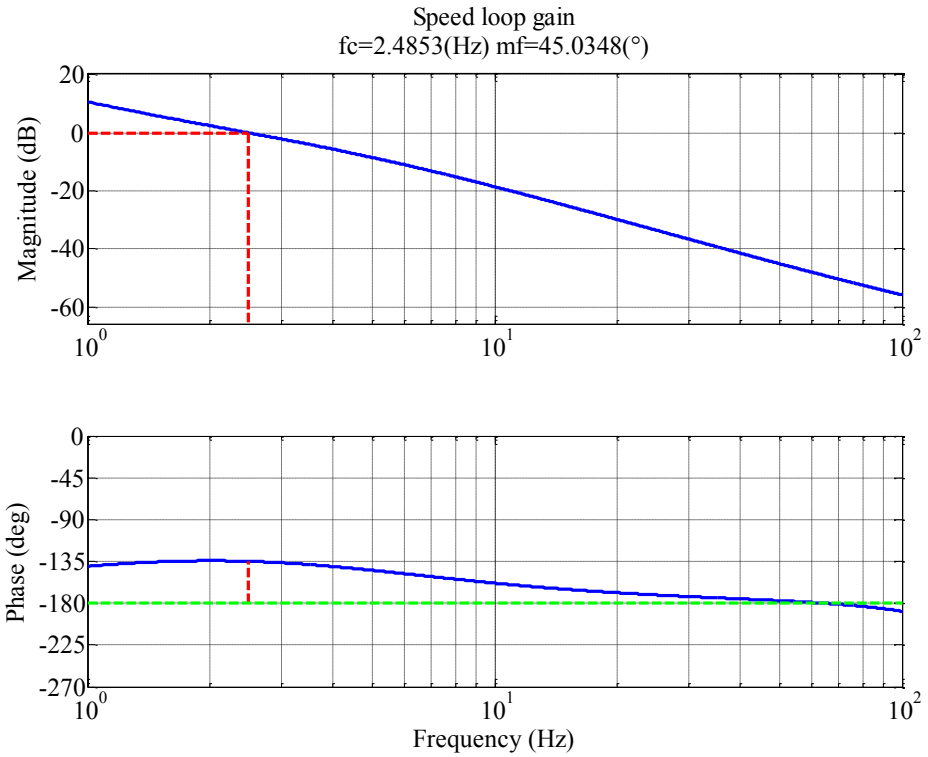

Fig. 6.8 Final speed loop gain – from Matlab design scripts

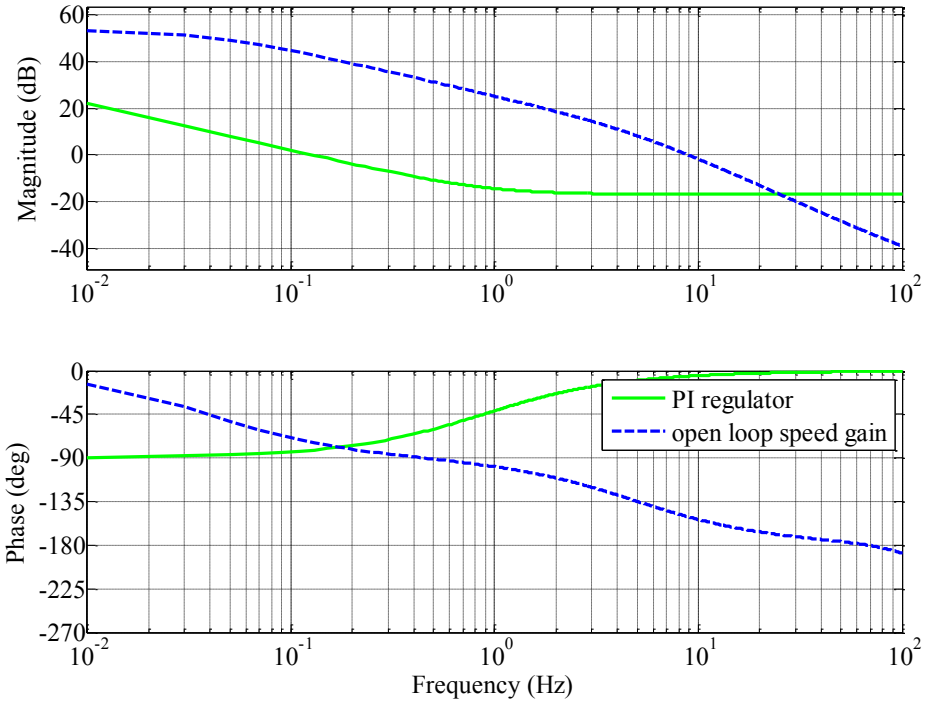

Fig. 6.9 Initial speed loop gain and designed PI regulator

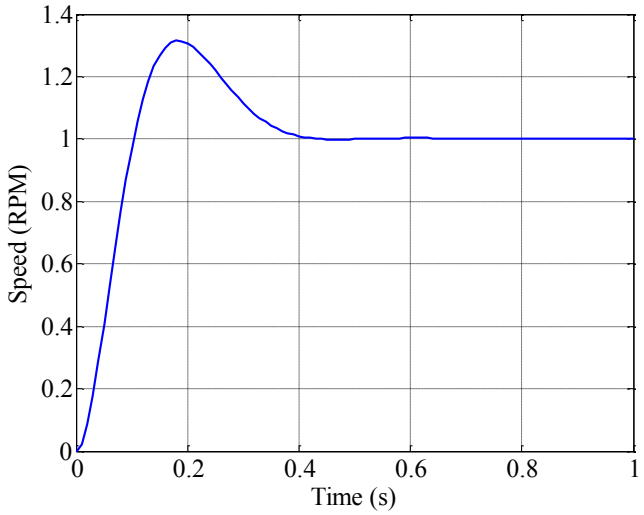

Fig. 6.10 Speed closed loop step response

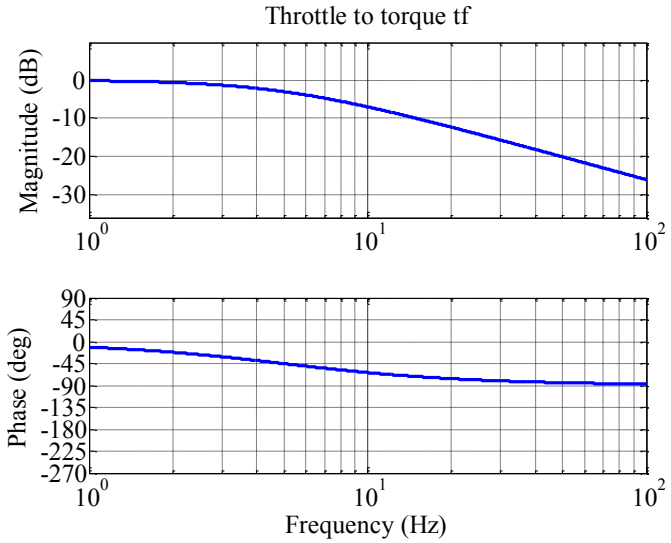

Fig. 6.11 throttle to torque approximated transfer function

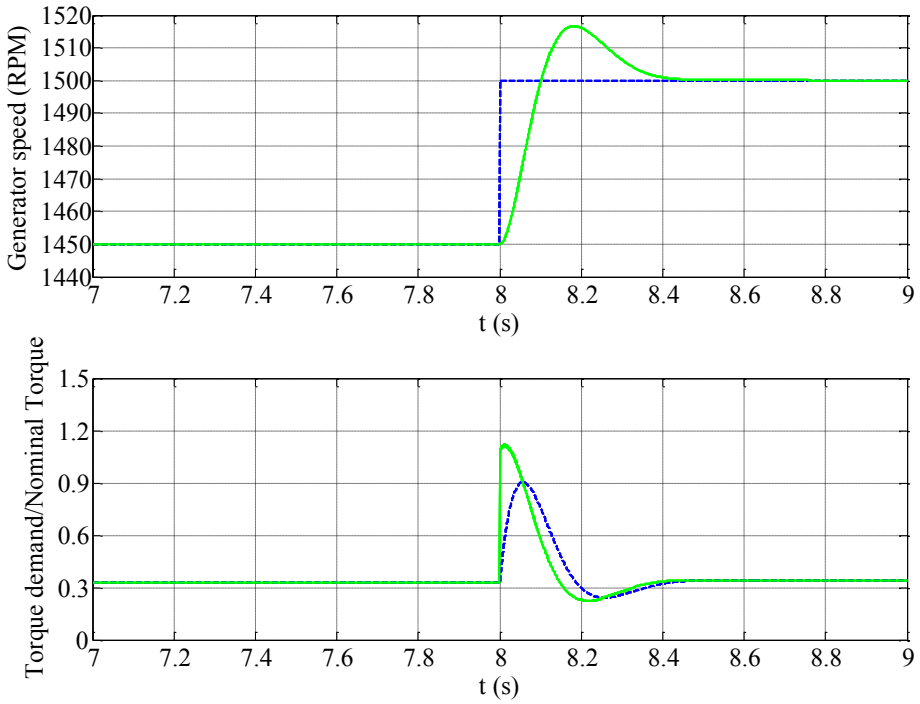

Fig. 6.12 Speed reference 50 RPM step (upper plot) and speed response; PI output (continuous line lower plot) and $G_{en}(s)$ output (dashed line).

6.4.Optimum load step control

The optimum load step control, described in Chapter 5 has been simulated merging together the STATCOM current control, the electrical model and the induction motor speed loop, adding the proposed non linear control action to minimize the speed variation during a load step. In the simulations, the transient detection delay has been neglected.

Parameter	Value
Induction machine pole pairs	2
Speed reference	3000 RPM
Mechanical inertia J_m	0.2 Kg*m^2
Mechanical friction B_m	0.02 Nms/rad
Maximum diesel (IM) torque	32 Nm
Maximum diesel (IM) power	10kW
Diesel throttle to torque time constant	100ms
Synchronous generator frequency	f_{REF}=50Hz
Generator phase rms voltage	V_{P_GEN}=100V
Generator internal inductances	L_{GEN}=1mH
STATCOM coupling inductors	L_S=5mH
STATCOM DC link	V_{DC}=400V
Electrical load before load step	R_{LA}=10Ω (P=3kW)
Electrical load after step	R_{LB}=5Ω (P=6kW)
STATCOM control frequency (DQ and load transient management)	f_1=5kHz
IM speed loop frequency	f_2=250Hz

Table 6.6 Final simulated system parameters

Parameter	Value
Speed loop bandwidth	15Hz
Speed loop phase margin	60°
STATCOM DQ current loop bandwidth	450Hz
STATCOM DQ current loop phase margin	80°
Optimum controller bandwidth	80Hz
Optimum controller phase margin	80°
PLL bandwidth	10Hz
PLL phase margin	60°

Table 6.7 Final simulated system control design specifications

Table 6.6 and Table 6.7 report the final system parameters and the final design requirements for all the control loops, i.e. STATCOM DQ control, induction motor speed control, approximated optimum load step control. For simplicity, being the considered bandwidths quite low, the fast induction motor drive current loop has been neglected. The specification about the closed loop system requirements during the load transient (new speed loop controlled by the STATCOM) are reported as "Optimum controller" bandwidth and phase margin.

Figures from Fig. 6.13 to Fig. 6.18 report the control loops designs with Matlab: in sequence, the DQ current loop for the STATCOM, diesel engine emulated speed loop and the proposed approximated optimum load step controller. For the three controllers, the bode plots of the final loop gain and the PI regulators are reported together with the resulting closed loop step response:

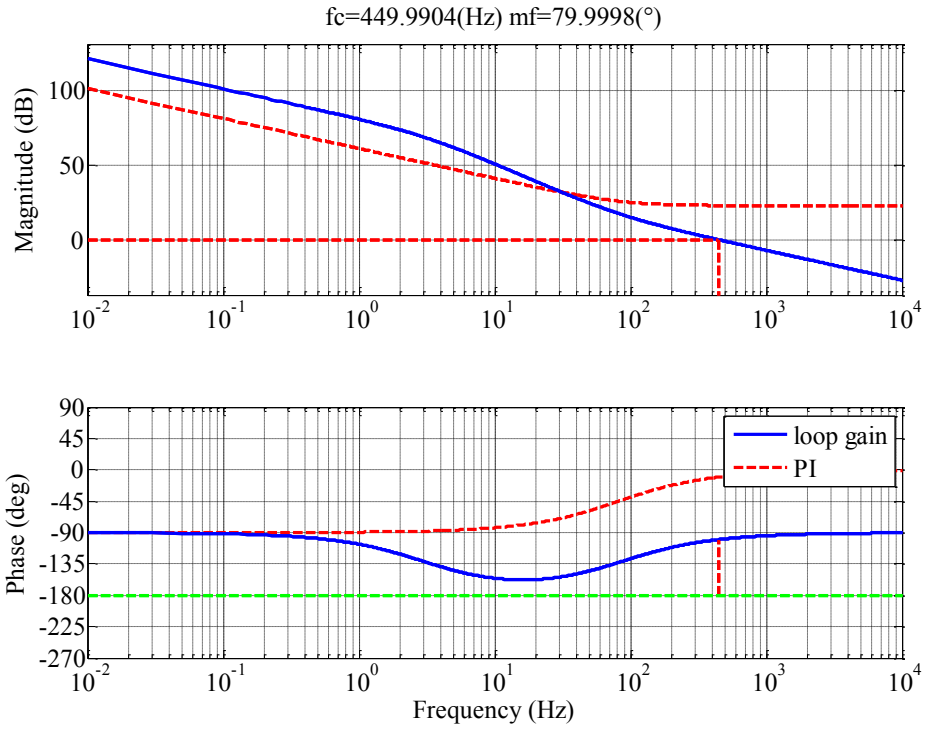

Fig. 6.13 STATCOM DQ current control final loop gain and PI regulator – from design scripts

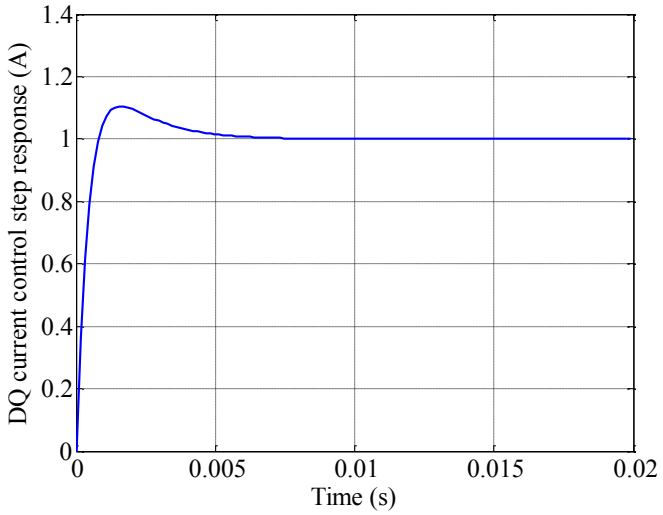

Fig. 6.14 STATCOM DQ current control closed loop step response

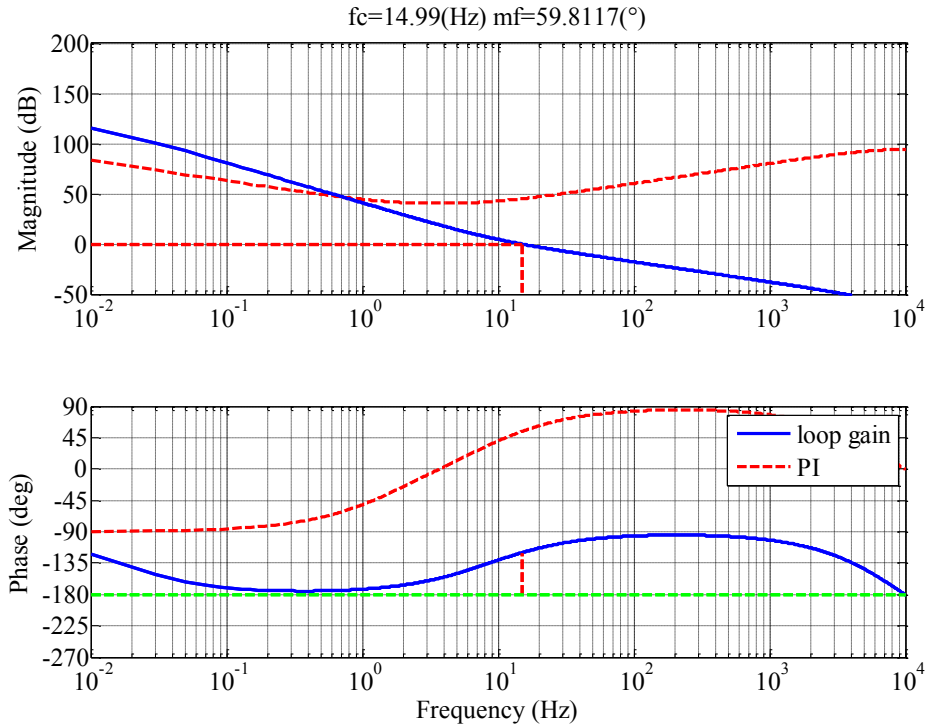

Fig. 6.15 Diesel engine speed loop gain and PI regulator – from design scripts

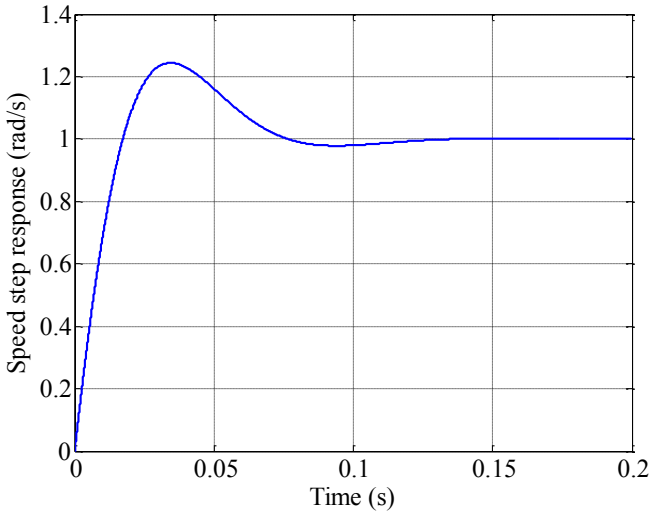

Fig. 6.16 Speed closed loop step response – from design scripts

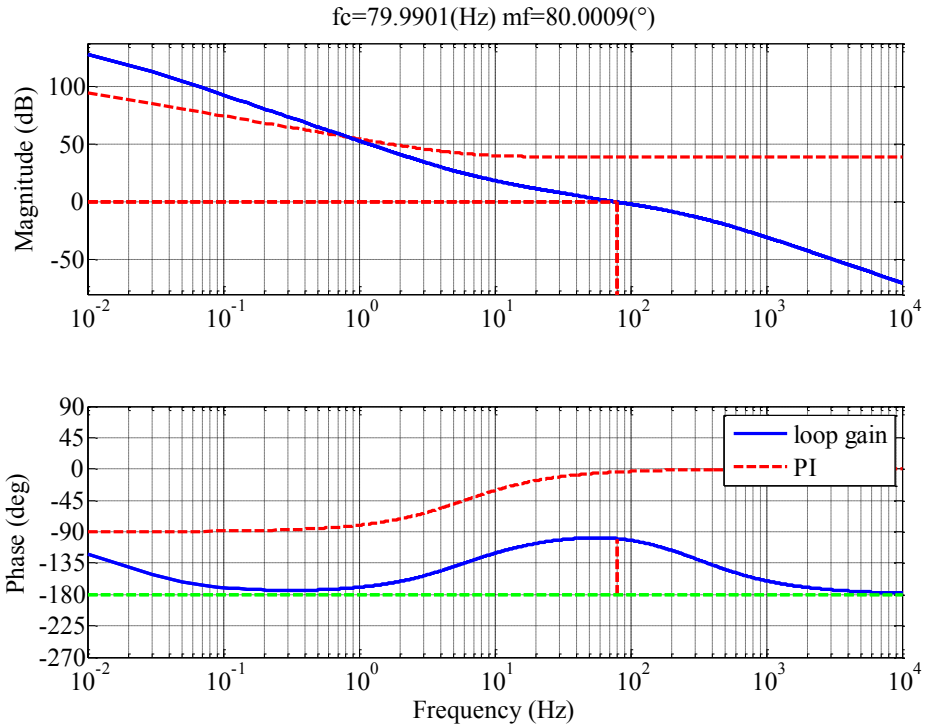

Fig. 6.17 Optimum step response PI controller – from design scripts

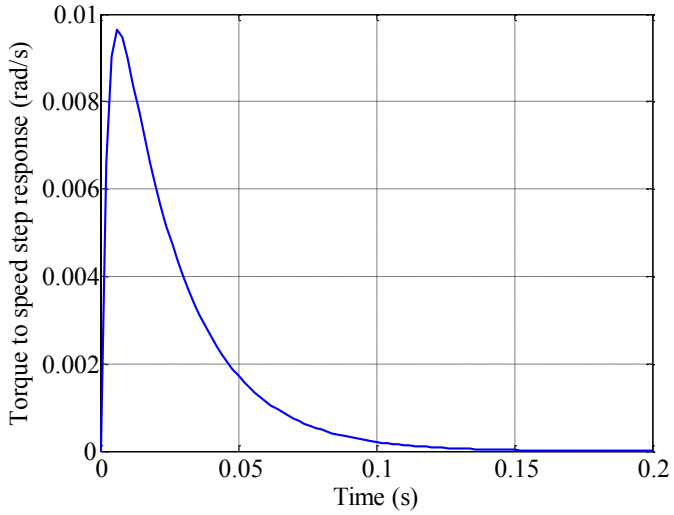

Fig. 6.18 Speed response to a disturbance step in the load torque -.from design scripts

Figures from Fig. 6.19 to Fig. 6.25 show the results from the optimum load step transient control Simulink model. The simulated load step is a 3kW load increase: the detection is assumed to be instantaneous, and instantaneously the speed control is switched from the conventional speed PI to the fast PI injecting the required power to keep the speed as constant as possible, and in the meanwhile the conventional PI output is set to the maximum available value. From When the impulsive injection, corresponding to the load torque step response of the new control loop in Fig. 6.18 zeroes, the control is switched back to the conventional PI, that sets as steady state value, i.e. in the integrator, the actual diesel engine generated torque at the instant of zero crossing. In the real implementation, the knowledge of this new steady state value is not possible, being the diesel engine torque non measured. In Chapter VII, the adopted solution in the real setup will be presented, where the STATCOM I_d current reference will be used to roughly estimate the load power step amplitude, and thus translate it in an approximated estimation of the load torque. This has been shown to be effective in the rig.

The results confirm the good potential of the proposed technique, showing a speed variation reduced from 21 RPM for the system without STATCOM to 1.2 RPM with the approximated optimum controller, corresponding to 94% of reduction.

The speed variation in Fig. 6.24 and Fig. 6.25 is due to the naturally limited bandwidth of the optimum controller, much faster than the conventional one but still non ideal. The non ideal injection is reflected also in the conventional PI resynchronization, causing a torque demand oscillation in Fig. 6.23 around t=1.6s that enlarge the speed transient duration. Moreover, in Fig. 6.23 the PI output is not limited to 1 but to the maximum torque: this is because the gain $G_{qr}(s)i_{sq\_NOM}$ is included in the PI block in Simulink.

Even with this non idealities, the performances are encouraging the prosecution of the activity, testing the solution in an experimental setup, presented in the next chapter.

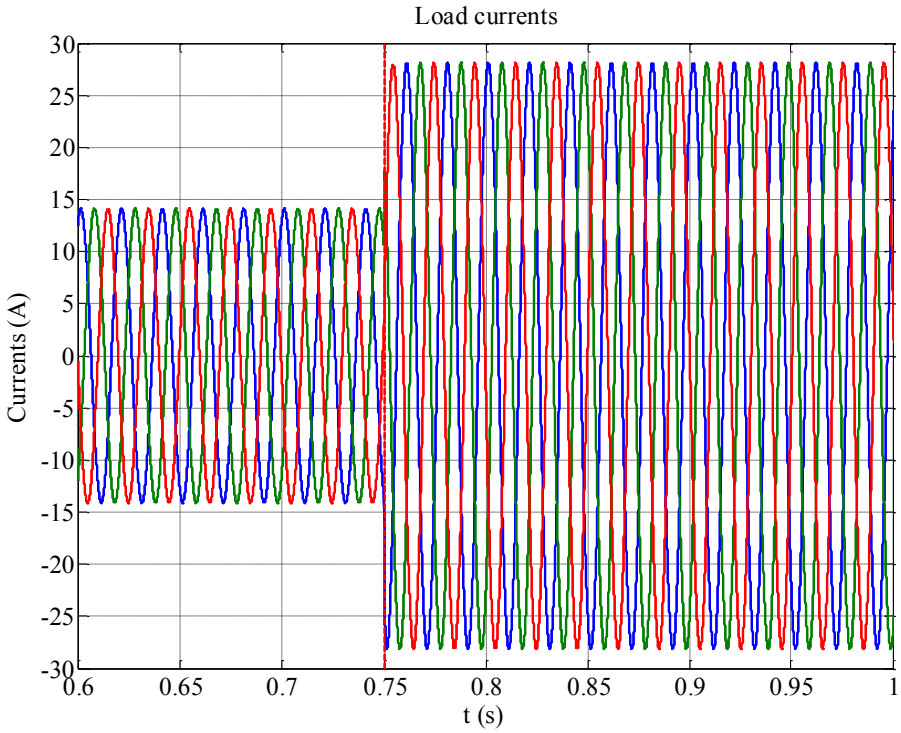

Fig. 6.19 Load currents during the step

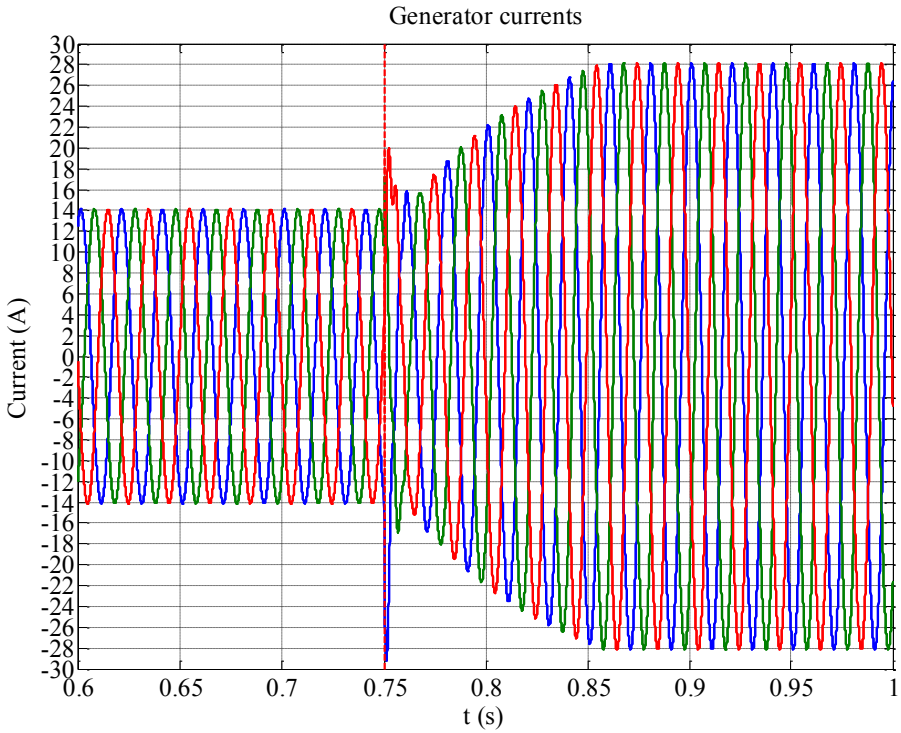

Fig. 6.20 Synchronous generator currents during load step with optimum controller

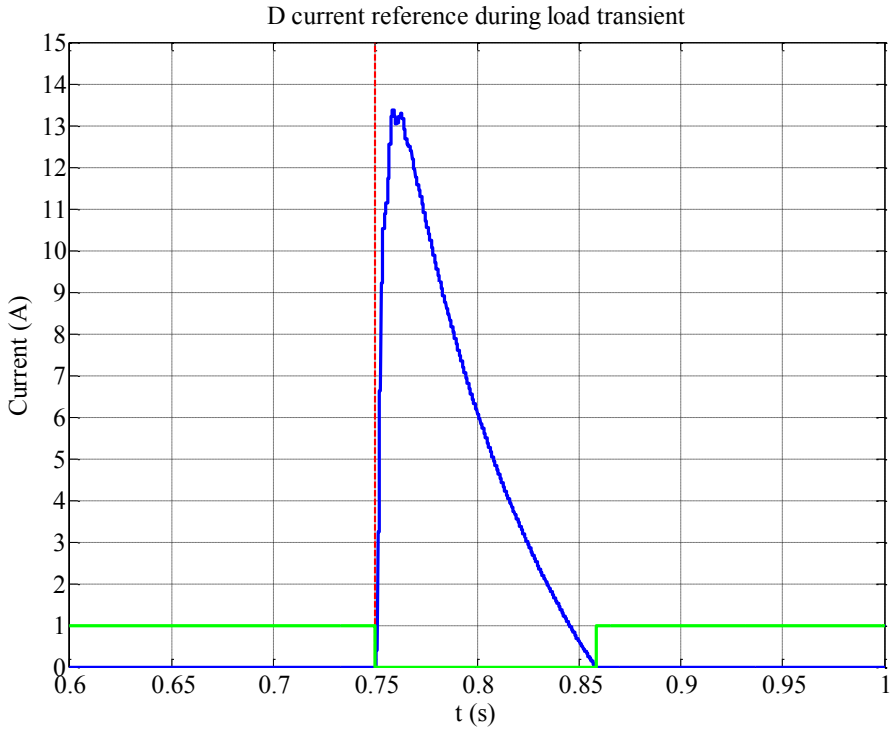

Fig. 6.21 Optimum controller PI enable (squared signal) and generated I_d reference

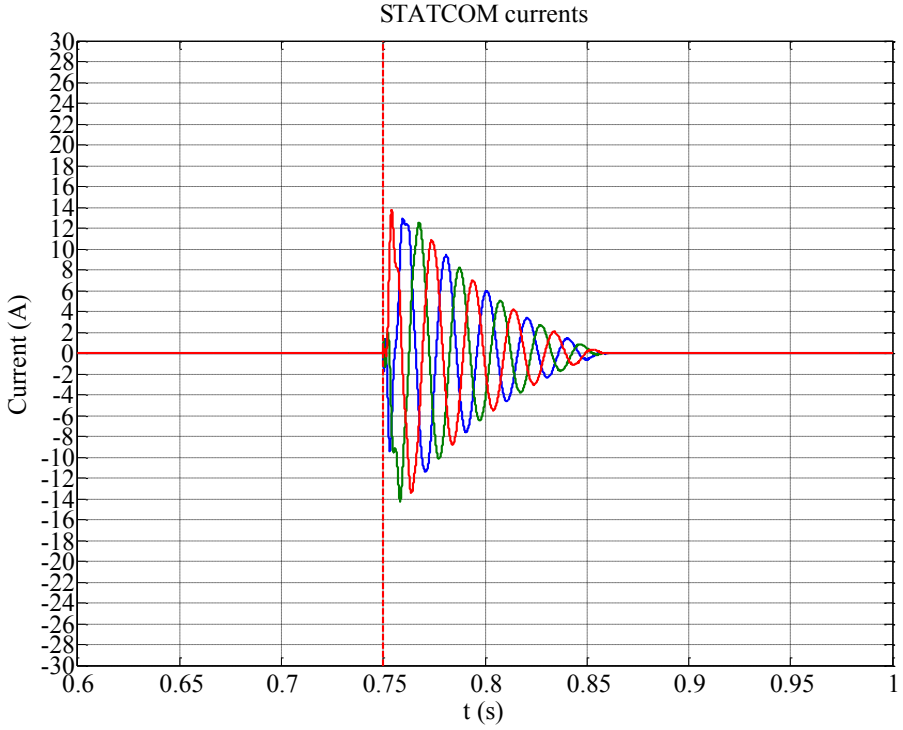

Fig. 6.22 STATCOM injected currents during the optimum control action

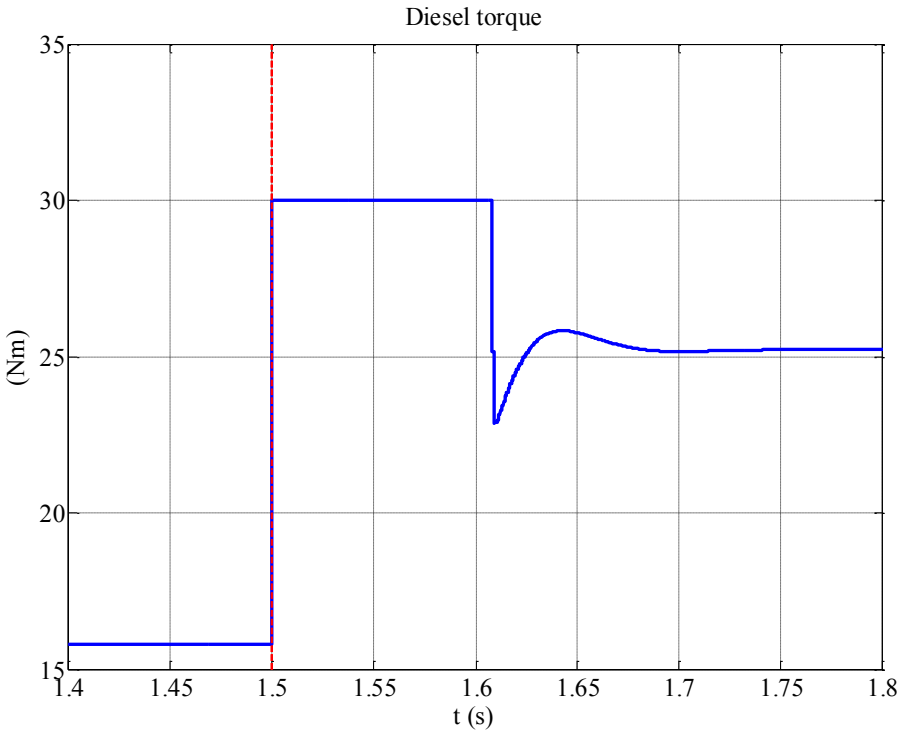

Fig. 6.23 Conventional PI output, before, during, and after the load step transient with optimum controller (in the figure the transient is at t=1.5s instead of 0.75s of the other waveforms)

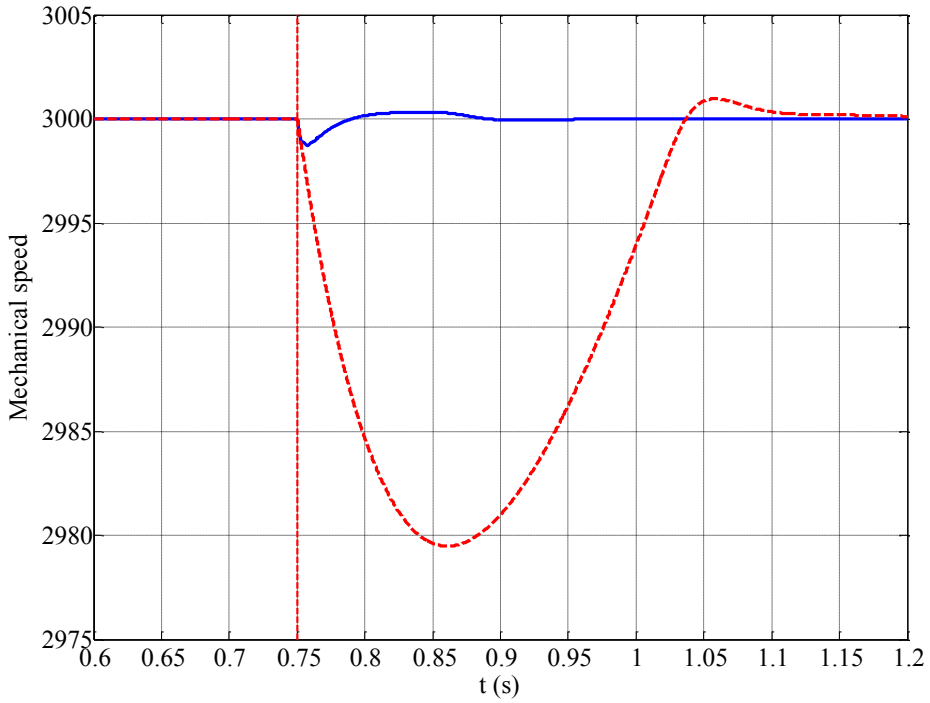

Fig. 6.24 Speed (RPM) response to 3kW electrical load step with optimum controller (continuous line) and without optimum controller (dashed line)

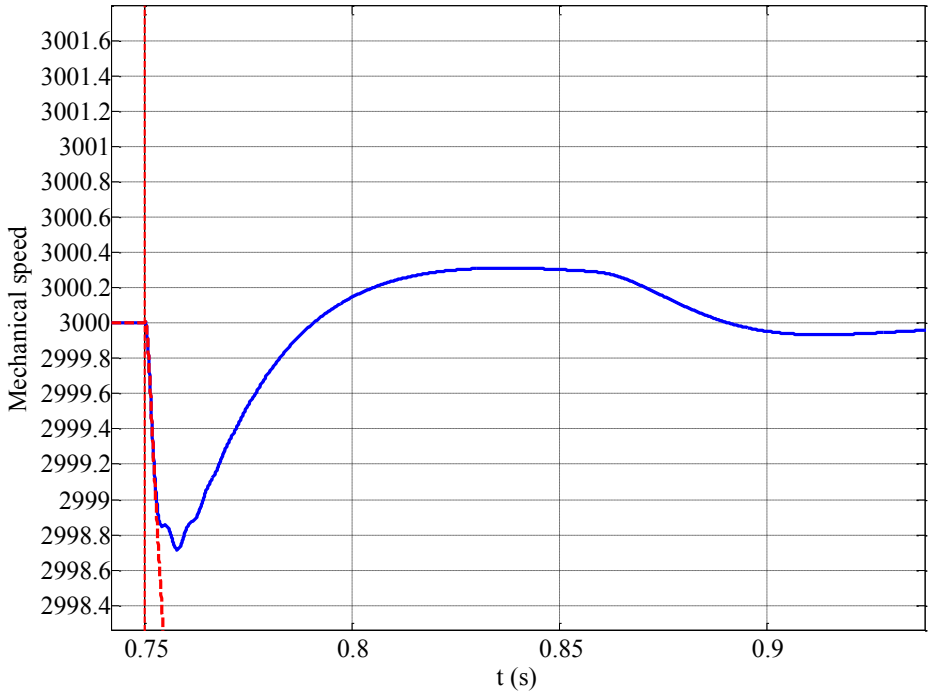

Fig. 6.25 Zoom on the speed (RPM) response to 3kW load step with optimum controller

Chapter 7

Experimental Results

7.1. General system description

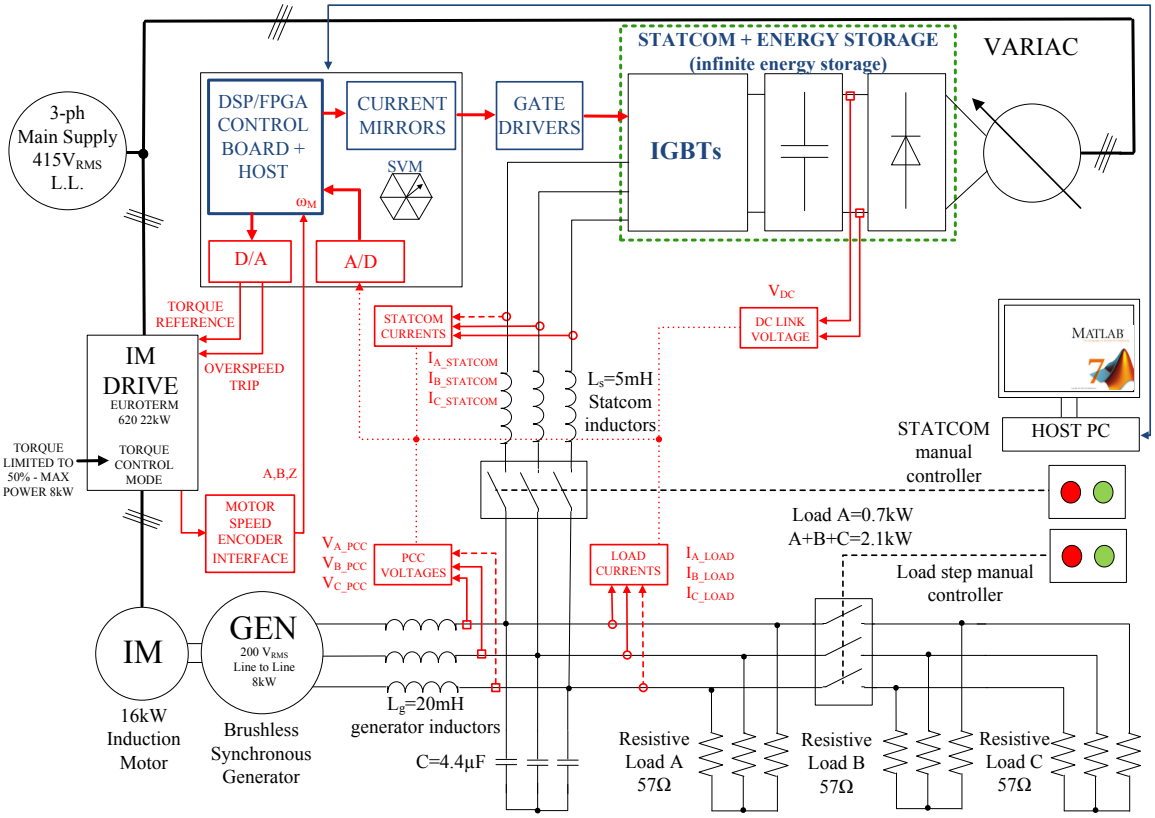

Fig. 7.1 Experimental rig

The proposed approximated optimum control has been tested in an experimental rig specifically developed for the application, as depicted in Fig. 7.1 . The energy storage is emulated using a rectifier connected to the main three phase grid through a VARIAC, to manually set the DC link voltage. The STATCOM is a 10kVA three phase inverter, and the generator a 10kVA, 8kW (cosφ=0.8) Leroy Somers LS 40 VS1 synchronous generator equipped with AVR (Automatic Voltage Regulator), with voltage amplitude set to $200V_{RMS}$ line to line through internal connections of the windings and AVR settings. Diesel engine prime mover is emulated using a induction motor and a dedicated drive. The inner DQ current loops of the FOC control are implemented in the

commercial 22kW drive Eurotherm 620, while the speed loop and regulator are in a DSP/FPGA board: the motor encoder digital outputs A-B-Z are read using a dedicated encoder reading block in the FPGA program, the motor speed is passed to the DSP interrupt routine and the speed error is calculated and processed through the speed regulator. The regulator output is sent to a DAC converter and eventually to the torque reference analog input of the Eurotherm 620 drive. The induction motor control system is reported in Fig. 7.2 . The diesel engine emulation is then obtained adding a further transfer function after the speed regulator, as already seen in Chapter 5 and 6.

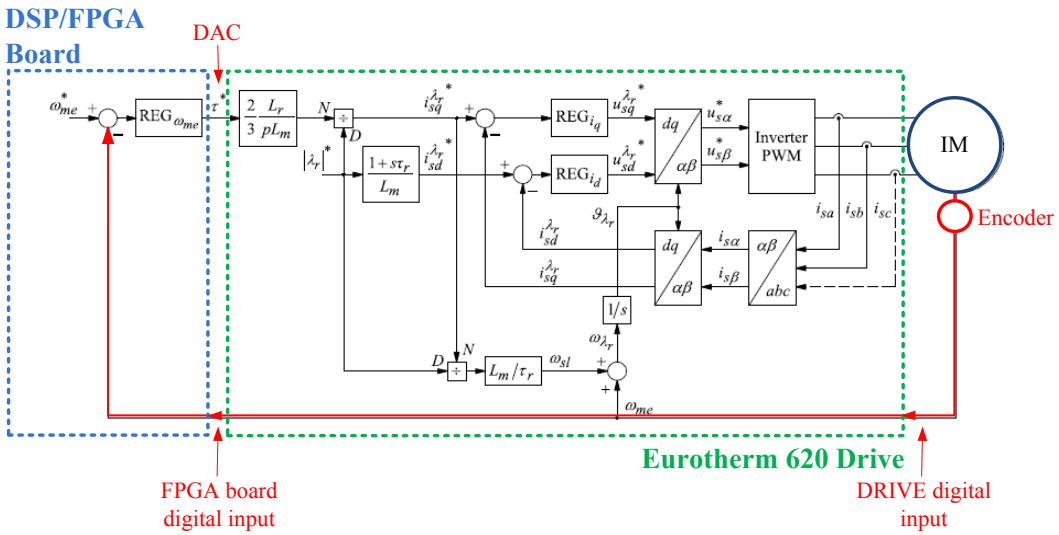

Fig. 7.2 Induction motor control architecture

With this architectural choice, the DSP will control both the speed loop of the induction motor and the STATCOM. The induction motor is connected to the synchronous generator, whose output feeds a set of resistive loads, representing a simplified micro grid. A contactor with a manual controller permits to test the system under sudden and asynchronous load transients. Another contactor controls the insertion in the PCC (Point of Common Coupling) of the STATCOM with energy storage, through the filter inductors L_s. Three capacitors are also added as EMI filter, to reduce the injection of high frequency current harmonics from the PWM controlled STATCOM into the synchronous generator, harmonics that would distort the PCC voltage, degrading the power quality of the system.

The STATCOM control is a standard synchronous frame DQ current control, fully developed and implemented during this project. From Fig. 7.1 , PCC voltages are measured and used into the interrupt routine to feed a DQ-PLL (Phase Locked Loop), required to get the DQ transformation angle ϑ. The STATCOM currents are then measured and converted in the DQ frame and the DQ current control is implemented in the DSP C code. The outputs of the current regulators are the DQ components of the STATCOM voltages, finally re-transformed in the αβ frame and sent to the SVM (Space Vector Modulator) to obtain the gate commands for the switches. The current control will be

further investigated in the next sections. The DC link voltage and the load currents are measured just for data acquisition and visualization through the host interface, being their value non influent in the system control. In Fig. 7.3 , a picture of the final system is reported, highlighting the main components.

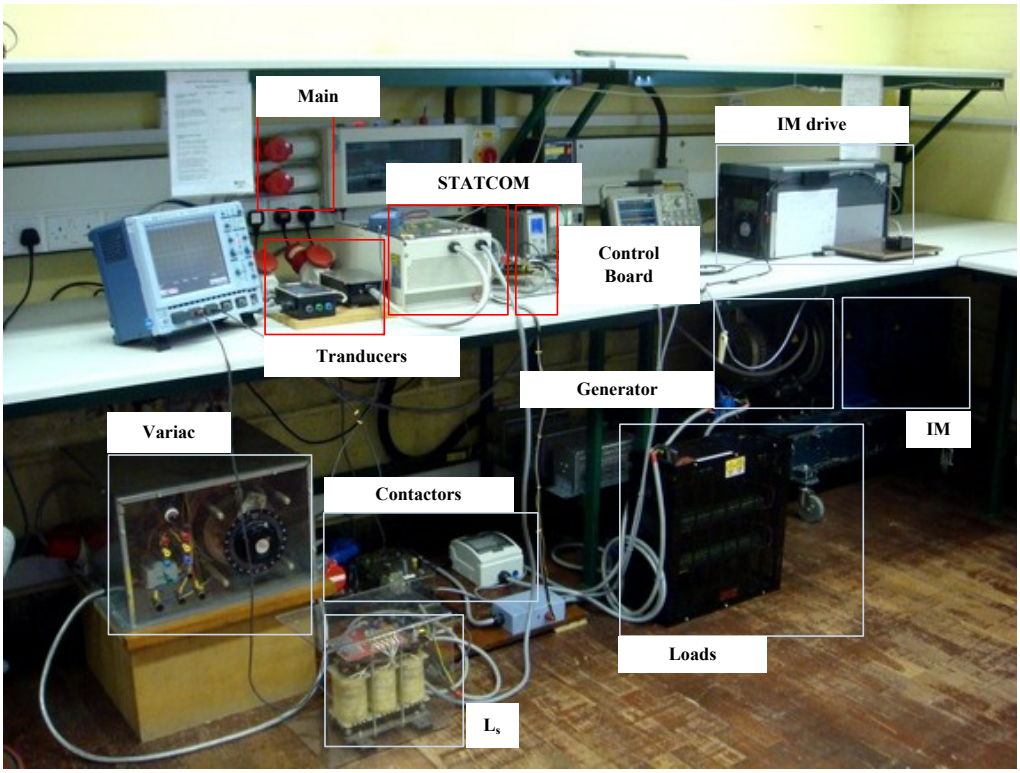

Fig. 7.3 Final system configuration

7.2. Control Board

The control platform, shown in Fig. 7.4 , is a flexible DSP/FPGA system, used in the PEMC group at the University of Nottingham, to digitally control different systems, from electrical drives to power converters. Moreover, the interaction with the system is made easier taking advantage of a Matlab based host interface, that guarantees a complete monitoring of the sampled, processed and generated signals, thus permitting an accurate debug and a faster code development. The base of the system is the Texas Instruments C6713 Floating Point DSP, in his Starter Kit, the DSK, with all the connection ports available for communication with the host PC and to connect the fast and fully customizable part of the control system, an ACTEL ProAsic3 FPGA board, fully developed in the PEMC group.

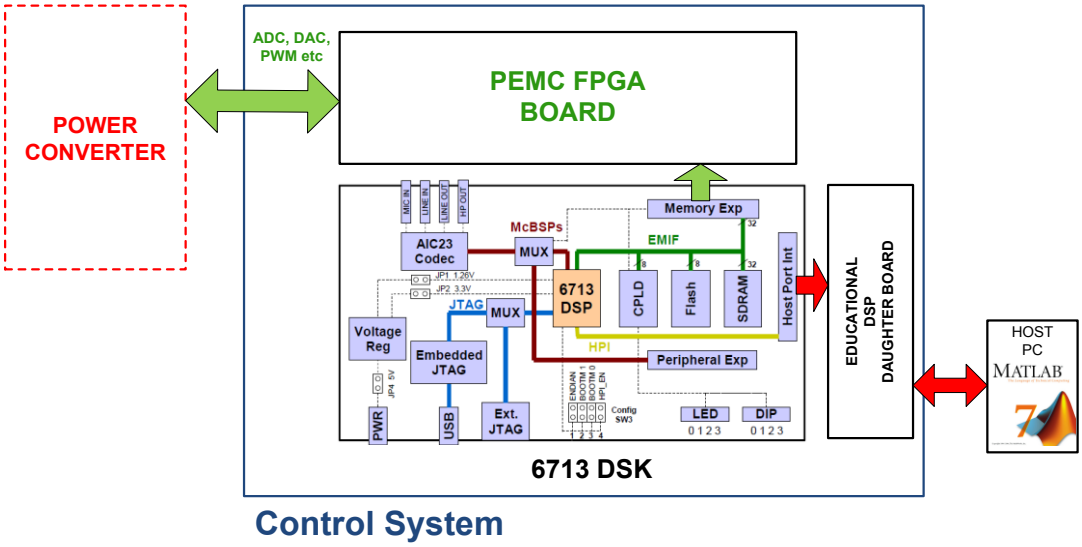

Fig. 7.4 Overview of the control platform

The C6713 is a high speed floating point digital signals processor, running at 225MHz performing up to eight operations per cycle. One of the major advantages of C6713 DSK is the availability of on board peripherals and the flexibility to add external custom peripherals. Above all the external memory interface (EMIF) which not only supports 16Mbytes of on board SDRAM memory, Flash ROM, I/O port but also expands the memory interface through an expansion memory interface connector for a customized daughter board. The DSP has four dedicated address spaces which allow both the on-board devices and the expansion memory interface to be selected individually without conflict. The expansion memory interface connector is mapped into the DSP's chip enable two (CE2) and chip enable three (CE3) address space. Only one of the two memory space enables (CE2) has been used in this application because only the FPGA card has been used as daughter board. All of the accesses to the EMIF are clocked at up to 100MHz while the CPU is clocked at 225MHz. Another daughter card by EDUCATIONAL DSP is used to be able to access the host port interface (HPI) of the C6713. The HPI port is a high speed data port which allows a host to access the internal memory of the C6713 without interrupting the CPU of the DSP. This allows a bi-directional data flow between the host PC and the DSP, enabling the online reading and writing of program variables. The parallel port interface also provides access to an embedded JTAG emulator for source code debugging. Basically, the FPGA sits in the memory map of the 6713DSK, and its registers are addressed by the DSP as memory addresses. It is connected using the External Memory Interface (EMIF) of the DSK board.. The FPGA is programmed with an interface to the address and data buses of the DSK. It is worth noting that to avoid using excessive "space" in the program, and complicating the PCB design for the FPGA, only a limited number of the bits of the address bus can be read using this interface. The group has developed a basic program which has been loaded into the FPGA contains everything required for a general purpose power converter, including:

- Register set for controlling the A2D triggering and access to the sampled data.
- Register set for setting "trips" on/off and for firing trips from hardware (e.g. If V>Vmax….turn the converter off).
- Register set for controlling the LED display which may be attached for showing trip register status etc.
- Registers for setting up an interrupt signal for the DSP- this is required for running.
- PWM registers including dead time (which can be bypassed if not required).

In the main routine of the source code, which is normally part of a project which is compiled using Texas Instruments Code Composer Studio, after having set all the bits to prepare the external memory interface, the FPGA configuration registers and the PWM generator period, the main routine of the DSP enables the PWM interrupt and then waits for the interrupt to occur, after the PWM generator timer is started. The resulting system is a powerful development kit, where the control routine is implemented in the DSP, and the modulation and any other required digital circuitry can be designed and implemented into the FPGA. In the following paragraphs, the most important parts of the FPGA program and board will be briefly presented, referring to Fig. 7.4 .

- **PWM**

The PWM block implemented in the FPGA, is first of all the interrupt generator for the DSP. Each time the PWM generator reaches the end of the current period, set by the user writing a configuration register in the FPGA, an interrupt is generated. During the interrupt routine the information from the A2D channels is extracted from the FPGA registers and used for the control. This information, together with all the information necessary according to the application, is used to calculate the duty cycles used in the space vector modulation algorithm (SVM). With the control cycle complete and the PWM demands calculated, the PWM vectors (the duty cycles coded as a "state" along with the number of clock cycles that that this state must be held for) are loaded into the appropriate internal FPGA register to allow it to perform the built in Space Vector PWM Generator. It is important to note that even if Space Vector Modulation has been described and used in this project, alternative strategies such as Discrete Regular Sampled PWM (Leading/Lagging Edge or centred) can easily be implemented using the same concept but different blocks implemented in the FPGA code. PWM signals are transmitted to the STATCOM gate drivers using current mirrors, to improve noise immunity.

- **CONVERTER TRIPS**

The trips are a method of turning the converter off automatically if an undesirable condition occurs in the converter, i.e. overcurrents, overvoltages etc. They provide a mandatory defence against converter destruction. There are several types of trip, some of them are listed below:

Hardware trips: Hardware trips are the fastest responding trip in the system, and thus the most important for the protection. They operate by comparing the transducers output signals with a digitally programmable reference. If the input is above the reference a trip is triggered and the converter will switch off.

Software Trips: These trips are set from the DSP interrupt routine and then latched from the FPGA, writing a specific register. This kind of trips is considerably slower than the hardware trips, being their action limited by the sampling delay.

- **DIGITAL I/O**

The FPGA board has 56 digital I/O ports, fully configurable from the VHDL program. Moreover, all the I/O are wired to buffers on the FPGA card to provide a link between the FPGA chip and the input/output headers of the board. This ensures that the FPGA is not driving over long track lengths and reinforces the signal which is being transmitted or received.

- **A2D (Analog to Digital) CONVERSION**

The A2D used on the FPGA board is a two channels 12bit converter. The A2D is serially interfaced with the FPGA, where an I^2C protocol is implemented to read the converted data. Moreover, a “busy A2D” bit in an FPGA register can be read into the C6713 PWM interrupt routine by reading the appropriate FPGA registers.

- **DAC – ANALOG OUTPUTS**

The FPGA board is also equipped with a digital to analog converter, a 12 bit converter with four analog outputs that can be used to interface the DSP/FPGA system with analog controllers. The data exchange between the DSP and the DAC is based on serial communication, managed by the DSP using the McBSP (Multichannel Buffered Serial Port) port. The DAC converter has been used to send the torque reference signal from the speed loop (speed PI output) in the DSP to the commercial drive. Another DAC output has been used as trip signal to shut down the drive in case of general trip in the control system.

- **ENCODER INPUT**

For the project, a simple encoder reading block has been implemented in the FPGA code. Coming from buffers that will be described later, the encoder digital outputs A,B,Z are read from the FPGA and translated into an IM speed measurement for the speed loop implemented in the DSP.

7.3.STATCOM

Fig. 7.5 and Table 7.1 report the main parts of the STATCOM:

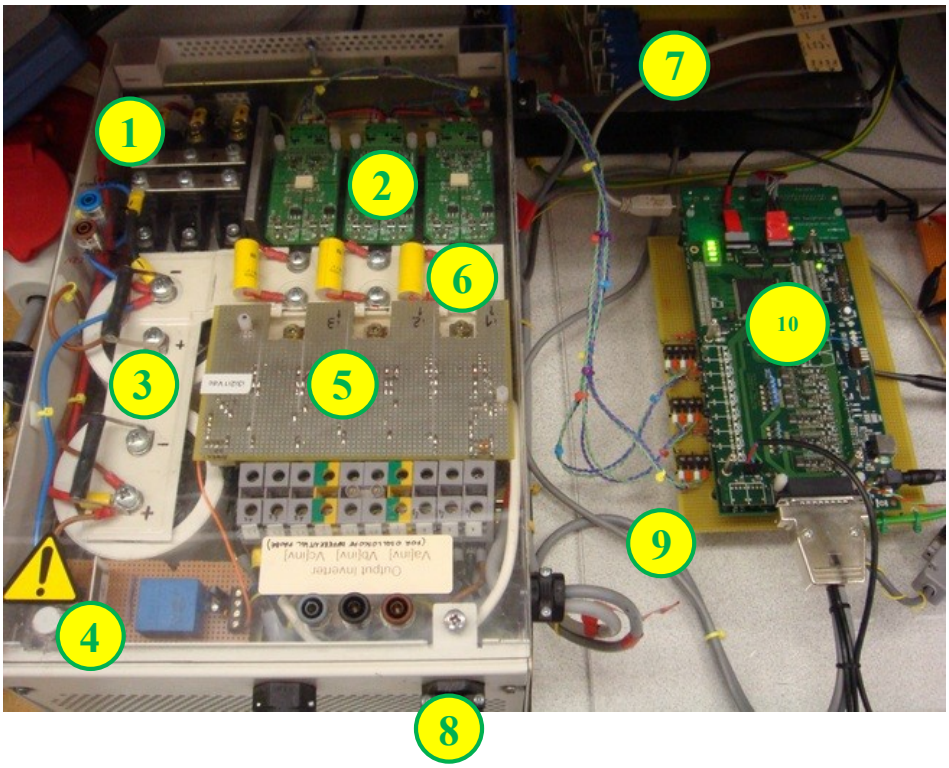

Fig. 7.5 STATCOM

1)DC-link rectifier
2)IGBT gate drives
3)DC-link capacitors
4)DC-link voltage transducer
5)STATCOM currents transducers
6)IGBT modules
7)PCC voltage transducers
8)Load current transducers
9)current mirrors board
10)DSP/FPGA control board

Table 7.1 STATCOM components

The STATCOM is a voltage source three phase inverter rated for 20kVA. It comprises six IGBTs from three Half Bridge IGBT Modules Semickron SKM100GB123D, gate drivers and DC-link capacitors. The inverter output is coupled with the PCC through 5mH coupling inductors. As in Fig.

7.5 , the three phase rectifier and the STATCOM DC-link voltage and output current measurement has been fitted in the same enclosure. In the PCC, a 44μF capacitors bank has been connected to attenuate the switching harmonics injection into the relatively high equivalent inductance of the synchronous generator.

The PWM/SVM signals coming from the control board has to be transmitted to the gate drives to commutate the IGBTs. Switching noise and environmental noise could affect these signals, possibly leading to failures in commutation. The best solution would be the use of optical fibres, that guarantee a complete immunity to disturbances. In the project the intermediate solution of using Wilson current mirrors has been adopted, thus transmitting gate signals as current instead of voltage, increasing the noise immunity.

The control system requires two PCC voltages and two STATCOM currents, in the hypothesis of balanced and equilibrated three phase system. The voltages are required for synchronization, the currents for the current control. In the experimental rig, other signals have been measured for diagnostic and debug purposes: the DC link voltage, considering the possibility in the future of adding a DC link control, the STATCOM output voltages, to check the modulation, the load currents to visualize the load step in the sampled variables. The adopted current transducers are the LEM LA-55P, with maximum current of 60A and bandwidth 200kHz. The voltage transducer is the LEM LV-25P. Their output is a current signal that is translated into a proportional voltage using burden resistors in the FPGA board before the A2D conversion.

7.4.Motor, Drive and Generator

The induction motor is the Magnetics MA 133 K F1, a 16kW two pole pairs induction motor. The motor has on board an incremental encoder, the Eltra EH 80 K 2048 Z 8/24 VLD. The maximum measurable frequency is fMAX=100kHz, and the resolution r=2048 impulses/turn, meaning that the maximum measurable speed is nMAX=fMAX*60/r=2920 RPM, that suites our needs being the nominal speed of the experimental rig equal to 1500 RPM, corresponding to 50Hz at the synchronous generator output. The encoder outputs A,B,Z have been sent to a Line Driver and connected to the FPGA. The encoder block in the FPGA simply counts the number of edges of the encoder signals, thus permitting to identify the speed and the direction. As usual, the encoder resolution is multiplied counting all the edges of A and B, thus obtaining a final resolution of 8192 impulses/turn. The count is stored in an FPGA register that will be read from the interrupt routine in the DSP code. If T_{speed} is the sampling period of the encoder register in the DSP code, the minimum measurable speed is $\omega_{min}=(1/8192)*2\pi/ T_{speed}$. Sampling at $T_{speed}=1/250=4$ms, the mechanical speed resolution is $\omega_{min}=0.2$rad/s.

The induction motor is run by the commercial drive Eurotherm 620, a 22kW drive implementing FOC and space vector modulation at switching frequency of 3kHz. For the project, the drive is a black box, and the operation has been set following the instructions in the data sheet. An autotuning procedure self define the internal DQ current control parameters, and the required magnetizing current reference. The drive is fully protected from overspeed, overcurrent, overvoltage.

The only interaction with the drive is done through the available I/O ports. In particular, following the I/O maps in the data sheet, an analog input has been re-wired to the internal torque reference, equivalent to the q current reference, expressed as a percent of the nominal torque, a driven by the DAC converter. Another input is an external trip, that permits the software synchronization between the STATCOM trips and the drive, shutting down all the system in case of alarm. Considering that the current loop is not accessible, for the design of the other loops a constant gain transfer function has been adopted, equal to the ratio between nominal torque and maximum analog input, thus neglecting the internal current control dynamic.

Eventually, the synchronous machine is a Leroy Somers brushless synchronous generator, rated for 8kW and wired to generate a PCC voltage of $200V_{RMS}$ line to line. The equivalent output inductance is around 20mH, and thus comparable with the STATCOM line inductors. For this reason a bank of 44μF capacitors has been connected to the PCC, to mitigate the switching noise and the inherent distortion of the PCC voltage. Considering that the power rating of the motor is approximately twice the generator, the torque reference of the drive has been set to 50%, so that the maximum generated power is around the generator power.

In the next section, the experimental results will be presented. Following the same structure of the simulations, first STATCOM DQ current control will be shown, than the induction motor speed loop and finally the approximated optimum load step control. The control loops have been first designed using the scripts developed for the simulations in chapter 6, adjusted with the required scale factors, and finally tuned on the rig.

7.5.Experimental Results

Referring to Fig. 7.1 , Table 7.2 and Table 7.3 reports the main system parameters and the trips active on the system:

Parameter	Value
Main supply (variac and drive)	$415V_{RMS}$ line to line, 50Hz
Variac and rectifier fuses	15A
STATCOM output fuses	20A
DC link capacitors	Series of two 4400μF 400V
DC link voltage	400V
STATCOM inductors	5mH
Switching frequency	5kHz (10kHz line to line)
PCC capacitors	44μF
Drive	Eurotherm 620 Vector
Induction motor	Magnetics MA 133 K F1 16kW
Minimum torque	0
Generator	Leroy Somers LS 40 VS1 shunt
Generator power	10kVA @cosφ=0.8
Generator voltage	$200V_{RMS}$ line to line
Frequency	50 Hz – 1500RPM
Generator equivalent inductors	20mH
Load before step	57Ω (700W)
Load after step	19 Ω (2100W)
3-phase Contactors	415 V, 60A, 50Hz

Table 7.2 Experimental rig hardware parameters

Parameter	Value
Maximum PCC voltage	$460V_{RMS}$ line to line
Maximum STATCOM current	$18A_{RMS}$
Maximum DC link voltage	650V
Maximum motor speed	2000RPM

Table 7.3 Trips settings

Based on these parameters, the software for the control loops has been developed in C language for the DSP/FPGA control board. The initial design of the controllers is based on the Matlab scripts developed for the simulations. The only upgrade is related to scale factors that have to be taken into account in the code, but the main transfer functions are the same. Table 7.4 reports the software

constraints and design specifications for the three control loops: DQ current control for the STATCOM, induction motor speed loop, optimum load step controller.

Parameter	Value
DQ STATCOM sampling frequency	5kHz
Speed loop sampling frequency	250Hz
Diesel emulation 1st order delay	100ms
Speed loop bandwidth	2.5Hz
Speed loop phase margin	50°
DQ current loop bandwidth	400Hz
DQ current loop phase margin	60°
Optimum load step control bandwidth	60Hz
Optimum load step control phase margin	60°
PLL bandwidth	5Hz
PLL phase margin	60°

Table 7.4 Experimental setup control parameters and specifications

The experimental results have been divided in two parts: the first reporting the behaviour of the different parts of the system, synchronous generator, induction motor speed control, STATCOM DQ current control, and the second comparing a 1.4kW load step with the conventional speed loop and with the proposed optimum load step control. The results confirm the performances already obtained in simulation, with the speed remaining almost flat during the load step variation. The only reasons for the small perturbation that is still present in the speed are the non idealities such as detection delay and speed PI re-synchronization, as already described in chapter 6.

All the presented waveforms have been acquired using the DSP/Matlab host interface, and thus are either the variables sampled by the control board or internal variables, e.g. the emulated actual torque from the throttle to torque first order transfer function that emulates the diesel engine. Some waveforms have been measured with a Le Croy digital oscilloscope and saved as Matlab data.

Figures from Fig. 7.6 to Fig. 7.8 reports the measured star voltages waveform generated by the Leroy-Somers synchronous generator when it is in steady state at 1500RPM (i.e. 50Hz for the electrical part) loaded with a 57Ω resistors bank and thus generating 700W. The STATCOM contactor is open. Fig. 7.6 show a large distortion in the voltages, as the FFT performed over a period in Fig. 7.7 and Fig. 7.8 confirms:

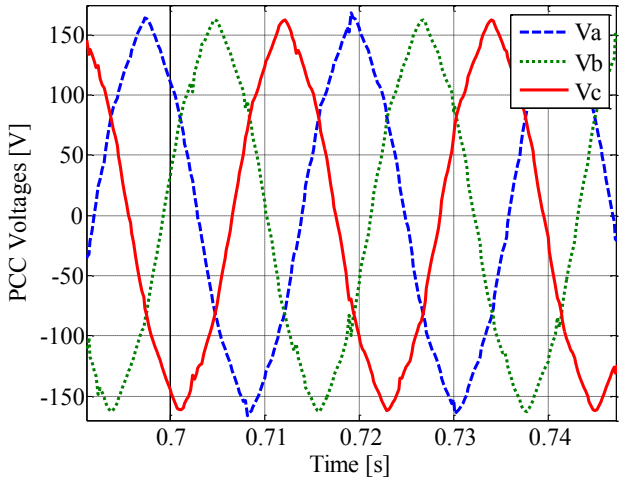

Fig. 7.6 Star voltages from the synchronous generator rotating at 1500RPM and loaded with 700W

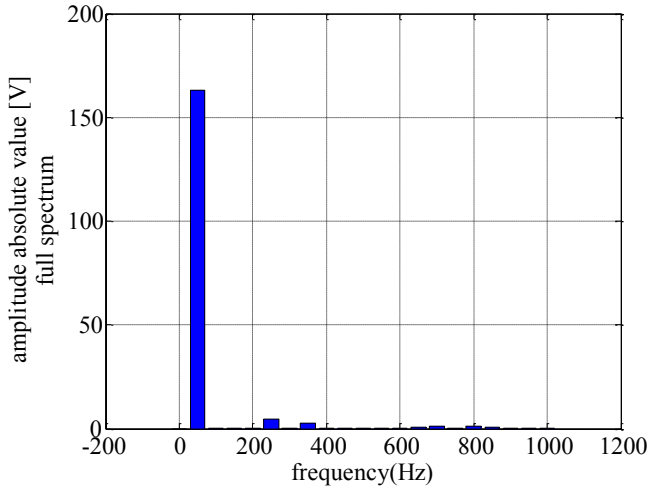

Fig. 7.7 DFT over a period T=20ms, sampled at 5kHz

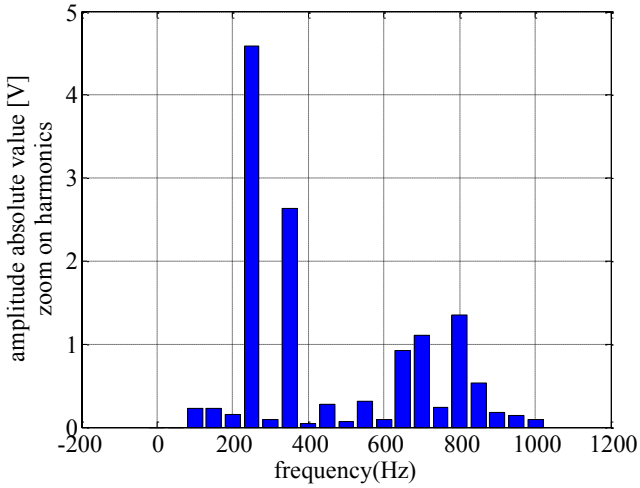

Fig. 7.8 Zoom of Fig. 2 for the harmonics greater than the fundamental

Fig. 7.7 and Fig. 7.8 show that the dominant harmonics are the 5th, with 2.9% of amplitude and the 7th, with 1.53%. Also the 13th, the 14th and the 16th are considerable, with amplitudes of 0.53%,

0.65% and 0.76%. Considering these harmonics, and neglecting the lower ones, the THD results 3.47%.

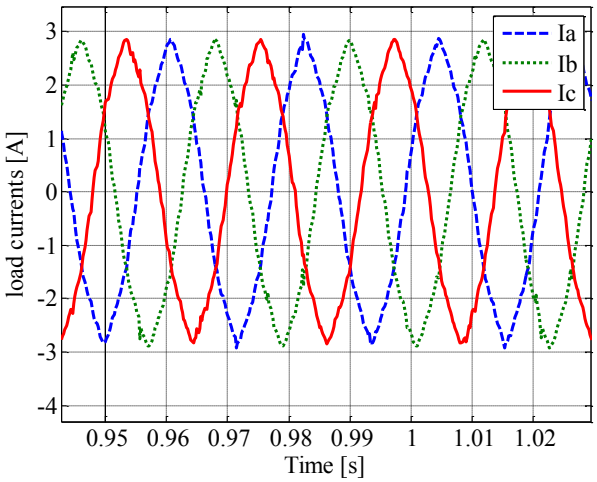

Fig. 7.9 Load currents with R=57Ω

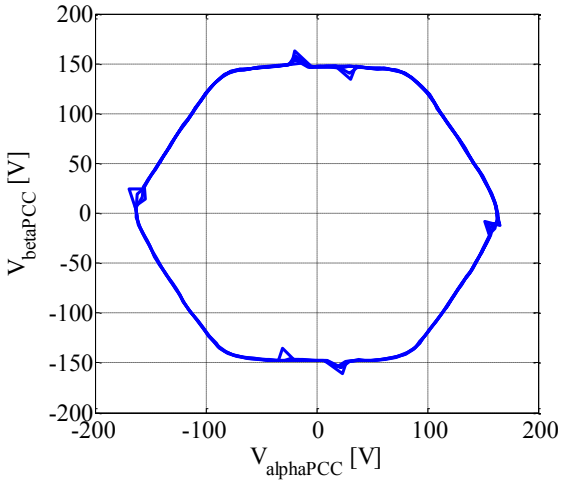

Fig. 7.10 Alpha-Beta transformation of the PCC star voltages, highlighting the distortion

Fig. 7.9 and Fig. 7.10 shows the currents absorbed by the three phase resistive load, and the Alpha-Beta transformation of the PCC voltages. In the next figures, the speed loop tuning and steady state behaviour is reported. The synchronous generator is loaded with a 57Ω three phase resistive load, and the STATCOM contactor is open. The DSP/FPGA only controls the induction motor speed. In Fig. 7.11 , the response to a 13 rad/s speed reference step is reported. Starting from the parameters obtained with the Matlab design, the regulator has been manually tuned to meet the specifications. It is worth to note that, as described in Table 7.2 , the minimum torque is set to zero, to properly emulate the behaviour of a diesel engine, where the power is unidirectional. For this reason, in Fig. 7.11 the significant transient is the step-up transient, while in the step-down transient the torque saturates rapidly and the resulting speed response is an open loop response. This can be easily seen in Fig. 7.12 , Fig. 7.13 and Fig. 7.14 , where the speed regulator torque demand, i.e.

speed PI output or throttle and the emulated actual torque demand, i.e. the output of the transfer function $G_{en}(s)$ emulating the diesel engine dynamic, are presented. In Fig. 7.15 , the PLL frequency is shown, and apart from the different scale due to the different speed for electrical and mechanical quantities, the profile reflects the mechanical speed one: that is a confirmation of the higher bandwidth of the PLL, set to 5Hz compared with the speed loop bandwidth. Fig. 7.16 reports the DQ components of the PLL.

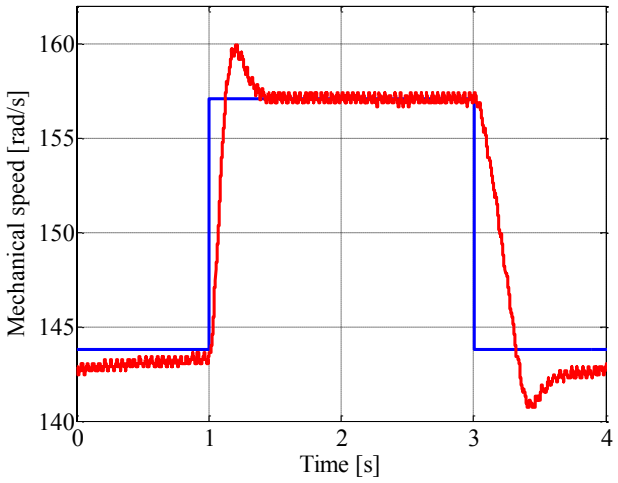

Fig. 7.11 Speed reference step response from 144 to 157 rad/s

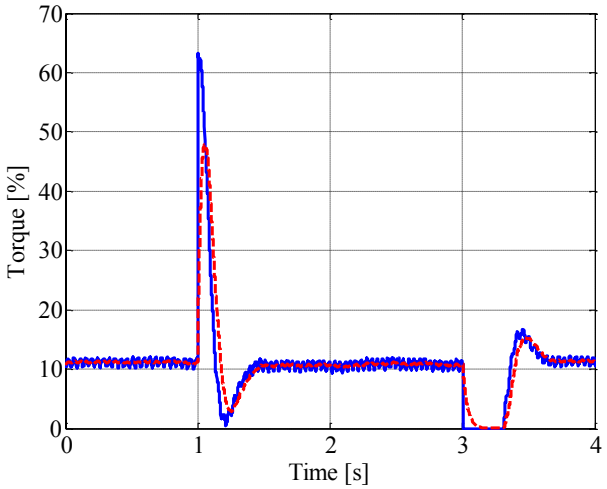

Fig. 7.12 Torque demand (continuous) and emulated actual torque (dashed) during speed reference step

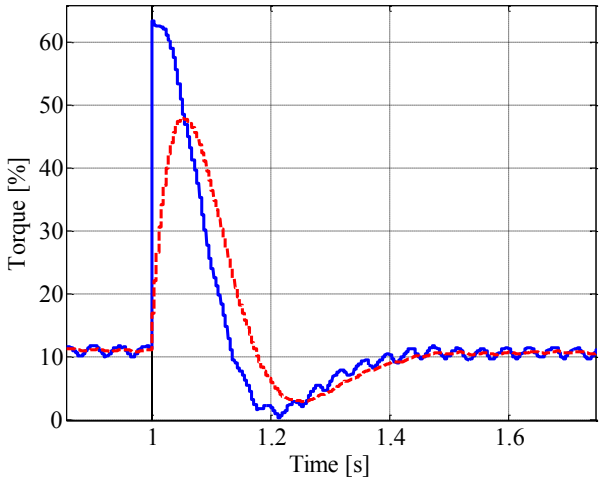

Fig. 7.13 Zoom on the demanded (continuous) and emulated actual (dashed) torque during the step-up transient

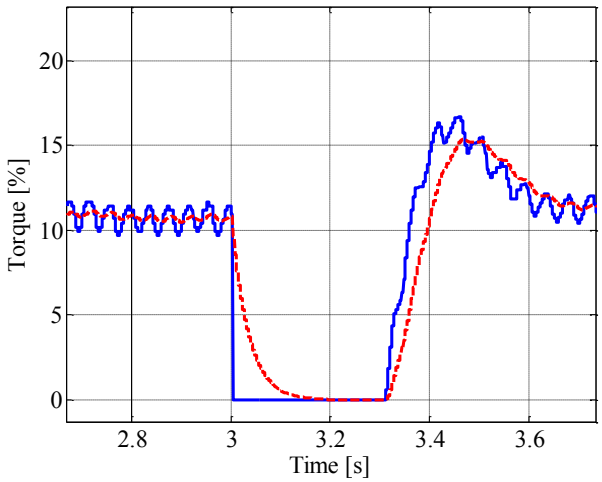

Fig. 7.14 Zoom on the demanded (continuous) and actual (dashed) torque during the step-down transient

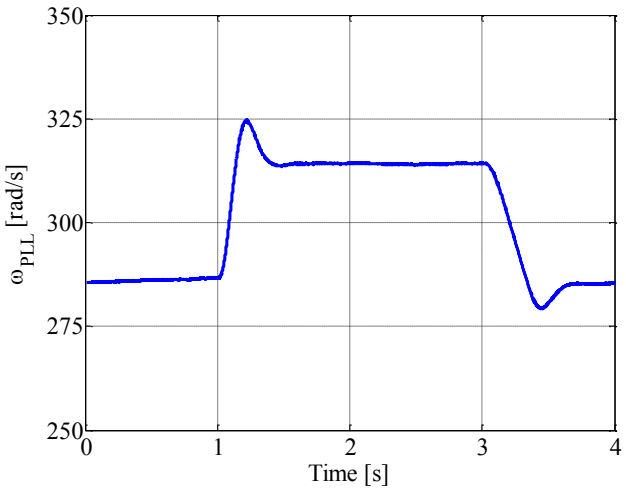

Fig. 7.15 Correspondent PLL response, based on PCC voltage measurements

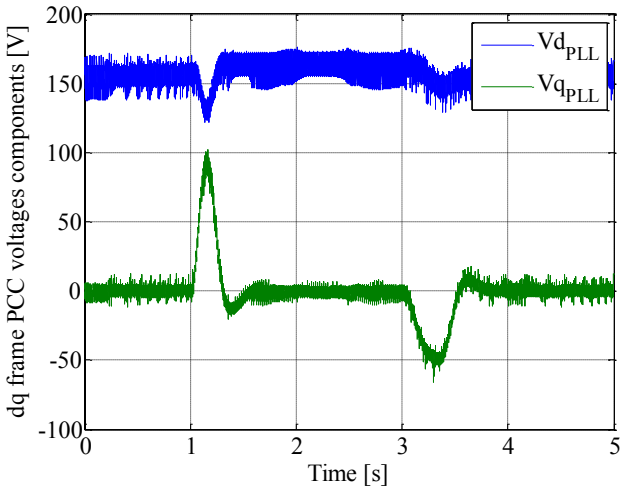

Fig. 7.16 PLL D and Q components during the transients

Fig. 7.17 and Fig. 7.18 shows the steady state behaviour of the speed control. In Fig. 7.17 , a limit cycle oscillation is observed on the speed. The amplitude of the oscillation is ±0.4 rad/s approximately. The origin is connected with the output quantization (speed measurement) and the input quantization, i.e. the torque quantization: this one depends on the DAC quantization and on the drive behaviour in the analog input channel that receives the torque reference. Being this information inaccessible for the drive user, the investigation on this problem has been left o future developments. Without modifying the power electronics part of the system, improvements in this limit cycle could be obtained increasing the inertia J of the mechanical system, leading to a lower quantization in the actuated speed, keeping the same torque quantization. Fig. 7.18 shows the oscillations of the torque demand and consequently in the emulated actual torque.

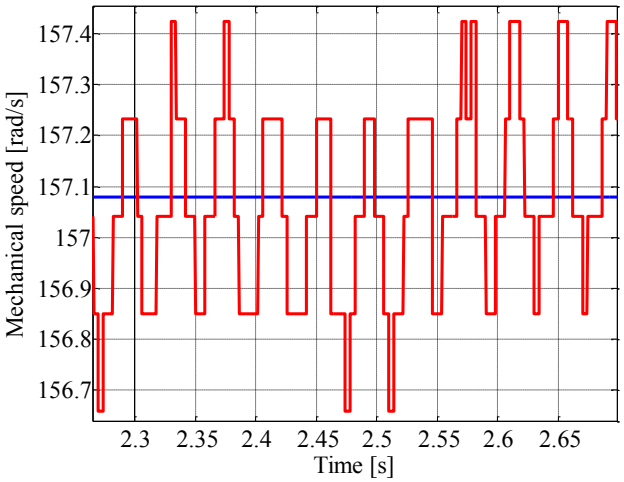

Fig. 7.17 Mechanical speed reference and encoder measured speed

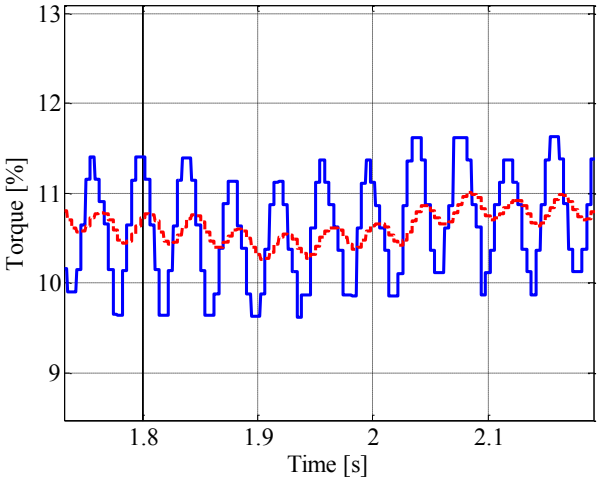

Fig. 7.18 Steady state torque demand (continuous) and emulated actual torque (dashed)

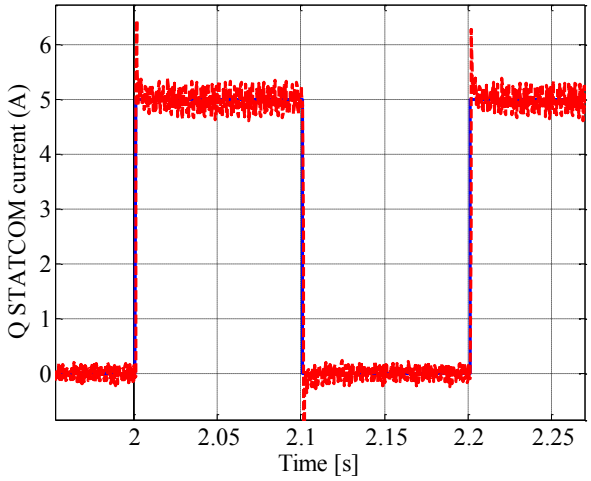

Fig. 7.19 Q STATCOM current during 0 to 5A Q reference step

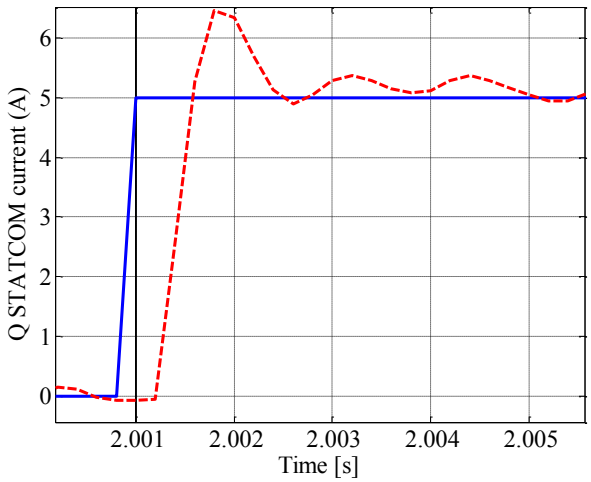

Fig. 7.20 Zoom on the step-up transient 0 to 5 A

From Fig. 7.19 to Fig. 7.26 , the STATCOM current loop has been tuned. The system configuration is as follows: 57Ω resistive three phase load, 44μF capacitors in the PCC, STATCOM contactor closed and initial D and Q current references set to zero. Then, both the D and Q loops have been tested through 0-5A current reference step and the regulators coefficients adjusted to meet the control specifications.

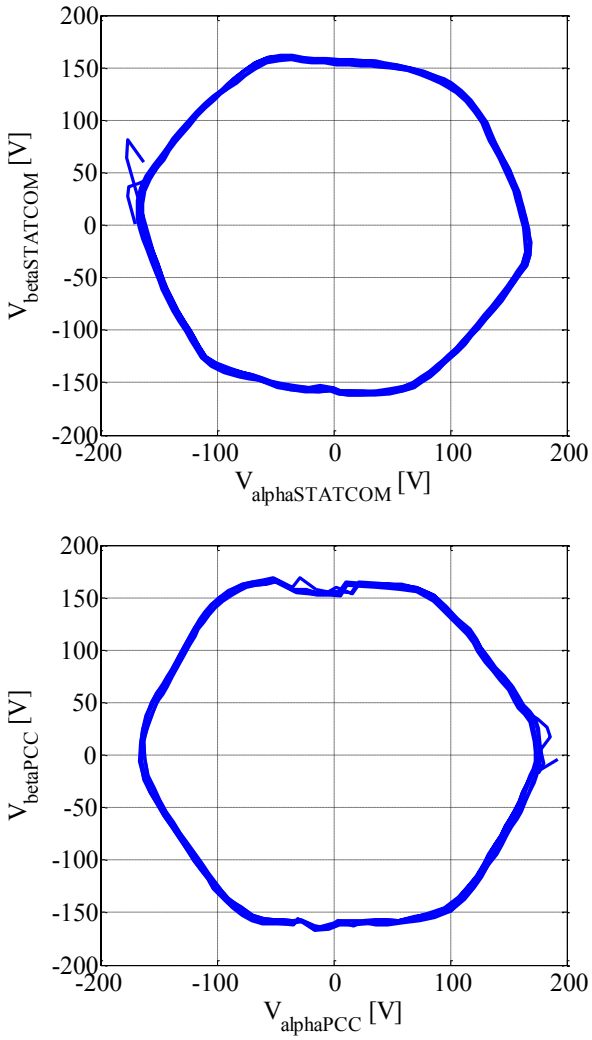

Fig. 7.21 Alpha Beta components of PCC and STATCOM voltages during 0-5A reference step for the Q current reference

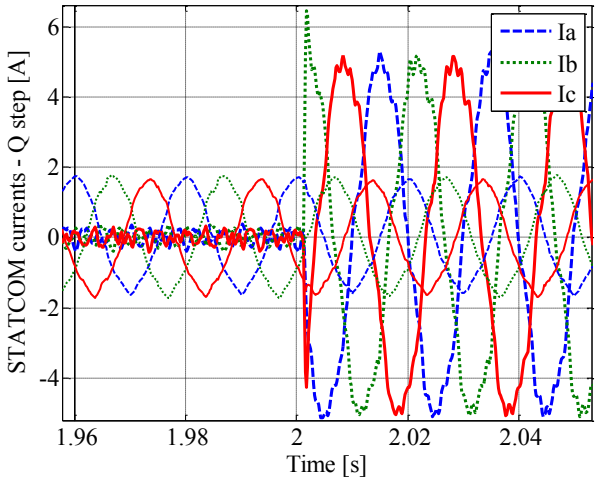

Fig. 7.22 STATCOM abc currents during the step-up transient 0-5A in the Q reference, and in lower thickness a signal proportional to PCC voltages

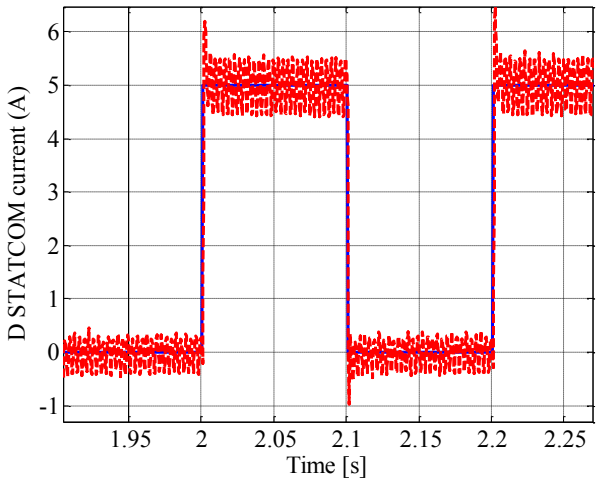

Fig. 7.23 D STATCOM current during 0 to 5A Q reference step

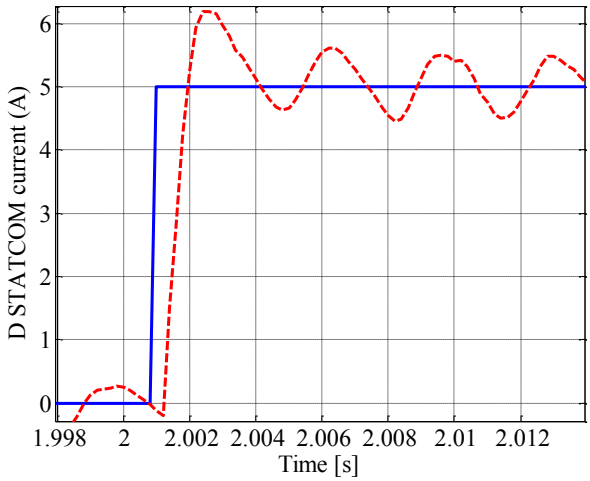

Fig. 7.24 Zoom on the step-up transient 0 to 5 A Fig. 19 Zoom on the step-up transient 0 to 5 A

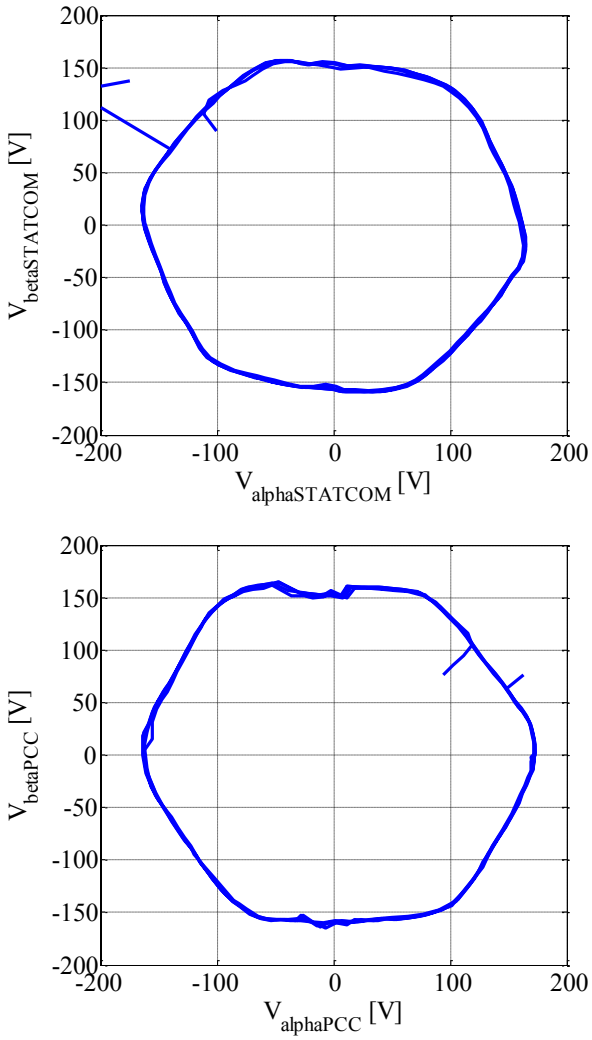

Fig. 7.25 Alpha Beta components of PCC and STATCOM voltages during 0-5A reference step for the D current reference

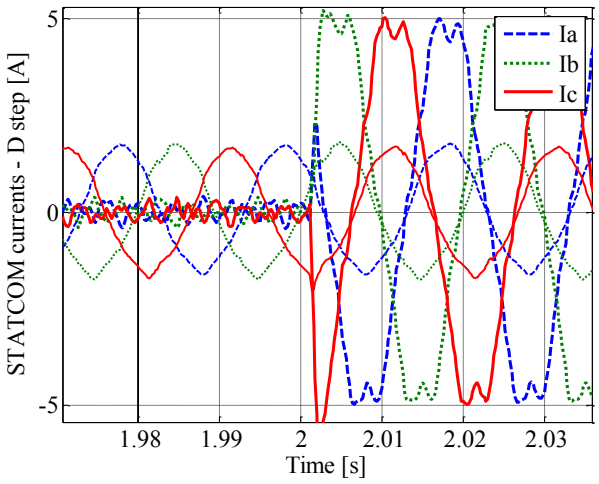

Fig. 7.26 STATCOM abc currents during the step-up transient 0-5A in the D reference, and in lower thickness a signal proportional to PCC voltages

From the figures it can be observed that the current waveforms result heavily distorted. The first test on the STATCOM current control had been done using and ideal sinusoidal PCC, and the sinusoidal current was controlled properly. Connecting the distorted source, i.e. the synchronous generator, the current control is affected by the voltage distortion, causing a distorted current to flow in the STATCOM inductors. The reason is that in this preliminary results a fundamental only voltage feed forward has been adopted in the DQ control implemented in the DSP. This is inefficient to properly compensate for harmonics in the PCC voltage, that should be included in the transformation to have a proper feed forward, cancelling the effect of the PCC voltage. Moreover, the limited (compared to the harmonics) bandwidth of the current control, can't help the compensation of the current disturbance due to the harmonic uncompensated part of the PCC voltage. A possible solution could be an increase in the sampling frequency to 10kHz, to be able to improve the current bandwidth and compensate the disturbances also coming from the other harmonics greater than the 7^{th}. Due to the limited time available for this project, these improvements have been left to future developments of the system.

Figures from Fig. 7.27 to Fig. 7.29 report the PCC voltage, and the currents injected in the PCC from the STATCOM during the 0-5A Q step and the 0-5A D step measured with the oscilloscope for the A phase. The figures highlight another problem of the configuration that is the high commutation noise distorting the PCC voltage: the cause is the high equivalent output inductance of the synchronous generator, causing the current harmonics to distort the voltage. The issue has been solved connecting in the PCC a 44μF capacitors bank, attenuating the switching noise of approximately 20dB, as reported in Fig. 7.30 for phase A PCC voltage when the STATCOM is controlling zero D and Q references.

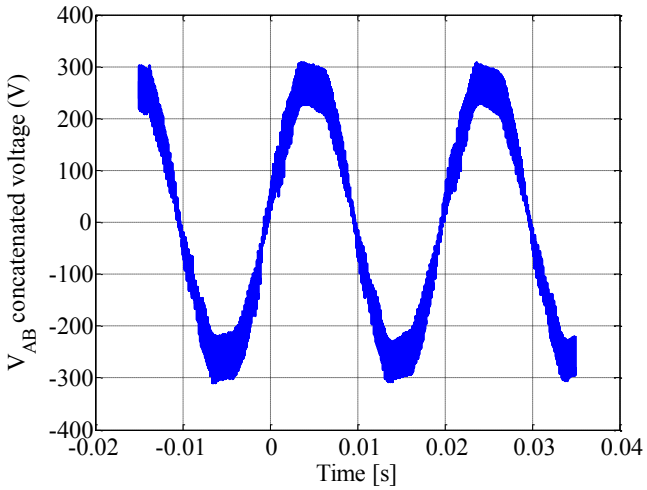

Fig. 7.27 V_{AB} concatenated voltage at the PCC

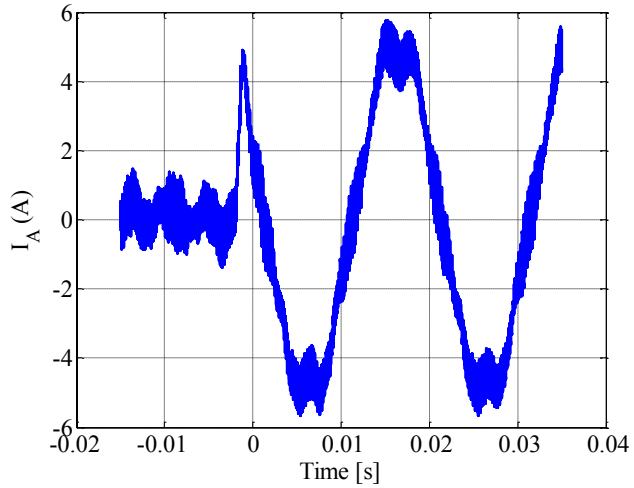

Fig. 7.28 STATCOM current during D current step – phase A

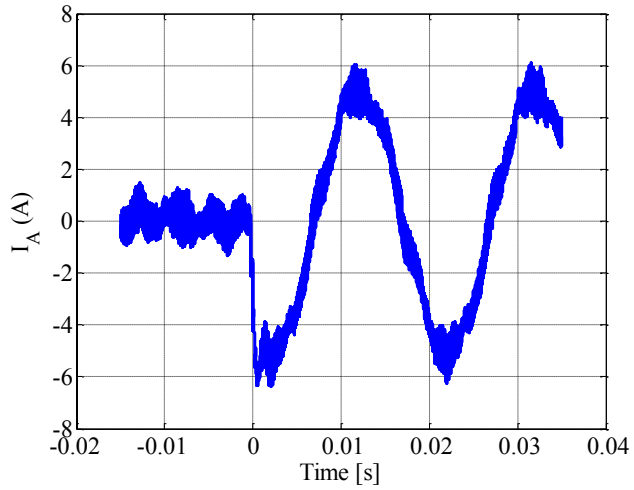

Fig. 7.29 STATCOM current during Q current step – phase A

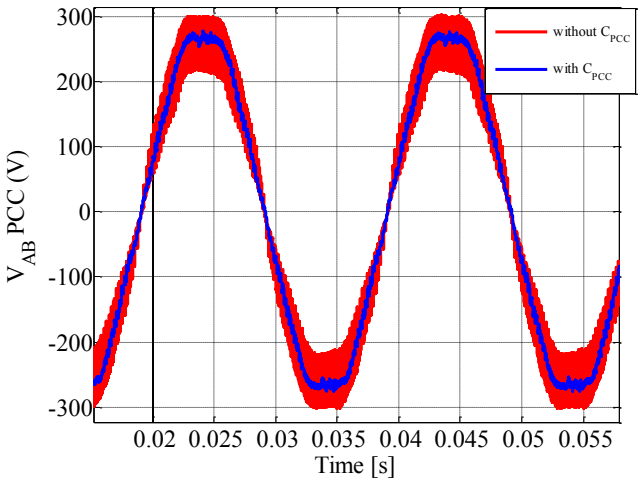

Fig. 7.30 PCC voltage with and without 44μF capacitors in the PCC – zero current references

The following figures report the final comparison between the system without the STATCOM and the proposed Optimum Load Step controller under a 700 to 2100W load step transient. Figures from Fig. 7.31 to Fig. 7.36 report the first case, while figures from Fig. 7.37 to Fig. 7.47 the second case, assuming ω_{th}=156 rad/s as mechanical underspeed detection threshold, corresponding to an electrical frequency f_{th}= 49.656 Hz.

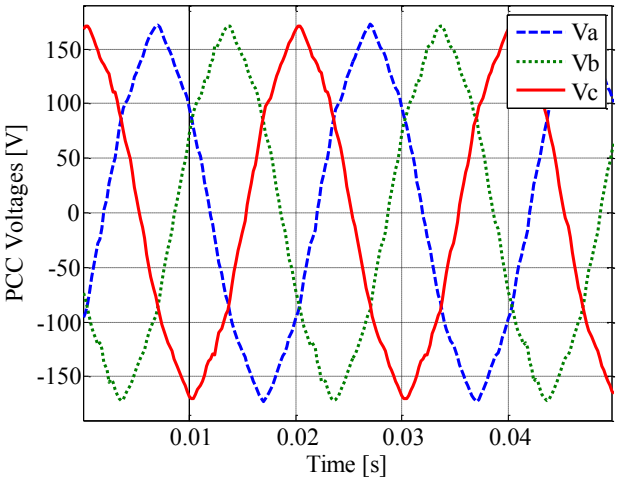

Fig. 7.31 PCC line voltages in steady state with 700W load

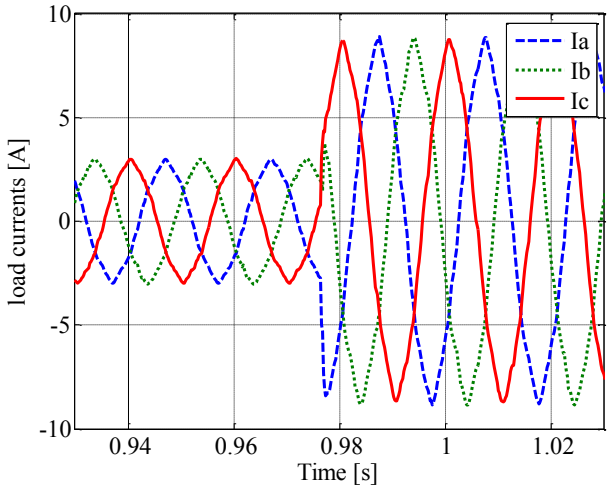

Fig. 7.32 Load currents during load step 700W to 2100W without STATCOM

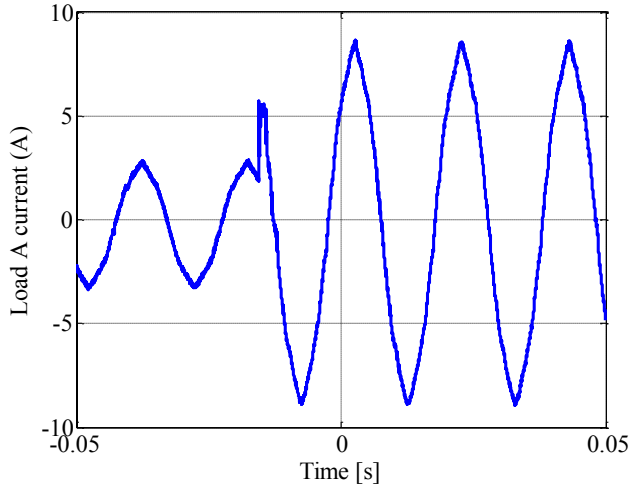

Fig. 7.33 waveform of A load current during 700W to 2100W load step without STATCOM

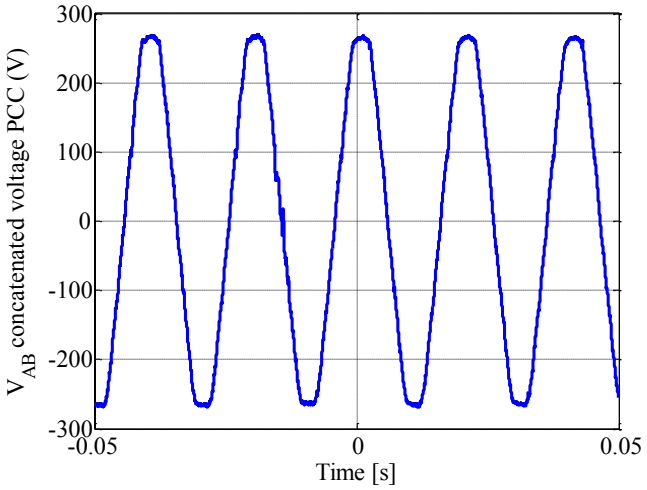

Fig. 7.34 Oscilloscope measured V_{AB} at the PCC during 700W to 2100W load step without STATCOM

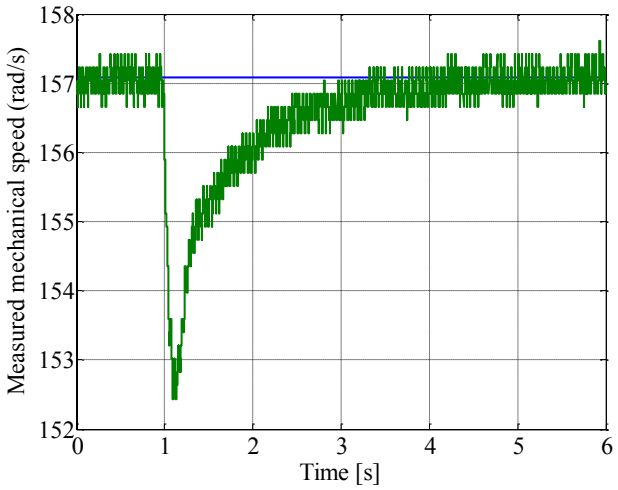

Fig. 7.35 Mechanical speed transient after 700W to 2100W load step occurring at t=1s without STATCOM

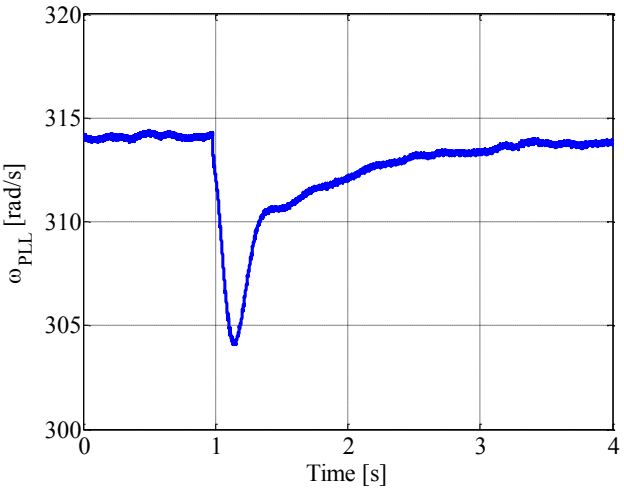

Fig. 7.36 PLL response to the speed variation of Fig. 7.35

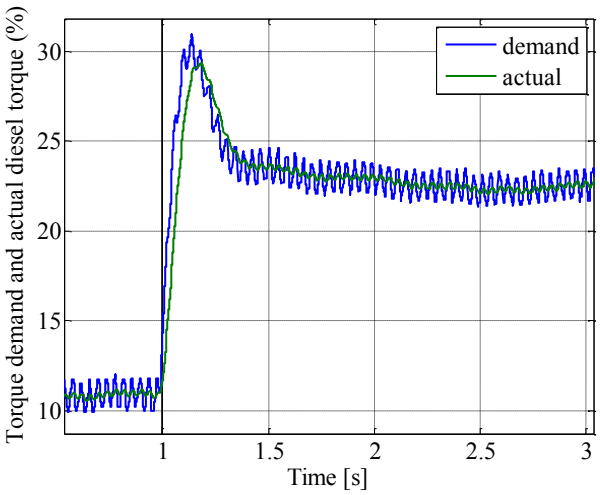

Fig. 7.37 Torque demand and emulated actual torque 700W to 2100W load step occurring at t=1s without STATCOM

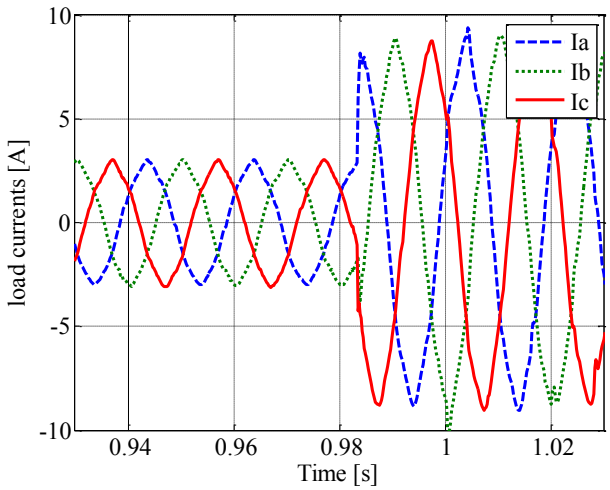

Fig. 7.38 Load currents during load step 700W to 2100W with STATCOM

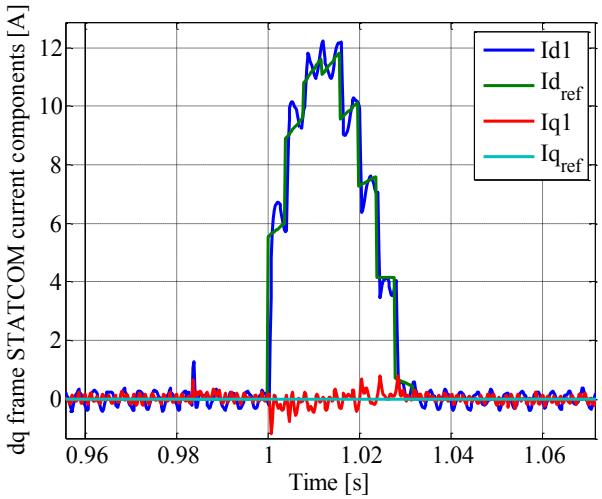

Fig. 7.39 STATCOM D and Q current references and emulated actual currents during the Optimum Load Step control following a 700W to 2100W load step detected at t=1s

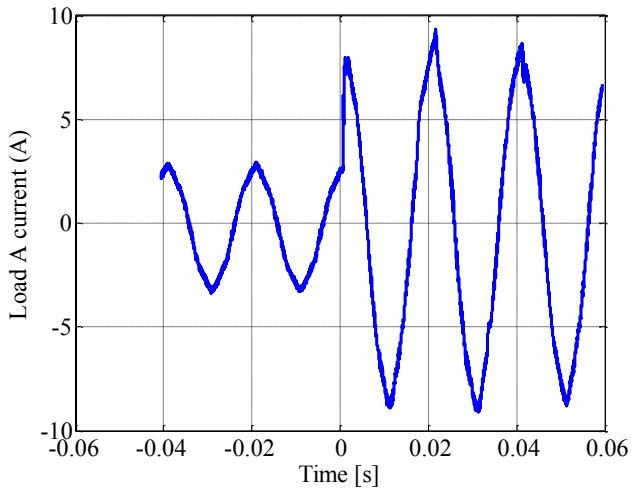

Fig. 7.40 Oscilloscope waveform of A load current during 700W to 2100W load step at t=0 with STATCOM

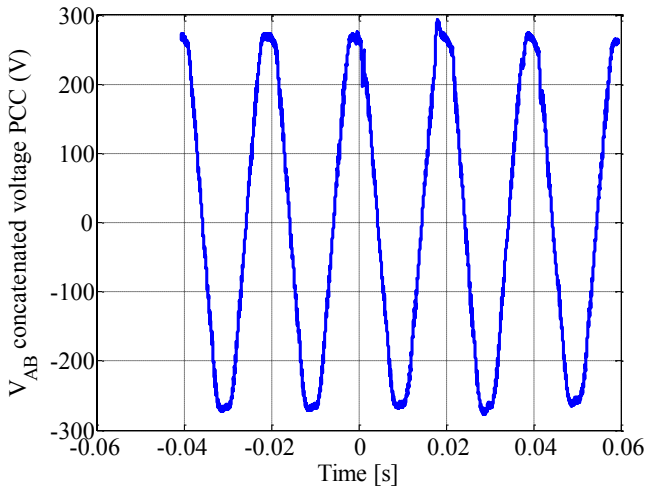

Fig. 7.41 Oscilloscope measured V_{AB} at the PCC during 700W to 2100W load step at t=0 with STATCOM

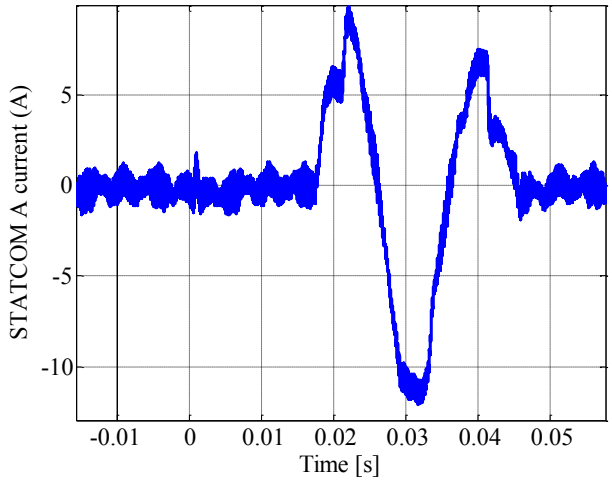

Fig. 7.42 Oscilloscope waveform of A STATCOM current during 700W to 2100W load step at t=0

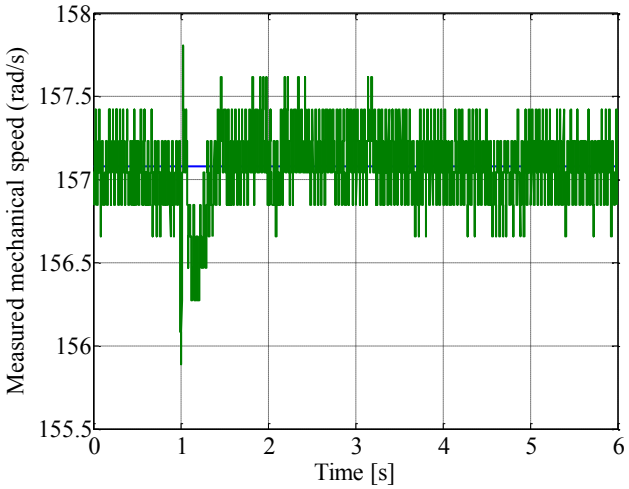

Fig. 7.43 Mechanical speed transient after a 700W to 2100W load step detected at t=1s with Optimum Load Step control

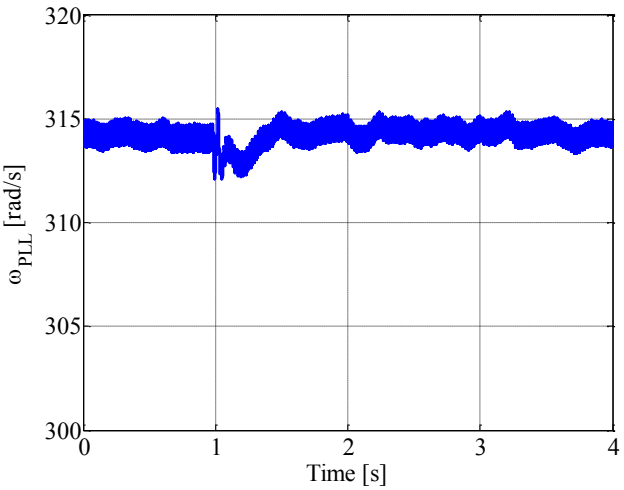

Fig. 7.44 PLL frequency during the transient of Fig. 7.43

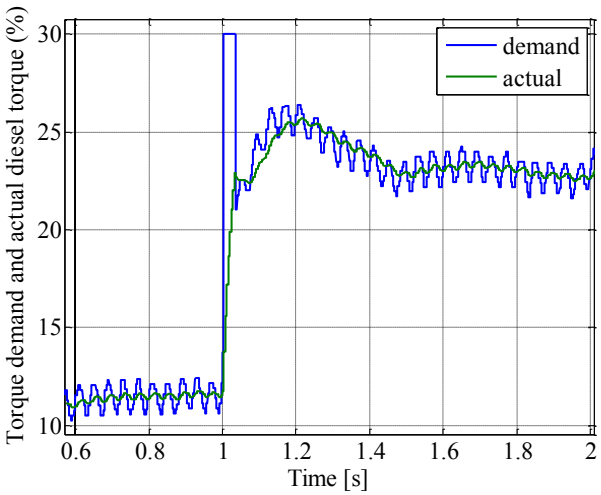

Fig. 7.45 Torque demand and emulated actual torque during the transient of Fig. 7.43

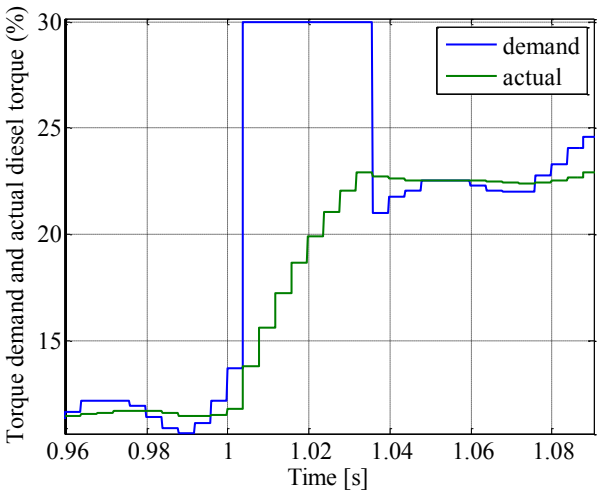

Fig. 7.46 Torque demand and emulated actual torque during the transient of Fig. 7.43 – zoom 1

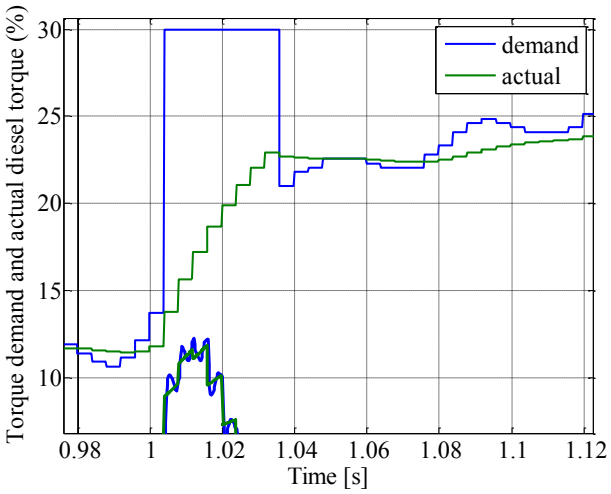

Fig. 7.47 Torque demand and emulated actual torque during the transient of Fig. 7.43 – zoom 2 and comparison with the current injection

From Fig. 7.37 -Fig. 7.47 , the effectiveness of the method can be appreciated: without the STATCOM, in Fig. 7.35 , the speed variation is $\Delta\omega$=4.5796 rad/s, while with the proposed controller the speed variation is limited to the detection threshold $\Delta\omega=\omega_{th}$. In Fig. 7.42 , the current injection is reported where the detection delay can be appreciated, approximately equal to 18ms, that compared with the frequency of the system is a considerable delay. It is worth to note that the figures acquired with the Matlab host, where the triggering instant is t=1s, are triggered on the event of underspeed detection. For this reason, the instant t=1s is not the load step instant but the transient detection instant.

Figures from Fig. 7.45 to Fig. 7.47 show the demanded and emulated actual torque: when the load step is detected through the underspeed threshold, the torque is set to the maximum value, equal in this case to the 30% of the nominal torque. This choice is due to the limited power step compared with the size of the system: setting the maximum to 100% the transient would have been too fast to measure a proper I_d injection, i.e. at least one period of the electrical system frequency. This could also be the case where a limited fuel is available and there is enough energy stored to accept this combination of fuel vs. stored energy to optimally overcome the load step. This considerations are part of a higher level energy management strategy, to optimally control the transients. In Fig. 7.45 to Fig. 7.47 , the throttle is kept constant until the STATCOM I_d current reference reaches the zero. Then, the resynchronization can be appreciated, with another speed transient, that recovers the system to the new steady state.

In the results, the new value for the speed PI, i.e. the new steady state torque demand, has been computed offline knowing the new load power. In a real implementation, the new value can be estimated based on the peak of the injected power, knowing the nominal frequency of the system, following the ideal derivation in chapter 5. The obtained result will be in general an underestimation of the final torque. The error can be reduced reducing the initial detection threshold and increasing the STATCOM . Further investigations will be part of future works.

Conclusions

Smart Grid is a complex topic where a large number of aspects are being investigated to improve energy distribution and transmission. From network and ICT architectural analysis, to control solutions, to new converters and storage solutions. In this work, two specific parts have been investigated.

In Part I, distribution loss minimization has been studied. Despite the generality of the topic, the focus has been on low voltage distribution microgrids, believed to be the first power system where new control solutions can be applied. The microgrid has been modelled with a simplified approach based on distributed generators represented by AC current sources, as well as the loads. This choice maintains the linearity of the system, and thus permits to analytically obtain distribution loss as a function of the injected currents. This analytical solution, based on microgrid parameters knowledge has been proposed to set a background of minimum theoretical distribution loss in a microgrid. Then, a set of possible distributed control solutions has been proposed to achieve loss minimization without the need for topology and impedances knowledge. Moreover, no centralized controller are considered, but the optimization is obtained with node to node communication, in a distributed manner. The proposed solutions have been analytically studied and compared in simulation, using a Matlab code specifically developed to model the microgrid and design the distributed control solutions. The simulations have been structured to represent a realistic scenario, that will be tested on an experimental setup in the future developments of this work.

In Part II, a different topic has been addressed, again in the field of Smart Grid. An islanded microgrid is considered, fed by a single synchronous generator powered by a combustion prime mover. A critic issue in such a system is the effect of load step changes in active power, causing the mechanical speed of the generator to increase or decrease, with consequent frequency variations. In low power microgrids, between 10kW and 100kW, synchronous generator has normally low inertia, and therefore the frequency regulation during transient becomes more challenging. To overcome the problem, the addition to the synchronous machine of a STATCOM equipped with energy storage is proposed: the converter injects the active power required by the load with faster dynamic than the

prime mover, thus avoiding the energy to be subtracted by the kinetic energy of the system. The result is stat a quasi-flat frequency profile can be guaranteed during load transients. The system has been designed and investigated in simulation and then tested in an experimental prototype rated for 10kW, confirming the effectiveness of the approach.

Appendix A

Power Systems Review

A.1. Review of Power Systems theory and methods

In this section, the main concepts related with power systems theory and control will be addressed, to give a general background. Considering the extension of the topic, the analysis is deliberately limited to the main topics, leaving the details to the vast technical literature. In particular, demonstrations and discussions of the exposed concepts can be found in [136].

A traditional power system can be generally identified through some basic characteristics, in particular:

- It is a three phase AC system, operated at constant voltage and constant frequency, where industrial loads are three phase and residential loads are single phase but equally distributed to keep the overall system as balanced as possible.

- The power generation is mainly demanded to Synchronous Generators, converting into electrical energy the mechanical energy coming from diverse prime movers: hydraulic, fossil (coal, diesel etc), nuclear.

- The power is delivered to users over a wide area, and converted to different voltage levels.

The power transmission system has an inherent hierarchic and modular structure, being horizontally divided in neighbour systems, and vertically in subsystems of decreasing power, voltage levels, covered geographic area. The main classification is between: 1)Transmission Systems, including the larger power plants and operated at rms voltage levels above 230kV, to limit the distribution loss caused by the large lines lengths. The generators are typically in the range 11-35kV, increased to 230kV using transformers. 2)Sub-transmission System, representing the bridge between transmission and distribution, with voltages stepped down to 69-138kV. From a functional point of view, Sub-transmission can be considered part of the high voltage transmission system.

3)Distribution System, where the power is delivered to the users. It can be divided into Medium Voltage (MV) Distribution, between 4 and 35kV, then stepped down to Low Voltage (LV) between 120 and 240V for residential users. Power generation in the distribution system, especially in the LV side, was rare in the past, while nowadays is the main driver for the change from a traditional grid to a smart grid, thanks to the development of renewable energy sources. Power systems are generally worldwide interconnected at the transmission level, to increase reliability.

A power system has to be able to meet the load demand in terms of active and reactive power. On the other hand, the loading is continuously varying. Statistical data and demand forecast are normally used to schedule the production in advance. Due to the non deterministic nature of the schedule, a safety margin is guaranteed all the time by energy reserves.

The design and control of a power system is a complex problem where a large number of agents interact, each of them with different static and dynamic behaviour. The complexity is even increased by the highly nonlinear behaviour of most of the agents. The only way to reduce the complexity to a reasonable level is the introduction of simplifications both in the single agents models and in the overall system model. The stability of a power system deals with two main issues: frequency stability, related with the isofrequency of all the synchronous generators, and voltage stability. The need for simplifications is even more important when it comes to stability studies. The typical approach is to slit the problem in simplified sub-problems, for specific kinds of instability.

A.2. Frequency stability

Addressing first the frequency stability, the basics of synchronous generation have to be recalled. The two main components of a synchronous machine are: the prime mover, i.e. the rotating mechanical energy source that guarantee the rotation of the shaft at a specified reference speed ω_{ref}, thus guaranteeing the generation of electrical power at the same frequency, and the DC excitation field controlling the terminals voltages through an AVR (Automatic Voltage Regulator). The normal configuration is the paralleling through the network of multiple synchronous generators, that has to be maintained in synchronism. The fundamental relation for synchronism is the power transfer versus rotor angular position described hereafter with Fig. A.1 and the phasorial diagram of Fig. A.2 . The machines are assumed to be ideal voltage sources, neglecting the output impedance. The line impedance is assumed purely inductive, as normally assumed in power transmission, and the generator V_1 is the reference for the phasorial representation of voltages and currents. The power flow from V_1 to V_2 is reported in the following equations. Assuming a balanced three-phase system, all the derivation is based on single-phase analysis.

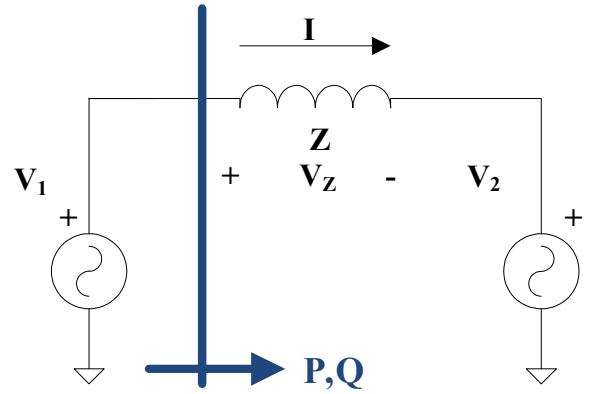

Fig. A.1 Parallel connection of synchronous generators through inductive line

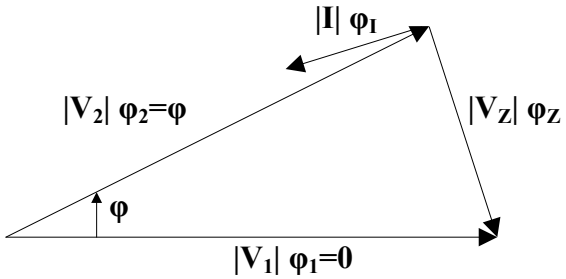

Fig. A.2 Phasorial diagram for Fig. A.1

The complex power flowing from V_1 is:

$$S = \dot{V}_1 \dot{I}^* \tag{A.1}$$

$$\dot{I} = \frac{\dot{V}_Z}{\dot{Z}} = \frac{\dot{V}_1 - \dot{V}_2}{\dot{Z}} = \frac{|V_1| - |V_2|\cos\varphi - j|V_2|sen\varphi}{j\omega L} \tag{A.2}$$

$$\dot{I}^* = \frac{j\left(|V_1| - |V_2|\cos\varphi\right) - |V_2|sen\varphi}{\omega L} \tag{A.3}$$

$$S = \dot{V}_1 \dot{I}^* = -\frac{|V_1||V_2|sen\varphi}{\omega L} + j\frac{|V_2|\left(|V_1|\cos\varphi - |V_2|\right)}{\omega L} = P + jQ \tag{A.4}$$

$$\begin{aligned} P &= -\frac{|V_1||V_2|sen\varphi}{\omega L} \cong -\frac{|V_1||V_2|\varphi}{\omega L} && if\ \varphi \approx 0 \\ Q &= \frac{|V_2|\left(|V_1|\cos\varphi - |V_2|\right)}{\omega L} \cong \frac{|V_2|\left(|V_1| - |V_2|\right)}{\omega L} && if\ \varphi \approx 0 \end{aligned} \tag{A.5}$$

Equations (A.5) can be rewritten in a general frame reference for the vectors as:

$$\begin{aligned} P &= \frac{|V_1||V_2|sen(\varphi_1 - \varphi_2)}{\omega L} \\ Q &= \frac{|V_2|\left(|V_1|\cos(\varphi_1 - \varphi_2) - |V_2|\right)}{\omega L} \end{aligned} \tag{A.6}$$

From the Q equation follows that the reactive power flow mainly depends on the voltage difference between V_1 and V_2. Another interpretation is that the injection of a positive reactive power, i.e. current I lagging voltage V_1 causes a decrease in voltage V_2, while injection of lagging current causes an increase in voltage V_2. The consequence is that, as general approach, the reactive power has to be supplied locally, because the long distance transmission would require a large voltage gradient.

Focusing now on the active power flow P, the power transferred from V_1 to V_2 depends on the phase difference between the voltages: when V_1 lags V_2, the phase difference is negative, and V_1 absorbs active power; instead, when V_1 anticipates V_2, V_1 injects active power. Being the relation dependent on a sine, the power transfer is a nonlinear function of the phase difference. The immediate consequence is the existence of a maximum absolute value of the transferable power, corresponding to a phase difference $\varphi_1-\varphi_2=\pm\pi/2$, and depending on the voltage amplitudes, the steady state frequency ω and the line inductance.

$$|P_{MAX}| = \frac{|V_1||V_2|}{\omega L} \tag{A.7}$$

The power-angle relation forms the base of generator paralleling using droop control, that will be briefly introduced later. From a qualitative point of view, when a generator tends to temporally increase its speed during a transient, the angular with respect to a slower machine will increase, naturally increasing the power injected by the faster machine. The increased power tends to slow down the machine, moving toward a new equilibrium. Stability issues arise approaching the limits of the power-angle equation: when an increased angle causes a decrease in transferred power, a positive feedback is triggered that leads to the frequency collapse of the system. If this happens, the generator has to be disconnected a specific control procedure starts to stabilize the network. In general terms, the frequency stability is classified into a small-signals stability, where the power system remains close to the steady state condition an responds to limited disturbances, and transient stability, when severe changes in the network move the steady state causing large variations in the system. While the small-signals stability is simplified by the linearization around the steady state, the large signals stability involves the non linearities of the power systems, resulting in a more challenging scenario.

A.3. Voltage stability

Instead, voltage stability is the capability of the power system of keeping the voltage at all the buses within nominal operation ranges, independently on transients occurring in the network. The voltage instability is normally referred to the progressive and uncontrollable drop of the voltage,

ending up in system collapse. This is typically caused by the inability of the power system in supplying the reactive power demanded by the load. In a qualitative analysis, the system is voltage stable if an injection of reactive power in a bus increases the bus voltage magnitude, reversely is unstable if the voltage decreases. A simple example is addressed in Fig. A.3 , for a generator-line-load system:

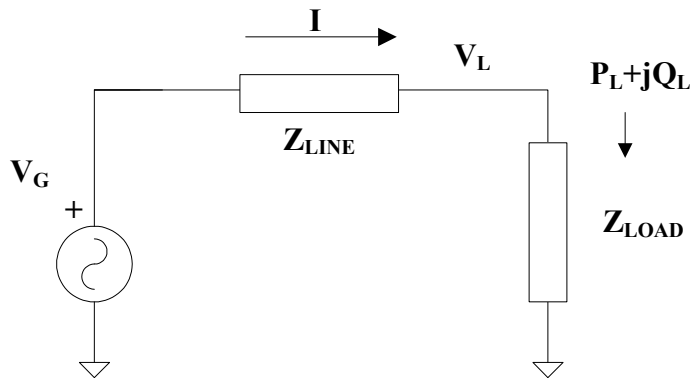

Fig. A.3 Simplified generator-line-load system for voltage stability definition

Defining the circuit impedances as:

$$\begin{aligned} \dot{Z}_{LINE} &= Z_{LINE}\angle\delta \\ \dot{Z}_{LOAD} &= Z_{LOAD}\angle\varphi \end{aligned} \tag{A.8}$$

The magnitude of the flowing current is:

$$\begin{aligned} I &= \frac{V_G}{\sqrt{(Z_{LINE}\cos\delta + Z_{LOAD}\cos\varphi)^2 + (Z_{LINE}\sin\delta + Z_{LOAD}\sin\varphi)^2}} = \\ &= \frac{\dfrac{V_G}{Z_{LINE}}}{\sqrt{1+\left(\dfrac{Z_{LOAD}}{Z_{LINE}}\right)^2 + 2\dfrac{Z_{LOAD}}{Z_{LINE}}\cos(\delta-\varphi)}} = \frac{\dfrac{V_G}{Z_{LINE}}}{\sqrt{F}} \end{aligned} \tag{A.9}$$

The voltage magnitude at the load side is:

$$V_L = Z_{LOAD} I = \frac{Z_{LOAD}}{Z_{LINE}} V_G \frac{1}{\sqrt{F}} \tag{A.10}$$

And finally, the load active power:

$$P_L = V_L I \cos\varphi = \left(\frac{V_G}{Z_{LINE}}\right)^2 \frac{Z_{LOAD}}{F}\cos\varphi \tag{A.11}$$

The equation are analyzed assuming a line impedance with tanδ=10 and an impedance with power factor cosφ=0.95 lagging, and thus absorbing inductive power. The current I, the load voltage V_L and the load active power P_L are reported in Fig. A.3 as a function of the ratio of the impedances modules Z_{LINE}/Z_{LOAD}. To obtain a result of general value, the magnitudes are normalized to the short circuit current V_G/Z_{LINE}, the generator voltage V_G and the maximum power (equation has been omitted for simplicity) respectively.

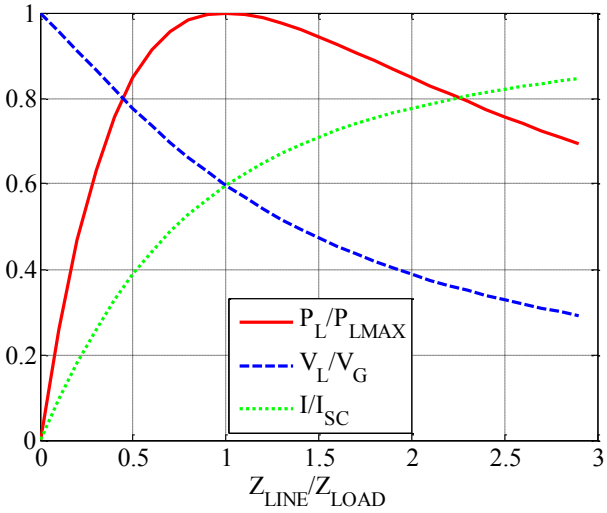

Fig. A.4 Normalized load current, voltage and active power for the circuit in Fig. A.3

From Fig. A.3 follows that the transmitted power is maximum when the line impedance and the load impedance have the same module, and this is true independently on the phase of the impedances. Of course the absolute maximum power correspond to the well known condition $Z_{LOAD}=Z_{LINE}^*$, where * is the complex conjugate. Progressively reducing the module of the load Z_{LOAD}, the load voltage V_L decreases, and after $Z_{LOAD}=Z_{LINE}$ the load power stars to decrease. If the load has a constant impedance, there are no stability issues involving voltage control. But when the load is controlled to absorb a constant power P_L, a safe operation of the control can be guaranteed only until the limit of the maximum power. Trying to control higher active power, the load control would cause voltage collapse, acting in the direction of continuously reducing the load module without any increase in deliverd power. This is a very common, even if largely simplified, voltage stability problem. Other contingency could potentially arise due to specific load behaviours different from constant impedance or constant power loads.

From the above equations, it is clear that the relation between load voltage and load active power depends on the load power factor. This is intuitive because the voltage drop along the line is function both of active and reactive power flowing to the load. From equations (A.10) and (A.11), a relation between P_L and V_L can be derived, assuming a constant line impedance module and phase, and generator voltage and plotting the power-voltage curves parameterized to the load phase, i.e. the

load power factor. This can be easily done by plotting the normalized voltage and power of Fig. A.3 in the Cartesian axes. The curves are reported in Fig. A.5 , where the power normalization is based on P_{UPF}, corresponding to the maximum transferable power with unity power factor.

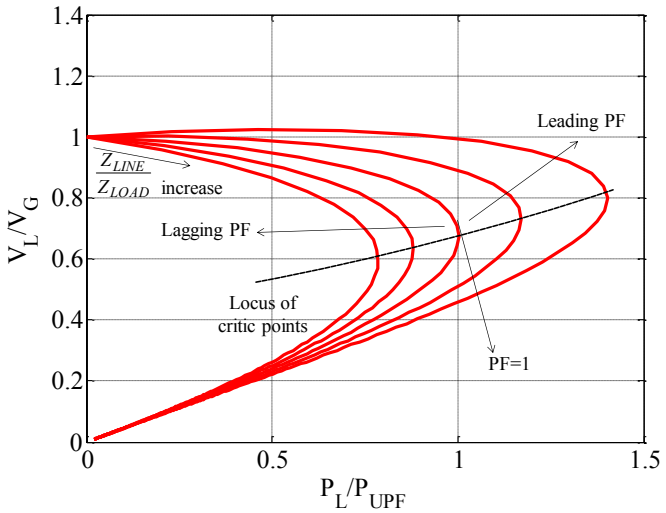

Fig. A.5 Load power versus load voltage as s function of the load power factor for the circuit in Fig. A.4

From Fig. A.5 follows that a stable operation is guaranteed in the upper part of the curves, above the locus of critic points (corresponding to the interval Z_{LINE}/Z_{LOAD}=[0,1] in Fig. A.3). Assuming a constant active power flow (controlled at the load side, typical example is an asynchronous motor with constant mechanical load) a change in the load reactive power, i.e. a change in the power factor, could move the system operating point in the lower part, where a decrease in power is followed by a decrease in voltage and the system could became unstable under certain load characteristics [137]. A typical example is a perturbation in the curves that leads to a maximum deliverable active power less than the load demand. From another point of view, referring to Fig. A.3 , assume constant load active power reference and constant line impedance. A sudden decrease in the load power factor with lagging current (increased inductive load), will vertically shrink the power curve (assuming to maintain the previous normalization): the result is that the maximum deliverable active power could become lower than the power reference, driving the load control toward instability.

A simplified conclusion is that an optimal condition for power systems is with load locally supplied of the required reactive power: circulation currents are limited, thus limiting the losses, and stability problems are attenuated. Considering the inductive nature of the lines, it is also important to note that unity power factor, i.e. equivalent resistive load, doesn't mean zero reactive power absorbed by the network, being reactive power required for the line magnetization, causing a slight voltage drop in the load side. To restore the voltage module to the nominal value, a reactive power

source, i.e. a capacitor of suitable value, should be connected at the load side: in this condition, there will be no reactive power absorbed by the feeder.

The stability analysis won't go in further details, a deep analysis can be found in [136, 137] for the interested reader.

A.4. Synchronous generators control

A single synchronous generator is normally connected to a prime mover, generating mechanical energy, such as steam turbines, hydro turbines, diesel engines. The prime mover speed is controlled in closed loop to guarantee the nominal electrical output frequency. When this simple structure is extended to a large power system, with a number of generators operating in parallel, loads and transmission lines, a feedback control is required to synchronize all the generators. In fact, the approach of simply imposing the same speed reference to each independent generator would be unpractical for two main reasons: the first is that it would be impossible to guarantee the exact speed synchronism, the second that even with synchronized generators, the phase shifts among the generators would be uncontrolled, causing circulation currents and non-optimized power sharing (also assuming limited phase differences to avoid destructive interference between the generators). The traditional and well known solution to this problem is the droop control of the generators: the system frequency is used as wireless communication channel to guarantee isosynchronous rotation and scheduled power sharing. From a steady state point of view, the droop control applied to a single generator represented in Fig. A.6 , where $G_{REG}=K/s$ is the droop controller, $G_{PM}(s)=K_{PM}$ is the prime mover transfer function (ideally assuming instantaneous power generation from the prime mover) and $G_{MEC}(s)=1/(B+Js)$ is the mechanical model:

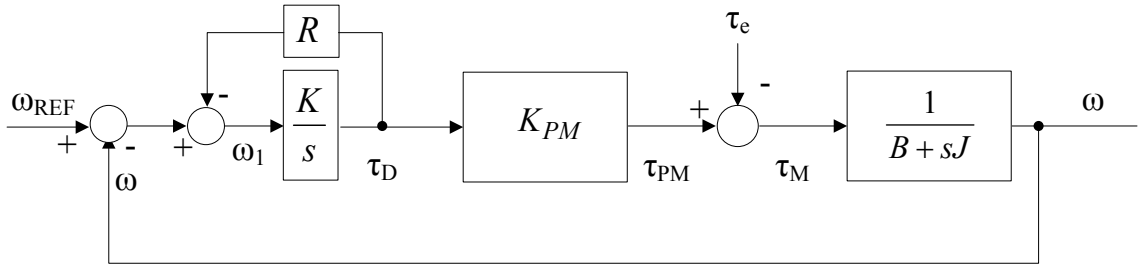

Fig. A.6 Synchronous generator speed control with droop

In the figure, the droop function is represented by the gain R, added to the integral speed regulator. The output of the droop controller has been named τ_D, assuming adimensional the gain K_{PM}. The net result from a control point of view is that the speed loop looses the integral gain, and is modified into a proportional gain. Thus, the steady state system frequency ω is no longer equal to the reference ω_{REF}. Assuming negligible the amount of power required to compensate the equivalent mechanical friction, the steady state of the system is described by the equations:

$$\omega_1 = 0 \rightarrow (\omega_{REF} - \omega) = R\tau_D = RK_{PM}\tau_{PM} = RK_{PM}\tau_e \tag{A.12}$$

Adding the approximations:

$$K_{PM} = 1,\ \tau_e = \frac{P_e}{\omega_{REF}} \tag{A.13}$$

The steady state frequency equation becomes:

$$\omega = \omega_{REF} - \frac{R}{\omega_{REF}} P_e = \omega_{REF} - DP_e \tag{A.14}$$

Where D is the droop coefficient. All the made approximations are reasonable considering that such a system is normally designed to have a frequency variation limited to 5% of the reference. Moreover, the reference speed ω_{REF} is usually set to be higher than the grid nominal frequency ω_{NF}, to use all the frequency span allowed by national regulations, and D is chosen to have the nominal frequency in correspondence of the nominal output power of the generator. Fig. A.7 reports the linear equation (A.14), assuming $\omega_{REF}=(1+0.025)\omega_{NF}$.

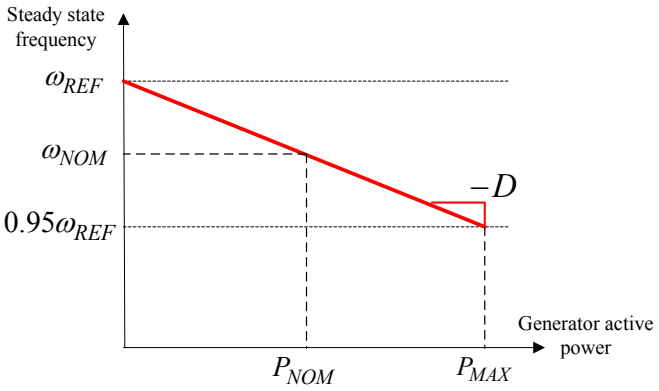

Fig. A.7 Steady state frequency versus generator output power for proportional droop controller (A.14)

So far, a simple variation in the control scheme for a single generator has been presented. The advantage of the adoption of such a scheme is the inherent paralleling capability, based on the inductive nature of the line (A.5). Consider the case of two generators 1 and 2, connected to a single load through inductive lines, as in Fig. A.8 :

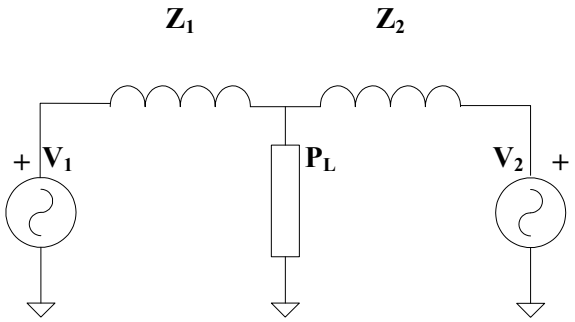

Fig. A.8 Parallel configuration of two synchronous machines feeding a single load of active power P_L

The generators are controlled with droop function coefficients D_1 and D_2, and assume for simplicity a common value for ω_{REF} and $D_1=2D_2$, meaning that at the nominal frequency, the output power P_2 of generator V_2 is twice the power P_1 of V_1. If the load demand has to be met, there exists only one frequency, common for both the generators, where the injected powers balance the load. The demand can be satisfied if and only if that configuration is stable, i.e. a perturbation in the load power always drives the system toward a new common steady state frequency. Consider the example of Fig. A.9 , with an initial value of load power $P_L=P_{L1}$, stable for hypothesis.

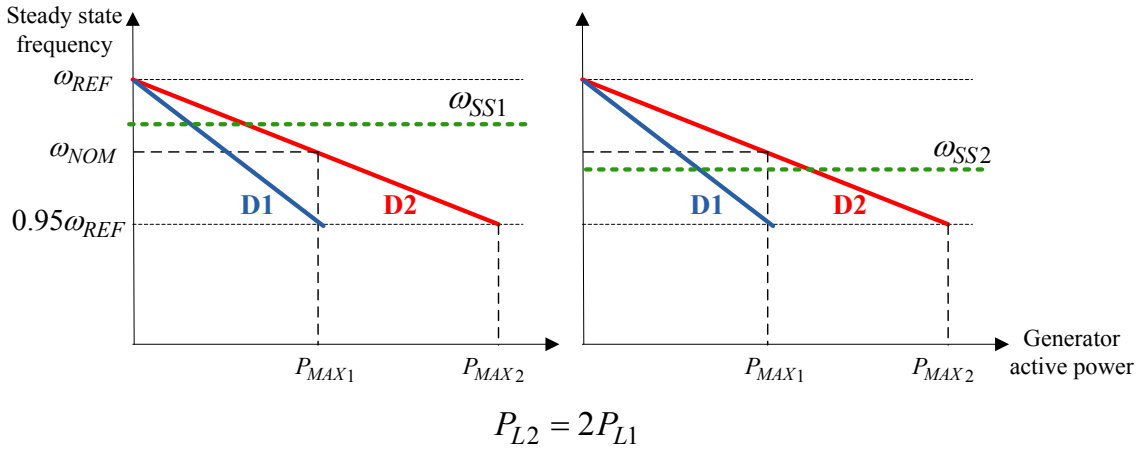

Fig. A.9 Droop control for the system in Fig. A.8 , during a load power step from P_{L1} to $P_{L2}=2P_{L1}$

The load power is then sudden increased to twice the initial value. Assume that during the transient V_2 tends to draw more power than the expected new steady state value: this will cause the frequency of V_2 to slow down, thanks to the droop characteristic. But a decrease in the speed means an decrease in the relative angle of V_2 with respect to the load connection point. But from equation (A.5), this means a reduction in the transferred power, that drives V_2 back toward the equilibrium, with a new frequency ω_{SS2} for both the generators. Similar considerations hold in the opposite case of V_2 drawing less power than the expected. All these qualitative considerations are valid assuming all the voltages at the nodes (V_1, V_2, Load) with constant module, so that (A.5) depends only on the phase shift, and assuming small phase shift and frequency deviation. In this hypothesis:

$$\Delta\varphi = \varphi_1 - \varphi_2 = \int_{t_0}^{t} (\omega_1 - \omega_2) d\gamma$$
$$P = \frac{|V_1||V_2| sen\Delta\varphi}{\omega_{SS} L} \tag{A.15}$$

The first of (A.15) is of general value, while de second require the hypothesis of ω_1-$\omega_2 \approx 0$, to avoid the generation of oscillatory power components.

This brief considerations are of general value for interconnecting a number of synchronous generators in parallel. The system adapts to load power variations guaranteeing a stable steady state with power sharing proportional to the power rating. Naming ΔP_1 and ΔP_2 the power variations for V_1 and V_2, and $\Delta\omega$ the frequency variation:

$$\left.\begin{aligned} \Delta P_1 &= \frac{\Delta\omega}{D_1} \\ \Delta P_2 &= \frac{\Delta\omega}{D_2} \end{aligned}\right\} \rightarrow \frac{\Delta P_1}{\Delta P_2} = \frac{D_2}{D_1} \tag{A.16}$$

For n generators with respective droops $D_1 ... D_n$:

$$\Delta P_L = P_{L2} - P_{L1} = \sum_{i=1}^{n} \Delta P_n = \sum_{i=1}^{n} \frac{\Delta\omega}{D_n} = \Delta\omega \sum_{i=1}^{n} \frac{1}{D_n} \rightarrow \Delta\omega = \frac{\Delta P_L}{\sum_{i=1}^{n} \frac{1}{D_n}} \tag{A.17}$$

A number of modifications exists to optimize the droop behaviour depending on the prime mover model (neglected here) and with respect to power sharing during transients, as well as to restore the nominal frequency of the network after any load change and to control the power sharing modifying the droops [136]. Of course the droop control has to be designed to guarantee the stability of the behaviour of each generator.

A.5. Voltage control

As anticipated in the previous paragraphs about the voltage stability and from the second of (A.5), voltage control is achieved through reactive power injections. Voltage is as crucial parameter from the point of view of the loads, being the equipments designed for operation within a specific voltage range. On the other hand, loads generally require an amount of reactive power that has to be provided from the grid. Excluding the possibility of a transmission over long distances, the only choice is to locally supply the reactive power, thus guaranteeing the load voltage support. The sign of the required reactive power, i.e. inductive or capacitive, depends on the load reactive power needs. As a qualitative rule, in the limits of Fig. A.4 , an inductive load causes a drop in the

connection point voltage, a capacitive load causes an increase in the voltage. Traditionally, the local supply of reactive power is demanded to several kind of devices, both autonomous and remotely controlled. Hereafter, first of all a short description of the most common sources of reactive power in a traditional power system:

- *Synchronous Generators:* a synchronous generator can inherently provide reactive power acting on the machine excitation system to control the connection point voltage through an AVR (Automatic Voltage Regulator). When the machine is overexcited, i.e. DC excitation higher than the one corresponding to unity power factor, the generator injects positive reactive power, reversely when it is underexcited it absorbs reactive power. This is true in the design limits of the machine, represented by the windings current limits.

- *Transmission Cables:* due to their parasitic capacitance, they normally generate reactive power, i.e. they can be loaded with reactive loads without need for compensation.

- *Loads:* loads absorb different amounts of reactive power. The typical condition in a loaded feeder is a net absorption of reactive power, i.e. the equivalent load has an equivalent inductive component.

- *Compensating devices:* their aim is to locally provide or absorb reactive power in order to control the voltage magnitude. In the next paragraphs, the main configurations will be mentioned with a brief description.

As stated before, each synchronous generator provides reactive power to the loads, to maintain its own voltage magnitude. Along the feeders, other devices are required to stabilize the voltage.

The most common compensating devices are fixed shunt capacitors and reactors. The shunt capacitors compensate for the load reactive power, basically showing at the connection point with the grid feeder an equivalent unity power factor load. In distribution systems they are connected close to the most reactive loads, while in transmission systems their position and sizing is designed through power flow analysis, to guarantee the voltage level even in critical conditions, i.e. lines overloading. Shunt reactors are usually required to compensate the long (>200km) cables capacitance effect under low load conditions. In this case, a mainly leading current is absorbed from the feeder, that causes along the light loaded line a voltage drop in phase with the feeder voltage, resulting in overvoltage at the end of the line. Another option are series capacitors, used to reduce the equivalent line reactance, thus increasing the loading capability of the line while keeping voltage control, as seen in Fig. A.4 .

It is important to note that for transmission lines the concentrated parameters analysis fails, due to the high line length. In such a scenario, the line has to be treated as a communication channel, with a characteristic impedance, and the voltage support becomes equivalent to closing the line on its characteristic impedance. Being the load normally fixed, the compensation acts on the impedance, distributing capacitors along the line. Being this work focused on microgrids, all these considerations will be neglected.

Moving toward active compensation schemes instead of fixed compensators, synchronous condensers are synchronous machines without prime mover and speed control, with the AVR only that maintains the terminals voltage by changing the excitation current (and thus the equivalent load represented by the machine) depending on reactive power needs of the network. Another important category of devices used both in distribution and transmission for voltage control are the transformers with tap-changer, where the turn ratio is automatically changes to compensate for voltage variations. More recent solutions are represented by Static VAR Compensators, TCR, TSC, TSR, and STATCOMs. TSR (Thyristor Switched Reactors) and TSC (Thyristor Switched Capacitors) are basically equivalent to static shunt compensators, with the addition of electronically controlled switches (SCR) to select the right amount of compensation, switching on and off the connections with the reactive components. Given a bank of inductors or capacitors, the number of connected devices is selected by a voltage controller. TCR (Thyristors Controlled Reactors) are variable equivalent inductors, where a single fixed inductor is present and the value of the required inductance is selected by a voltage controller. The controller selects the firing angle of the thyristors in order to reduce the current and obtain the desired equivalent inductive behaviour. STATCOM is a power converter able to inject the reactive power required to control the voltage. The performances of a STATCOM are generally better than the SVCs, for different reasons. First, the V-I characteristic is improved, because the STATCOM can control the rated current even with very low PCC voltages, while the SVCs have a reactive current proportional to the PCC voltage. This is an advantage especially during transient events, where the voltage could vary significantly. Fig. A.10 reports a simplified structure of SVCs and STATCOM:

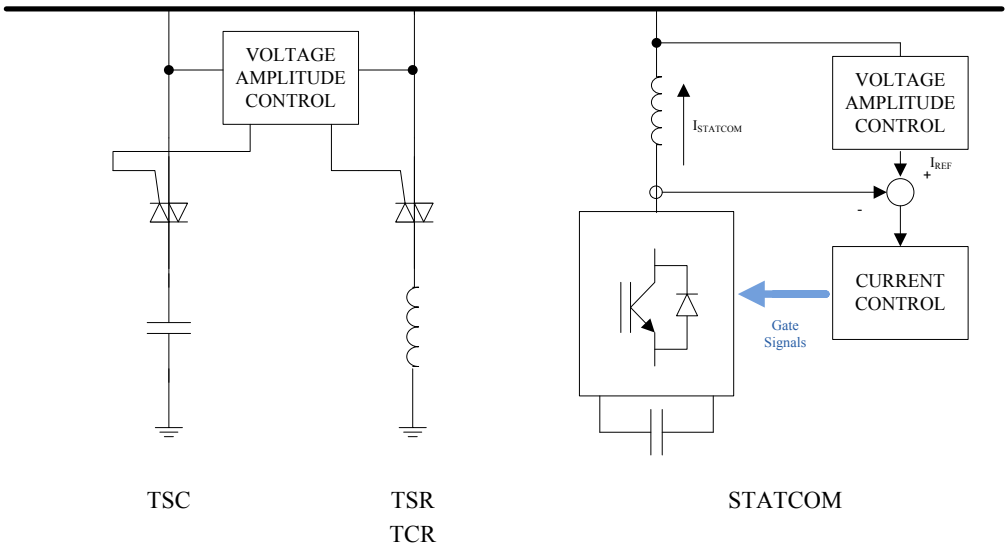

Fig. A.10 SVCs and STATCOM: simplified blocks model

Before concluding this part, is worth to spend few word about the specific voltage regulation techniques traditionally adopted in distribution systems, schematically reported in Fig. A.11 , that are the core of this work. Distribution system can be divided into MV (Medium Voltage) distribution and LV (Low Voltage) distribution. Voltage control is usually done at the substation with the transmission (HV, High Voltage) system and at the beginning of each MV/LV feeder, using transformers with tap changers. Along the LV feeders, SVCs are commonly used to support the voltage, especially in case of critical loads or long feeders. This is simply a hierarchical organization of voltage support, in general other compensating devices can be planned in the network.

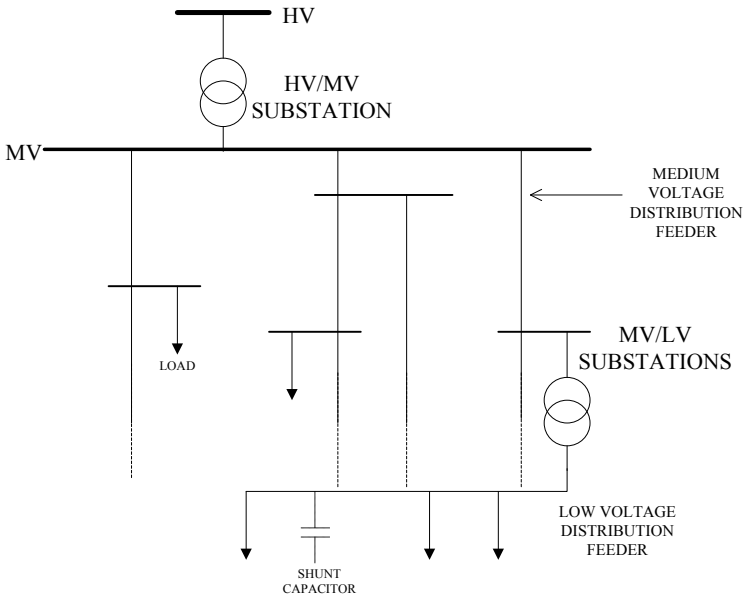

Fig. A.11 Schematic representation of a distribution system

A.6. Power flow equations

All the general considerations made so far, have been related to very simple equivalent circuit configurations. A real power system is a complex network of interacting loads, generators and connections with other networks. The functionality of the power system supervision system, requires the knowledge of the state of the system, i.e. the complex values of the voltages at each node of the network, or in other words the voltages at the terminations of each branch. The typical scenario presents a limited knowledge over the system, meaning that only a partial information on the system state can be derived from the limited available information. Assuming a known model of the network, i.e. a known topology, the remaining information on the state can be derived. This task of extracting all the network state is solved through the Power Flow Analysis. The brief introduction of this analysis can be presented from the nodal representation of a generic network, where a the structure of a node X is reported in Fig. A.12 . $\dot{I}_n$ is the net current injected by the generators and loads connected to node n. From the loads, the admittance $\dot{Y}_n$ is excluded and will be included in the network topology. $\dot{I}_{nm}$ and $\dot{I}_{nz}$ are the currents in the paths toward the other nodes connected to node n.

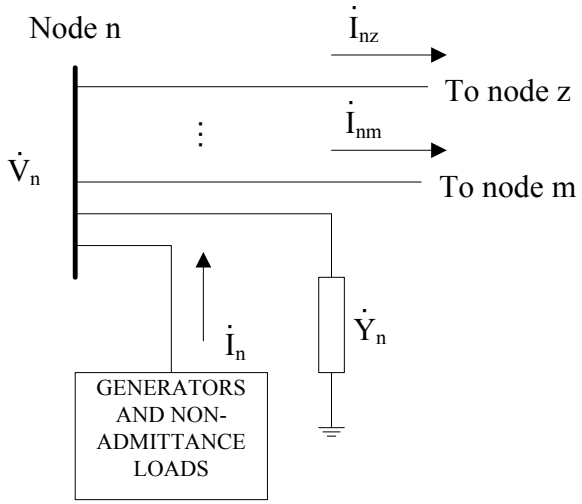

Fig. A.12 Generic network node

The model of the network can be easily built assuming to know all the node voltages. In that case, the Substitution Theorem can be applied, substituting all the loads (excluding the fixed admittances) and generators connected to the node with a voltage generator. Simply applying the superposition of effects, the following model results:

$$I = YV \tag{A.18}$$

Where I and V are the vectors of complex nodes voltages and currents ($\dot{I}_n$ and $\dot{V}_n$ in Fig. A.12), sized respectively 1xN and Nx1 where N is the total number of nodes. The elements nn of matrix Y are the sum of all the admittances directly connected to node n (admittance $\dot{Y}_n$ and impedances of the paths connecting n with the neighbour nodes), while elements nm are the negative sum of the impedances in the path connecting neighbour nodes n and m. So far, the model is linear. The actual problem is that normally the currents are not a known variable, and power representation is preferred. Hence, defining H the set of neighbour nodes, including the centre n, from current $\dot{I}_n$, the complex power $\dot{S}_n$ can be written from (A.18) as:

$$\begin{aligned}
&\dot{I}_n = \sum_{m\in H} \dot{Y}_{nm}\dot{V}_m \\
&\dot{S}_n = \dot{V}_n \dot{I}_n^{\,*} = \dot{V}_n \left(\sum_{m\in H} \dot{Y}_{nm}\dot{V}_m \right)^* = V_n e^{j\varphi_n} \sum_{m\in H} (G_{nm} - jB_{nm}) V_m e^{-j\varphi_m} = \\
&= V_n \sum_{m\in H} V_m \left(G_{nm}\cos\varphi_{nm} + B_{nm}\sin\varphi_{nm} + j(G_{nm}\sin\varphi_{nm} - B_{nm}\cos\varphi_{nm}) \right)
\end{aligned} \tag{A.19}$$

Where $\varphi_{nm} = \varphi_n - \varphi_m$. From the complex power, the active and reactive power injected by node n results:

$$\begin{aligned}
P_n &= V_n \sum_{m\in H} V_m \left(G_{nm}\cos\varphi_{nm} + B_{nm}\sin\varphi_{nm} \right) = \sum_{m\in H} P_{nm}(V_n, V_m, \varphi_n, \varphi_m) \\
Q_n &= V_n \sum_{m\in H} V_m \left(G_{nm}\sin\varphi_{nm} - B_{nm}\cos\varphi_{nm} \right) = \sum_{m\in H} Q_{nm}(V_n, V_m, \varphi_n, \varphi_m)
\end{aligned} \tag{A.20}$$

Where P_{nn} and Q_{nn} are the powers of the nod admittances. From (A.20), four variables for each node are involved in the model: the active and reactive power, the voltage magnitude and phase. The resulting model is non linear. Depending on the node type, some variables are known. In a PQ node, the powers are known, while voltage and phase are unknown. In a PU node, active power and voltage are known, reactive power and phase have to be calculated. This bus is related with a voltage controlled node. Finally, a single Uφ node is always required, with full voltage information and unknown power. Its phase is usually taken as reference for the other voltages. This node represents the main generator, or the connection with a neighbour system, and guarantees power balance. For the loads and generators, other models than the constant PQ or PU models could be used, substituting the known values of P and Q with functions of the voltages (see ZIP load models, [136]). If N_{PQ} and N_{PU} are the number of PQ and PU nodes, the final system results in $N_{PQ}+N_{PU}$ unknown voltage phases plus N_{PQ} unknown voltage magnitudes, for a total of $2N_{PQ}+N_{PU}$ unknowns. From the N_{PQ} nodes, N_{PQ} equations (A.20) can be written, and N_{PU} are written from PU active power equations. The equations and the unknown are balance, that is a required condition to possibly find a

solution. Once all the voltages are known, the remaining reactive power of the PU units are derived. The analytical solution of the power flow non linear equations is analytically possible only for small systems. Normally, a solver based on iterative numeric methods (Gauss-Seidel Iteration, Newton-Raphson Method, LinDistFlow equations) is used. Power systems textbooks contain all the details for the interested reader.

Appendix B

Coordinates transformation, DQ current control and Space Vector Modulation

B.1. Coordinates transformation

The abc to DQ transformation is a coordinates change from a three phase system to a rotating DQ frame. The transformation can be divided in two stages, passing through the αβ stationary frame. Globally we have an abc to αβ transformation and an αβ to DQ transformation. These coordinates changes are independent on the initial three phase system, for this reason in the following definition of the transformation matrices a general three phase vector will be considered, and then the sinusoidal case will be introduced:

$$\overline{X}_{abc}(t) = \begin{bmatrix} X_a(t) \\ X_b(t) \\ X_c(t) \end{bmatrix} \tag{B.1}$$

The abc to αβ transformation is obtained as:

$$\overline{X}_{\alpha\beta 0}(t) = T_{abc/\alpha\beta 0}\,\overline{X}_{abc}(t) \tag{B.2}$$

Where the matrix $T_{abc/\alpha\beta 0}$ is defined as:

$$T_{abc/\alpha\beta 0} = \frac{2}{3}\begin{bmatrix} 1 & -\frac{1}{2} & -\frac{1}{2} \\ 0 & \frac{\sqrt{3}}{2} & -\frac{\sqrt{3}}{2} \\ \frac{1}{2} & \frac{1}{2} & \frac{1}{2} \end{bmatrix} \tag{B.3}$$

And then

$$\begin{aligned} X_\alpha(t) &= \frac{2}{3}\left(X_a(t) - \frac{1}{2}X_b(t) - \frac{1}{2}X_c(t) \right) \\ X_\beta(t) &= \frac{2}{3}\left(\frac{\sqrt{3}}{2}X_b(t) - \frac{\sqrt{3}}{2}X_c(t) \right) \\ X_0(t) &= \frac{2}{3}\left(\frac{1}{2}\left(X_a(t) + X_b(t) + X_c(t) \right) \right) \end{aligned} \tag{B.4}$$

Where the coefficient *2/3* has been added to conserve the amplitude, of the transformed signals in the sinusoidal case, and X_0 is the omopolar component. From another point of view, that will become clearer in the sinusoidal case, the transformation can be seen as a linear transformation of the concatenated variables:

$$\begin{aligned} X_\alpha(t) &= \frac{1}{3}\left((X_a(t) - X_b(t)) - (X_c(t) - X_a(t)) \right) = \frac{1}{3}\left(X_{ab}(t) - X_{ca}(t) \right) \\ X_\beta(t) &= \frac{\sqrt{3}}{3}\left(X_b(t) - X_c(t) \right) = \frac{\sqrt{3}}{3}X_{bc}(t) \\ X_0(t) &= \frac{1}{3}\left(X_a(t) + X_b(t) + X_c(t) \right) \end{aligned} \tag{B.5}$$

If the generic three phase system is balanced, i.e. $X_a(t)+X_b(t)+X_c(t)=0$, the omopolar component vanishes, and the result is the change from a three phase system to a two phase (two dimensions) orthogonal system, where the orthogonal axis are:

$$\begin{aligned} \bar{v}_{\alpha 0} &= [1 \quad 0] \\ \bar{v}_{\beta 0} &= [0 \quad 1] \end{aligned} \tag{B.6}$$

And thus

$$\bar{X}_{\alpha\beta}(t) = \bar{v}_{\alpha 0}X_\alpha(t) + \bar{v}_{\beta 0}X_\beta(t) \tag{B.7}$$

Equivalently, the α component can be seen as the real part and the β component as the imaginary part of the complex number:

$$\dot{X}_{\alpha\beta}(t) = X_\alpha(t) + jX_\beta(t) \tag{B.8}$$

Moving back to the (A.1), the initial generic three phase system (independently on the sinusoidal waveform or not) can always be written as a *space vector* in the complex plane using the following notation, that will turn out to be equivalent to (B.8):

$$\dot{X}_{abc}(t) = \frac{2}{3}(X_a(t) + X_b(t)e^{\frac{2\pi}{3}j} + X_c(t)e^{\frac{4\pi}{3}j} \tag{B.9}$$

The real part of (B.9) corresponds to the α component of (B.8):

$$\mathrm{Re}\left[\dot{X}_{abc}(t)\right]=\frac{2}{3}(X_a(t)-\frac{1}{2}X_b(t)+-\frac{1}{2}X_c(t))=X_\alpha(t) \tag{B.10}$$

And the imaginary part to the β component:

$$\mathrm{Im}\left[\dot{X}_{abc}(t)\right]=\frac{2}{3}\left(\frac{\sqrt{3}}{2}X_b(t)-\frac{\sqrt{3}}{2}X_c(t)\right)=X_\beta(t) \tag{B.11}$$

And if $X_a(t)+X_b(t)+X_c(t)=0$:

$$\mathrm{Re}\left[\dot{X}_{abc}(t)\right]=X_a(t)=X_\alpha(t) \tag{B.12}$$

For this reason the α axis is also denoted as *a* axis.

In the more general case of unbalanced three phase system, $(X_a(t)+X_b(t)+X_c(t))/3\neq 0$, and the three phase vector can be written as the sum of a balanced three phase, plus a common function $X_0(t)$, the omopolar component:

$$X_0(t)=\frac{X_a(t)+X_a(t)+X_a(t)}{3} \tag{B.13}$$

$$\begin{aligned}\overline{X}^{u}{}_{abc}(t)&=\overline{X}^{b}{}_{abc}(t)+\overline{X}_0(t)\\ \overline{X}_0(t)&=\begin{bmatrix}X_0(t)\\X_0(t)\\X_0(t)\end{bmatrix}\end{aligned} \tag{B.14}$$

Where the apices *b* and *u* stand for *balanced* and *unbalanced*. From (B.9), (B.10) and (B.11), and also from (B.3), the omopolar component has no effects on the αβ components. This is a general result, the information related with the omopolar component is never reflected on the orthogonal transformation, and for this reason in (B.3) the omopolar component is kept in the transformation, to transfer all the information from the original system. The inverse transform, directly comes inverting $T_{abc/\alpha\beta 0}$, obtaining:

$$T_{\alpha\beta 0/abc}=\begin{bmatrix}1 & 0 & 1\\ -\frac{1}{2} & \frac{\sqrt{3}}{2} & 1\\ -\frac{1}{2} & -\frac{\sqrt{3}}{2} & 1\end{bmatrix} \tag{B.15}$$

The space vector $\dot{X}_{\alpha\beta}(t) = X_\alpha(t) + jX_\beta(t)$ is a rotating vector in the stationary frame αβ. If the three phase system is sinusoidal and balanced, the resulting space vector rotates at constant ω, that is the pulsation of the system, but in general ω is not constant.

Moreover, in different control applications, from drives to power electronics systems, is useful to express the rotating vector in a synchronous rotating frame, the DQ frame, instead of a stationary frame. Fig. B.1 schematically reports this concept:

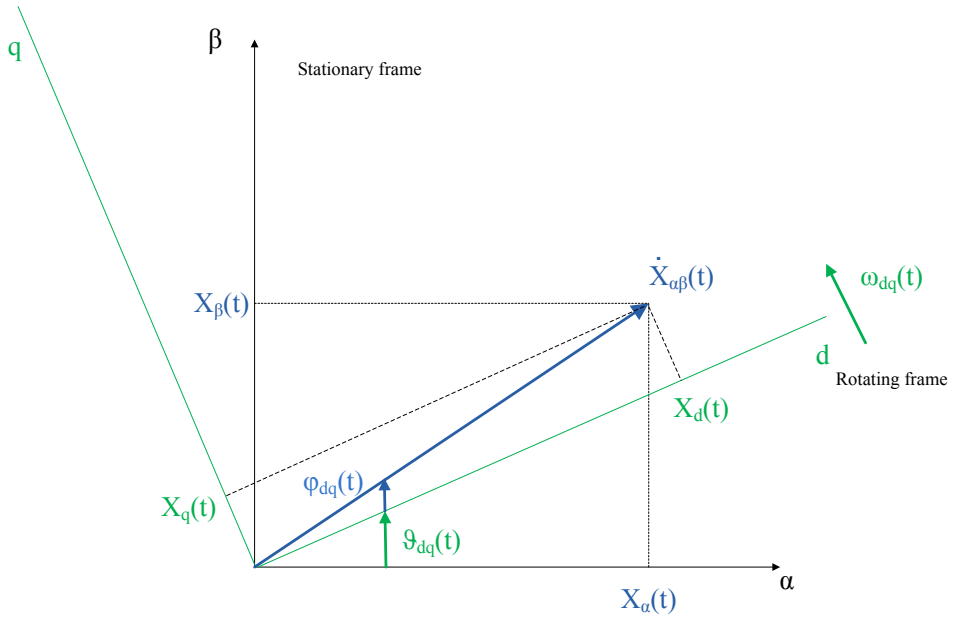

Fig. B.1 Rotating and stationary frames

From Fig. B.1 follows the αβ to DQ transformation:

$$\begin{aligned} X_d(t) &= X_\alpha(t)\cos\vartheta_{dq} + X_\beta(t)\sin\vartheta_{dq} \\ X_q(t) &= -X_\alpha(t)\sin\vartheta_{dq} + X_\beta(t)\cos\vartheta_{dq} \end{aligned} \tag{B.16}$$

The transformation matrix, including the omopolar component, that passes through the transformation is:

$$T_{\alpha\beta0/dq0} = \begin{bmatrix} \cos\vartheta_{dq} & \sin\vartheta_{dq} & 0 \\ -\sin\vartheta_{dq} & \cos\vartheta_{dq} & 0 \\ 0 & 0 & 1 \end{bmatrix} \tag{B.17}$$

The correspondent inverse transformation is:

$$T_{dq0/\alpha\beta0} = \begin{bmatrix} \cos\vartheta_{dq} & -\sin\vartheta_{dq} & 0 \\ \sin\vartheta_{dq} & \cos\vartheta_{dq} & 0 \\ 0 & 0 & 1 \end{bmatrix} \tag{B.18}$$

The global transformation from abc to dq is:

$$T_{abc/dq0} = \frac{2}{3}\begin{bmatrix} \cos\vartheta_{dq} & \cos\left(\vartheta_{dq}-\frac{2\pi}{3}\right) & \cos\left(\vartheta_{dq}-\frac{4\pi}{3}\right) \\ -\sin\vartheta_{dq} & -\sin\left(\vartheta_{dq}-\frac{2\pi}{3}\right) & -\sin\left(\vartheta_{dq}-\frac{4\pi}{3}\right) \\ \frac{1}{2} & \frac{1}{2} & \frac{1}{2} \end{bmatrix} \quad \text{(B.19)}$$

Note that ϑ_{dq} is the angle between the stationary frame and the rotating frame.

If the three phase system is asymmetric, that is the case for example of s sinusoidal system with phase legs different from $2\pi/3$ between the phases, the resulting αβ transform is the sum between a positive and a negative sequence, i.e. an anticlockwise rotating space vector ($e^{j\omega t}$) and a clockwise rotating one ($e^{-j\omega t}$).

All the general consideration that have been done so far, also apply for purely sinusoidal three phase systems. It is worth to mention the case of a fundamental system with harmonics, that is one of the most common scenario in power electronics systems. For example, using the fundamental dq reference frame transformation the fifth and seventh harmonic both appear as sixth harmonic, and in particular, if the fundamental component is the positive sequence, the fifth and seventh harmonic are negative and positive sequence respectively. Table B.1 resumes the most relevant harmonics:

abc harmonic order	Sequence	Harmonic and sequence in fundamental dq rotating frame
5	Negative	6 negative (clockwise)
7	Positive	6 positive (anticlockwise)
9	Negative	12 negative (clockwise)
11	Positive	12 positive (anticlockwise)
13	Negative	18 negative (clockwise)
19	Positive	18 positive (anticlockwise)

Table B.1 D DQ harmonics

B.2. DQ current control

Fig. B.2 reports the simplified schematic of a grid connected STATCOM. V_{aS},V_{bS},V_{cS} are the STATCOM output voltages, while V_{aPCC},V_{bPCC},V_{cPCC} the grid voltages at the point of common coupling (PCC). The dq current control is a rotating frame control, and thus, compared with a stationary frame control, ensure zero error in steady state following a fundamental frequency current reference, being voltages and currents constant in the dq reference.

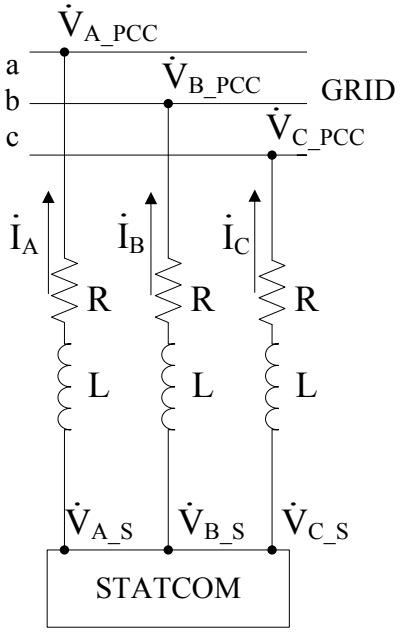

Fig.B.2 Grid connected STATCOM

Assuming an ideal sinusoidal three phase system at the PCC, and sinusoidal generation from the STATCOM (an average model is considered that neglects the commutations), equations (B.20) follow:

$$\begin{aligned} v_{A\_S}(t) &= Ri_A(t) + L\frac{di_A(t)}{dt} + v_{A\_PCC}(t) \\ v_{B\_S}(t) &= Ri_B(t) + L\frac{di_B(t)}{dt} + v_{B\_PCC}(t) \\ v_{C\_S}(t) &= Ri_C(t) + L\frac{di_C(t)}{dt} + v_{C\_PCC}(t) \end{aligned} \tag{B.20}$$

Moreover, a three wires three phase system , i.e. without neutral, is assumed, so that $i_A+ i_B+ i_C=0$, and the same holds for the current derivatives. In Fig. B.2, the voltages are referred to an arbitrary common point, being the current independent on any omopolar component of the voltages. In these condition, the abc to αβ transformation can be applied to equations (B.20). Neglecting the omopolar part in (B.3), and for the linearity of the transformation:

$$\begin{aligned} v_{\alpha\_S}(t) &= Ri_{\alpha}(t) + L\frac{di_{\alpha}(t)}{dt} + v_{\alpha\_PCC}(t) \\ v_{\beta\_S}(t) &= Ri_{\beta}(t) + L\frac{di_{\beta}(t)}{dt} + v_{\beta\_PCC}(t) \end{aligned} \tag{B.21}$$

A general DQ transformation is now applied, defining without loss of generality $\vartheta_{dq}=\omega t$, where ω is the fundamental frequency of the PCC voltage. From (B.17)

$$T_{\alpha\beta/dq} = \begin{bmatrix} \cos\vartheta_{dq} & \sin\vartheta_{dq} \\ -\sin\vartheta_{dq} & \cos\vartheta_{dq} \end{bmatrix} = \begin{bmatrix} T_d \\ T_q \end{bmatrix} \tag{B.22}$$

Hence:

$$\begin{aligned} v_{d\_S}(t) &= Ri_{d}(t) + C_1 + v_{d\_PCC}(t) \\ v_{q\_S}(t) &= Ri_{q}(t) + C_2 + v_{q\_PCC}(t) \end{aligned} \tag{B.23}$$

Where:

$$\begin{aligned} &\begin{bmatrix} C_1 \\ C_2 \end{bmatrix} = \begin{bmatrix} T_d \\ T_q \end{bmatrix} L \begin{bmatrix} \frac{di_{\alpha}(t)}{dt} \\ \frac{di_{\beta}(t)}{dt} \end{bmatrix} = L \begin{bmatrix} \frac{di_{d}(t)}{dt} \\ \frac{di_{q}(t)}{dt} \end{bmatrix} - L \begin{bmatrix} \frac{dT_d}{dt} \\ \frac{dT_q}{dt} \end{bmatrix} \begin{bmatrix} i_{\alpha}(t) \\ i_{\beta}(t) \end{bmatrix} = \\ &= L \begin{bmatrix} \frac{di_{d}(t)}{dt} \\ \frac{di_{q}(t)}{dt} \end{bmatrix} - L \begin{bmatrix} -\omega\sin\omega t & \omega\cos\omega t \\ -\omega\cos\omega t & -\omega\sin\omega t \end{bmatrix} \begin{bmatrix} i_{\alpha}(t) \\ i_{\beta}(t) \end{bmatrix} = \\ &= L \begin{bmatrix} \frac{di_{d}(t)}{dt} \\ \frac{di_{q}(t)}{dt} \end{bmatrix} + \omega L \begin{bmatrix} \sin\omega t & -\cos\omega t \\ \cos\omega t & \sin\omega t \end{bmatrix} \begin{bmatrix} i_{\alpha}(t) \\ i_{\beta}(t) \end{bmatrix} = L \begin{bmatrix} \frac{di_{d}(t)}{dt} \\ \frac{di_{q}(t)}{dt} \end{bmatrix} + \omega L \begin{bmatrix} -i_{q}(t) \\ i_{d}(t) \end{bmatrix} \end{aligned} \tag{B.24}$$

And finally:

$$\begin{aligned} v_{d\_S}(t) &= Ri_{d}(t) + L\frac{di_{d}(t)}{dt} - \omega L i_{q}(t) + v_{d\_PCC}(t) \\ v_{q\_S}(t) &= Ri_{q}(t) + L\frac{di_{q}(t)}{dt} + \omega L i_{d}(t) + v_{q\_PCC}(t) \end{aligned} \tag{B.25}$$

Equation (B.25) can be translated into the Laplace transforms block diagram of Fig. B.3:

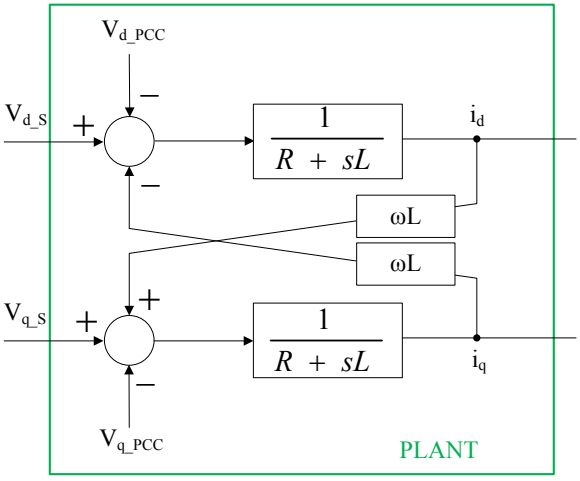

Fig. B.3 DQ reference frame plant

From Fig. B.3, representing just the plant to be controlled, in Fig. B.4 the whole control system is reported, assuming for simplicity ideal STATCOM (inverter) and an analog control. To control two independent currents for the D and the Q component, the PCC voltage feed forward and the cross coupling compensation have been added:

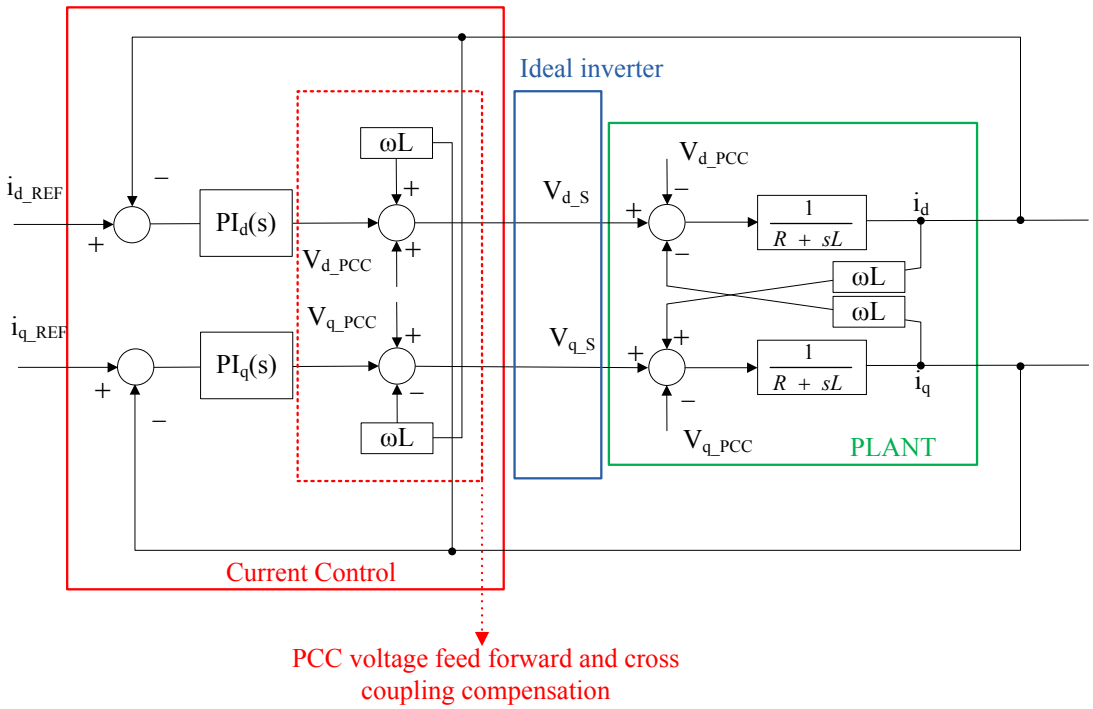

Fig. B.4 Current control scheme

The result obtained from the control system in Fig. B.4, is a complete decoupling of the D and the Q current controllers, leading to the final scheme of Fig. B.5, where a digital control implementation is assumed, taking into account the sampling delay, and the inverter and the digital modulator are modeled as a ZOH:

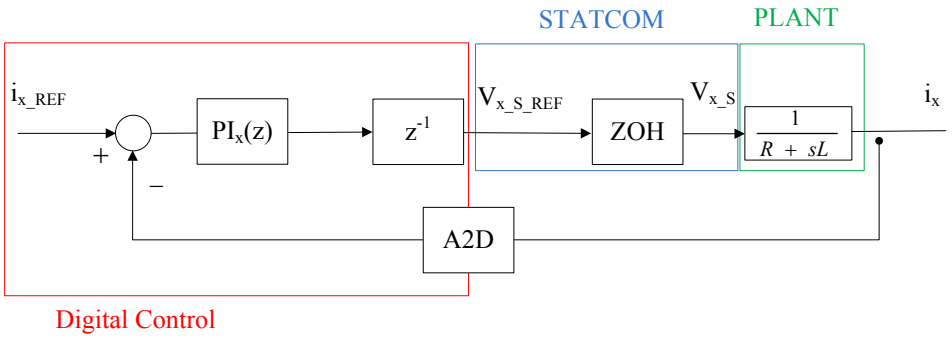

Fig. B.5 Final current control loop, where x is D or Q, z^{-1} is the sampling delay, A2D the analog to digital conversion and $PI_X(z)$ the digital PI controller

In Fig. B.5, a mixed Z-transform and Laplace-transform notation has been used, to highlight the different nature of the system components. In the controller design, an approximated approach has been used, neglecting the effects of the delay and of the ZOH, designing the continuous time $PI_x(s)$ based on the plant transfer function and eventually discretizing to obtain the regulator $PI_x(z)$ in the discrete time domain. The resulting approach is quite simplified, but justified in the specific application by the need for a fast prototyping of the system.

B.3. Space Vector Modulation SVM

Once the DQ components for the STATCOM control, $V_{D\_REF\_S}$ and $V_{Q\_REF\_S}$ have been determined from Fig. B.5, they have to be translated in a switching sequence for the converter IGBTs. One of the most common techniques for implementing a PWM in three phase systems with insulated neutral is the Space Vector Modulation, SVM. The SVM guarantees a maximum exploitation of the hardware, thanks to an automatic third harmonic injection (see Flat Top modulation in literature). To explain the SVM, Fig. B.6 has been used, derived from Fig. B.2 adding the switches and the DC link voltage:

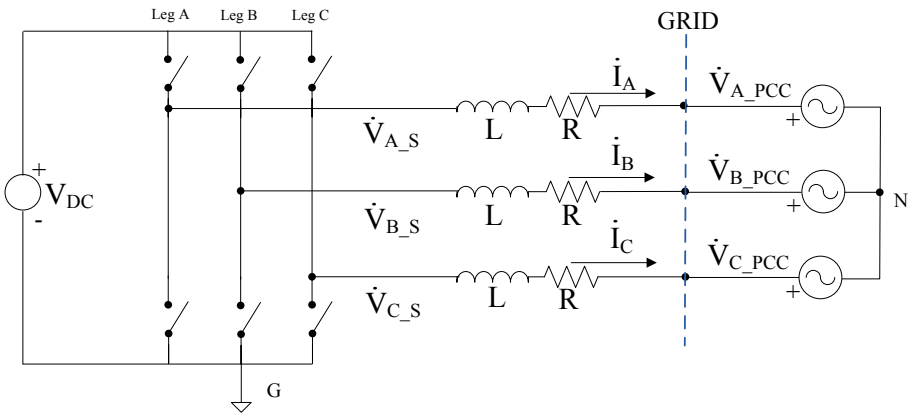

Fig. B.6 Three phase STATCOM, simplified scheme

First of all, some preliminary consideration:

- The neutral cable, N in Fig. B.6, is insulated, and V_{A_PCC} V_{B_PCC} V_{C_PCC} are referred to N
- The phase voltages V_{A_S} V_{B_S} V_{C_S} generated by the STATCOM are referred to the ground G, that is the negative terminal of the single ended DC link voltage
- L, R and V_{X_PCC} are symmetrical and balanced

The DQ components of the STATCOM voltage are firstly transformed back into the αβ reference frame, and thus sent to the SVM block. From Fig. B.6, each STATCOM voltage can assume either the value zero or V_{DC}, being complementary the modulation of the switches in each leg. The three phase output of the STATCOM can therefore assume eight different instantaneous values, reported in Table B.2. Each of the possible combinations, can be transformed in the αβ frame, applying (B.3). Doing the transformation, the STATCOM states are translated into space vectors in the αβ plane. Naming the space vectors V_{000}… V_{111} as in table B.2, the result of the transformation is reported in Fig. B.7.

STATE	V_A_S	V_B_S	V_C_S
V000	0	0	0
V001	0	0	VDC
V010	0	VDC	0
V011	0	VDC	VDC
V100	VDC	0	0
V101	VDC	0	VDC
V110	VDC	VDC	0
V111	VDC	VDC	VDC

Table B.2 STATCOM output voltages

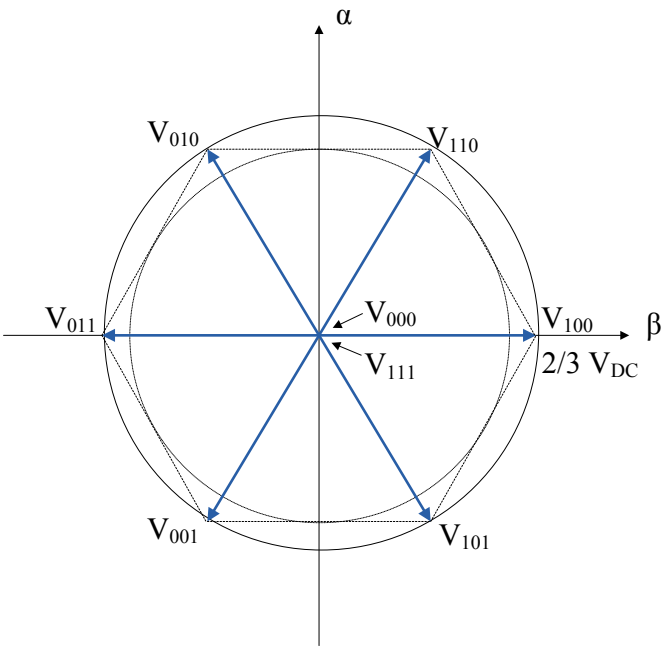

Fig. B.7 STATCOM output states in the αβ plane

From Fig. B.7, SVM results straightforward: each modulation period T_S the current control requests a specific space vector $V^*_{\alpha\beta}$ to be generated by the STATCOM. The requested space vector, in steady state will be a constant module, constant frequency vector, rotating in the αβ plane. The values of this vector, sampled at T_S, can be obtained in each modulation cycle, i.e. PWM interrupt routine execution, combining three space vectors representing the output states of the STATCOM, applying each of them for a portion of the modulation period, so that the average vector in the modulation period corresponds to the requested $V^*_{\alpha\beta}$. Fig. B.8 reports an arbitrary $V^*_{\alpha\beta}$, showing how the reference vector is obtained as combination of the two nearest inverter states, i.e. with only one leg changing state during the application of the vectors sequence. Naming V_1 the projection of $V^*_{\alpha\beta}$ on the first nearest state, i.e. V_{110} in the example, and V_2 the projection on the second state:

$$\begin{aligned} V_1 &= V_{110}\delta_1 \\ V_2 &= V_{100}\delta_2 \\ V^*_{\alpha\beta} &= V_1 + V_2 \end{aligned} \tag{B.26}$$

It is possible to derive the duty cycles δ_1 e δ_2 of the two vectors:

$$\begin{aligned} \delta_1 &= \frac{|V_1|}{|V_{110}|} \\ \delta_2 &= \frac{|V_2|}{|V_{100}|} \end{aligned} \tag{B.27}$$

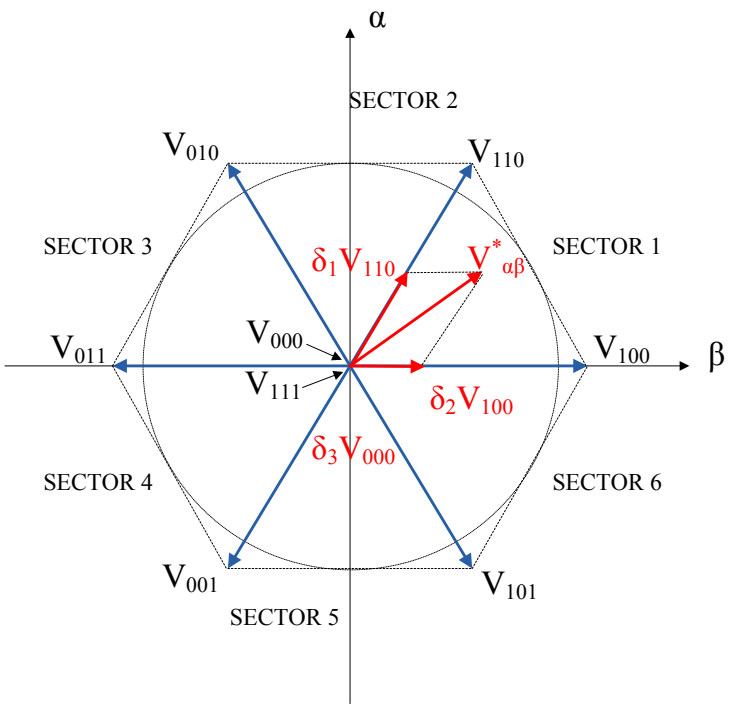

Fig. B.8 Definition of the applied output vectors and duty cycles

Moreover, a null state, i.e. V_{111} or V_{000}, with duty cycle δ_3 is generally required to fulfil the constraint of the total duration limited to the modulation period T_S:

$$\delta_1 + \delta_2 + \delta_2 = 1 \tag{B.28}$$

The sequence of application of the calculated vectors within the modulation period T_S is a degree of freedom, and another degree of freedom is the choice of the null state, being V_{111} and V_{000} equivalent in terms of average effect on the output vector. A possible choice is to select the sequence that minimizes the IGBTs commutations, thus minimizing the losses. Another choice is the sequence that minimizes the current ripple. The two possible solutions are depicted in Fig B.9:

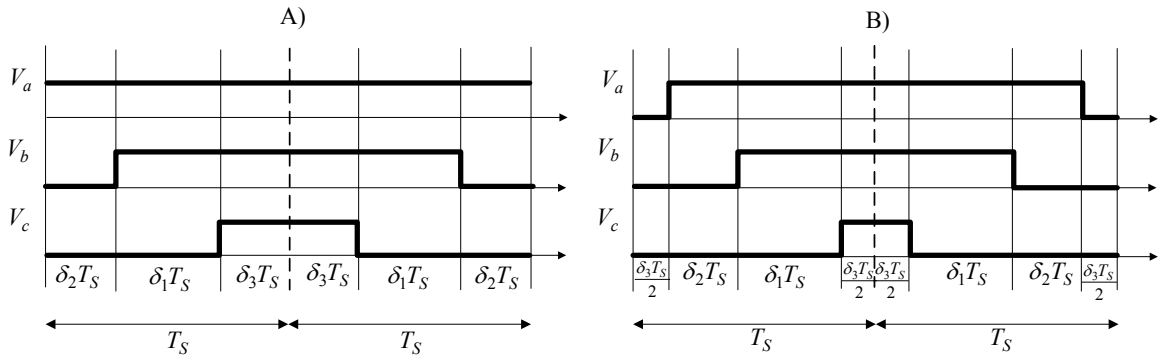

Fig. B.9 A) Minimum loss SVM, B)Minimum current ripple SVM, referred to a $V^*_{\alpha\beta}$ in sector 1

It must be noted that the resulting switching frequency T_{SW} of the IGBTs is half the sampling frequency. For this reason, the complete SVM sequence is exploited in two sequential modulation periods T_S. This result can also be considered from the very basic concepts of three phase systems with insulated neutral: the inductors currents only depends on the concatenated voltages. In this modulation, the concatenated voltages have a frequency that is twice the line voltages frequency (intending with frequency the modulation frequency and not the low frequency of the modulant signal), thanks to the cantered proposed modulation. Of course this is not the only possible solution, the SVM could potentially be used also with different symmetries.

Moreover, it can be verified that a $V^*_{\alpha\beta}$ lying within the inscribed circle in Fig. B.8, can always be represented by a valid triplet δ_1 δ_2 δ_3. Out of the circle, a limited number of vectors results to be allowed, e.g. a vector $V^*_{\alpha\beta}$ exactly matching one of the STATCOM output states is one of the allowed, thus causing distortion of the generated waveform, that can be sinusoidal if and only if its amplitude is less than the inscribed circle. The maximum amplitude of the generated voltage, i.e. of the STATCOM generated voltage sinusoid, neglecting switching harmonic components and omopolar values is derived through trigonometry equations from Fig. B.8:

$$V_{MAX} = V_{STATE\_MAX} * \cos\frac{\pi}{6} = \frac{2}{3}V_{DC} * \frac{\sqrt{3}}{2} = 1.15\frac{V_{DC}}{2} \tag{B.29}$$

When an higher voltage is demanded, the output of the SVM saturates, thus causing a distorted generated voltage. There are different strategies to manage the saturation: once a saturation is detected, i.e. sum of the three duty cycles greater than one, all the values can be proportionally reduced to come back to an allowed combination or just the lower component can be reduced to fulfil the unity sum. The first solution ensures phase conservation, the second one doesn't conserve the phase but has the interesting property of collapsing the SVM into a six-steps modulation in case of deep saturation.

Equation B.29 also shows one of the main advantages of the SVM, that is the capability of generating output line (and thus concatenated) voltages 15% higher than half the DC link voltage. The reason is the omopolar component of the STATCOM line generated voltages with respect to G in Fig. B.6, that always have an added or subtracted $V_{DC}/2$ constant voltage. This can be easily seen applying the transformation $T_{abc/\alpha\beta0}$ of (a.3) to the STATCOM output states, that are referred to G. Keeping G as reference, the instantaneous N voltage can be written as (referring to Fig. B.6 and assuming symmetrical impedances):

$$v_{NG}(t) = \frac{1}{3}\left((v_{A\_S} + v_{B\_S} + v_{C\_S}) - (v_{A\_PCC} + v_{B\_PCC} + v_{C\_PCC})\right)(t) \tag{B.30}$$

Assuming the grid with zero omopolar component, the N voltage with respect to G equals the omopolar component of the STATCOM generated voltages. An omopolar component in the voltages doesn't affect the line currents and the concatenated voltages, but affects v_{NG}. The sequence of SVM states generates a $v_{NG}(t)$ that turns out to be equivalent to a third harmonics injection in the STATCOM voltages, a commonly used technique used in PWM controlled three phase inverters without neutral, that adding a third harmonic to all the STATCOM phase voltages leads to an increased linearity region of the converter, fully exploiting the hardware. In the SVM, the added omopolar component to the STATCOM voltages referred to G, will correspond, averaging over T_{SW}, to a constant voltage $V_{DC}/2$ with a superposed third harmonic with amplitude $0.196*V_{DC}/2$.

Bibliography

[1] A. Ipakchi and F. Albuyeh, "Grid of the future," *Power and Energy Magazine, IEEE*, vol. 7, no. 2, pp. 52 –62, march-april 2009.

[2] H. Farhangi, "The path of the smart grid," *Power and Energy Magazine, IEEE*, vol. 8, no. 1, pp. 18 –28, january-february 2010.

[3] J. Momoh, "Smart grid design for efficient and flexible power networks operation and control," in *Power Systems Conference and Exposition, 2009. PSCE '09. IEEE/PES*, march 2009, pp. 1 –8.

[4] L. Tsoukalas and R. Gao, "From smart grids to an energy internet: Assumptions, architectures and requirements," in *Electric Utility Deregulation and Restructuring and Power Technologies, 2008. DRPT 2008. Third International Conference on*, april 2008, pp. 94 –98.

[5] S. Collier, "Ten steps to a smarter grid," in *Rural Electric Power Conference, 2009. REPC '09. IEEE*, april 2009, pp. B2 –B2–7.

[6] T. Jin and M. Mechehoul, "Ordering electricity via internet and its potentials for smart grid systems," *IEEE T. Smart Grids*, vol. 1, no. 3, pp. 302 –310, dec. 2010.

[7] K. Moslehi and R. Kumar, "A reliability perspective of the smart grid," *IEEE T. Smart Grids*, vol. 1, no. 1, pp. 57 –64, june 2010.

[8] R. Anderson, A. Boulanger, W. Powell, and W. Scott, "Adaptive stochastic control for the smart grid," *Proc. IEEE*, vol. 99, no. 6, pp. 1098 –1115, june 2011.

[9] A. Cagnano, E. De Tuglie, M. Liserre, and R. Mastromauro, "Online optimal reactive power control strategy of pv inverters," *IEEE T. Ind. Electron.*, vol. 58, no. 10, pp. 4549 –4558, oct. 2011.

[10] Y. Wang and W. Xu, "An investigation on the reactive power support service needs of power producers," in *Power Engineering Society General Meeting, 2004. IEEE*, june 2004, p. 843 Vol.1.

[11] J. Li, C.-C. Liu, and K. Schneider, "Controlled partitioning of a power network considering real and reactive power balance," *IEEE T. Smart Grids*, vol. 1, no. 3, pp. 261 –269, dec. 2010.

[12] K. Bhattacharya and J. Zhong, "Reactive power as an ancillary service," *IEEE T. Power. Syst.*, vol. 16, no. 2, pp. 294 –300, may 2001.

[13] K. Turitsyn, P. Sulc, S. Backhaus, and M. Chertkov, "Options for control of reactive power by distributed photovoltaic generators," *Proc. IEEE*, vol. 99, no. 6, pp. 1063 –1073, june 2011.

[14] M. C. Ahn and T. K. Ko, "Proof-of-concept of a smart fault current controller with a superconducting coil for the smart grid," *IEEE T. Appl. Supercon.*, vol. 21, no. 3, pp. 2201 –2204, june 2011.

[15] U. Khan, J. Seong, S. Lee, S. Lim, and B. Lee, "Feasibility analysis of the positioning of superconducting fault current limiters for the smart grid application using simulink and simpowersystem," *IEEE T. Appl. Supercon.*, vol. 21, no. 3, pp. 2165 –2169, june 2011.

[16] M. Kezunovic, "Smart fault location for smart grids," *IEEE T. Smart Grids*, vol. 2, no. 1, pp. 11 –22, march 2011.

[17] M. He and J. Zhang, "A dependency graph approach for fault detection and localization towards secure smart grid," *IEEE T. Smart Grids*, vol. 2, no. 2, pp. 342 –351, june 2011.

[18] A. Gomez-Exposito, A. Abur, A. de la Villa Jaen, and C. Gomez-Quiles, "A multilevel state estimation paradigm for smart grids," *Proc. IEEE*, vol. 99, no. 6, pp. 952 –976, june 2011.

[19] F. Li, W. Qiao, H. Sun, H. Wan, J. Wang, Y. Xia, Z. Xu, and P. Zhang, "Smart transmission grid: Vision and framework," *IEEE T. Smart Grids*, vol. 1, no. 2, pp. 168 –177, sept. 2010.

[20] D. Bakken, A. Bose, C. Hauser, D. Whitehead, and G. Zweigle, "Smart generation and transmission with coherent, real-time data," *Proc. IEEE*, vol. 99, no. 6, pp. 928 –951, june 2011.

[21] M. Kezunovic, "Translational knowledge: From collecting data to making decisions in a smart grid," *Proc. IEEE*, vol. 99, no. 6, pp. 977 –997, june 2011.

[22] W. Xu and W. Wang, "Power electronic signaling technology ; a new class of power electronics applications," *IEEE T. Smart Grids*, vol. 1, no. 3, pp. 332 –339, dec. 2010.

[23] N. Amjady, F. Keynia, and H. Zareipour, "Short-term load forecast of microgrids by a new bilevel prediction strategy," *IEEE T. Smart Grids*, vol. 1, no. 3, pp. 286 –294, dec. 2010.

[24] T. Vandoorn, B. Meersman, L. Degroote, B. Renders, and L. Vandevelde, "A control strategy for islanded microgrids with dc-link voltage control," *IEEE T. Power. Deliver.*, vol. 26, no. 2, pp. 703 –713, april 2011.

[25] K. De Brabandere, B. Bolsens, J. Van den Keybus, A. Woyte, J. Driesen, R. Belmans, and K. Leuven, "A voltage and frequency droop control method for parallel inverters," in *Power*

Electronics Specialists Conference, 2004. PESC 04. 2004 IEEE 35th Annual, vol. 4, 2004, pp. 2501 – 2507 Vol.4.

[26] J. Guerrero, J. Vasquez, J. Matas, L. de Vicuna, and M. Castilla, "Hierarchical control of droop-controlled ac and dc microgrids; a general approach toward standardization," *IEEE T. Ind. Electron.*, vol. 58, no. 1, pp. 158 –172, jan. 2011.

[27] J. Rocabert, G. Azevedo, A. Luna, J. Guerrero, J. Candela, and P. Rodriguez, "Intelligent connection agent for three-phase grid-connected microgrids," *IEEE T. Power. Electr.*, vol. 26, no. 10, pp. 2993 –3005, oct. 2011.

[28] A. Meliopoulos, G. Cokkinides, R. Huang, E. Farantatos, S. Choi, Y. Lee, and X. Yu, "Smart grid technologies for autonomous operation and control," *IEEE T. Smart Grids*, vol. 2, no. 1, pp. 1 –10, march 2011.

[29] A. Vaccaro, M. Popov, D. Villacci, and V. Terzija, "An integrated framework for smart microgrids modeling, monitoring, control, communication, and verification," *Proc. IEEE*, vol. 99, no. 1, pp. 119 –132, jan. 2011.

[30] J.-Y. Kim, J.-H. Jeon, S.-K. Kim, C. Cho, J. H. Park, H.-M. Kim, and K.-Y. Nam, "Cooperative control strategy of energy storage system and microsources for stabilizing the microgrid during islanded operation," *IEEE T. Power. Electr.*, vol. 25, no. 12, pp. 3037 –3048, dec. 2010.

[31] M. Molina and P. Mercado, "Power flow stabilization and control of microgrid with wind generation by superconducting magnetic energy storage," *IEEE T. Power. Electr.*, vol. 26, no. 3, pp. 910 –922, march 2011.

[32] Y. Li, D. Vilathgamuwa, and P. C. Loh, "Microgrid power quality enhancement using a three-phase four-wire grid-interfacing compensator," *IEEE T. Ind. Appl.*, vol. 41, no. 6, pp. 1707 – 1719, nov.-dec. 2005.

[33] I. Maity and S. Rao, "Simulation and pricing mechanism analysis of a solar-powered electrical microgrid," *Systems Journal, IEEE*, vol. 4, no. 3, pp. 275 –284, sept. 2010.

[34] M. Baran and N. Mahajan, "Dc distribution for industrial systems: opportunities and challenges," *IEEE T. Ind. Appl.*, vol. 39, no. 6, pp. 1596 – 1601, nov.-dec. 2003.

[35] K. Fleischer and R. Munnings, "Power systems analysis for direct current (dc) distribution systems," *IEEE T. Ind. Appl.*, vol. 32, no. 5, pp. 982 –989, sep/oct 1996.

[36] P. Bresesti, W. Kling, R. Hendriks, and R. Vailati, “Hvdc connection of offshore wind farms to the transmission system,” *IEEE T. Energy. Conver.*, vol. 22, no. 1, pp. 37 –43, march 2007.

[37] D. Salomonsson, L. Soder, and A. Sannino, “An adaptive control system for a dc microgrid for data centers,” in *Industry Applications Conference, 2007. 42nd IAS Annual Meeting. Conference Record of the 2007 IEEE*, sept. 2007, pp. 2414 –2421.

[38] H. Kakigano, Y. Miura, and T. Ise, “Low-voltage bipolar-type dc microgrid for super high quality distribution,” *IEEE T. Power. Electr.*, vol. 25, no. 12, pp. 3066 –3075, dec. 2010.

[39] A. Kwasinski, “Quantitative evaluation of dc microgrids availability: Effects of system architecture and converter topology design choices,” *IEEE T. Power. Electr.*, vol. 26, no. 3, pp. 835 –851, march 2011.

[40] D. Boroyevich, I. Cvetkovic, D. Dong, R. Burgos, F. Wang, and F. Lee, “Future electronic power distribution systems a contemplative view,” in *Optimization of Electrical and Electronic Equipment (OPTIM), 2010 12th International Conference on*, may 2010, pp. 1369 –1380.

[41] B. Irving and M. Jovanovic, “Analysis, design, and performance evaluation of droop current-sharing method,” in *Applied Power Electronics Conference and Exposition, 2000. APEC 2000. Fifteenth Annual IEEE*, vol. 1, 2000, pp. 235 –241 vol.1.

[42] A. Molderink, V. Bakker, M. Bosman, J. Hurink, and G. Smit, “Management and control of domestic smart grid technology,” *IEEE T. Smart Grids*, vol. 1, no. 2, pp. 109 –119, sept. 2010.

[43] R. DeBlasio and C. Tom, “Standards for the smart grid,” in *Energy 2030 Conference, 2008. ENERGY 2008. IEEE*, nov. 2008, pp. 1 –7.

[44] A. Mohd, E. Ortjohann, W. Sinsukthavorn, M. Lingemann, N. Hamsic, and D. Morton, “Supervisory control and energy management of an inverter-based modular smart grid,” in *Power Systems Conference and Exposition, 2009. PSCE ’09. IEEE/PES*, march 2009, pp. 1 –6.

[45] R. Majumder, A. Ghosh, G. Ledwich, and F. Zare, “Power management and power flow control with back-to-back converters in a utility connected microgrid,” *IEEE T. Power. Syst.*, vol. 25, no. 2, pp. 821 –834, may 2010.

[46] E. Serban and H. Serban, “A control strategy for a distributed power generation microgrid application with voltage- and current-controlled source converter,” *IEEE T. Power. Electr.*, vol. 25, no. 12, pp. 2981 –2992, dec. 2010.

[47] S. Iyer, M. Belur, and M. Chandorkar, "A generalized computational method to determine stability of a multi-inverter microgrid," *IEEE T. Power. Electr.*, vol. 25, no. 9, pp. 2420 –2432, sept. 2010.

[48] E. Barklund, N. Pogaku, M. Prodanovic, C. Hernandez-Aramburo, and T. Green, "Energy management in autonomous microgrid using stability-constrained droop control of inverters," *IEEE T. Power. Electr.*, vol. 23, no. 5, pp. 2346 –2352, sept. 2008.

[49] N. Pogaku, M. Prodanovic, and T. Green, "Modeling, analysis and testing of autonomous operation of an inverter-based microgrid," *IEEE T. Power. Electr.*, vol. 22, no. 2, pp. 613 –625, march 2007.

[50] Q.-C. Zhong and G. Weiss, "Synchronverters: Inverters that mimic synchronous generators," *IEEE T. Ind. Electron.*, vol. 58, no. 4, pp. 1259 –1267, april 2011.

[51] C. Sao and P. Lehn, "Autonomous load sharing of voltage source converters," *IEEE T. Power. Deliver.*, vol. 20, no. 2, pp. 1009 – 1016, april 2005.

[52] J. Eto, R. Lasseter, B. Schenkman, J. Stevens, D. Klapp, H. Volkommer, E. Linton, H. Hurtado, and J. Roy, "Overview of the certs microgrid laboratory test bed," in *Integration of Wide-Scale Renewable Resources Into the Power Delivery System, 2009 CIGRE/IEEE PES Joint Symposium*, july 2009, p. 1.

[53] P. Piagi and R. Lasseter, "Autonomous control of microgrids," in *Power Engineering Society General Meeting, 2006. IEEE*, 0-0 2006, p. 8 pp.

[54] R. Majumder, B. Chaudhuri, A. Ghosh, R. Majumder, G. Ledwich, and F. Zare, "Improvement of stability and load sharing in an autonomous microgrid using supplementary droop control loop," *IEEE T. Power. Syst.*, vol. 25, no. 2, pp. 796 –808, may 2010.

[55] Y. W. Li and C.-N. Kao, "An accurate power control strategy for power-electronics-interfaced distributed generation units operating in a low-voltage multibus microgrid," *IEEE T. Power. Electr.*, vol. 24, no. 12, pp. 2977 –2988, dec. 2009.

[56] Y. Li and Y. W. Li, "Power management of inverter interfaced autonomous microgrid based on virtual frequency-voltage frame," *IEEE T. Smart Grids*, vol. 2, no. 1, pp. 30 –40, march 2011.

[57] S.-J. Ahn, J.-W. Park, I.-Y. Chung, S.-I. Moon, S.-H. Kang, and S.-R. Nam, "Power-sharing method of multiple distributed generators considering control modes and configurations of a microgrid," *IEEE T. Power. Deliver.*, vol. 25, no. 3, pp. 2007 –2016, july 2010.

[58] J. Guerrero, J. Vasquez, J. Matas, M. Castilla, and L. de Vicuna, "Control strategy for flexible microgrid based on parallel line-interactive ups systems," *IEEE T. Ind. Electron.*, vol. 56, no. 3, pp. 726 –736, march 2009.

[59] J. Kim, J. Guerrero, P. Rodriguez, R. Teodorescu, and K. Nam, "Mode adaptive droop control with virtual output impedances for an inverter-based flexible ac microgrid," *IEEE T. Power. Electr.*, vol. 26, no. 3, pp. 689 –701, march 2011.

[60] D. De and V. Ramanarayanan, "Decentralized parallel operation of inverters sharing unbalanced and nonlinear loads," *IEEE T. Power. Electr.*, vol. 25, no. 12, pp. 3015 –3025, dec. 2010.

[61] J. Guerrero, L. GarciadeVicuna, J. Matas, M. Castilla, and J. Miret, "Output impedance design of parallel-connected ups inverters with wireless load-sharing control," *IEEE T. Ind. Electron.*, vol. 52, no. 4, pp. 1126 – 1135, aug. 2005.

[62] P.-T. Cheng, C.-A. Chen, T.-L. Lee, and S.-Y. Kuo, "A cooperative imbalance compensation method for distributed-generation interface converters," *IEEE T. Ind. Appl.*, vol. 45, no. 2, pp. 805 –815, march-april 2009.

[63] M. Prodanovic and T. Green, "High-quality power generation through distributed control of a power park microgrid," *IEEE T. Ind. Electron.*, vol. 53, no. 5, pp. 1471 –1482, oct. 2006.

[64] T. Vandoorn, B. Renders, L. Degroote, B. Meersman, and L. Vandevelde, "Active load control in islanded microgrids based on the grid voltage," *IEEE T. Smart Grids*, vol. 2, no. 1, pp. 139 –151, march 2011.

[65] B. Zhao, C. Guo, and Y. Cao, "A multiagent-based particle swarm optimization approach for optimal reactive power dispatch," *IEEE T. Power. Syst.*, vol. 20, no. 2, pp. 1070 – 1078, may 2005.

[66] K. Rogers, R. Klump, H. Khurana, A. Aquino-Lugo, and T. Overbye, "An authenticated control framework for distributed voltage support on the smart grid," *IEEE T. Smart Grids*, vol. 1, no. 1, pp. 40 –47, june 2010.

[67] C. Hernandez-Aramburo, T. Green, and N. Mugniot, "Fuel consumption minimization of a microgrid," *IEEE T. Ind. Appl.*, vol. 41, no. 3, pp. 673 – 681, may-june 2005.

[68] A. Mehrizi-Sani and R. Iravani, "Potential-function based control of a microgrid in islanded and grid-connected modes," *IEEE T. Power. Syst.*, vol. 25, no. 4, pp. 1883 –1891, nov. 2010.

[69] A. Dimeas and N. Hatziargyriou, “Operation of a multiagent system for microgrid control,” *IEEE T. Power. Syst.*, vol. 20, no. 3, pp. 1447 – 1455, aug. 2005.

[70] A. Conejo, J. Morales, and L. Baringo, “Real-time demand response model,” *IEEE T. Smart Grids*, vol. 1, no. 3, pp. 236 –242, dec. 2010.

[71] A. Mohsenian-Rad, V. Wong, J. Jatskevich, R. Schober, and A. Leon-Garcia, “Autonomous demand-side management based on game-theoretic energy consumption scheduling for the future smart grid,” *IEEE T. Smart Grids*, vol. 1, no. 3, pp. 320 –331, dec. 2010.

[72] F. Rahimi and A. Ipakchi, “Demand response as a market resource under the smart grid paradigm,” *IEEE T. Smart Grids*, vol. 1, no. 1, pp. 82 –88, june 2010.

[73] C. Yuen, A. Oudalov, and A. Timbus, “The provision of frequency control reserves from multiple microgrids,” *IEEE T. Ind. Electron.*, vol. 58, no. 1, pp. 173 –183, jan. 2011.

[74] S. Chowdhury, S. Chowdhury, C. Ten, and P. Crossley, “Operation and control of dg based power in smart grid environment,” in *Electricity Distribution - Part 1, 2009. CIRED 2009. 20th International Conference and Exhibition on*, june 2009, pp. 1 –5.

[75] C. Moreira and J. Pecas Lopes, “Microgrids dynamic security assessment,” in *Clean Electrical Power, 2007. ICCEP ’07. International Conference on*, may 2007, pp. 26 –32.

[76] R. Best, D. Morrow, D. Laverty, and P. Crossley, “Techniques for multiple-set synchronous islanding control,” *IEEE T. Smart Grids*, vol. 2, no. 1, pp. 60 –67, march 2011.

[77] A. Mohd, E. Ortjohann, A. Schmelter, N. Hamsic, and D. Morton, “Challenges in integrating distributed energy storage systems into future smart grid,” in *Industrial Electronics, 2008. ISIE 2008. IEEE International Symposium on*, 30 2008-july 2 2008, pp. 1627 –1632.

[78] B. Roberts, “Capturing grid power,” *Power and Energy Magazine, IEEE*, vol. 7, no. 4, pp. 32 –41, july-aug. 2009.

[79] J. Crider and S. Sudhoff, “Reducing impact of pulsed power loads on microgrid power systems,” *IEEE T. Smart Grids*, vol. 1, no. 3, pp. 270 –277, dec. 2010.

[80] S. Han, S. Han, and K. Sezaki, “Development of an optimal vehicle-to-grid aggregator for frequency regulation,” *IEEE T. Smart Grids*, vol. 1, no. 1, pp. 65 –72, june 2010.

[81] A. Boulanger, A. Chu, S. Maxx, and D. Waltz, “Vehicle electrification: Status and issues,” *Proc. IEEE*, vol. 99, no. 6, pp. 1116 –1138, june 2011.

[82] D. Tran, H. Zhou, and A. Khambadkone, “Energy management and dynamic control in composite energy storage system for micro-grid applications,” in *IECON 2010 - 36th Annual Conference on IEEE Industrial Electronics Society*, nov. 2010, pp. 1818 –1824.

[83] H. Zhou, T. Bhattacharya, D. Tran, T. Siew, and A. Khambadkone, “Composite energy storage system involving battery and ultracapacitor with dynamic energy management in microgrid applications,” *IEEE T. Power. Electr.*, vol. 26, no. 3, pp. 923 –930, march 2011.

[84] H. Nikkhajoei and R. Lasseter, “Distributed generation interface to the certs microgrid,” *IEEE T. Power. Deliver.*, vol. 24, no. 3, pp. 1598 –1608, july 2009.

[85] M. Glinkowski, J. Hou, and G. Rackliffe, “Advances in wind energy technologies in the context of smart grid,” *Proc. IEEE*, vol. 99, no. 6, pp. 1083 –1097, june 2011.

[86] A. Elmitwally and M. Rashed, “Flexible operation strategy for an isolated pv-diesel microgrid without energy storage,” *IEEE T. Energy. Conver.*, vol. 26, no. 1, pp. 235 –244, march 2011.

[87] A. Saha, S. Chowdhury, S. Chowdhury, P. Crossley, and C. Gaunt, “Microturbine based distributed generator in smart grid application,” in *Electricity Distribution - Part 1, 2009. CIRED 2009. 20th International Conference and Exhibition on*, june 2009, pp. 1 –6.

[88] S. Bifaretti, P. Zanchetta, A. Watson, L. Tarisciotti, and J. Clare, “Advanced power electronic conversion and control system for universal and flexible power management,” *IEEE T. Smart Grids*, vol. 2, no. 2, pp. 231 –243, june 2011.

[89] M. Shahraeini, M. Javidi, and M. Ghazizadeh, “Comparison between communication infrastructures of centralized and decentralized wide area measurement systems,” *IEEE T. Smart Grids*, vol. 2, no. 1, pp. 206 –211, march 2011.

[90] T. Sauter and M. Lobashov, “End-to-end communication architecture for smart grids,” *IEEE T. Ind. Electron.*, vol. 58, no. 4, pp. 1218 –1228, april 2011.

[91] Y.-J. Kim, M. Thottan, V. Kolesnikov, and W. Lee, “A secure decentralized data-centric information infrastructure for smart grid,” *Communications Magazine, IEEE*, vol. 48, no. 11, pp. 58 –65, november 2010.

[92] G. Arnold, “Challenges and opportunities in smart grid: A position article,” *Proc. IEEE*, vol. 99, no. 6, pp. 922 –927, june 2011.

[93] A. Mahmood, M. Aamir, and M. Anis, “Design and implementation of amr smart grid system,” in *Electric Power Conference, 2008. EPEC 2008. IEEE Canada*, oct. 2008, pp. 1 –6.

[94] S. Galli, A. Scaglione, and Z. Wang, “For the grid and through the grid: The role of power line communications in the smart grid,” *Proc. IEEE*, vol. 99, no. 6, pp. 998 –1027, june 2011.

[95] G. Srinivasa Prasanna, A. Lakshmi, S. Sumanth, V. Simha, J. Bapat, and G. Koomullil, “Data communication over the smart grid,” in *Power Line Communications and Its Applications, 2009. ISPLC 2009. IEEE International Symposium on*, 29 2009-april 1 2009, pp. 273 –279.

[96] Y. Kim, J. N. Bae, and J. Y. Kim, “Performance of power line communication systems with noise reduction scheme for smart grid applications,” *IEEE T. Consum. Electr.*, vol. 57, no. 1, pp. 46 –52, february 2011.

[97] D. Guezgouz, D. Chariag, Y. Raingeaud, and J.-C. Le Bunetel, “Modeling of electromagnetic interference and plc transmission for loads shedding in a microgrid,” *IEEE T. Power. Electr.*, vol. 26, no. 3, pp. 747 –754, march 2011.

[98] V. Gungor, B. Lu, and G. Hancke, “Opportunities and challenges of wireless sensor networks in smart grid,” *IEEE T. Ind. Electron.*, vol. 57, no. 10, pp. 3557 –3564, oct. 2010.

[99] Z. Fadlullah, M. Fouda, N. Kato, A. Takeuchi, N. Iwasaki, and Y. Nozaki, “Toward intelligent machine-to-machine communications in smart grid,” *Communications Magazine, IEEE*, vol. 49, no. 4, pp. 60 –65, april 2011.

[100]M. Erol-Kantarci and H. Mouftah, “Wireless sensor networks for cost-efficient residential energy management in the smart grid,” *IEEE T. Smart Grids*, vol. 2, no. 2, pp. 314 –325, june 2011.

[101]H. Gharavi and B. Hu, “Multigate communication network for smart grid,” *Proc. IEEE*, vol. 99, no. 6, pp. 1028 –1045, june 2011.

[102]B. Sadler and A. Swami, “Synchronization in sensor networks: an overview,” in *Military Communications Conference, 2006. MILCOM 2006. IEEE*, oct. 2006, pp. 1 –6.

[103]R. Carli and S. Zampieri, “Networked clock synchronization based on second order linear consensus algorithms,” in *Decision and Control (CDC), 2010 49th IEEE Conference on*, dec. 2010, pp. 7259 –7264.

[104]J. De La Ree, V. Centeno, J. Thorp, and A. Phadke, “Synchronized phasor measurement applications in power systems,” *IEEE T. Smart Grids*, vol. 1, no. 1, pp. 20 –27, june 2010.

[105]G. Ericsson, “Cyber security and power system communication ;essential parts of a smart grid infrastructure,” *IEEE T. Power. Deliver.*, vol. 25, no. 3, pp. 1501 –1507, july 2010.

[106]T. Overman, R. Sackman, T. Davis, and B. Cohen, “High-assurance smart grid: A three-part model for smart grid control systems,” *Proc. IEEE*, vol. 99, no. 6, pp. 1046 –1062, june 2011.

[107]H. Khurana, M. Hadley, N. Lu, and D. Frincke, “Smart-grid security issues,” *Security Privacy, IEEE*, vol. 8, no. 1, pp. 81 –85, jan.-feb. 2010.

[108]T. Kim and H. Poor, “Strategic protection against data injection attacks on power grids,” *IEEE T. Smart Grids*, vol. 2, no. 2, pp. 326 –333, june 2011.

[109]G. Heydt, “The next generation of power distribution systems,” *IEEE T. Smart Grids*, vol. 1, no. 3, pp. 225 –235, dec. 2010.

[110]K. Macken, M. Bollen, and R. Belmans, “Mitigation of voltage dips through distributed generation systems,” in *Industry Applications Conference, 2003. 38th IAS Annual Meeting. Conference Record of the*, vol. 2, oct. 2003, pp. 1068 – 1074 vol.2.

[111]E. Jauch, “Possible effects of smart grid functions on ltc transformers,” in *Rural Electric Power Conference (REPC), 2010 IEEE*, may 2010, pp. B1 –B1–10.

[112]H. Nikkhajoei and R. Iravani, “Steady-state model and power flow analysis of electronically-coupled distributed resource units,” *IEEE T. Power. Deliver.*, vol. 22, no. 1, pp. 721 – 728, jan. 2007.

[113]K. Schneider, D. Chassin, Y. Chen, and J. Fuller, “Distribution power flow for smart grid technologies,” in *Power Systems Conference and Exposition, 2009. PSCE ’09. IEEE/PES*, march 2009, pp. 1 –7.

[114]H. Laaksonen, “Protection principles for future microgrids,” *IEEE T. Power. Electr.*, vol. 25, no. 12, pp. 2910 –2918, dec. 2010.

[115]D. Divan and H. Johal, “A smarter grid for improving system reliability and asset utilization,” in *Power Electronics and Motion Control Conference, 2006. IPEMC 2006. CES/IEEE 5th International*, vol. 1, aug. 2006, pp. 1 –7.

[116]R. Brown, “Impact of smart grid on distribution system design,” in *Power and Energy Society General Meeting - Conversion and Delivery of Electrical Energy in the 21st Century, 2008 IEEE*, july 2008, pp. 1 –4.

[117]M. Sebastian, J. Marti, and P. Lang, “Evolution of dso control centre tool in order to maximize the value of aggregated distributed generation in smart grid,” in *SmartGrids for Distribution, 2008. IET-CIRED. CIRED Seminar*, june 2008, pp. 1 –4.

[118]R. Belhomme, R. De Asua, G. Valtorta, A. Paice, F. Bouffard, R. Rooth, and A. Losi, “Address - active demand for the smart grids of the future,” in *SmartGrids for Distribution, 2008. IET-CIRED. CIRED Seminar*, june 2008, pp. 1 –4.

[119]L. de Souza Ribeiro, O. Saavedra, S. de Lima, and J. Gomes de Matos, “Isolated micro-grids with renewable hybrid generation: The case of lencois island,” *Sustainable Energy, IEEE Transactions on*, vol. 2, no. 1, pp. 1 –11, jan. 2011.

[120]J.-H. Jeon, J.-Y. Kim, H.-M. Kim, S.-K. Kim, C. Cho, J.-M. Kim, J.-B. Ahn, and K.-Y. Nam, “Development of hardware in-the-loop simulation system for testing operation and control functions of microgrid,” *IEEE T. Power. Electr.*, vol. 25, no. 12, pp. 2919 –2929, dec. 2010.

[121]*Aristoncavi, General Catalogue, Technical data for low voltage cables www.aristoncavi.com*.

[122]*"1547 Standard for Interconnecting Distributed Resources With Electric Power Systems", March 1999*, IEEE Std.

[123]C. Smythe, “Iso 8802/5 token ring local-area networks,” *Electronics Communication Engineering Journal*, vol. 11, no. 4, pp. 195 –207, aug 1999.

[124]S. Gezici, Z. Tian, G. Giannakis, H. Kobayashi, A. Molisch, H. Poor, and Z. Sahinoglu, “Localization via ultra-wideband radios: a look at positioning aspects for future sensor networks,” *Signal Processing Magazine, IEEE*, vol. 22, no. 4, pp. 70 – 84, july 2005.

[125]D. Dardari, A. Conti, U. Ferner, A. Giorgetti, and M. Win, “Ranging with ultrawide bandwidth signals in multipath environments,” *Proc. IEEE*, vol. 97, no. 2, pp. 404 –426, feb. 2009.

[126]M. C. T. Aysal, B. Oreshkin, “Accelerated distributed average consensus via localized node state prediction,” *IEEE Trans. on Signal Processing*, vol. 57, no. 4, p. 1563–1576, Apr. 2009.

[127]J. M. S. Kar, “Distributed consensus algorithms in sensor networks with imperfect communication: Link failures and channel noise,” *IEEE Trans. on Signal Processing*, vol. 57, no. 1, p. 355–369, Jan. 2009.

[128]F. Carastro, “Power quality enhancement using a shunt active filter with energy storage”, Ph.D. dissertation, University of Nottingham, UK, May 2008.

[129]P. Srithorn, “Control of a STATCOM with supercapacitor energy storage”, Ph.D. dissertation, University of Nottingham, UK, June 2009.

[130]R. Best, D. Morrow, D. McGowan, and P. Crossley, “Synchronous islanded operation of a diesel generator,” *IEEE T. Power. Syst.*, vol. 22, no. 4, pp. 2170 –2176, nov. 2007.

[131]K. L. Cheong, P. Li, and J. Xia, “Control oriented modeling and system identification of a diesel generator set (genset),” in *American Control Conference (ACC), 2010*, 30 2010-july 2 2010, pp. 950 –955.

[132]S. Roy, O. Malik, and G. Hope, “An adaptive control scheme for speed control of diesel driven power-plants,” *IEEE T. Energy. Conver.*, vol. 6, no. 4, pp. 605 –611, dec 1991.

[133]B. Singh and J. Solanki, “Load compensation for diesel generator-based isolated generation system employing dstatcom,” *IEEE T. Ind. Appl.*, vol. 47, no. 1, pp. 238 –244, jan.-feb. 2011.

[134]B. Singh, J. Solanki, A. Chandra, and Kamal-Al-Haddad, “A solid state compensator with energy storage for isolated diesel generator set,” in *Industrial Electronics, 2006 IEEE International Symposium on*, vol. 3, july 2006, pp. 1774 –1778.

[135]L. Wang and D.-J. Lee, “Load-tracking performance of an autonomous sofc-based hybrid power generation/energy storage system,” *IEEE T. Energy. Conver.*, vol. 25, no. 1, pp. 128 –139, march 2010.

[136]P. Kundur, *Power systems stability and control*, M. G. L. Neal J.Balu, Ed. McGraw-Hill, 1994.

[137]C. V. Thierry Van Cutsem, *Voltage stability of electric power systems*, Springer, Ed., 2007.

Publications by the author

International journals

[1] L. Corradini, A. Costabeber, P. Mattavelli, and S. Saggini, "Parameter-independent time-optimal digital control for point-of-load converters," *IEEE T. Power. Electr.*, vol. 24, no. 10, pp. 2235 –2248, oct. 2009.

[2] A. Costabeber, P. Mattavelli, and S. Saggini, "Digital time-optimal phase shedding in multiphase buck converters," *IEEE T. Power. Electr.*, vol. 25, no. 9, pp. 2242 –2247, sept. 2010.

[3] S. Saggini, A. Costabeber, and P. Mattavelli, "A simple digital autotuning for analog controller in smps," *IEEE T. Power. Electr.*, vol. 25, no. 8, pp. 2170 –2178, aug. 2010.

[4] A. Costabeber, P. Mattavelli, S. Saggini, and A. Bianco, "Digital autotuning of dc-dc converters based on a model reference impulse response," *IEEE T. Power. Electr.*, vol. 26, no. 10, pp. 2915 –2924, oct. 2011.

[5] P. Tenti, A. Costabeber, P. Mattavelli, and D. Trombetti, "Distribution loss minimization by token ring control of power electronic interfaces in residential micro-grids," *IEEE T. Ind. Electron.*, vol. PP, no. 99, p. 1, 2011.

[6] G. Spiazzi, P. Mattavelli, and A. Costabeber, "High step-up ratio flyback converter with active clamp and voltage multiplier," *IEEE T. Power. Electr.*, vol. 26, no. 11, pp. 3205 –3214, nov. 2011.

International conferences

[1] A. Costabeber, T. Erseghe, P. Tenti, S. Tomasin, and P. Mattavelli, "Optimization of micro-grid operation by dynamic grid mapping and token ring control," in *Power Electronics and Applications (EPE 2011), Proceedings of the 2011-14th European Conference on*, 30 2011-sept. 1 2011, pp. 1 –10.

[2] A. Costabeber, T. Erseghe, P. Tenti, and S. Tomasin, "Optimum control of distributed energy resources in residential micro-grids," in *PowerTech, 2011 IEEE Trondheim*, june 2011, p. 1.

[3] G. Spiazzi, P. Mattavelli, and A. Costabeber, "Analysis of a high step-up ratio flyback converter with active clamp and voltage multiplier," in *Energy Conversion Congress and Exposition (ECCE), 2010 IEEE*, sept. 2010, pp. 535 –541.

[4] H. Morales Paredes, A. Costabeber, and P. Tenti, “Application of conservative power theory to cooperative control of distributed compensators in smart grids,” in *Nonsinusoidal Currents and Compensation (ISNCC), 2010 International School on*, june 2010, pp. 190 –196.

[5] P. Tenti, A. Costabeber, D. Trombetti, and P. Mattavelli, “Plug and play operation of distributed energy resources in micro-grids,” in *Telecommunications Energy Conference (INTELEC), 32nd International*, june 2010, pp. 1 –6.

[6] P. Tenti, A. Costabeber, and P. Mattavelli, “Improving power quality and distribution efficiency in micro-grids by cooperative control of switching power interfaces,” in *Power Electronics Conference (IPEC), 2010 International*, june 2010, pp. 472 –479.

[7] A. Costabeber, P. Mattavelli, S. Saggini, and A. Bianco, “Digital autotuning of dc-dc converters based on model reference impulse response,” in *Applied Power Electronics Conference and Exposition (APEC), 2010 Twenty-Fifth Annual IEEE*, feb. 2010, pp. 1287 –1294.

[8] P. Tenti, D. Trombetti, A. Costabeber, and P. Mattavelli, “Distribution loss minimization by token ring control of power electronic interfaces in residential micro-grids,” in *Industrial Electronics (ISIE), 2010 IEEE International Symposium on*, july 2010, pp. 2377 –2381.

[9] A. Costabeber, P. Mattavelli, L. Peretti, and M. Zigliotto, “A speed loop autotuning method based on signal injection for electrical drives,” in *Power Electronics, Machines and Drives (PEMD 2010), 5th IET International Conference on*, april 2010, pp. 1 –6.

[10] A. Costabeber, P. Tenti, and P. Mattavelli, “Surround control of distributed energy resources in micro-grids,” in *Sustainable Energy Technologies (ICSET), 2010 IEEE International Conference on*, dec. 2010, pp. 1 –6.

[11] S. Saggini, A. Costabeber, and P. Mattavelli, “A simple digital auto-tuning for analog controller in smps,” in *Applied Power Electronics Conference and Exposition, 2009. APEC 2009. Twenty-Fourth Annual IEEE*, feb. 2009, pp. 252 –258.

[12] A. Costabeber, P. Mattavelli, and S. Saggini, “Fpga implementation of phase shedding with time-optimal controller in multi-phase buck converters,” in *Industrial Electronics, 2009. IECON ’09. 35th Annual Conference of IEEE*, nov. 2009, pp. 2919 –2924.

[13] G. Spiazzi, P. Mattavelli, and A. Costabeber, “Effect of parasitic components in the integrated boost-flyback high step-up converter,” in *Industrial Electronics, 2009. IECON ’09. 35th Annual Conference of IEEE*, nov. 2009, pp. 420 –425.

[14] A. Costabeber, L. Corradini, P. Mattavelli, and S. Saggini, "Time optimal, parameters-insensitive digital controller for dc-dc buck converters," in *Power Electronics Specialists Conference, 2008. PESC 2008. IEEE*, june 2008, pp. 1243 –1249.

[15] L. Corradini, A. Costabeber, P. Mattavelli, and S. Saggini, "Time optimal, parameters-insensitive digital controller for vrm applications with adaptive voltage positioning," in *Control and Modeling for Power Electronics, 2008. COMPEL 2008. 11th Workshop on*, aug. 2008, pp. 1 –8.